HARVARD UNIVERSITY
Graduate School of Arts and Sciences

DISSERTATION ACCEPTANCE CERTIFICATE

The undersigned, appointed by the

Department of Physics

have examined a dissertation entitled

BAT Slew Survey (BATSS): Slew Data Analysis for the *Swift*-BAT Coded Aperture Imaging Telescope

presented by

Antonio Julio Copete

candidate for the degree of Doctor of Philosophy and hereby certify that it is worthy of acceptance.

Signature _____

Typed name: Professor Jonathan E. Grindlay, Co-Chair

Signature _____

Typed name: Professor Christopher Stubbs, Co-Chair

Signature _____

Typed name: Professor Matthew Schwartz

Date: November 2, 2012

BAT Slew Survey (BATSS): Slew Data Analysis for the *Swift*-BAT Coded Aperture Imaging Telescope

A dissertation presented

by

Antonio Julio Copete

to

The Department of Physics

in partial fulfillment of the requirements

for the degree of

Doctor of Philosophy

in the subject of

Physics

Harvard University

Cambridge, Massachusetts

November, 2012

Dissertation Advisor: Professor Jonathan E. Grindlay Antonio J. Copete

BAT Slew Survey (BATSS): Slew Data Analysis for the *Swift*-BAT Coded Aperture Imaging Telescope

Abstract

The BAT Slew Survey (BATSS) is the first wide-field survey of the hard X-ray sky (15–150 keV) with a slewing coded aperture imaging telescope. Its fine time resolution, high sensitivity and large sky coverage make it particularly well-suited for detections of transient sources with variability timescales in the ∼1 sec–1 hour range, such as Gamma-Ray Bursts (GRBs), flaring stars and Blazars. As implemented, BATSS observations are found to be consistently more sensitive than their BAT pointing-mode counterparts, by an average of 20% over the 10 sec–3 ksec exposure range, due to intrinsic systematic differences between them. The survey's motivation, development and implementation are presented, including a description of the software and hardware infrastructure that made this effort possible.

The analysis of BATSS science data concentrates on the results of the 4.8-year BATSS GRB survey, beginning with the discovery of GRB 070326 during its preliminary testing phase. A total of nineteen (19) GRBs were detected exclusively in BATSS slews over this period, making it the largest contribution to the *Swift* GRB catalog from all ground-based analysis. The timing and spectral properties of prompt emission from BATSS GRBs reveal their consistency with *Swift* long GRBs (L-GRBs), though with instances of GRBs with unusually soft spectra or X-Ray Flashes (XRFs), GRBs near the faint end of the fluence distribution accessible to *Swift*-BAT, and a probable short GRB with extended emission, all uncommon traits within the general *Swift* GRB population. In addition, the BATSS overall detection rate of 0.49 GRBs/day of instrument time is a significant increase (45%) above the BAT pointing detection rate. This result was confirmed by a GRB detection simulation model, which further showed the increased sky coverage of slews to be the dominant effect in enhancing GRB detection probabilities.

A review of lessons learned is included, with specific proposals to broaden both the number and range of astrophysical sources found in future enhancements. The BATSS survey results provide solid empirical evidence in support of an all-slewing hard X-ray survey mission, a prospect that may be realized with the launch of the proposed *MIRAX-HXI* mission in 2017.

Page intentionally left blank

Contents

List of Figures

List of Tables

Page intentionally left blank

To the memory of Dr. Graham Charles Grindlay,

a brilliant young researcher whose life was cut short much too soon

Page intentionally left blank

Acknowledgements

The Grindlay group and I in particular are grateful for the support from the *Swift* Guest Investigator program, under grants NNX07AF78G, NNX08AN85G and NNX09AL07G. We also appreciate the feedback and technical support received from S. D. Barthelmy, C. B. Markwardt, H. Krimm and J. Tueller from the *Swift*-BAT team at Goddard Space Flight Center (GSFC).

I owe a great debt of gratitude to other members of the Grindlay group as well, in particular Jae-Sub Hong, Branden Allen, and above all Prof. Grindlay himself, for their formidable and unflinching support throughout this complex research project, their commitment to my education, and their patience during challenging times.

I would also like to acknowledge the support and encouragement of the Harvard Physics and Astronomy Departments at all stages of my graduate education, in particular Profs. Christopher Stubbs and Melissa Franklin, as well as Sheila Ferguson, Kyle Welch, Peggy Herlihy and Lisa Cacciabudo from the technical and administrative staff.

Last but not least, the unconditional love and support of my family, which they have spontaneously demonstrated in many more ways than I can count, have been to me nothing short of invaluable and essential, and I only hope my professional and personal successes can at least serve as a small tribute to their caring efforts.

Page intentionally left blank

Chapter 1

Introduction

The *BAT Slew Survey (BATSS)* is an experimental High-Energy Astrophysics project based on observations with the BAT instrument aboard the *Swift* mission, which has been in orbit since November, 2004. The BAT is a hard X-ray telescope (15–150 keV) employing the *coded aperture imaging* observational technique, and whose primary purpose is the detection of early emission from *Gamma-Ray Bursts (GRBs)*, intense flashes of γ radiation originating at cosmological distances, and believed to be the most luminous objects in the universe. The BAT presented an interesting research opportunity given its ability to collect photon-by-photon data during slews of the *Swift* spacecraft, but which the mission's scientific team was not employing for the purposes of burst imaging and detection during those periods. By seizing on this opportunity, we would first be contributing to *Swift*'s primary science goals by expanding its spatial and temporal window for discovery of GRBs. Further, given our own research group's prior experience in studying the enhanced properties of scanning (slewing) coded aperture imaging as an observational technique (Grindlay & Hong 2004), BATSS observations would constitute the first demonstration of the use of the technique in a fully operating space-based telescope, and would be in a

potentially unique position to explore the faint, high-variability phase space of hard X-ray transients. Added to this was the opportunity to perform the first ever all-sky, hard X-ray slew survey with a coded aperture telescope, as well as the personal challenge of single-handedly building the data analysis infrastructure needed to achieve those goals. For the rest of this Chapter, I delve further into the context the BATSS survey operates on, its motivation from the scientific and technical standpoints, and provide an overview of how I have organized and presented the results of the first 4.8 years of the BATSS survey into the contents of this doctoral dissertation.

Swift-BAT and BATSS

Conceived as a multi-wavelength observatory for the study of Gamma-Ray Bursts (GRBs) as its primary science, *Swift* (Gehrels et al. 2004) is an ongoing NASA medium-sized explorer (MIDEX) mission launched on November 20, 2004. During its remarkably successful run, *Swift* has opened a new era in GRB science exploration by providing by far the largest number of GRB detections with accurate positions, afterglow emission observations and redshift determinations of any past or current mission, becoming in the process the primary GRB observatory that is currently in operation (Gehrels & Mészáros 2012; Gehrels et al. 2009). To this day it continues to enjoy excellent prospects for continued operation, with recommended funding through 2016 and an orbit that will be stable until at least 2020.

The *Swift* spacecraft is characterized by its rapid slewing response (likened to the flight pattern of the namesake bird the mission derives its name from) to on-board detection of flaring astrophysical sources which —in typically less than 90 sec— enables prompt pointed observation of new targets by its two narrow-field instruments (NFIs): the *X-Ray Telescope*

(XRT, 0.3-10 keV, 23.6′ FoV,[1] Burrows et al. 2005) and the *Ultra-Violet/Optical Telescope* (UVOT, 170–650 nm, 17′ FoV, Roming et al. 2005). The third instrument on board, the *Burst Alert Telescope* (BAT, 15–150 keV, Barthelmy et al. 2005), is on the other hand the wide-field telescope ($80^\circ \times 53^\circ$ FoV, FWHM) which, as its name suggests, is responsible for the initial triggering of the slewing response upon detection of the prompt, bright γ-ray emission that is the signature of a new GRB-type of event. A depiction of the *Swift* spacecraft and its three instruments is shown in Figure 1.1.

The BAT is a telescope that employs the *coded aperture imaging* observational technique, which I will review in Chapter 2 within the context of this dissertation. Because of the requirements of the spacecraft's NFIs, which must remain pointed towards a locked position in the sky in order to observe a given target within their narrow FoV, the BAT must perform most of its observations in this "pointing mode" of operation as well, and in fact its software system and figure-of-merit (FOM) algorithm were designed in order to detect GRBs only while observing in this mode (Barthelmy et al. 2005). However, the BAT also has the capability of collecting and recording photon-by-photon data at all times, including during periods of spacecraft slewing, a feature originally implemented with the sole purpose of reconstructing finely time-resolved lightcurves (i.e. emission profiles in the time domain) of early γ-ray emission from GRBs, and for that reason these so-called "event mode" data used to be discarded whenever a candidate GRB discovery was not made.

Recognizing that the BAT's photon-by-photon data collection capability could also be exploited in order to perform imaging and detection of sources during periods of slewing to *Swift* targets, my research group, headed by Prof. Jonathan E. Grindlay, sought to propose the development of a survey that specifically analyzed observations made in the telescope's

[1] FoV = telescope field-of-view, quoted as the diameter in angular units of the portion of the sky viewable by the instrument at any given time.

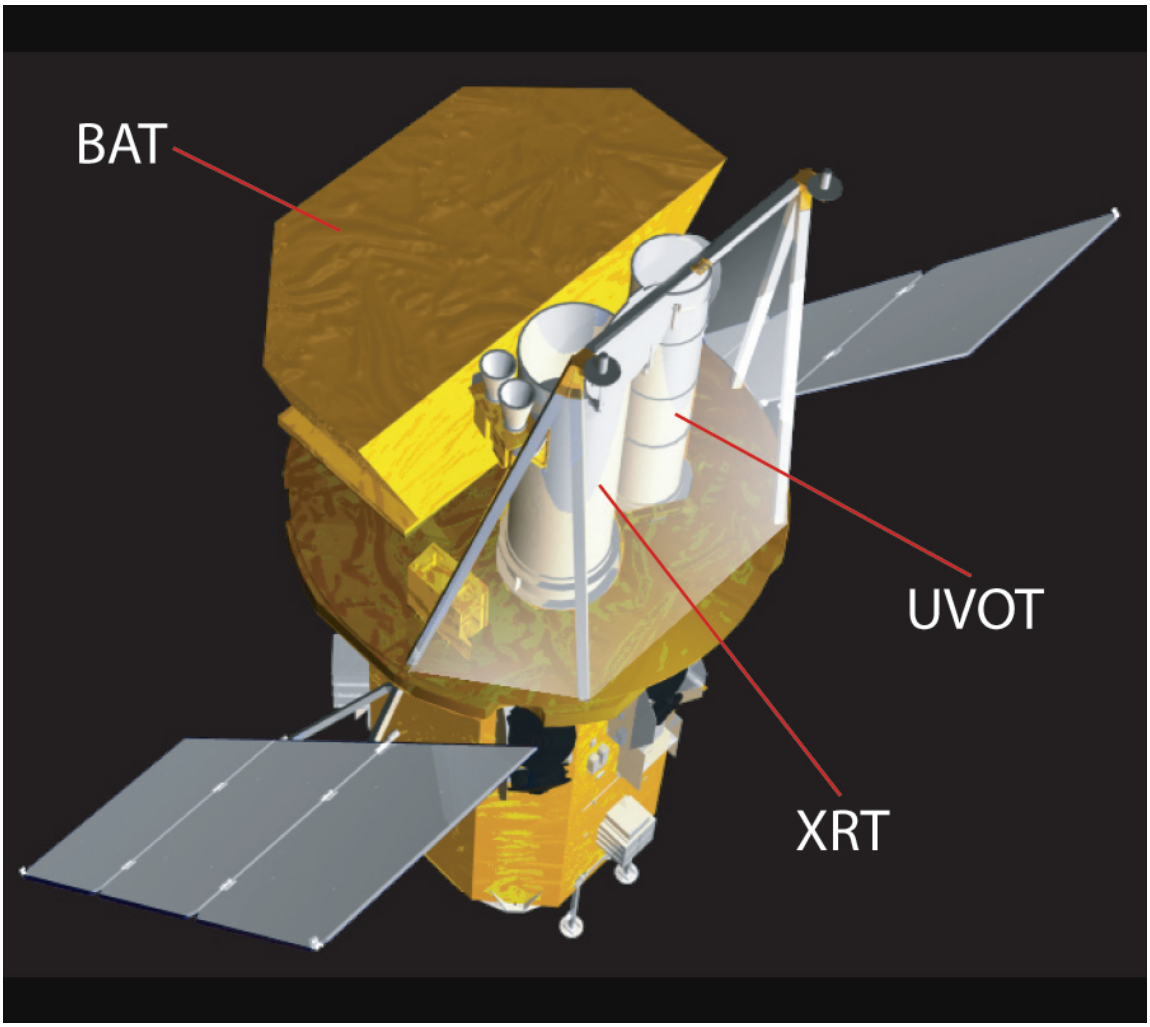

FIGURE 1.1: The *Swift* satellite and its three instruments (Gehrels et al. 2004): the *Burst Alert Telescope* (BAT), the *X-Ray Telescope* (XRT), and the *Ultra-Violet/Optical Telescope* (UVOT), the latter two collectively referred to as the *Narrow-Field Instruments* (NFIs)

"slew mode" of operation, thereby enhancing at a minimum the mission's spatial and time coverage, and possibly also its science discovery domain. All that would be required from *Swift* mission operations would be the enabling of regular capture and downlink of the event data from the BAT that the satellite would discard otherwise, but no other change whatsoever in the way the mission regularly operated, as we would provide the processing capability required once the data was on the ground. This research effort, the *BAT Slew Survey (BATSS)*, is a project I have been thoroughly involved with as the sole doctoral student working on it ever since it was first conceived it in 2005, and its development and main technical and scientific findings are the core subject of this dissertation.

Motivation for BATSS

As originally proposed by Grindlay & Copete (2006–2011) for the *Swift* Guest Investigator (GI) Program, the overall science motivation for BATSS is to conduct a wide-field, hard X-ray (15–150 keV) survey of transient sources with variability timescales in the $\sim$1 sec–1 hr range, as well as low-duty cycle repeated flaring on these timescales, which may have been missed in BAT pointed observations. The survey would begin by focusing primarily on the detection of Gamma-Ray Bursts (GRBs) over individual spacecraft slews in an effort to contribute to the *Swift* mission's primary science goals, and eventually it would expand to study a larger set of objects in this phase space of Time Domain Astrophysics whose underlying physics still remains poorly understood, such as flaring stars and extreme Blazar flares, while allowing for the discovery of new classes of sources as well. Previous efforts of surveying the hard X-ray/soft γ-ray sky include those by the X-ray and Low-Energy γ-ray instrument (A-4) aboard the High Energy Astrophysics Observatory 1 (HEAO 1 A-4, 1977–1979, 13–180 keV, Levine et al. 1984) and by the Burst and Transient Source Experiment (BATSE) aboard the Compton Gamma-Ray Observatory (CGRO, 1991–2000, 20 keV–1 MeV, Harmon et al. 2004). Current ones include those by

INTEGRAL/IBIS (2003–, 17–60 keV, Krivonos et al. 2012), MAXI/GSC (2009–, 4–20 keV, Hiroi et al. 2011), and the *Swift*-BAT's own ongoing pointing survey (2005–, 14–195 keV, Baumgartner et al. 2010, 2011; Markwardt et al. 2005; Tueller et al. 2010, 2008).

The *Swift*-BAT pointing survey is in fact the deepest and most sensitive hard X-ray survey ever made, and the first true full-sky survey of its kind ever since HEAO 1 A-4, as all the other past and current survey missions mentioned are significantly limited in some way in their sky coverage. For comparison, the limiting sensitivity of HEAO 1 A-4 all-sky survey was 17 mCrab,[2] which allowed it to detect only 77 sources (Levine et al. 1984), compared to the limiting BAT survey sensitivity of $\sim$3 mCrab near strong Galactic sources to $\sim$1 mCrab in the high Galactic latitude ($>45^\circ$) sky, i.e. an improvement of 5–17 times over the HEAO 1 A-4 sensitivity (Gehrels et al. 2004). With BATSS having access to the same all-sky area of the BAT pointing survey, and with a higher net sky area and frequency of coverage on short timescales of $\lesssim 1$ day, it also has the potential to make an important scientific contribution to that deepest of all hard X-ray surveys. Slew surveys in general have played important roles in complementing and adding detail to their pointing survey counterparts; prominent examples in High-Energy Astronomy include the *Einstein* Slew Survey (Elvis et al. 1992), a soft X-ray survey (0.3–3.5 keV) carried out with the Imaging Proportional Counter (IPC) instrument aboard the *Einstein Observatory* (HEAO 2, 1978–1982, Giacconi et al. 1979), and the XMM-*Newton* Slew Survey (2005–, 0.2–12 keV, Read et al. 2005; Saxton et al. 2008) currently being performed with data from its namesake soft X-ray observatory. As for slewing coded aperture imaging, it is a technique first proposed only recently by our own research group (Grindlay & Hong 2004), and BATSS would constitute its first realization on a space-based telescope.

[2]The [mCrab] units are commonly used in High-Energy Astrophysics in order to quote source fluxes measured by telescopes of varying spectral responses, as well as instrument sensitivities expressed as the flux of their faintest detectable source, in units of their count rate [cts/cm^2/sec] as a fraction of the count rate of the Crab nebula —the so-called "standard candle" of the high-energy sky— measured by the same instrument in the same energy range. Also, since the Crab nebula greatly outshines most other hard X-ray sources at any given time, it is also standard practice to quote count rates in units of 1/1000 of the Crab count rate.

The technical justification for BATSS on the other hand rests on two inherent features of slew observations: one is their predicted ability to span major parts of the sky in a short period of time, both in terms of area and frequency of coverage, and a quantitative analysis of this property is presented in the remainder of this section based on studies of *Swift* spacecraft pointing directions (*spacecraft attitude*) data. The second is an increased sensitivity relative to pointings of equal exposure, which is attributed to the effect of scanning the detector plane across the sky that effectively translates into a measurable reduction of systematic effects. BATSS sensitivity studies are the subject of Section 2.5, since they first require an understanding of the BATSS imaging technique and its associated systematics. Combined, these properties of BAT slew observations favor an increment with respect to pointing observations in the detection probabilities for astrophysical sources such as GRBs and fast transients. Simulation work done to predict such probabilities, as well as estimates of BATSS trigger rates along with summaries of confirmed detections to date, are presented in Chapter 4 on BATSS GRB science results, using observed GRB detection rates over the course of the survey as a proxy for the effective overall slew- and pointing-mode sensitivities after taking into account all contributing effects.

BATSS sky coverage is a function of the orbital properties and observing strategy of *Swift*. The spacecraft flies in a low-Earth ($\sim$600 km) orbit, with an orbital period of approximately 95 min, and is subject to several Sun-Moon-Earth observing constraints (*Swift* Science Center 2008). Therefore, it does not have a continuous viewing zone in pointing mode and must slew between targets approximately 6 times per orbit, with a maximum slewing speed of $\sim 1^\circ$/sec. Figure 1.2a illustrates the corresponding spacecraft attitude for a typical day's worth of observations (11/08/08), with slews represented as tracks drawn by the center of the BAT FoV, while Figure 1.2b shows a plot of slewing speeds over the course of the same day. At the same time, the BAT instrument covers a D-shaped area of

$100^\circ \times 60^\circ$ (1.4 sr, half-coded[3]) around each attitude position, and the resulting total daily sky exposures in pointing and slew modes are shown in Figures 1.2c and 1.2d, respectively. It can be seen in those figures that despite a nearly 10-fold difference in total exposures, the slew observations as a whole provide a larger and more uniform coverage of the full sky than do the pointing observations over a typical day.

In order to draw an absolute comparison of time-dependent sky coverages in slew vs. pointing mode, we have computed the cumulative percentages of covered sky over the course of the same typical day as in Figure 1.2 (11/08/08) and plotted the results in Figure 1.3. The calculation assumes continuous coverage and complete data recovery in both modes of observation, except for periods of passage over the South Atlantic Anomaly (SAA),[4] and includes all portions of the sky in the BAT FoV above 3 coding fraction (CF) thresholds: 1%, 10%, and 30%. Furthermore, the curves have been smoothed by averaging over the starting time of the cumulative distribution. The result is a distribution that shows a consistent advantage for the slew-mode coverage over the course of a day, despite a difference in total exposure time of 17.75 hr in pointing mode vs. 2.90 hr in slew mode.

At the short end of the distribution in clock time (Figure 1.3a), i.e. in the first few minutes of the day, the slew-mode coverage appears lower only because of the greater

[3]As will be further explained in Chapter 2, the *partial coding fraction* (CF) is a fundamental characteristic of the FoV of a coded aperture telescope, equal to the total fraction of the detector plane exposed to each location within the FoV. Locations near the center have a 100% CF and make up the instrument's *fully-coded field-of-viev* (FCFV), whereas locations near the edges, where the coding fraction monotonically decreases with increasing distance from the center of the FoV, make up its *partially-coded field-of-view* (PCFV). The half-coded FoV is made up of all locations at 50% CF or above.

[4]The SAA is a region above the South Atlantic Ocean where the Earth's inner Van Allen radiation belt comes closest to the Earth at an altitude of ∼200 km, causing a high flux of protons in satellites flying in a low-Earth orbit including *Swift*. The spacecraft's 20.6° orbital inclination is meant to minimize this problem, but it still manages to pass through the SAA in ∼7 consecutive orbits a day (i.e. nearly half of all orbits), as the periods highlighted in red in Figure 1.2b clearly show for 11/08/08. The high particle flux during these periods affect all of *Swift*'s detectors, to the point that data collection and voltages are turned off altogether for the XRT and UVOT. For the BAT, throughout this work we assume no useable data collection in either slew or pointing modes during these periods, as on-board event processing itself is turned off during those periods (*Swift* Science Center 2008)

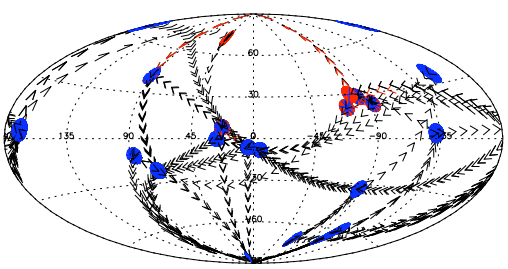

(a) Spacecraft attitude

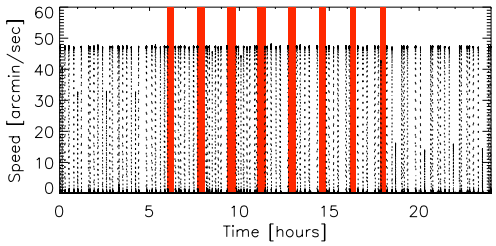

(b) Slewing speeds

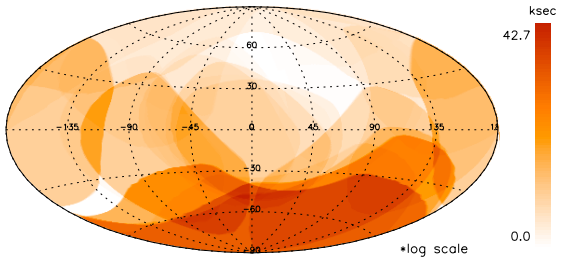

(c) Exposure map — pointing mode

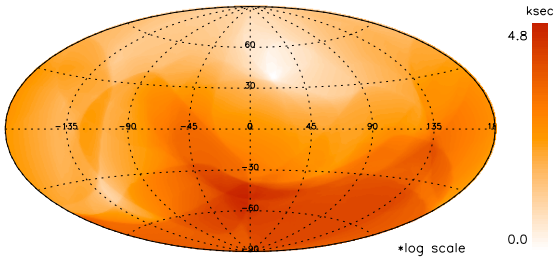

(d) Exposure map — slew mode

FIGURE 1.2: General features of *Swift*'s slew maneuvers, derived from a typical day's worth of operations (11/08/08). (a) Spacecraft attitude (Galactic coordinates): pointing-mode locations are shown a blue dots, along with slew-mode trajectories shown as strings of black arrows. Attitude records taken over the South Atlantic Anomaly (SAA) are shown in red, and disregarded from subsequent analysis. (b) Plot of slewing speeds, illustrating the typical daily frequency of slew maneuvers and maximum speeds achieved. Periods of SAA passage are highlighted in red. (c)–(d) Maps of corresponding absolute daily exposures of the BAT instrument (in Galactic coordinates), in pointing and slew modes respectively.

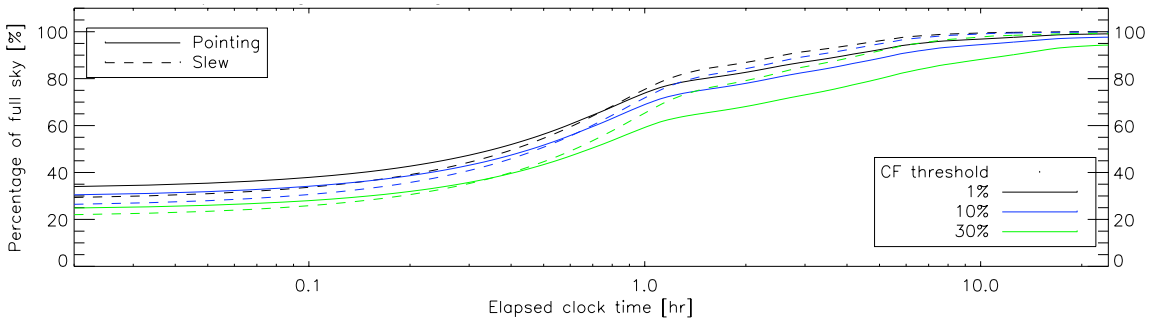

(a)

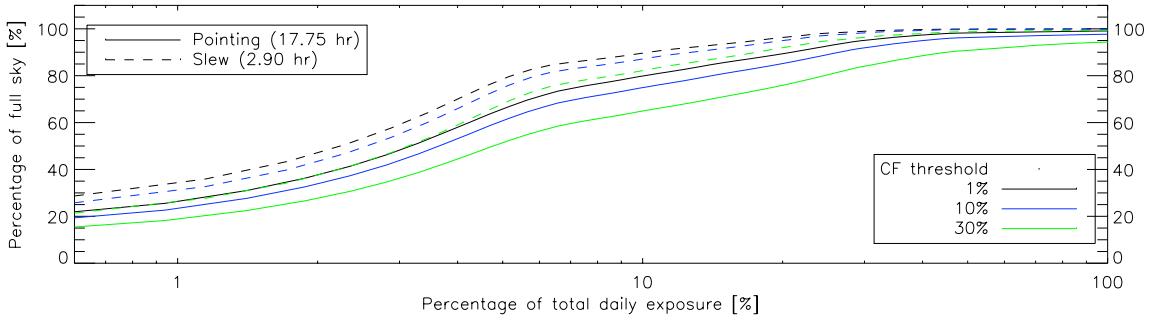

(b)

FIGURE 1.3: BATSS cumulative sky coverage over the course of a typical day (11/08/08) in pointing mode (solid lines) and slew mode (segmented lines), assuming complete data recovery for both modes of observation. The results are shown for 3 coding fraction (CF) thresholds (1%, 10% and 30%), and they are plotted as a function of (a) clock time (0–24 hr range), and (b) percentage of the total daily exposure spent on each observation mode (17.75 hr for pointings and 2.90 hr for slews).

probability that the spacecraft is pointing rather than slewing at the very beginning of the day, as it would likely be at any other given time. However, the coverage curves always cross over by the end of the first hour of the day, after which the cumulative slew coverage becomes noticeably larger, especially in the 1-10 hour range, and the effect is more pronounced the higher the CF threshold. Therefore, under the typical *Swift* observing plan, the accumulated sky coverage after integrating over any random fraction of a day will likely be greater in the slew mode than in the pointing mode, and always greater after the first $\sim$1 hr of integration in clock time, regardless of the partial coding threshold employed.

On the other hand, a more general statement can be derived from the result when displayed as a function of daily exposure in each observation mode, which only takes into account the "instrument time" spent either slewing or pointing. Figure 1.3b shows that the total sky coverage in slew mode is always above the coverage in pointing mode, regardless of partial coding threshold, which means the cumulative slew coverage is always greater for any fraction of daily instrument time elapsed. Given the large difference in absolute exposure times between the pointing and slew modes in the particular case of *Swift*, the relative comparison as a function of instrument time shown in this plot becomes more relevant when considering the inherent properties of each observational technique in a more general context beyond *Swift*. Though this analysis based on spacecraft attitude data alone already shows clear advantages for the slewing mode of operation based on its sky coverage properties, in Section 4.6 we will return to the issue of the impact of this feature on the overall survey performance by making a realistic simulation that takes in all contributing effects, having in hand also data from the BATSS detection performance over the first 4.8 years of the survey.

Organization of this dissertation

The body of this dissertation is organized into three main chapters —plus introduction and conclusions— over which I make the transition from the methodology and technical aspects of the BATSS survey to presenting its main findings after 4.8 years of operation, with particular attention to GRB science results. Having presented in this Chapter the scientific and technical motivations for developing a slew survey with the *Swift*-BAT telescope and the context within which it operates, in Chapter 2 I continue by presenting a description of the imaging and detection technique employed in our implementation of the survey. In the latter part of the chapter I concentrate on a quantitative analysis of

the various systematic effects associated with the resulting BATSS images, culminating with a study of the survey sensitivity in comparison with the analogous sensitivity for pointing-mode observations. In Chapter 3 I then focus on the more technical aspects of the survey, by presenting the processing pipeline I developed in order to generate and analyze all data products for BATSS. Chapter 4 then moves on to the end of the 4.8-yr period of the survey I report here, first by reviewing the general statistics of the slew observations that were analyzed under BATSS' observational program. I then concentrate on reviewing our findings from the detection and observation of the prompt γ-ray emission of a set of GRBs that were detected exclusively during BATSS observations, followed by an analysis of the observed BATSS GRB detection rate and its implications. Finally, Chapter 5 reviews the conclusions derived from the results presented here, with a particular focus on the lessons learned, and the proposed improvements with the greatest potential impact in broadening the number and range of astrophysical sources discovered by the BATSS survey. I present a glance into the survey's immediate and long-term prospects as well, including our current work on the BATSS Multi-slew Hard X-ray Survey, and how the results of the survey can inform the planning of future coded aperture imaging-based missions, of which *MIRAX-HXI* (Grindlay 2012) is a prime example.

Chapter 2

BATSS Imaging Technique

Abstract

Beginning from a complete understanding of the characteristics of the *Swift*-BAT telescope and its properties as coded aperture imaging instrument, we hereby present our methodology for developing a survey capable of performing imaging and detection on photon-by-photon "event" data acquired during spacecraft slew maneuvers, generating data products of comparable if not superior source imaging and local noise properties to those produced in the instrument's canonical pointing mode of operation. We evaluate those properties by carrying out a quantitative study of the systematics of BATSS images, including their noise distribution and signal-to-noise ratios, uncertainties in source flux measurements, and accuracy of source localization, using both single-slew and multi-slew data from the period 2008–2010. The study concludes with an analysis of survey sensitivity in the 10s $< T_{\rm eff} <$ 3ks exposure range, which reveals a consistent advantage of $\sim$20 % in the sensitivity of slew observations over analogous pointing observations of equal exposure. This difference becomes significantly more pronounced in the $T_{\rm eff} <$ 150s single-slew exposure regime, as well as in the $T_{\rm eff} >$ 1ks regime, due to intrinsic properties of both modes of operation, and despite a more sophisticated pointing data pipeline aimed at eliminating systematic effects.

2.1 Introduction

The BAT instrument (Barthelmy et al. 2005) aboard the *Swift* mission (Gehrels et al. 2004) lies at the core of the research effort presented in this work. Therefore, an understanding of its main features, observational technique and modes of operation is fundamental towards understanding the main characteristics and capabilities of the BAT Slew Survey (BATSS) itself. We devote this section to a review of those aspects of the BAT telescope as they pertain to how the BATSS survey operates, as they lay the groundwork for the description of the survey's imaging algorithm provided in Section 2.2, followed by its detection algorithm in Section 2.3. Section 2.4 then presents a study from both the analytical and empirical perspectives of the systematic effects that characterize BATSS images in the current implementation of the BATSS imaging and detection algorithms, which the results in this work are derived from. This study culminates in Section 2.5 with a discussion of the survey sensitivity derived from the local noise properties of BATSS sky images in the 10 sec–30 ksec timescale, with particular emphasis placed on how it compares to the analogous sensitivity derived from sky images taken the BAT's canonical pointing mode of operation.

2.1.1 The *Swift*-BAT instrument: general features

Figure 2.1 and Table 2.1, respectively, show a schematic of the *Swift*-BAT instrument with its main components, and a list of the instrument parameters that characterize it. As mentioned in Chapter 1's Introduction, the BAT employs the *coded aperture imaging* observational technique, a non-focusing technique of frequent use in hard X-ray and γ-ray astronomy which generally features much higher image backgrounds than do its focusing telescope counterparts, but on the other hand allows for very large telescope fields-of-view (FoV) and source localizations in the arcminute scale. In the case of the BAT, its

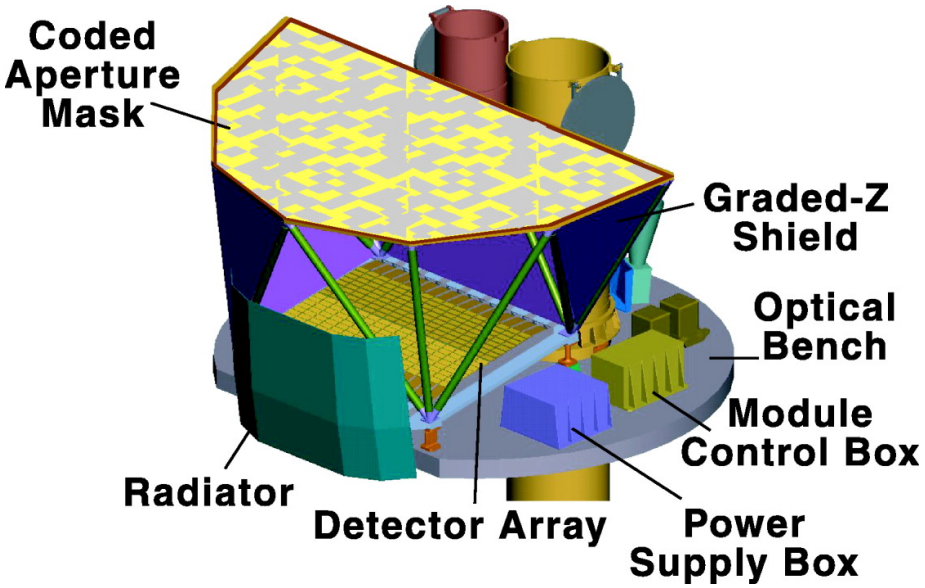

FIGURE 2.1: The *Swift*-BAT instrument and its main components (Gehrels et al. 2004)

TABLE 2.1
Instrument parameters of the *Swift*-BAT telescope (Markwardt et al. 2007)

Parameter	Value
Energy Range	15–150 keV
Energy Resolution	∼5 keV at 60 keV
Aperture	Coded mask, random pattern, 50% open
Detecting Area	5,240 cm^2
Effective Area	∼1400 cm^2 (maximum, on-axis)
Detector Material	CdZnTe (CZT)
Detector Operation	Photon counting
Field-of-View (FoV)	1.4 sr (half-coded), $80° \times 53°$ (FWHM)
Detector Elements	256 Modules of 128 elements/Module
Detector Element Size	$4.00 \times 4.00 \times 2.00$ mm^3
Detector Plane Pixel Pitch	4.20 mm × 4.20 mm
Coded Mask Cell Size	$5.00 \times 5.00 \times 1.00$ mm^3 Pb tiles
Focal Distance	1 m
Instrument Dimensions	2.4 m × 1.2 m × 1.2 m
Telescope PSF	$22'$ (FWHM)
Source Position Accuracy	$1'$–$4'$
Sensitivity (for exposure T)	$\sim 2 \times 10^{-10}$ erg/cm^2/sec $(T/20\text{ks})^{-0.5}$ (5σ, 15–150 keV)
Number of bursts detected	>100/year

ability to observe as much as 1/9 of the full sky at any given time, as well as its $1'$–$4'$ precision in measuring source positions, are fundamental features in the detection of the randomly-occurring and isotropically-distributed Gamma-Ray Bursts (GRBs), and readily enable follow-up observations and arcsecond-precision localizations within the $\sim 20'$ FoVs of *Swift*'s Narrow-Field Instruments (NFIs: XRT and UVOT). In the next subsection (2.1.2), we provide further details on the BAT's properties as a coded aperture telescope and how they manifest themselves in the instrument's FoV and sky images.

The BAT's 5,240 cm^2 detector array (shown in the schematic of Figure 2.1) is an early example of the use of solid-state CdZnTe (CZT) detectors for observations in the hard X-ray band. The material and its associated electronics are responsible for setting the telescope's 15–150 keV energy range and ∼5 keV energy resolution, obtained from measurements of the 60 keV photons of the two on-board ^{241}Am "tagged sources" for energy calibration. The detector plane's pixel pitch of 4.20 mm in both dimensions, with 0.2 mm gaps between detectors, is relatively coarse compared to current instrumentation projects including those carried out by our own research group. Our *ProtoEXIST* pathfinder program, for instance, conducted the *ProtoEXIST1* balloon experiment on October 9, 2009, in which a prototype telescope with a detector plane made up of closely-packed (gapless), pixellated CZT detectors with a 2.5 mm pixel pitch was successfully tested (Allen et al. 2010; Hong et al. 2011). Even more recently and as part of the same effort, the launch of the *ProtoEXIST2* payload, carrying a prototype coded aperture telescope with a detector pixel pitch of 600 μm —1/7 that of *Swift*-BAT— was successfully carried out on October 10, 2012, and the data reduction effort from the experiment is a work in progress at the time of submission of this dissertation.

Other main components of the BAT telescope featured in Figure 2.1 include a graded-Z fringe shield to reduce the instrumental background event rate and cosmic diffuse back-

ground, and a thermal radiator and control system to keep the detector plane at a constant temperature. The control of the BAT instrument is done through the Image Processor which also does the on-board event processing, including burst trigger detection, burst location calculations, and burst figure-of-merit (FOM) calculation (Barthelmy et al. 2005).

2.1.2 The BAT as a coded aperture imaging telescope

At its most fundamental level, coded aperture imaging (Caroli et al. 1987) is a non-focusing observational technique devised from the basic concept of the pinhole camera, subsequently expanded in order to achieve maximum photon influx at the detector plane and a unique imaging of each sky location within the telescope's FoV. For hard X-ray photons of energies $\gtrsim 10$ keV, which can no longer be focused by arrays of grazing-incidence mirrors the way their soft X-ray counterparts can, this technique becomes the only choice when the goal is to produce hard X-ray sky images where sources need to be located with arcminute-level precision.

A coded aperture telescope has two essential components: a detector plane capable of detecting incoming photons in the energy range of interest, and an aperture (*coded mask*) made up of a tiled pattern of openings and closings which lends its name to the technique itself. The "coded" term comes from the fact that images in the detector plane are not true sky images in the way they would be in a focusing telescope, but they are rather a convolution of the images formed by each of the individual holes in the mask pattern. Producing actual sky images from a coded aperture telescope therefore requires the images formed in the detector plane to go through a deconvolution procedure that takes into account the specific mask pattern used in the telescope, and is in general a computationally intensive process with a number of theoretical and technical issues that need to be taken into consideration (see e.g. Skinner 1995; Skinner et al. 1987; Willmore et al. 1992).

The placement of the coded aperture mask and detector array within the BAT telescope can be seen in the schematic of Figure 2.1, and their main characteristics are summarized in Table 2.1. Figure 2.2 shows pictures of what the actual components look like. The choice of a mask with a random pattern —unlike other possible choices such as the Uniformly Redundant Array pattern (URA, Fenimore & Cannon 1978)— has the advantage of producing a unique image at all points of the BAT's FoV. However, random-pattern masks also introduce a type of systematic noise —the so-called *coding noise*— which is added to the statistical Poisson noise of the incoming photons and all systematics associated with the detector plane and other telescope elements, and becomes the ultimate theoretical boundary in limiting the sensitivity of this type of instrument (Caroli et al. 1987).

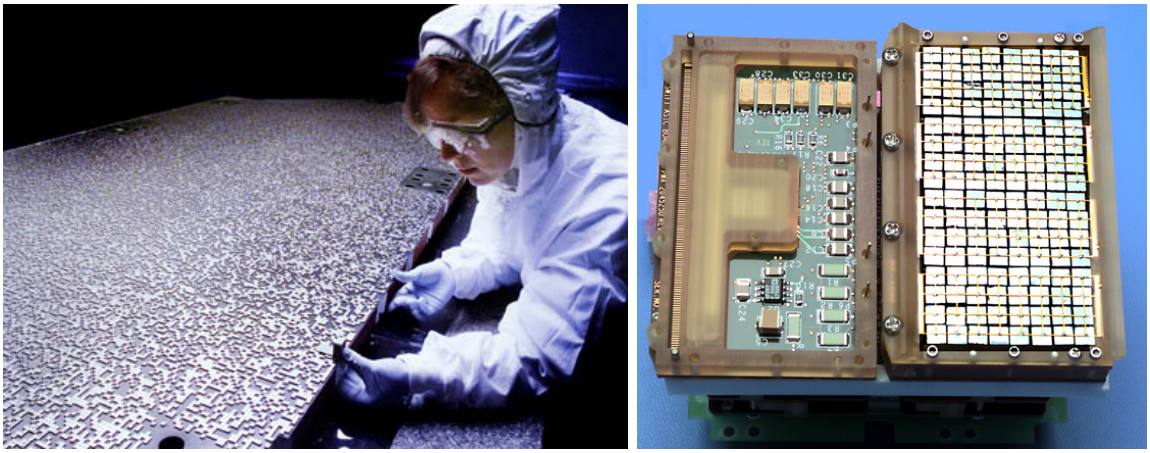

(a) BAT coded aperture mask (b) BAT Detector Module (DM)

FIGURE 2.2: Pictures of the two essential components of the BAT coded aperture telescope (Myers 2012): (a) Coded aperture mask, made up of a D-shaped random pattern of 5 mm $\times$ 5 mm $\times$ 1 mm Pb tiles; (b) Detector plane, made up of 128 (8×16) Detector Modules (DM) such as the one shown in the picture, which is in turn made up of two 8×16 sub-arrays of 4 mm $\times$ 4 mm $\times$ 2 mm CdZnTe (CZT) detectors, for a total detecting area of 5,240 cm^2 composed of 32,678 individual CZT detectors. The arrangement of the two components within the telescope is shown in the schematic of Figure 2.1.

The *Field-of-View* (FoV) of a coded aperture telescope is determined by the physical

dimensions of both its coded mask and detector plane, as well as the distance between them (i.e. the telescope's *focal distance*). Figure 2.3a illustrates how those three elements combine to determine the *Fully-Coded FoV* (FCFV), made up of all sky locations that are projected onto the entire detector plane, and the *Partially-Coded FoV* (PCFV), made up of those locations projected onto only part of the detector plane. The fraction of the detector plane exposed to a particular sky location x is called its *Coding Fraction* $\mathrm{CF}(x)$, and is a fundamental characteristic associated with each location within a coded aperture telescope's FoV.

Figure 2.3b shows the BAT's wide FoV, whose shape is determined by a combination of the rectangular shape of the detector plane and the D-like shape of the coded mask. The boundaries of its FCFV and PCFV are shown as well, and also the $\sim 100^\circ \times 60^\circ$ contour of the 1.4-sr half-coded (>50%) FoV, quoted in Table 2.1.

Regarding the deconvolution of the BAT's *Detector Plane Images* (DPIs) to produce sky images, this procedure is implemented by the tool `batfftimage` of the BAT software package (Markwardt et al. 2007), shown schematically in Figure 2.4. The tool uses a Fast Fourier Transform (FFT) procedure to perform the deconvolution of the DPI from the mask pattern, taking into account in the process the complications introduced by the gaps between Detector Modules (DMs) in the detector plane (spaced so as to enable `batfftimage` to handle them as dead pixels), as well as the need to eliminate the effects of individual noisy/disabled CZT detectors. The use of this tool is assumed by the BATSS imaging algorithm of Section 2.2, and its implementation within the BATSS software package is described in Section 3.7 within the context of the imaging thread of the BATSS pipeline.

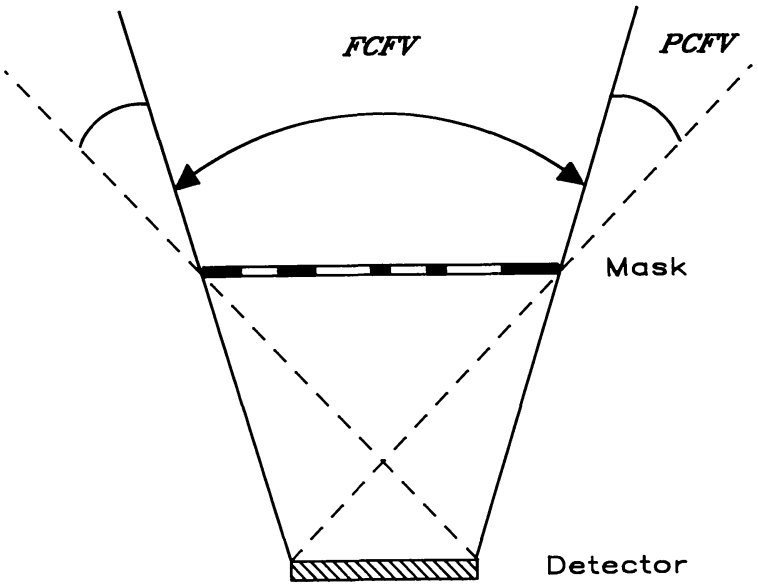

(a) The fully-coded and partially-coded FoVs of a coded aperture telescope (Caroli et al. 1987)

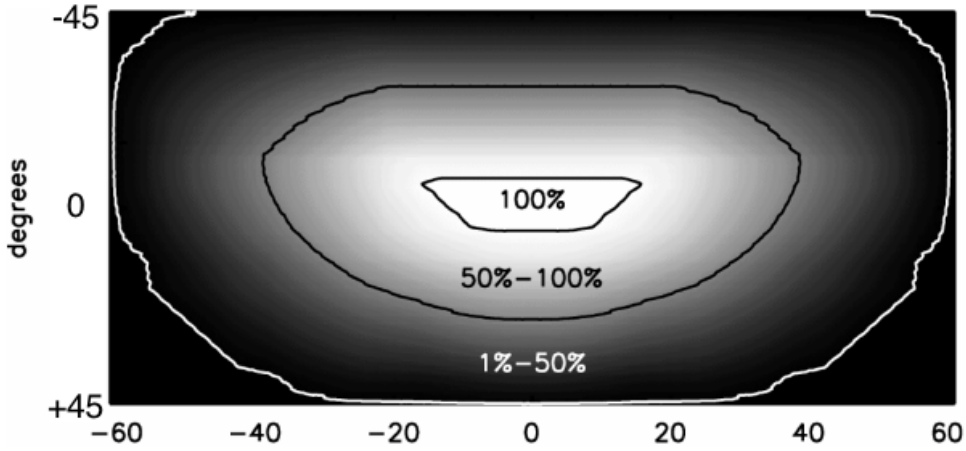

(b) The BAT field-of-view (Markwardt et al. 2007)

FIGURE 2.3: Field-of-view (FoV) of a coded aperture imaging telescope: (a) Fully-Coded FoV (FCFV) and Partially-Coded FoV (PCFV) for a generic coded aperture telescope, illustrating how the physical dimensions of the mask and detector determine the angular dimensions of the FoV; (b) BAT FoV, occupying a wide area of $120^\circ \times 90^\circ$, along with contours at 1%, 50% and 100% coding fractions (CF), which illustrate the relative sizes of the instrument's FCFV and PCFV, assuming a fully functional detector plane. The half-coded (>50%) FoV of the BAT subtends a solid angle of 1.4 sr and is quoted in Table 2.1.

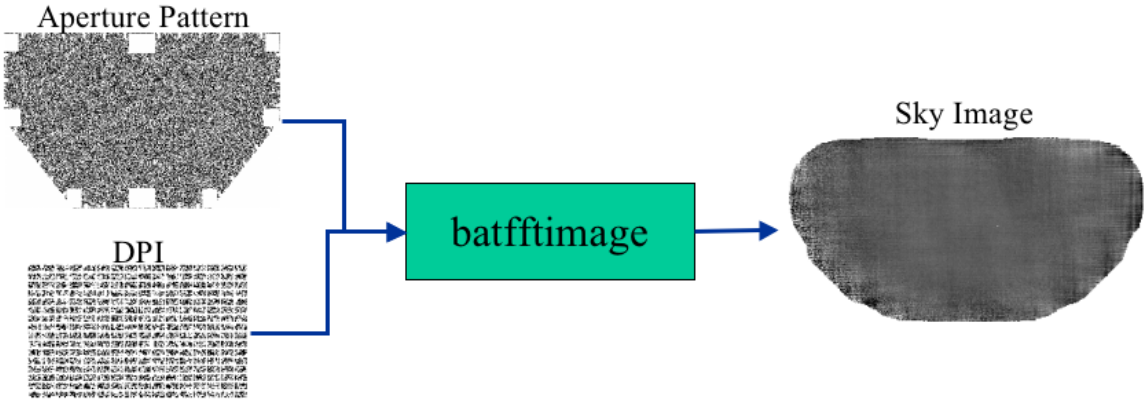

FIGURE 2.4: Schematic input/output diagram of the BAT tool `batfftimage`, which takes the telescope's coded aperture mask pattern and a Detector Plane Image (DPI), along with a map of hot/cold/disabled pixels, to produce a sky image (Markwardt et al. 2007). Also, the sky image in this example visually shows how the noise level increases in the PCFV with decreasing coding fraction.

2.1.3 BAT operations: *survey* and *event* data

While taking data during a pointing, the BAT will normally operate in "survey" mode, wherein photon events are accumulated as *Detector Plane Histograms* (DPH), which are 3-dimensional arrays of counts across the 286×173 pixels of the BAT detector plane (including gaps between DMs) and a standard array of 80 energy bins, taken in 5-min time bins. Given the fixed spacecraft attitude, pointing DPHs can be readily collapsed into 286×173 pixel Detector Plane Images (DPIs) in the desired energy range, and correlated with the BAT coded mask pattern to yield sky images in said energy band. By contrast, slew observations require imaging over short time intervals of approximately constant attitude, which in turn requires a fine time resolution of input photon events unlike that provided by survey-mode data. Hence, BATSS observations require input data in BAT's "event" mode —already introduced in Chapter 1 when presenting the motivations for the BATSS survey—, wherein event-by-event data are provided with a time resolution of 0.1 msec. BATSS imaging is based on producing full-sky images out of this input event-

mode data over several energy bands, followed by a detection phase based on triggering on these images while requiring coincident detection across energy bands. The processing algorithm developed for this purpose is described in the following Sections 2.2 and 2.3.

2.2 BATSS imaging algorithm

The BATSS imaging algorithm, summarized in the diagram in Figure 2.5, can be divided into three major phases: a first phase that implements the coded aperture imaging technique, from accumulation of events in the BAT detector plane to correlation with the coded mask to produce sky images, while relying on the use of the dedicated BAT software package (Markwardt et al. 2007) to handle peculiarities of the BAT instrument. The second phase implements projection of images onto the BATSS full-sky projection, which we developed to allow for imaging and detection in the large FoVs that are characteristic of BATSS images, while the third phase performs addition of the projected images to produce a final set of images per slew.

2.2.1 Coded aperture imaging

As a first step in the imaging of a given slew, the input event-mode data is accumulated into Detector Plane Images (DPIs), through the use of the standard BAT software tool `batbinevt`, for every 0.2-sec time bin (the same rate at which spacecraft attitude data records are taken), in 2 independent energy bands: 15–50 keV (hereafter called the "Soft band") and 50–150 keV (hereafter called the "Hard band"). Then, given that DPIs lack information on hot/cold detector pixels that must be screened out from the imaging phase, it is necessary at the same time to create a detector quality map for the entire slew. Given the low number of counts on each of the 0.2-sec DPIs, a single DPI is created from all the events in the 15–150 keV energy range accumulated over the course of the slew, only

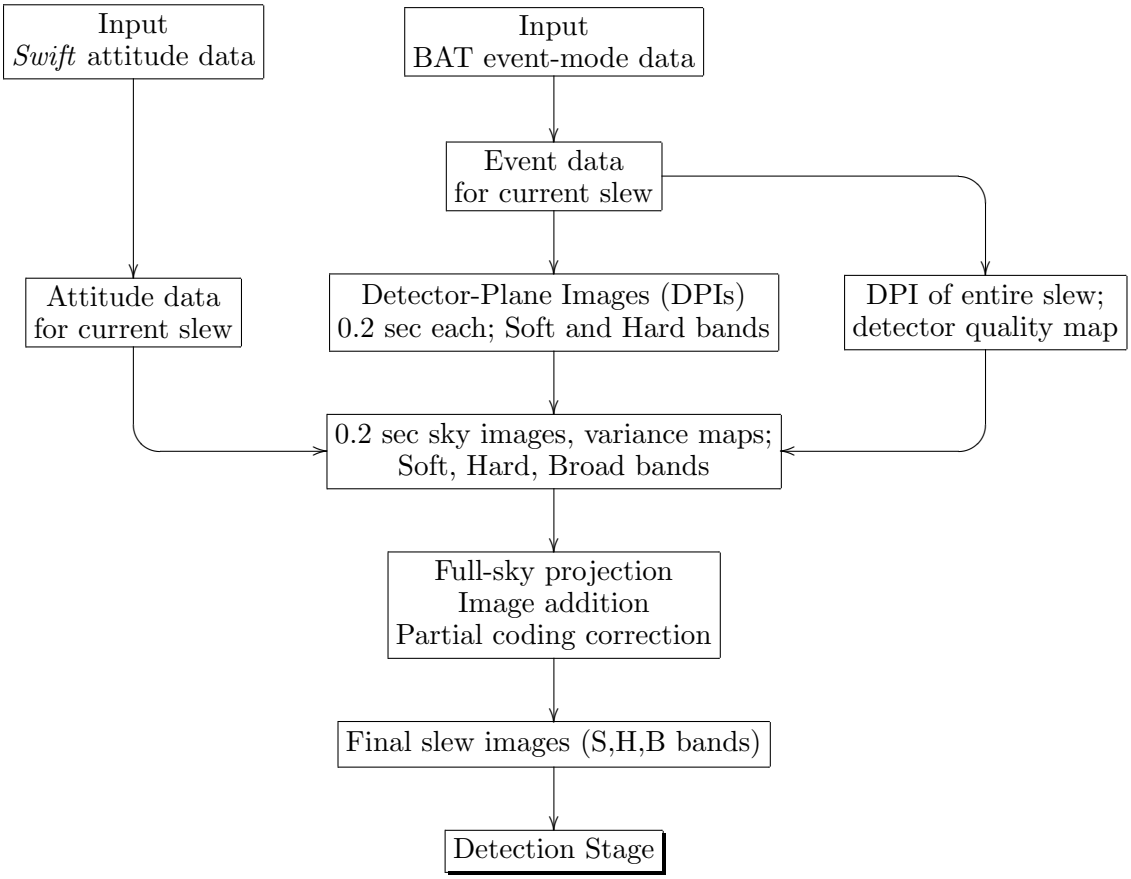

FIGURE 2.5: Flow chart of BATSS imaging algorithm

for the purposes of screening pixels with unusually high/low count rates. The standard BAT software routine `bathotpix` performs the final screening, taking also as input the map of known enabled/disabled pixels that is regularly telemetered along with the input event data.

The next imaging step involves the creation of 0.2-sec sky images and variance maps by cross-correlation with (deconvolution from) the BAT coded mask, given the input DPIs, detector quality map, and attitude data for the slew, with the FFT operation performed by the BAT software tool `batfftimage`, introduced in Section 2.1.2. All standard corrections for geometrical effects are performed except for the correction for partial coding, which is done only after a co-added slew image has been obtained. Following this, sky images for the 15–150 keV energy band (hereafter called the "Broad band") are produced by co-adding the corresponding 0.2-sec sky images in the soft and hard energy bands, in order to enable image triggering based on any combination of detections in the three energy bands.

2.2.2 Full-sky projection

A particular issue for BATSS concerns the sky projection to be used in co-adding the individual 0.2-sec sky images, each of which having the standard size and D-shaped FoV of the BAT (Figure 2.3b), but with the varying astrometry parameters characteristic of slew images. The resulting slew image would span a large FoV of several steradians, and for this reason it was necessary to adopt a new standard sky projection for BATSS images.

The standard BATSS projection, shown in Figure 2.6, was chosen to be a full-sky projection in Galactic coordinates, with a fixed set of astrometry parameters, which readily enables addition of images not only within a slew, but also later across several slews for deeper survey observations. Furthermore, for the new projection not to introduce significant systematic effects at the detection stage, it was necessary for it to be approximately

equal-area and conformal (i.e. local axis angles and scales are preserved). The zenithal gnomonic (tangential) projection used in standard BAT images, defined as a function of polar angle θ as $R_\theta = \frac{180^\circ}{\pi} \tan\theta$, was evidently not appropriate for this purpose, however, since it introduces distortions in the shape of the PSF as large as a factor of 2 at $\theta = 45^\circ$ from the center of the projection, and eventually diverges at $\theta = 90^\circ$. Instead, we made use of a projection of the generic type quadrilateralized spherical cube (*quad-cube*), whereby the celestial sphere is projected onto the 6 faces of an enclosing cube, so every point in the projection lies within a maximum of 55° off the center of a sub-projection.

The sub-classes of quad-cube projections defined for the FITS standard by Calabretta & Greisen (2002) all have the property that the edges of contiguous sub-projections match each other exactly, and at these regions the source PSF may differ significantly from the Gaussian shape that is assumed by the detection routine. In order to avoid these projection edge effects, we have instead extended the FoV of each of the 6 sub-projections by 5° from each edge, as illustrated by the shaded areas of Figure 2.6. In addition, in order to ensure a uniform solid angle to be subtended by each image pixel (a size of $8' \times 8'$ was chosen to optimize for processing speed), for each sub-projection we have implemented a *zenithal equal area* (ZEA) projection type, whose parameterization for FITS is specified by Calabretta & Greisen (2002), and is defined as a function of the polar angle θ from the center of each sub-projection as

$$R_\theta = \frac{180^\circ}{\pi}\sqrt{2(1-\cos\theta)} = \frac{360^\circ}{\pi}\sin\frac{\theta}{2}$$

The resulting BATSS full-sky projection of Figure 2.6, where a full single-slew image is depicted as an example, illustrates several of the features of the model chosen. First, the fact that no pixel in the projection lies further than 54.73° from the center of a sub-projection means that the PSF is distorted by a maximum factor of 0.89 (an 11% reduction)

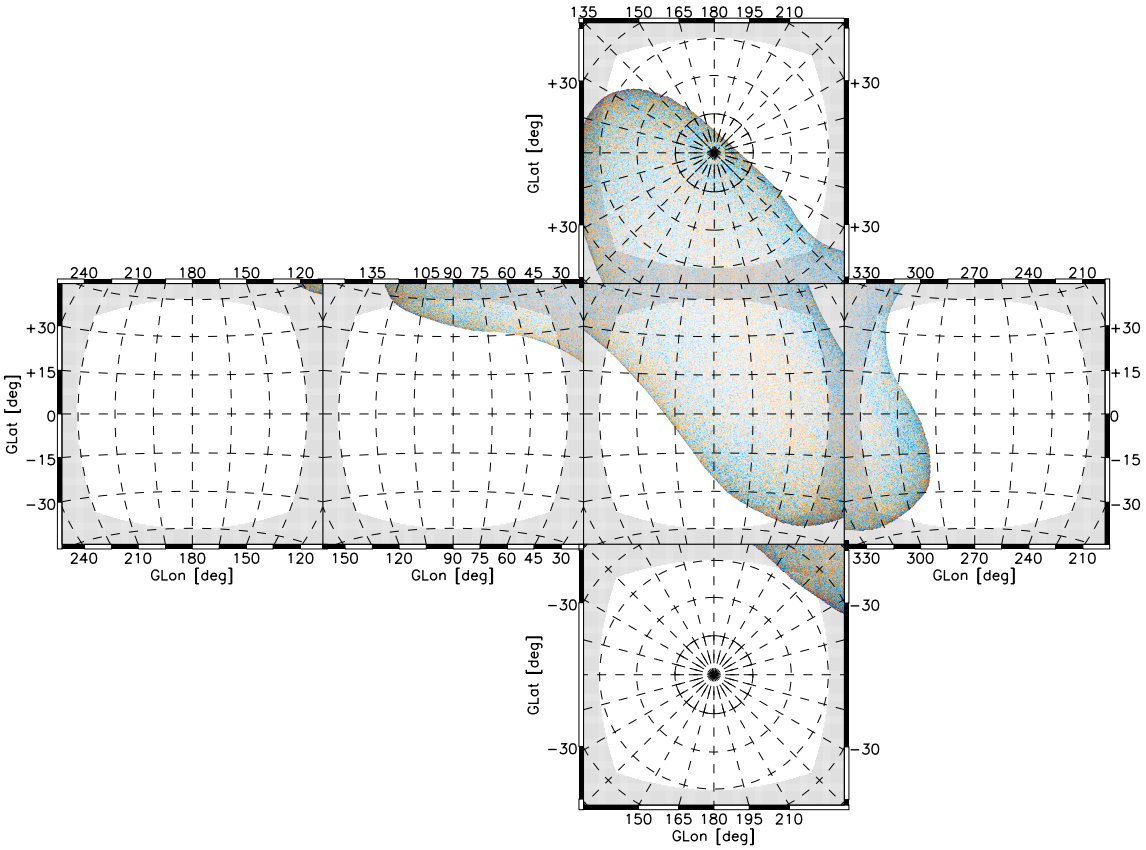

FIGURE 2.6: Standard BATSS full-sky projection for slew images: *quad-cube* arrangement with *zenithal equal area* (ZEA) sub-projections (Galactic coordinates), with a co-added slew image shown as an example. The projection adds a 5° buffer region (shaded) to the edges of each sub-projection, in order to avoid projection edge effects upon running detection. Unlike BAT sky images obtained from `batfftimage`, images with the fixed astrometry parameters of this projection can be readily co-added with images from any other slew or portion of a slew.

in the radial direction. Compared to a PSF enlargement of 26% at the same distance in BAT-standard gnomonic projection, this means that PSF distortion effects are not only minimized but also improved upon with respect to standard BAT imaging. Second, the addition of a large buffer (shaded) region at the edges of each sub-projection allows for the detection routine to be run independently on each of the sub-projections without any bias due to the presence of the edges of the sub-projection. For the probable case of duplicate detections near the edges of adjacent sub-projections, we keep only the detection whose centroid lies within the boundaries of a sub-projection (i.e. outside the buffer region). Finally, once a slew or a portion of a slew has been projected onto the BATSS full-sky projection, it can be readily co-added with any other slew or portion of a slew.

2.2.3 Image addition

Following projection onto the standard BATSS full-sky projection, the individual 0.2-sec images that were obtained from the coded aperture imaging phase are then co-added by variance-weighted addition, producing a single image for the full slew in each of the 3 energy bands, as illustrated in the Figure 2.6 example. Given that every sky pixel is swept over by a range of BAT detector coding fractions, it is possible that the low-coding fraction, less-sensitive regions near the edge of the BAT FoV in the 0.2-sec images have an effect on the full co-added image that negatively affects the overall slew sensitivity, thereby raising the question of imposing a threshold in the range of BAT coding fractions that are used in BATSS images. In order to derive such a coding fraction threshold, we selected a number of slew observations over the Crab —the "standard candle" of the hard X-ray sky, with nearly constant flux—, wherein it goes from outside of the BAT FoV to the fully-coded region over the course of the slew, and co-added the regions of the 0.2-sec images above a pre-set threshold in the range 1% (minimum allowed) to 80% coding, in 5% increments.

The results of this test are shown in Figure 2.7, where the Crab detection's signal-to-noise ratio (S/N) is plotted against the range of chosen coding fraction thresholds, from images in the three BATSS energy bands. The results for all observations agree in the monotonic improvement of the sensitivity up to a ∼20% threshold level, after which the improvement reaches a plateau and eventually begins to decrease monotonically above ∼60%, where the reduced source exposure time finally outweighs the gains of co-adding only regions of high source coding fraction. From this analysis, we impose a threshold of 15% coding for all 0.2-sec images as they are co-added into a BATSS slew image.

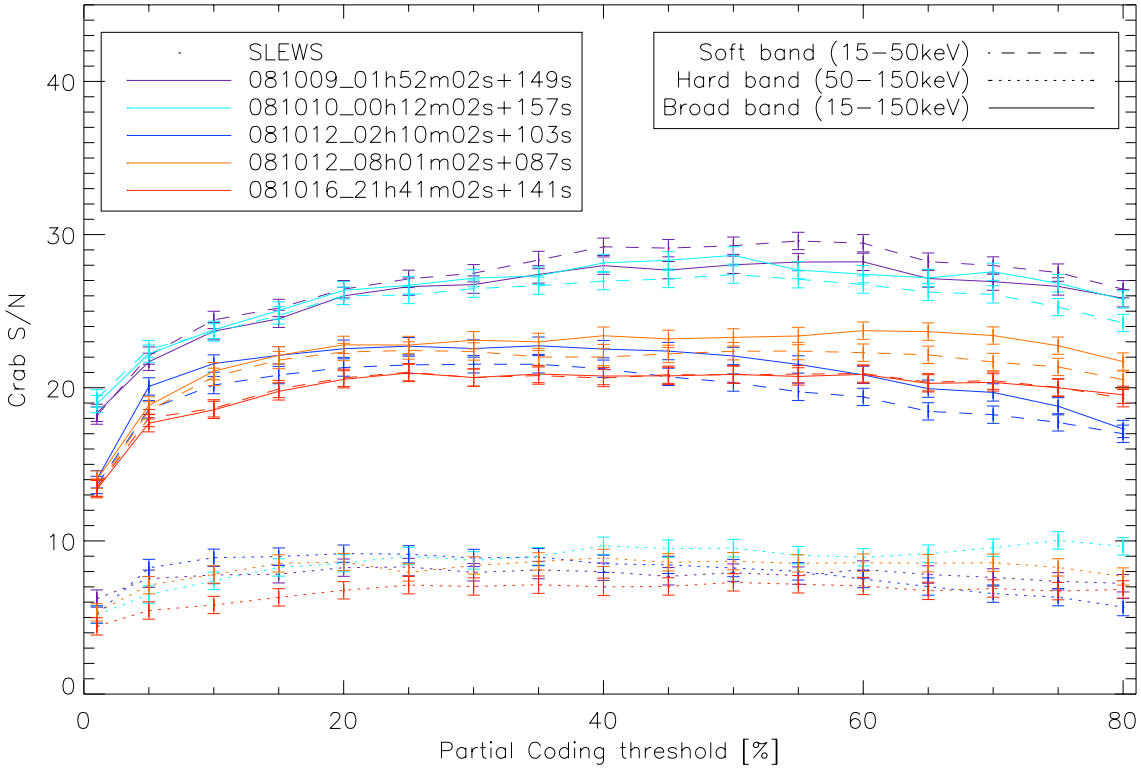

FIGURE 2.7: Derivation of coding fraction threshold for BATSS images from selected slew observations over the Crab. The Crab S/N as a function of coding fraction threshold for each energy band detection is shown, starting with the minimum threshold level of 1% and up to 80% CF threshold in 5% increments

As a final step in the BATSS imaging stage, the image counts are corrected for partial coding, so as to recover the correct source fluxes in the detection stage, by dividing the images by the time-averaged partial coding map for the slew. In slew observations this is the analogous operation to the standard partial-coding correction of pointing-mode images (Markwardt et al. 2007), whereby the sky image is divided by the BAT partial coding map. The systematic effects of this imaging method on detected sources are described and quantified in Section 2.4.

2.3 BATSS detection algorithm

Taking the co-added slew images in Soft, Hard, and Broad energy bands as input, as well as other auxiliary images, the BATSS detection stage then follows as summarized by the diagram in Figure 2.8. The first step involves the use of the BAT standard detection tool `batcelldetect`, which is called to perform detection on the three sky images separately (six ZEA sub-projections each, as explained in section 2.2.2), using blind detection for uncatalogued sources, and also forcing detection of catalogued sources for monitoring and calibration purposes. As parameterized in BATSS, the blind detection algorithm of `batcelldetect` (further described by Markwardt et al. 2007) uses a circular sliding cell to find pixels that exceed a pre-set 3.5σ threshold (i.e. a signal-to-noise ratio $S/N \geq 3.5$) above the background level on the cell, and then on a second pass fits for position and flux by employing a Gaussian PSF of fixed width 22.5 arcmin (FWHM), which corresponds to the BAT instrumental PSF (*Swift* Science Center 2008). This produces a catalog of detections which are then sorted according to whether they match a catalog of known transients. Those found to coincide with a catalogued transient are set aside for monitoring of source activity, whereas unidentified detections are further processed for classification as either candidate GRBs or transients.

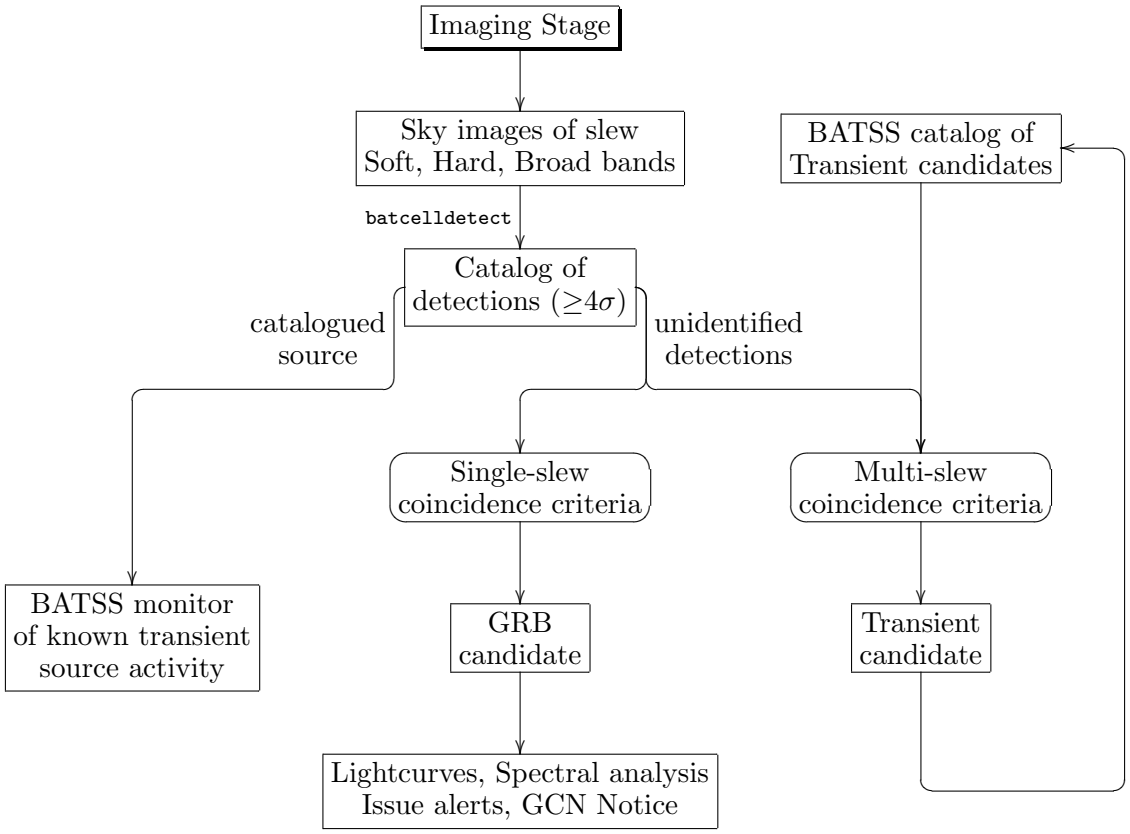

FIGURE 2.8: Flow chart of BATSS detection algorithm

Given the likelihood that a number of unidentified detections will correspond to background fluctuations rather than emission from real point sources, the BATSS detection algorithm additionally employs criteria that require spatial coincidence between several detections in order to categorize them as source candidates. The first set of criteria apply to single-slew (i.e. simultaneous) detections across different energy bands, which give rise to candidate GRBs. These criteria, laid out in detail in Section 3.9 on triggering requirements for the BATSS pipeline, assign an "index number" (figure-of-merit) to each candidate according to its likelihood of corresponding to a real source, which for a single-slew detection would most likely be a GRB. Those with the highest index numbers are in turn subject to further analysis, including derivation of mask-tagged lightcurves and spectra, and generate a set of automated alerts, ending with the issuance of a Gamma-ray bursts Coordinates Network (GCN, Barthelmy et al. 1998) Notice that is readily distributed to the world via the GCN Network,[1] and in a format designed specifically for BATSS GRB detections. The data reduction and analysis methods employed by the BATSS pipeline for candidate GRBs are described in detail in Section 4.3 within the context of the BATSS GRB survey, and the details of the contents and formatting of the BATSS GCN Notice type `SWIFT_BAT_SLEW_GRB_POSITION` are provided in Appendix C.

The second set of criteria for candidate source classification employ a multi-slew coincidence scheme that takes the unidentified detections for the current slew and match them against those from all previous slews, in order to identify new candidate transients, particularly repeating ones. Though these candidates do not currently produce worldwide automated alerts, they are kept in an ongoing BATSS catalog of transient candidates for further analysis within the BATSS Multi-slew Hard X-ray Survey, an ongoing project whose results are not presented in this work but that is introduced in Chapter 5 as part as the future directions for the BATSS project.

[1] `http://gcn.gsfc.nasa.gov`

2.4 Systematic effects

The imaging method used by BATSS and described in Section 2.2 leaves a residual set of systematic errors that differ from those found in observations made in the nominal BAT fixed-pointing mode of operation (Tueller et al. 2010). First, signal-to-noise ratios calculated in the detection stage must be properly calibrated to conform to a proper Gaussian statistical distrubution. In addition, errors in flux estimates and source positions must include a systematic component that reflects the effects due to the instrument as well as the imaging method employed by BATSS. They are to be reported in the first alerts that are issued once a candidate GRB or Transient is initially detected, and the quantitative analysis of such effects is described in this section.

2.4.1 Signal-to-noise calibration

As indicated in Section 2.3, BATSS detection relies on the use of the standard BAT software tool `batcelldetect` (Markwardt et al. 2007) applied to BATSS slew images. This tool uses a two-step method that first applies a sliding-cell algorithm to find count excesses in the image, followed by a PSF-fitting procedure that computes the signal-to-noise ratio of a detection by comparison against the background level in an annulus around the local region of the image fluctuation. In the absence of systematic effects and neighboring real sources in the image (in the background annulus), it would be expected that these local background fluctuations would conform to a Gaussian statistical regime at the global scale, though the detection method does not enforce this condition. In the presence of systematics, on the other hand, the distribution of fluctuations may deviate from the expected normal distribution, and thus the signal-to-noise ratios must be corrected so as to preserve their meaning in a statistical sense.

For this purpose, we have employed the detection tool to force detection on a number of blank sky points over a wide range of slew images that spans two years of BATSS observations (2008–2009), and consequently obtained a global distribution of background fluctuations based on the detected signal-to-noise ratios, shown in Figure 2.9. In order to compare with analogous calibration results obtained from pointed data, we have used the same sample of 106 blank sky locations used in the calibration of fluxes of sources in the Swift/BAT Hard X-ray Transient Monitor (Krimm 2006), first announced in ATel. #904 (Krimm et al. 2006). These locations were selected such that they were located at least $10'$ away from any known bright X-ray source, and are displayed in the sky map (in Galactic coordinates) of Figure 2.9a.

The data sample used corresponds to blank point detections made on a total of 28,074 slews, whose S/N (significance) distribution is shown in Figure 2.9b, imaged independently in the 15–50 keV and 50–150 keV energy bands, as well as 6,557 higher-order observations (orbit, day, week, month, and year, combined into Figure 2.9c) obtained by co-adding individual slews. For each detection, in order to remove any positive or negative bias that may arise from attempting to fit a PSF at the location of a blank sky point, the value of the pixel closest to the location has been sampled from the image in the calculation of the significance. The widths of the corresponding single-slew and multi-slew distributions are both found to be 0.998σ, which suggests that 1) for single slews and in the absence of nearby bright sources, the BATSS imaging method makes a negligible systematic contribution to the image background aside from the expected Gaussian fluctuations due to Poisson statistics in the detector counts characteristic of the photon-counting coded aperture detector; and 2) for co-added slews, the systematic contributions are uncorrelated over time at least up to the exposure range of yearly observations (236 ksec for this sample). This stands in contrast to the width of 1.12σ that is obtained by an analogous method

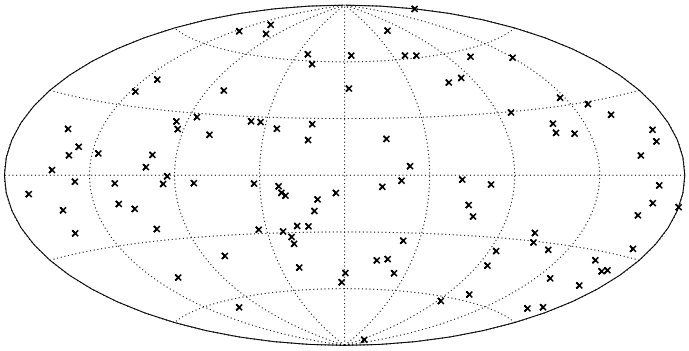

(a) Sky map of 106 blank points for S/N calibration

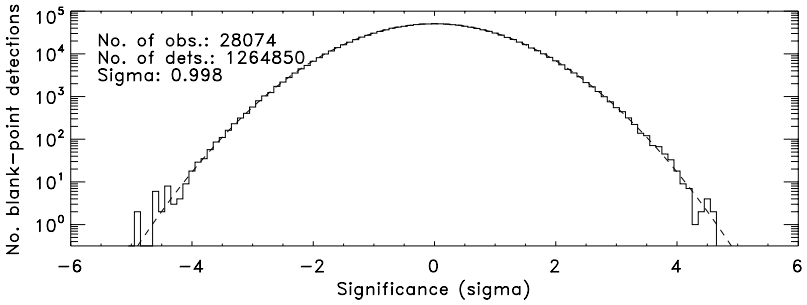

(b) Distribution of blank point S/N in BATSS single slews

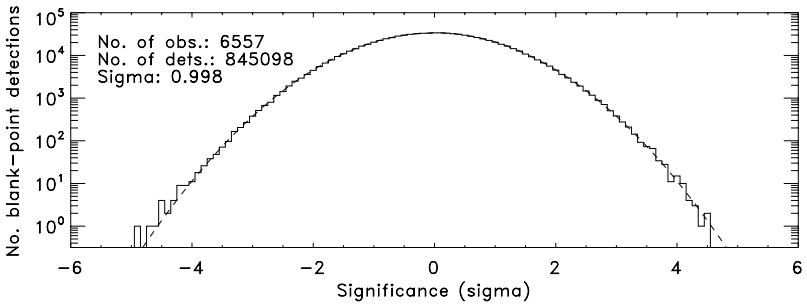

(c) Distribution of blank point S/N in BATSS multi-slew observations

FIGURE 2.9: (a) Sky map of 106 blank points for S/N calibration, shown on an Aitoff projection in Galactic coordinates. Distributions of significances of blank point detections in (b) individual slews, and (c) co-added slews (orbital through full-year), over two years' worth of BATSS observations (2008–2009). For each case, the total number of observations, number of detections and width of the distribution are shown in the figure, along with a dashed line that represents a Gaussian distribution of width 1.0σ. This demonstrates that slew images on blank sky are very accurately Gaussian in their significance distribution.

for single-pointing observations in the Swift/BAT Hard X-ray Transient Monitor, and the corresponding 1.23σ for daily observations from mosaicked (co-added) pointings (Krimm 2006). The connection between background noise and exposure time, their relation to the sensitivity to real sources in BATSS observations, and the comparison with the sensitivity of analogous pointing-mode observations are further discussed in Section 2.5.

2.4.2 Source flux uncertainty: analytical model

Initial flux measurements for a given source x from BATSS slew image photometry in a given energy band E can be estimated in instrument-independent units by assuming a Crab-like spectrum for the source and expressing the flux $S_{x,E}$ as a function of the Crab count rate in the same energy band as

$$S_{x,E}\ [\text{mCrab}] = \frac{S_{x,E}\ [\text{cts/cm}^2\text{/sec}]}{S_{\text{Crab},E}\ [\text{cts/cm}^2\text{/sec}]} \cdot 10^3\ \text{mCrab} \tag{2.1}$$

For a coded aperture telescope, the source count rate in image units is in turn determined analytically by the difference between the observed count rate in the direction of the source (hereafter referred to as the *on-axis* count rate, different from the common definition as along the telescope's focal axis), minus the count rate observed in the annulus region surrounding the source (the *off-axis* count rate). Over an instrument exposure time of T_0, the total observed on-axis counts $N_{x,E,\text{on-axis}}(T_0)$ are directly proportional to the sum of the source rate and the diffuse background rate $S_{x,E} + B_E$, to the fraction of total detector area A exposed to the source, $A \cdot M \cdot p_x$, where M is the mask open fraction ($\approx 1/2$ for the BAT) and p_x is the partial coding fraction of source x, and to T_0 itself, as

$$N_{x,E,\text{on-axis}}(T_0) = K \cdot AM \cdot p_x T_0 (S_{x,E} + B_E) \tag{2.2}$$

where K is a geometrical factor that depends on the physical dimensions of the telescope that define its FoV and which also accounts for the number of hot/cold/disabled pixels in the detector plane. Similarly, the off-axis counts $N_{x,E,\text{off-axis}}(T_0)$ recorded over the same interval share approximately the same partial coding factor p_x as the source itself, so a similar number of detector pixels are exposed to each off-axis sky location. The detector pixels in each set, however, are modulated differently by the BAT's random coded mask compared to the on-axis pixels, hence only a fraction $\sim M$ of them is exposed to the source, yielding

$$N_{x,E,\text{off-axis}}(T_0) = K \cdot AM \cdot p_x T_0 (M S_{x,E} + B_E) \tag{2.3}$$

From here it follows that the dependence between the source count rate $S_{x,E}$ and the observed source counts $N_{x,E}(T_0)$ is

$$N_{x,E}(T_0) \equiv N_{x,E,\text{on-axis}}(T_0) - N_{x,E,\text{off-axis}}(T_0) = K \cdot AM \cdot pT_0 \cdot (1-M) S_{x,E}$$

$$N_{x,E}(T_x) = K \cdot AMT_x \cdot (1-M) S_{x,E}$$

$$S_{x,E}\ [\text{cts/cm}^2\text{/sec}] = \frac{1}{K(1-M)} \cdot \frac{N_{x,E}(T_x)}{AMT_x}$$

where we have made use of the effective source exposure $T_x \equiv p_x T_0$. Furthermore, the uncertainty in the source count rate obtained by PSF fitting of the decoded sky image is a function of the uncertainties in the parameters of the Gaussian function

$$F(r, T_x) = a_0(T_x) + a_1(T_x) \cdot e^{-\frac{r^2}{2\sigma^2}}$$

where r is the distance from the source centroid and σ is fixed by the BAT PSF width of $22'$ (FWHM, Table 2.1, Markwardt et al. 2007). The dependence of the fit uncertainty

$\sigma_F(r, T_x)$ on the uncertainties of the free parameters $a_0(T_x)$ and $a_1(T_x)$ is thus given by

$$\begin{aligned}\sigma_F^2(r, T_x) &= \left(\frac{\partial F}{\partial a_0}\right)^2 \sigma_{a_0}^2(T_x) + \left(\frac{\partial F}{\partial a_1}\right)^2 \sigma_{a_1}^2(T_x) \\ &= \sigma_{a_0}^2(T_x) + \sigma_{a_1}^2(T_x) \cdot e^{-\frac{r^2}{\sigma^2}}\end{aligned} \tag{2.4}$$

Evaluating this function at the off-axis region of the image ($r \gg \sigma$) yields

$$\sigma_F^2(r, T_x)|_{r \gg \sigma} \equiv \sigma_{F,\text{off-axis}}^2(T_x) = \sigma_{a_0}^2(T_x)$$

In turn, $\sigma_{F,\text{off-axis}}^2$ is directly proportional to the background variance $\sigma_{x,E,\text{bkg}}^2$ obtainted from `batcelldetect` in the annulus region around source x; the proportionality constant K_0 is given by the fit and depends on the χ^2 and the degrees of freedom involved. At the same time, $\sigma_{x,E,\text{bkg}}^2$ is equal to the variance $\sigma_{x,E,\text{off-axis}}^2$ in the observed off-axis counts given by equation 2.3. $\sigma_{x,E,\text{off-axis}}^2$ can be determined analytically from the assumption that it is dominated by the statistical Poisson noise, as expected given the short exposure time of individual slew observations. The other component to the theoretical uncertainty in $N_{x,E,\text{off-axis}}$, the coding noise —introduced in Section 2.1.2 on the BAT's characteristics as a coded aperture telescope—, arises from the fact that in a random coded mask, the mask open fraction M actually varies across neighboring sky locations, and this determines the ultimate sensitivity limit for very long exposures. Coding noise is given by the variance in open/closed hole numbers, which for a mask containing N total holes (both open and closed), is proportional to $\sqrt{N}$. Thus coding noise limits the maximum $(S/N)_{\max} \lesssim N/\sqrt{N} = \sqrt{N}$, regardless of integration time. In practice, high CXB backgrounds in wide-field coded aperture telescopes and declining photon fluxes with energy make most sources limited by Poisson statistics —not coding noise— even for long observations. For instance, in the results from the BAT 22-month survey (Tueller et al. 2010), it is

shown that for exposures as long as ∼1 Msec (still well above those achieved by BATSS so far), the BAT noise regime is still Poisson-dominated. The uncertainty in the fit parameter $a_0(T_x)$ can therefore be expressed as

$$\begin{aligned}\sigma^2_{a_0}(T_x) &= \sigma^2_{F,\text{off-axis}}(T_x) = K_0\,\sigma^2_{x,E,\text{bkg}} \\ &= K_0\,\sigma^2_{x,E,\text{off-axis}} \\ &= K_0\left(\frac{1}{AMT_x}\right)^2 N_{x,E,\text{off-axis}}(T_x) \\ &= K_0\left(\frac{K}{AMT_x}\right)\left[B_E + MS_{x,E}\right] \end{aligned} \tag{2.5}$$

Now, evaluating equation 2.4 at $r=0$ yields the on-axis variance $\sigma^2_{F,\text{on-axis}}$, which is equivalent to the variance $\sigma^2_{x,E}$ of the source count itself

$$\begin{aligned}\sigma^2_{x,E} \equiv \sigma^2_{F,\text{on-axis}} &= \sigma^2_F(r,T_x)|_{r=0} \\ &= \sigma^2_{a_0}(T_x) + \sigma^2_{a_1}(T_x) \end{aligned} \tag{2.6}$$

As in the off-axis case, $\sigma^2_{F,\text{on-axis}}$ is directly proportional to the variance $\sigma^2_{x,E,\text{on-axis}}$ of the on-axis counts given by equation 2.2, which in a Poisson-dominated regime is given by

$$\begin{aligned}\sigma^2_{F,\text{on-axis}}(T_x) &= K_0\,\sigma^2_{x,E,\text{on-axis}} \\ &= K_0\left(\frac{K}{AMT_x}\right)\left[B_E + S_{x,E}\right] \end{aligned} \tag{2.7}$$

Combining equations 2.5, 2.6 and 2.7 yields an expression for the uncertainty in the fit parameter $a_1(T_x)$

$$\begin{aligned}\sigma^2_{a_1}(T_x) &= \sigma^2_{F,\text{on-axis}}(T_x) - \sigma^2_{F,\text{off-axis}}(T_x) \\ &= K_0 \left(\frac{K}{AMT_x}\right)(1-M)\, S_{x,E} \end{aligned} \tag{2.8}$$

Finally, equations 2.5 and 2.8 give the analytical expressions for the terms of the source count variance in equation 2.6, which can be summarized as

$$\begin{aligned}\sigma^2_{x,E} &= K_0\, \sigma^2_{x,E,\text{bkg}} + K_1 \left(\frac{1-M}{AMT_x}\right) S_{x,E} \\ &\equiv \sigma^2_{x,E,\text{stat}} + \sigma^2_{x,E,\text{sys}} \end{aligned} \tag{2.9}$$

Therefore, the uncertainty in the source count rate (and thereby in the estimated source flux) can be seen analytically as being composed of a *statistical* term $\sigma_{x,E,\text{stat}}$ that is directly proportional to the measured local image background, and a *systematic* term $\sigma_{x,E,\text{sys}}$ (in the sense that it deviates from the empty-space statistics from section 2.4.1) that depends on the source count rate $S_{x,E}$ and its effective exposure T_x as $\sqrt{S_{x,E}/T_x}$. Though we have not yet enforced this condition, evidently the statistical term dominates in most cases (given $B_E \gg S_{x,E}$, as is typical of coded aperture telescopes), except those of bright persistent sources and prompt-emission GRBs, where the systematic term may become dominant.

2.4.3 Source flux uncertainty: empirical analysis

To provide an empirical measure of the uncertainties in equation 2.9 and how they apply specifically to BATSS, we have used a 3-year (November, 2007, to November, 2010) sample of BATSS detections of the Crab in the $E = 15$–50 keV energy band, a choice of imaged source which isolates the additional systematic effects due to source variability

and energy-dependent background rates. In addition, blind detection has been used in order to decouple from the effect of source position uncertainty which will be discussed in Section 2.4.4. The sample of Crab observations included both 5,674 single slews (characteristic exposure up to 120 sec) and 2,541 co-added slews up to the full-month level (∼10 ksec exposure), and the measured Crab count rates and their individual statistical errors as obtained from `batcelldetect` are shown in Figure 2.10. In order to translate this result to other sources, we have plotted the Crab signal count rates as percent deviations from the weighted mean count rate over the entire sample, and displayed them as a function of the effective exposure $T_x \equiv p_x T_0$, as defined in Section 2.4.2 in terms of the source's effective coding fraction and absolute exposure. The data points have been binned into a log-normal distribution in T_x, and both the total 1-sigma width $\sigma_{x,E}$ of the distribution for each bin and the statistical width $\sigma_{x,E,\mathrm{stat}}$ as obtained from the individual data points are displayed in the top panel of the figure as well. The resulting systematic distribution width $\sigma^2_{x,E,\mathrm{sys}} = \sigma^2_{x,E} - \sigma^2_{x,E,\mathrm{stat}}$ of the binned data and its dependence on T_x are displayed on the bottom panel of the figure along with the corresponding statistical distribution widths.

The statistical component to the Crab rate error was fitted to a Poisson-dominated function of the form $\sigma^2_{x,E,\mathrm{stat}} = K_{x,E,\mathrm{stat}}\, S_x/T_x$ (shown in Figure 2.10) which yielded

$$\sigma^2_{\mathrm{Crab},E,\mathrm{stat}} = 5.15 \times 10^{-5}\ \mathrm{cts/cm^2/s} \cdot S_{\mathrm{Crab},E} \left(\frac{T}{100\mathrm{s}}\right)^{-1} \tag{2.10}$$

where we have normalized at the characteristic slew exposure of 100 sec. The proportionality constant $K_{\mathrm{Crab},E,\mathrm{stat}} = 5.15 \times 10^{-5}$ cts/cm^2/s, though dependent on the source count rate $S_{\mathrm{Crab},E}$, is also a function of the diffuse background B_E, as shown by equation 2.5, and implicitly on the energy band E used for this data sample as well, and thus does not apply generally to other observations at different energy bands and background rates. It is noteworthy, however, that the dependence on $T^{-0.5}$ holds over the entire exposure range

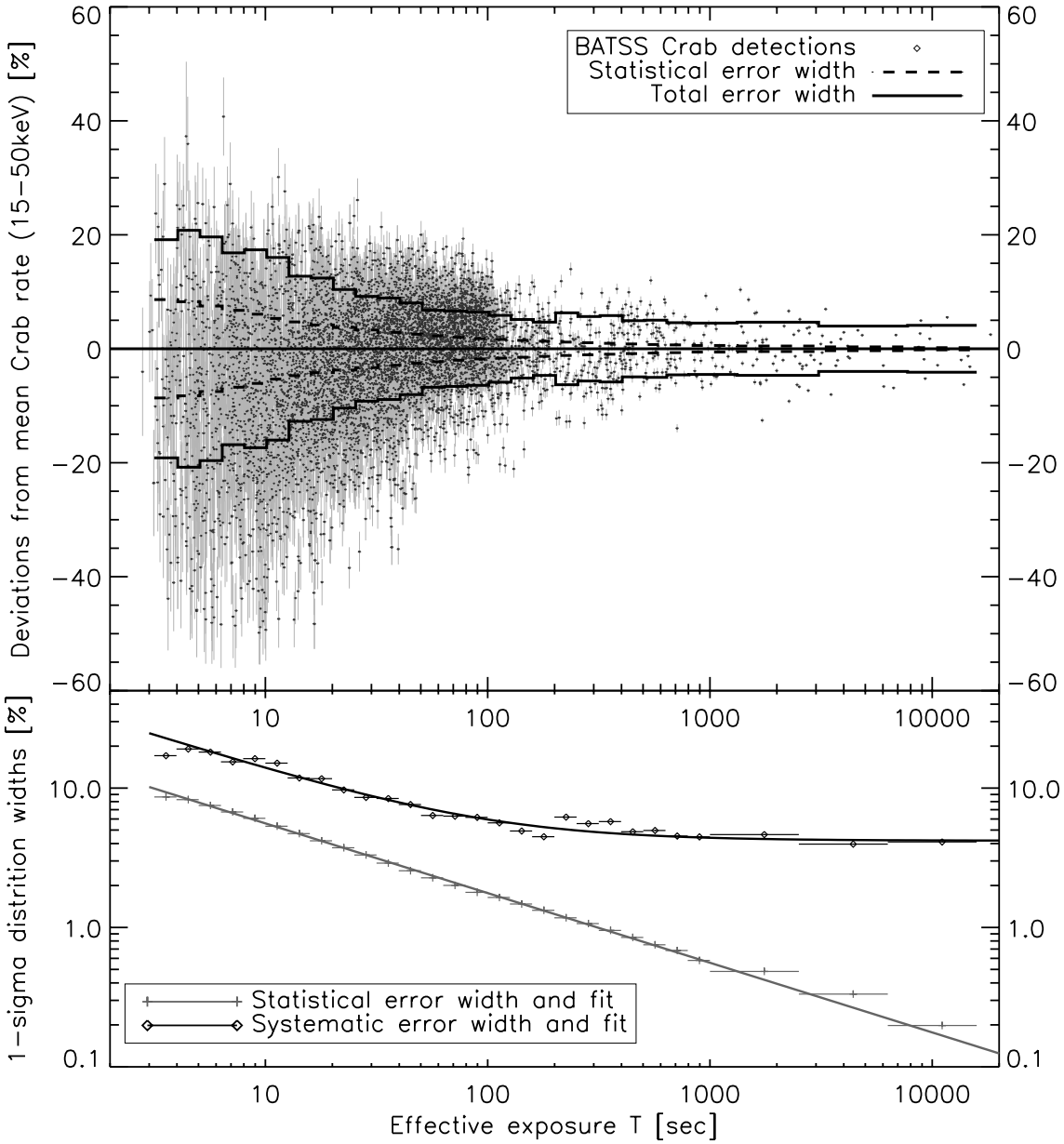

FIGURE 2.10: Log-normal distribution of deviations of measured Crab flux from overall mean count rate (15–50 keV), obtained from image photometry on single-slew through monthly multi-slew observations (top panel), and fits to the statistical and systematic components of the measured source flux uncertainties (bottom panel). The total deviations as well as the distribution widths are provided as a percentage of the mean Crab flux, so they can be applied generally to flux measurements from other sources.

considered; with $\sigma^2_{\rm stat}$ being a direct measure of the local background variance $\sigma^2_{\rm bkg}$, this suggests that even in the presence of a bright source such as the Crab and without source cleaning of the detector plane images, BATSS sky images do not yet become systematics-limited in regards to source detection and Poisson noise still dominates.

On the other hand, the source-dependent systematic uncertainty $\sigma^2_{{\rm Crab},E,{\rm sys}}$ is not found to conform to the analytic form $S_{x,E}/T_x$ of equation 2.9 for all exposures, and rather conforms more generally to the function

$$\sigma^2_{x,E,{\rm sys}} = K_{0,{\rm sys}}\, S_{x,E} \left(\frac{1}{T_x}\right) + \left(K_{1,{\rm sys}}\, S_{x,E}\right)^2 \tag{2.11}$$

which in the case of this set of Crab count rate measurements yields

$$\sigma^2_{{\rm Crab},E,{\rm sys}} = 2.96 \times 10^{-4}\ {\rm cts/cm^2/s} \cdot S_{{\rm Crab},E} \left(\frac{T}{100{\rm s}}\right)^{-1} + \left(4.19\%\, S_{{\rm Crab},E}\right)^2 \tag{2.12}$$

The first term of this equation corresponds to the expected theoretical dependence, drawn from the intrinsic Poisson statistical regime of source counts, and the second is assumed to be an independent systematic limit to the precision of measured source count rates when derived from a PSF fit to BATSS images. As seen in Figure 2.10, the constant term becomes dominant for exposures $T \gtrsim 200$ sec, all of which lie in the domain of co-added slew observations; the likely implication is that these higher-order slew images have more irregular source PSFs which do not necessarily conform to the fixed-width Gaussian PSF that is assumed by `batcelldetect`. Importantly, however, this limitation in the precision does not affect the *accuracy* of the count rates, which at large exposures do not appear biased either to the positive or negative side of the mean, nor does it affect the *sensitivity* of the observation, since this is determined by the local background rate which is still a Poisson-dominated function of $T^{-0.5}$.

Unlike the case of the statistical error constant $K_{\mathrm{Crab},E,\mathrm{stat}}$ of equation 2.10, which was energy- and background-dependent, the systematic error constants $K_{0,\mathrm{sys}}$ and $K_{1,\mathrm{sys}}$ of equation 2.11, having been decoupled from the count rate $S_{\mathrm{Crab},E}$, can be generally applied to other BATSS source count rates derived from PSF fitting, and are thus an intrinsic characteristic of BATSS detections. From equation 2.12, at the characteristic slew exposure time of 100 sec and 100% source coding, the net systematic source count uncertainty is 6.5%, and at the characteristic monthly exposure time of 10 ksec it is 4.2%. By comparison, in the *Swift*-BAT Hard X-ray Transient Monitor, the systematic errors found from Crab detections in the same 15–50 keV energy band for single-pointing observations ($T \sim 1$ ksec) and daily pointing observations ($T \sim 10$ ksec) were found to be 4.6% and 3.5% of source flux, respectively (Krimm 2006). It should be noted that in both the slew and pointing cases, however, when converting count rates to source fluxes in instrument-independent units (equation 2.1), it is always more accurate to do so by first performing a spectral fit which, unlike PSF fitting, does take into account the instrument spectral response and does not assume a Crab-like spectrum, which can lead to differences in the order of 10% or more in the measured source flux.

2.4.4 Source position uncertainty

An accurate estimation of the error circles of reported BATSS positions is essential for the subsequent observation of new bursts by the *Swift* narrow-field instruments as well as the optical observations by ground telescopes. In further offline analysis, they are also important in matching detections to each other and to likely counterparts, and as in the case of signal-to-noise ratios and source fluxes, they must be calibrated independently for the particular systematic conditions of BATSS observations. The estimation of source position uncertainties was done by running blind detection of 3 bright, persistent sources

(Crab, Cyg X-1, Sco X-1) on a set of 64,794 images of both single and co-added slews over a period of three years (November, 2007 to November, 2010). The blind detection uses the tool `batcelldetect` and a fixed-width Gaussian PSF to fit for the position of these sources in the neighborhood of their catalogued position; this differs from a regular BATSS run where the positions of catalogued sources are held fixed while blind detection is only used to search for new sources. Figure 2.11 shows a scatter plot of the resulting offsets between the blind and catalogued positions as a function of the signal-to-noise ratio (S/N), with the signal value given by the image pixel value at the position of the blind detection centroid.

In order to provide an empirical fit to the error radii at various confidence levels, we first binned the raw data along the S/N domain such that all bins would contain an equal number of sources if the detections had been sampled from a cumulative $\log N$–$\log S$ distribution of slope 3/2, as would be expected of a uniform, isotropic distribution of persistent sources throughout space; those bins are to be weighted equally in the fit. Within the sample of detections in each bin, we interpolate to find the 68%, 90% and 99% error radii for the data bin, thus providing the raw data to be fitted at each confidence level. The resulting binned sample for the 90% confidence level is illustrated in Figure 2.11, as well as the resulting fits for all three confidence levels.

For a given confidence level α, the parameterization of the error radius function $r_\alpha(S/N)$ is composed of a constant term $r_{0,\alpha}$ which represents the systematic error radius for very significant detections ($S/N \gtrsim 100$), added in quadrature with a power-law function of S/N of the general form

$$r_\alpha^2(S/N) = r_{0,\alpha}^2 + \left[r_{1,\alpha} \left(\frac{(S/N)_{r_1} - a_\alpha}{S/N - a_\alpha} \right)^{b_\alpha} \right]^2 \tag{2.13}$$

This model and its parameters factor in a number of systematic effects that combine to create the distribution shown in Figure 2.11. Most relevant among them are: 1) the smear-

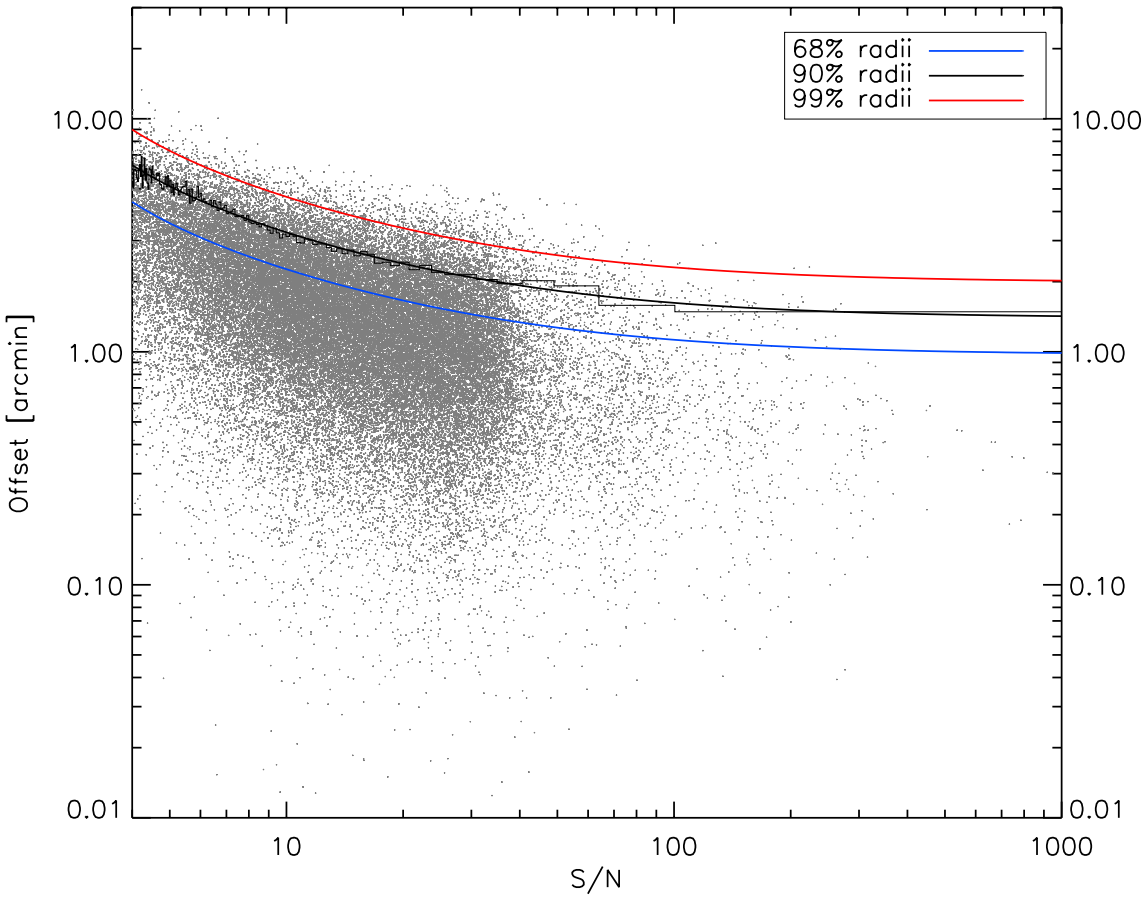

FIGURE 2.11: Position uncertainty vs. S/N of three persistent sources (Crab, Cyg X-1, Sco X-1) from BATSS single-slew and co-added slew images taken over a period of 3 years (November, 2007, to November, 2010)

ing of the image along the slew direction, given the *Swift* slewing speeds of up to $60'$/sec (Gehrels et al. 2004); 2) the distortion of the PSF shape created along the radial direction with increasing distance from the centers of the ZEA sub-projections of the BATSS full-sky images, as equal-area projections do not preserve shapes (Calabretta & Greisen 2002); 3) distortions of up to $2'$ in the azimuthal (rolling) direction of the BAT FoV which primarily affect areas of low partial coding fraction; 4) the image oversampling factor of 2 employed at the FFT imaging stage, which generates coarser raw images than would be obtained with a higher oversampling factor, and thus results in a less precise PSF centroiding in comparison.

In the parameterization of the power-law function of equation 2.13, $r_{1,\alpha}$ represents the contribution to the error radius at a given characteristic significance $(S/N)_{r_1}$, and the parameters a_α and b_α determine the functional dependence of the error radius at other significance levels. The model can be further simplified by decoupling the dependence on the confidence level α from the dependence on S/N by including it only as a multiplicative constant K_α, giving the relation the final form

$$r_\alpha(S/N) = K_\alpha \sqrt{r_0^2 + \left[r_1 \left(\frac{(S/N)_{r_1} - a}{S/N - a} \right)^b \right]^2} \tag{2.14}$$

We thus need only determine the parameters r_0, r_1, a and b, given a chosen characteristic significance $(S/N)_{r_1}$, at an arbitrary confidence level α_0 where $K_{\alpha_0} \equiv 1$, and then do a least-squares minimization at all other confidence levels to calculate the corresponding K_α. The confidence level chosen for the initial fit was $\alpha_0 \equiv 90\%$, since this is the characteristic level at which error radii are normally reported to the GCN system, and the choice $(S/N)_{r_1} \equiv 6.0$ was made in order to define the boundary between the regimes of high-significance and low-significance detections. The resulting values of the 4-parameter fit of equation 2.14 to the

90% BATSS error radii are shown in Table 2.2 below.

TABLE 2.2
Model parameters for BATSS 90% confidence error radii (equation 2.14), including both statistical and systematic effects, and defined for $S/N \geq 4.0$

Parameter	Value	Description
r_0	$1.40'$	Systematic error radius at high-significance limit ($S/N \gtrsim 100$)
r_1	$4.23'$	Significance-dependent contribution at $(S/N)_{r_1} \equiv 6.0$
a	2.20	S/N offset
b	0.51	Power-law index of significance-dependent contribution

For the 68% and 99% confidence levels, the corresponding values of the multiplicative constant K_α are shown in Table 2.3 below, along with the resulting error radii at a few critical significance values. The fits for all three confidence levels are displayed along the raw data in Figure 2.11.

TABLE 2.3
Multiplicative constant K_α (equation 2.14) for selected confidence levels, and resulting BATSS position uncertainties $r_\alpha(S/N)$ at critical significance values

CL[a](α)	K_α[b]	$r_\alpha(S/N)$ [arcmin]				
		4.0σ	5.0σ	6.0σ	10.0σ	100.0σ
68%	0.69	4.40	3.56	3.09	2.26	1.13
90%	1.00	6.33	5.13	4.46	3.26	1.62
99%	1.42	8.99	7.29	6.33	4.62	2.30

[a]Confidence Level α

[b]By definition, for $\alpha = \alpha_0 \equiv 90\%$, $K_{\alpha_0} \equiv 1$

2.5 BATSS sensitivity

The combined effects of the instrument systematics and imaging methods employed in BATSS observations yield an overall survey sensitivity to point sources that is measurably different from that achieved in pointing observations, even after subtraction of systematic

effects that can be modeled in the ground analysis. In order to draw a global empirical comparison of sensitivities in the two observation modes, we have run a survey from a selection of slew and pointing data, where we have paid special attention to isolating systematic effects that are dependent on the instrument and observation mode employed from those due to the effects of external individual sources in the field-of-view. The slew observation data has been taken from BATSS results over the full month of October, 2008, while the pointing data was, for the purposes of increasing the number of data points used, drawn from six full months' worth of observations in the period between May, 2008, to June, 2010, spaced by regular intervals of 5 months. The pointing data was downloaded from the *Swift* archive and processed making standard use of the analysis tool `batsurvey`, developed by the BAT team for ground-analysis processing of the *Swift*-BAT Hard X-ray Survey (Tueller et al. 2010). This survey sample employs a more careful treatment of systematic effects in pointing observations than either the regular on-board or ground BAT data analysis, or other long-term surveys by the BAT team such as the *Swift*-BAT Hard X-ray Transient Monitor (Krimm et al. 2006), and is thus the one we employed for all pointing-mode results that are quoted in this section.

For the purposes of this comparison, it is appropriate to distinguish among three sources of systematics that negatively impact the instrument sensitivity from its theoretical value: 1)The presence of bright sources within the BAT FoV, which add both Poisson and coding noise in any sky image from a coded aperture telescope; 2)Non-uniformities across pixels in the detector plane, including hot/cold and disabled pixels, as well as large-scale effects across groups of pixels; 3)Other instrument-dependent systematics such as mask autocollimation effects and shadows from support structures. In order to measure the sky background while avoiding the bias introduced by the first of these effects, in the images used for this analysis we have measured the background not in the neighborhood of point

sources within the BAT FoV, but rather at a set of 106 fixed "blank" sky points, each of which is located at least $10'$ away from any known X-ray source. In order to derive an equivalent comparison across different surveys, these points were chosen to coincide with the same calibration points employed by the *Swift*-BAT Hard X-ray Transient Monitor and which are listed on its webpage,[2] and are displayed in the sky map of Figure 2.9a in the context of the discussion of Section 2.4.1 on calibration of BATSS detection signal-to-noise ratios. Still, since the presence of bright sources anywhere within the BAT's wide FoV also affects the background measured at blank sky points, we have made sure to provide an independent analysis for those observations without bright sources (defined as those with $S/N > 9.0$) in the FoV, which are those with a truly instrument-dependent sensitivity.

The raw results of this comparative survey are summarized in the scatter plots of Figure 2.12, which show the 5σ survey sensitivity as a function of effective exposure time $T_{\rm eff}$, defined for each sky location x as the product of its instrument exposure time $T_{0,x}$ by its mean partial coding fraction p_x. Slew and pointing images have been derived independently for two energy bands: 14–50 keV (Figures 2.12a and 2.12b), roughly equivalent to the BATSS Soft energy band, and 14–195 keV (Figures 2.12c and 2.12d), the energy band used in BAT pointing survey results (Markwardt et al. 2005; Tueller et al. 2010). In each case, the detection results have been divided between those with the presence of bright sources in the FoV ($S/N > 9.0$), for which a source cleaning procedure —which is not implemented in BATSS images— is implemented in pointing observations, and those without bright sources and no such source cleaning in either case. In order to quote the results in mCrab units, a standard Crab count rate was used for each energy band, equal to the average of the measured rate from the BAT survey results taken over all individual pointings with the Crab in the FoV, so the result is entirely dependent on the blank

[2] `http://heasarc.nasa.gov/docs/swift/results/transients/BAT_blank.html`

sky point backgrounds measured either over individual pointings or co-added slews. As to the range of effective exposures $T_{\rm eff}$ considered, this was constrained by the duration of individual pointings continuously locked to fixed positions in the sky, and where data was accumulated in snapshots of 300 sec each; such exposures ranged from ∼10 sec in the case of short intervals left over after the last 300-sec snapshot of a longer pointing, and up to ∼3 ksec in the case of several snapshots taken consecutively within the same pointing. Accordingly, slew images were co-added in order to extend the exposure range from the maximum 120 sec of individual slews up to >10 ksec after co-adding all slews in the month-long sample considered here, thereby exceeding the corresponding pointing exposure range. Overplotted on all these figures is the ideal Poisson-limited sensitivity of the BAT instrument as derived by Tueller et al. (2010), which extended to this time domain can be quoted as being 99 mCrab $(T_{\rm eff}/100{\rm s})^{-0.5}$. Also plotted is the extrapolation from the BAT 3-month high-latitude survey sensitivity result (Markwardt et al. 2005) of (8.5 ± 1.5) mCrab $(T_{\rm eff}/20{\rm ks})^{-0.5}$, which was derived from BAT high-latitude pointing survey data at 30 ksec $< T_{\rm eff} <$ 1 Msec.

In order to derive the intrinsic sensitivity of BATSS observations, i.e. that due only to instrument-dependent effects, without regard for the effect of external bright sources, we binned the data from individual blank point detections into logarithmic time bins and fitted it to a power-law model, first without assuming a square-root dependence on $T_{\rm eff}$. This fit is overplotted on figures 2.12b (14–50 keV) and 2.12d (14–195 keV), and yielded 5σ flux sensitivities $S_{5\sigma}$ of

$$S_{5\sigma,{\rm slew}}(14\text{–}50\ {\rm keV}) = (117.8 \pm 3.5)\ {\rm mCrab} \cdot \left(\frac{T_{\rm eff}}{100{\rm s}}\right)^{-0.4991\pm0.0023} \tag{2.15}$$

$$S_{5\sigma,{\rm slew}}(14\text{–}195\ {\rm keV}) = (120.1 \pm 3.5)\ {\rm mCrab} \cdot \left(\frac{T_{\rm eff}}{100{\rm s}}\right)^{-0.4988\pm0.0022} \tag{2.16}$$

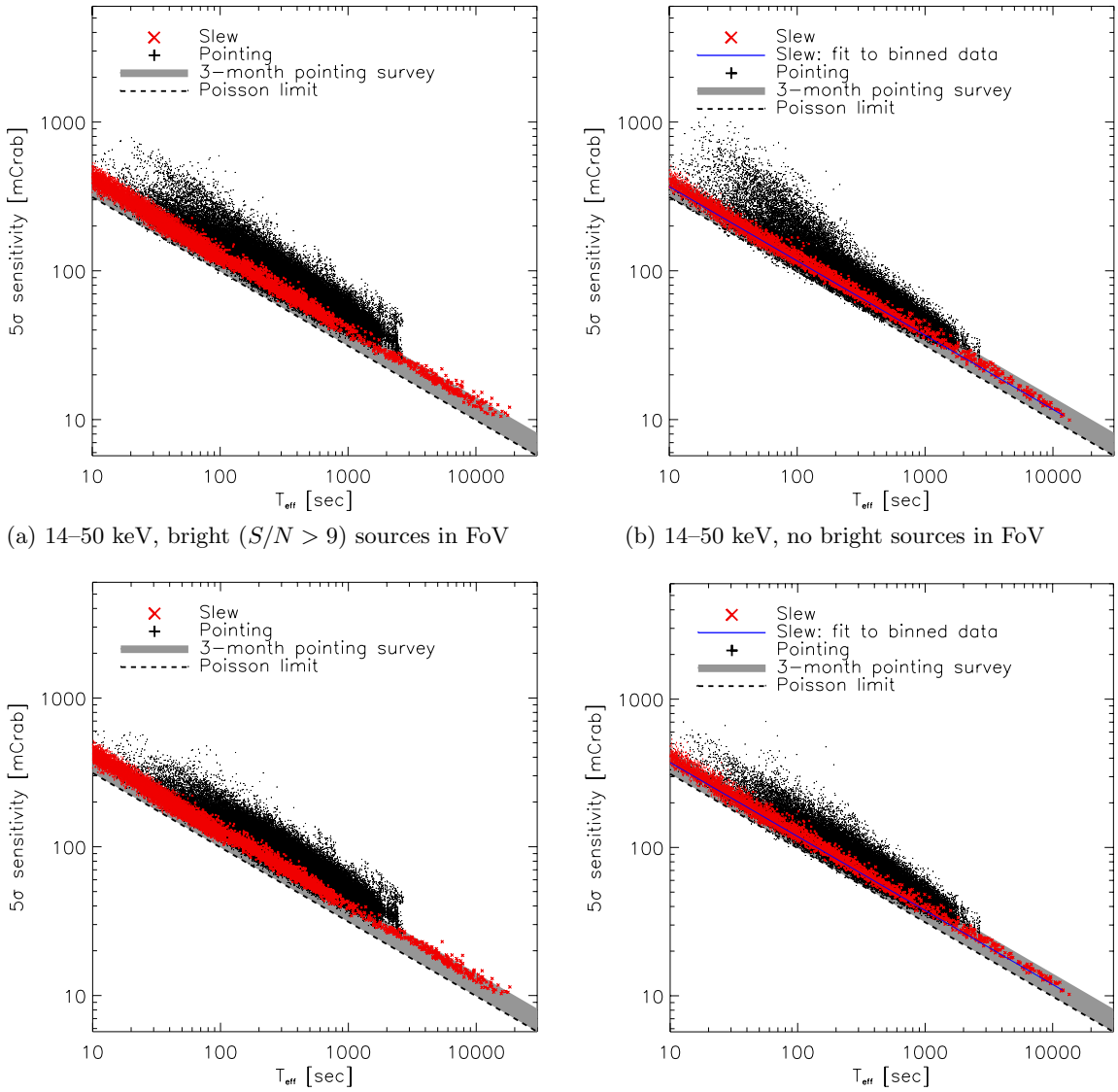

(a) 14–50 keV, bright ($S/N > 9$) sources in FoV

(b) 14–50 keV, no bright sources in FoV

(c) 14–195 keV, bright ($S/N > 9$) sources in FoV

(d) 14–195 keV, no bright sources in FoV

FIGURE 2.12: Scatter plots of 5σ sensitivities [mCrab] from slew (red) vs. pointing (black) observations as a function of effective exposure time $T_{\rm eff}$ in two energy bands: (a)-(b) 14–50 keV and (c)-(d) 14–195 keV. The left-hand panels are from observations with bright sources ($S/N > 9$) in the BAT FoV, while the detections in the right-hand panels are from observations with no bright sources in the BAT FoV. The extrapolated sensitivity from the BAT 3-month high-latitude pointing survey (gray, Markwardt et al. 2005) and the Poisson limit for the BAT (dashed line) are provided as well for comparison.

Given the consistency of these fits with a Poisson-dominated dependence of $T_{\rm eff}^{-0.5}$, we further derived a 1-parameter fit to these sensitivities of

$$S_{5\sigma,\rm slew}(14\text{–}50\ \rm keV) = (116.7 \pm 1.1)\ \rm mCrab \cdot \left(\frac{T_{\rm eff}}{100s}\right)^{-0.5} \tag{2.17}$$

$$S_{5\sigma,\rm slew}(14\text{–}195\ \rm keV) = (119.6 \pm 1.2)\ \rm mCrab \cdot \left(\frac{T_{\rm eff}}{100s}\right)^{-0.5} \tag{2.18}$$

The comparison with the pointing data results can be most clearly observed in Figure 2.13, where the sensitivity data has been binned into logarithmic bins in the effective time $T_{\rm eff}$, and the ratios of slew-to-pointing sensitivities have been derived for each bin in all cases considered here. The top panel in Figure 2.13a shows the ratios in the 14–50 keV band, both for the entire data sample and for those observations without bright sources in the FoV only; the bottom panel shows the same ratios for the 14–195 keV band. Figure 2.13b summarizes the results for both energy bands as a comparison of the intrinsic, instrument-dependent sensitivities for both modes of observation, as derived from the detections from observations without bright sources in the FoV.

Given the Poisson-dominated dependence of the slew sensitivity over the entire exposure domain considered here, the overall results illustrated in Figure 2.13b show there are several exposure regimes where the pointing sensitivity becomes dominated by systematics, as illustrated in particular by the data at $T_{\rm eff} < 150$ sec (I) and $T_{\rm eff} > 1$ ksec (III), where there is an evident deviation from the $T_{\rm eff}^{-0.5}$ dependence expected from a Poisson-dominated regime. Even though no pointing data was collected for $T_{\rm eff} < 10$ sec, it is expected that at very short exposures the noise regime will be dominated by Poisson noise, so the pointing results below ∼300 sec already suggest the onset of a systematics-dominated regime below 100 sec, if no corrections are applied. However, the BAT survey analysis does apply a number of systematics corrections on the detector plane, as described by Tueller et al.

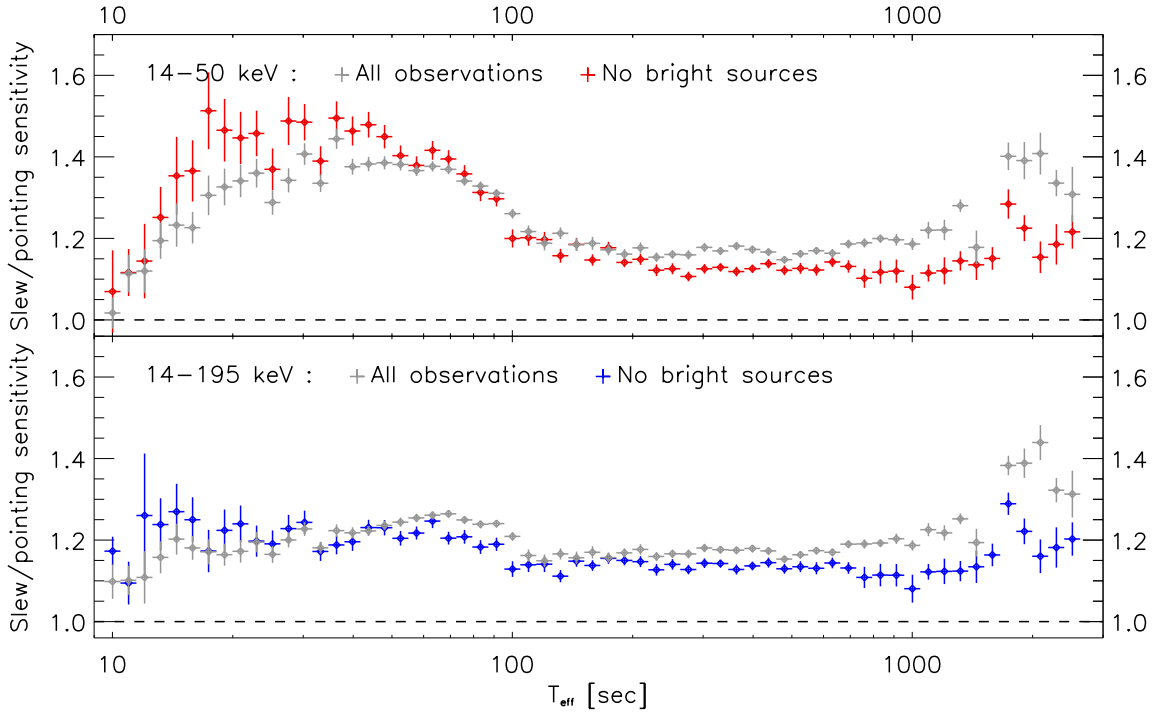

(a)

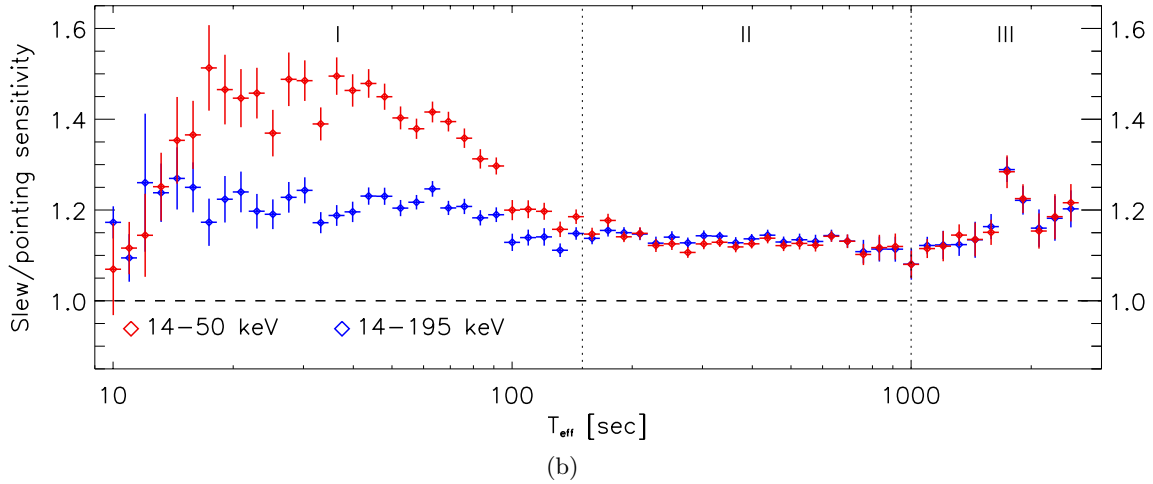

(b)

FIGURE 2.13: (a) Slew/pointing sensitivity ratios as a function of effective exposure time $T_{\rm eff}$ in all observations in the sample compared to only those without bright sources in the FoV, for both 14–50 keV (top panel) and 14–195 keV (bottom panel). (b) Intrinsic (i.e. instrument-dependent) slew/pointing sensitivity ratios summarized for both energy bands, featuring three clear exposure regimes where the dominance of systematic effects on pointing-mode sensitivity varies.

(2010). These include the removal of hot/cold/disabled detector pixels, modeled large-scale detector background, the coding noise due to bright sources, and also of detector pixels that deviate by more than 4σ from the mean count rate even after background subtraction. Of these, only the initial removal of hot/cold/disabled pixels is implemented as part of the BATSS slew processing, although global background or count rate variations across the detector could also be included for a full BATSS slew as part of a future upgrade to BATSS processing. The effectiveness of all of these corrections in improving pointing-mode sensitivity directly depends on photon count statistics, however, which explains why only for a long enough effective exposure of $T_{\rm eff} > 100$–300 sec and a broad energy band (14–195 keV instead of 14–50 keV as illustrated by Figure 2.12) does the sensitivity finally become Poisson-dominated.

The pointing sensitivity curve features again the onset of a systematics-dominated regime above $T_{\rm eff} > 1$ ksec which, unlike at the short-exposure regime, equally affects the data at both 14–50 keV and 14–195 keV. This can no longer be explained by poor photon count statistics, but rather by the unmodeled cumulative systematic effects of fixed pointing, such as those caused by the finite thickness of the mask and its support structure, an imperfect instrument shielding, and having each sky location being observed by a different but fixed set of of detector pixels. These systematics would become monotonically dominant as suggested by the results up to $T_{\rm eff} \sim 3$ ksec, unless the instrument's pointing direction and/or roll angle are changed, as it is indeed done for longer exposures. The extrapolated results from the BAT 3-month pointing survey suggest that indeed a Poisson-dominated sensitivity is recovered when many pointings are co-added, which is an analogous operation to what is done in a slew observation.

In contrast to the pointing results, the slew-mode sensitivity results feature a much longer range of effective exposure times where the noise regime is dominated by statistics,

as evidenced by the dependence on $T_{\rm eff}$ of the 2-parameter fits to the slew-mode sensitivities $S_{5\sigma,\rm slew}$ in equations 2.15 (14–50 keV) and 2.16 (14–195 keV). These fits are consistent with the $T_{\rm eff}^{-0.5}$ dependence expected of a Poisson-dominated regime, and apply to the entire range of effective exposures of 10 sec $< T_{\rm eff} <$ 20 ksec that were achieved over this 1-month survey, in particular when no bright sources are located within the BAT FoV.

As to the slew/pointing sensitivity ratio over the various $T_{\rm eff}$ regimes, the results in figure 2.13b show that at the short-exposure end (regime I: $T_{\rm eff} <$ 150 sec) there is a clear advantage for slew observations, the narrower the energy band concerned the more pronounced the difference —due to the reduced photon count statistics—, reaching up to a ∼50% improvement over pointings of equal exposure in the soft 14–50 keV energy band. Then, at intermediate exposures (regime II: 150 sec $< T_{\rm eff} <$ 1 ksec), the systematic corrections applied to the pointing data become most effective in yielding an approximately Poisson-dominated regime, but the slew sensitivity is still greater by a factor of over 10% over the entire range, despite the smaller number of corrections applied. Lastly, at the long-exposure end (regime III: $T_{\rm eff} >$ 1 ksec), the intrinsic systematics of fixed pointing become increasingly dominant and allow for a greater slew sensitivity of up to ∼30% at the longest allowable pointing exposures of a few ksec for the BAT telescope.

2.6 Conclusions

The BATSS survey employs slewing coded aperture imaging as its observational method, a technique first proposed by Grindlay & Hong (2004) from our own research group, but which had not yet been demonstrated on a fully operational space-based telescope such as *Swift*-BAT. We began this chapter by providing the background in coded aperture imaging and the BAT telescope necessary to understand the context within which BATSS operates. This introduction was then followed by a description of the imaging algorithm developed to

generate BATSS images, taking into account the general features of the BAT telescope, the particular issues involved in imaging slew data in this coded aperture imaging telescope, and the software package developed by the BAT team for the use of researchers who want to analyze BAT data. The three main stages devised in the BATSS imaging process for individual slews were:

1. The implementation of the coded aperture imaging process on 0.2-sec sky images, taking into account the large slewing speeds of up to $\sim 1^{\circ}$/sec that are typical of *Swift*.

2. The projection of these images onto a quad-cube, zenithal equal area (ZEA), full-sky projection we developed for the imaging and analysis of BATSS slew observations.

3. The variance-weighted addition of projected sky images to produce a full single-slew image, after the imposition of a 15% coding fraction (CF) threshold in order to minimize the noise contribution from low-partial coding regions, an optimization reached by analyzing the behavior of source S/N as a function of CF threshold in a selection of slew observations over the Crab.

Taking the resulting sky images from the imaging phase in the Soft (15–50 keV), Hard (50–150 keV) and Broad (15–150 keV) energy bands, along with an array of auxiliary data products associated with them, the BATSS detection phase then follows by:

1. Forcing detection on a number of input known sources as part of BATSS' monitoring of transient source activity.

2. Performing blind detection to look for new candidate sources by using a sliding-cell algorithm to find count excesses in the slew image, followed by fitting to the Gaussian point-spread function (PSF) of the BAT instrument.

3. Enforcing a set of coincidence criteria (figure-of-merit algorithm), to be presented in Chapter 3 within the context of the BATSS pipeline implementation, on unidentified blind detections of two types: 1) across energy bands within a single slew, in order to identify candidate GRBs, whose detection parameters would then be relayed to the world via the Gamma-ray burst Coordinates Network (GCN); and 2) across multiple slews in order to identify candidate transients for BATSS' Multi-slew Hard X-ray Survey.

The description of the BATSS imaging and detection algorithms were then followed by a quantitative analysis of systematic effects on BATSS images, which revealed the following important findings:

- The detection significances of blank points in both BATSS single-slew and BATSS multi-slew images (up to the 1-year timescale) are very nearly Gaussian in their distribution, which means no corrections are necessary in the reported signal-to-noise ratios of BATSS detection, unlike the case of BAT pointed observations which featured larger widths of 1.12σ and 1.23σ in the corresponding distributions for single pointings and 1-day mosaicked pointings.

- From an analytical model to estimate source flux uncertainty, we found that it is composed of a statistical term proportional to the local image background, and a systematic term attributed to the coding noise due to the source itself in its local region, which depends on the source count rate $S_{x,E}$ and its effective exposure T_x as $\sqrt{S_{x,E}/T_x}$, and may therefore become a dominant source of systematic noise when estimating fluxes of bright sources.

- When applying the analytical model to an empirical analysis of BATSS Crab observations up to the 1-month timescale, it was found that the statistical term followed the $T_{\rm eff}^{-0.5}$ dependence of a Poisson-dominated regime, which would consequently apply to

the local background as well. However, the systematic term had an additional constant contribution equal to 4.19% of the source count rate, and which becomes important at $T_{\rm eff} \gtrsim 200$ sec, i.e. in the regime of multi-slew observations. This does not imply a limiting sensitivity in the BATSS survey, however, since image backgrounds have been shown to be Poisson-dominated, but it does imply that the BATSS source PSF in multi-slew observations may become appreciably different from the $22.5'$ (FWHM) BAT PSF.

- BATSS position uncertainties, including both statistical and systematic effects, fit a 4-parameter empirical model, characterized at the 90% confidence level by a constant systematic component of $1.40'$ at the high-significance limit ($S/N \gtrsim 100$), and a power-law function of S/N with index 0.51, which gives an additional contribution of $4.23'$ at the characteristic $S/N = 6.0$, the boundary between the regimes of high-significance and low-significance detections. Error radii at other significances are related in the model to the 90% confidence values though a multiplicative constant, which we found to be 0.69 at the 68% confidence level, and 1.42 at the 99% confidence level.

This study culminated with an empirical analysis of the BATSS survey sensitivity in the range of effective exposures 10 sec $< T_{\rm eff} <$ 3 ksec for two energy bands, 14–50 keV and 14–195 keV, where we were able to compare the results with analogous BAT pointing survey sensitivities over the same exposure range. The analysis was based on the observed background levels in the local region of 106 blank sky locations, which allowed us to isolate the systematic effects that were truly dependent on the BAT instrument itself and the mode of observation employed (i.e. either slewing or pointing), from those due to external individual sources in in the FoV. The analysis revealed a Poisson-dominated, $T_{\rm eff}^{-0.5}$ dependence of the background of slew images over the entire exposure range, with an intrinsic sensitivity of 116.7 ± 1.1 mCrab at 100-sec exposure in the 14–50 keV band, and 119.6 ± 1.2 mCrab at 100-sec exposure in the 14–195 keV band. By contrast, the pointing-

mode sensitivity, despite a larger set of systematic corrections applied, was worse than the slew-mode sensitivity by an average of 20% across the entire exposure range considered, and showed to become significantly limited by systematics in two exposure regimes in particular:

1. $T_{\rm eff} \lesssim 150$ sec —the exposure regime for single slews—, where the small amount of photon count statistics prevent the systematic corrections applied to pointed images from becoming effective, and which therefore becomes more pronounced the narrower the energy band considered.

2. $T_{\rm eff} \gtrsim 1$ ksec, where the cumulative systematic effects of fixed pointing —e.g. those related to unmodeled shadowing due to the mask's thickness and support structures, imperfect instrument shielding, and a fixed set of detector pixels recording the counts for each sky location— become increasingly dominant. Photon count statistics is no longer the relevant factor, so the magnitude of the systematic effects is equally large for each energy band. A Poisson-dominated regime for pointings is only recovered at very long exposures, when many different pointings have been co-added in a similar fashion as slew images are built, as revealed by the sensitivities reported by the BAT team in their 3-month, 9-month and 22-month pointing survey publications (Markwardt et al. 2005; Tueller et al. 2010, 2008), where they report sensitivities in the 20 ksec $< T_{\rm eff} <$ 1 Msec regimes that are consistent with BATSS sensitivities at $T_{\rm eff} < 3$ ksec.

The overall result of this study on the systematic effects associated with our implementation of the BAT Slew Survey, and in particular our study on survey sensitivity, reveal an experimental confirmation of one of our two primary technical motivations for conducting this survey, as presented in the corresponding section of the Introduction (Chapter 1): an increased sensitivity compared to that of analogous surveys in the hard X-ray band, in

particular that being carried out by the BAT telescope itself while operating in pointing mode. As mentioned in the Introduction chapter as well, that survey has already managed become the deepest, most sensitive all-sky hard X-ray survey to date, and we have shown in this chapter to be in a position to replicate its role at the short end of the exposure timescale, where pointing observations become limited by a number of systematic effects in relation to BATSS slews, despite the sophisticated imaging data pipeline of the BAT pointing survey, which we made use of in generating the pointing data sample for this analysis. Though several improvements are certainly possible in the BATSS imaging technique presented here, which we will refer to in the Conclusions of this dissertation (Chapter 5), the current implementation has already revealed to be an important development towards the goal of achieving a highly sensitive, all-sky, hard X-ray slew survey, with a clear potential to broaden *Swift*'s domain of scientific discovery.

Chapter 3

BATSS Data Pipeline

Abstract

The BAT Slew Survey (BATSS) imaging and detection algorithms, introduced in Chapter 2, are implemented in the BATSS data pipeline presented in this Chapter. The pipeline, written in the Interactive Data Language (IDL), has been designed as a modular system composed of independent stages, capable of handling analysis tasks that range from the pre-processing of raw, uncalibrated event-by-event data from the *Swift*-BAT telescope that have been received in real time after being downlinked to the Malindi ground station, to the creation of a series of high-level (Level 3) data products. Chief among the high-level products is a database of candidate Gamma-Ray Bursts and Transient sources, built from analysis of unidentified detections in single-slew and multi-slew observations (orbital, daily, weekly, monthly, yearly, and full-survey) produced as part of the pipeline. Each pipeline stage is implemented as a stand-alone BATSS software tool, all of which have undergone successive upgrades, and the current version presented here dates from March, 2011, when work on the BATSS trigger database was completed. Also included here is a description of the dedicated BATSS hardware system at the Harvard-Smithsonian Center for Astrophysics that has made this effort possible.

3.1 Introduction

A primary technical challenge for the BAT Slew Survey (BATSS) is the creation and implementation of a processing pipeline that is able to perform imaging on the input *Swift*-BAT raw event-by-event data received in real time from the *Swift* Data Center (SDC) at Goddard Space Flight Center (GSFC), shortly after the data has been telemetered down from the spacecraft via the Malindi ground station. Such a data pipeline must be capable of producing both single-slew and multi-slew images, taking into consideration the continuously changing spacecraft attitude that is characteristic of slew observations, continuing with detection and identification of both new and catalogued bursts and transient sources, and doing so in a fast, automated fashion that allows for follow-up by other observatories as quickly as possible. This requires both a software system that is specifically designed and optimized for this purpose, and a hardware system capable of handling the corresponding data rate. The BATSS data pipeline, illustrated in the flow chart of Figure 3.3, is a software package written in the Interactive Data Language (IDL) which constitutes the implementation of this effort, and its main stages are described in the following sections of this Chapter, following a description of the system architecture tasked with running the BATSS software tools while providing the necessary data handling and storage.

3.2 Equipment

The raw science data for BATSS is relayed by the *Swift* ground system described by Gehrels et al. (2004) and illustrated in Figure 3.1. The Italian Space Agency's (ASI) Malindi ground station in Kenya is *Swift*'s primary communications support, both for downloading real-time data and for uploading commands between the spacecraft and the

Mission Operation Center (MOC) at Penn State University (PSU). The satellites of the NASA Tracking and Data Relay Satellite System (TDRSS) are also available for the downloading of source localizations and optical finding charts from *Swift* on-board triggers, so that rapid alerts to the astronomical community can subsequently be issued, and also for the uploading of commands for observation of Targets of Opportunity (ToOs). However, the raw data for BATSS is regularly downlinked only during the passes over the Malindi ground station.

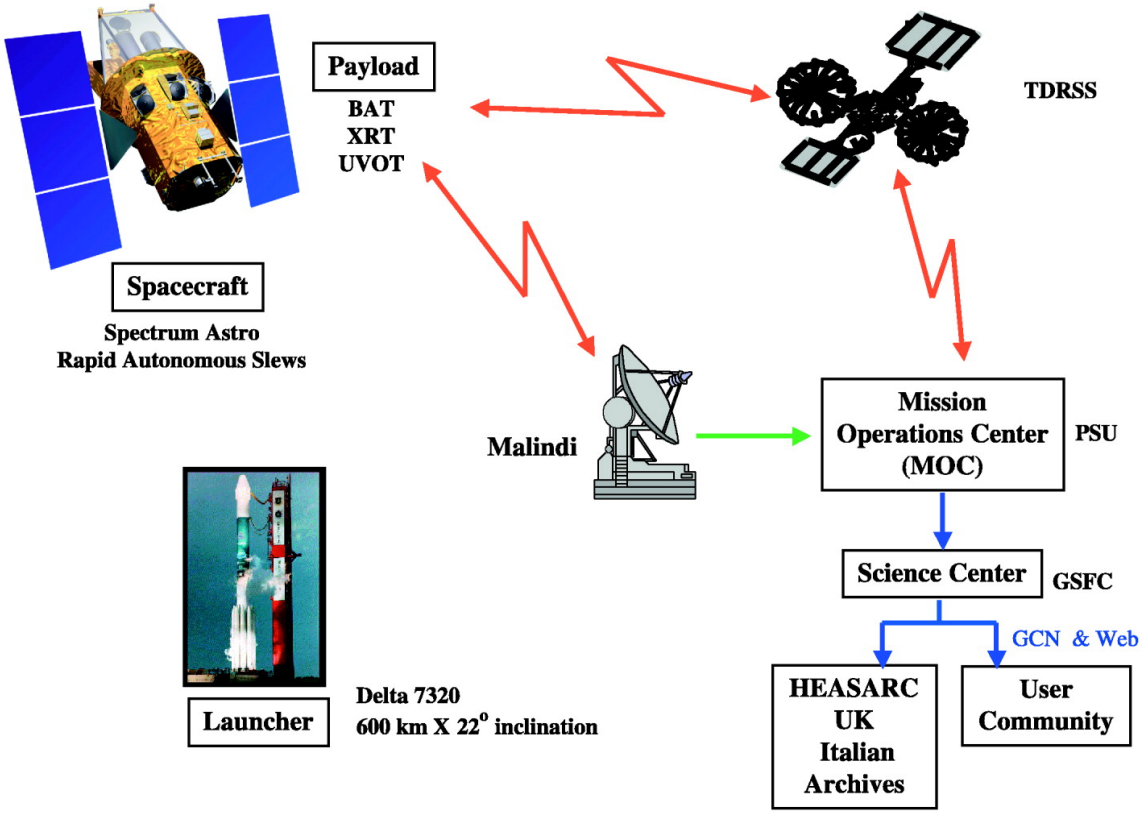

FIGURE 3.1: *Swift* mission architecture (Gehrels et al. 2004)

The MOC in turn relays the telemetry (*Level 0*) data collected to the *Swift* Data Center (SDC) at NASA's GSFC, where *Level 1*, *2*, and *3* data products in the astronomy-standard

Flexible Image Transport System (FITS)[1] format are made.[2] These data products are eventually posted permanently to the *Swift* Data Archive[3] and made available to the astronomical community via the database of the High Energy Astrophysics Science Archive Research Center (HEASARC).[4] However, the final data products for archiving are not normally posted to the HEASARC database until several days (typically 1 week) after they have been received at the SDC.

Through BATSS's association with *Swift*'s Guest Investigator (GI) program, the SDC automatically forwards the pre-processed Level 1 raw data products in real time to the dedicated BATSS servers at the Harvard-Smithsonian Center for Astrophysics (CfA). The current computer system at the CfA is composed of three (3) dedicated servers (`luna`, `mond`, and `dahl`), the first of which regularly establishes the SSH connection with the servers at the SDC, reads and pre-processes the data for offline BATSS processing, and then forwards it to the other machines for processing of individual BATSS observations. Figure 3.2 shows pictures of the three BATSS machines as currently installed at the CfA's computer facility at the Cambridge Discovery Park complex in Cambridge, Massachusetts. Table 3.1 shows their technical specifications.

---

[1] `http://heasarc.gsfc.nasa.gov/docs/heasarc/fits.html`

[2] In accordance with HEASARC standards, *Swift* Level 1 products correspond to *raw data* (Level 0) converted to FITS format, Level 2 products correspond to *reduced data* (normally calibrated and pre-processed), and Level 3 are *high-level data products* of source data for use by the scientific community in the first stages of analysis (*Swift* Science Center 2008).

[3] `http://swift.gsfc.nasa.gov/docs/swift/archive/`

[4] `http://heasarc.gsfc.nasa.gov`

FIGURE 3.2: BATSS machines `luna`, `dahl`, and `mond` at the Harvard-Smithsonian Center for Astrophysics' computational facility

TABLE 3.1
Technical specifications of BATSS machines

Machine	Processor	Memory	Hard drives	
			Volume	Size and RAID type
`luna`	Intel Xeon E5520 2.26GHz	16 GB	`luna0`	4.5 TB (RAID 1)
			`luna1`	13.0 TB (RAID 6)
`mond`	Intel Core 2 Quad Q6600 2.4GHz	8 GB	`mond1`	8.0 TB (RAID 6)
`dahl`	Intel Core 2 Quad Q6600 2.4GHz	8 GB	`dahl1`	9.6 TB (RAID 6)

Though the hardware system has undergone consecutive upgrades since it was first set up in August, 2007, the current configuration has remained the same since the major hard drive upgrade of January, 2010.[5] The `luna0` volume is the target disk where raw BATSS

[5]This upgrade was prompted by a massive system failure in December, 2009, when a disk failure in `luna` caused all of the raw slew data for BATSS to be lost, as well as a significant portion of the high-level BATSS products. The upgrade included a significant expansion of the capacity of the hard drives of all 3 machines, as well as increased security measures to prevent data loss. All disk arrays were upgraded to a RAID 6 configuration or better, so no data would be lost as a consequence of a failure of 2 individual SATA disks. A substantial software update was also implemented at the time, which included the download and full processing of all of the raw slew data from the *Swift* archive up to that point, with significant enhancements over the previous version of the analysis package.

data from the SDC are dumped by default, and it is also the disk that stores the final (Level 3) BATSS data products after detection has been run on the individual images. As such, it has been configured as a RAID 1 (mirrored) array of SATA disks, so there are always two individual copies of the contents of the drive.

On the other hand, the `luna1`, `mond1` and `dahl1` volumes are those where all of the intermediate (Level 2) data products are stored from the processing of individual observations by each machine; such data products include final sky images for every observation. They have all been configured as RAID 6 (double parity) arrays in order to prevent any data loss upon failure of any two individual SATA disks in the array. A comprehensive review of the different types of BATSS Level 1, 2, and 3 data products and their locations on disk is provided in Appendix A.

In addition to the dedicated servers, the BATSS pipeline is capable of working with any number of additional machines with the purposes of processing a greater number of individual observations in parallel. As will be described in Sections 3.7 and 3.8, each BATSS observation is normally processed in 2 parallel threads, which means the quad-core processors of each of the machines should be able to process 2 observations simultaneously without compromising pipeline performance, and consequently the dedicated BATSS system is capable of handling 6 observations simultaneously, approximately the same number of slew maneuvers that *Swift* performs over the course of each 1.5-hour orbit. At times of heavy data load to be processed, we have made occasional use of additional computational resources at the CfA by running the BATSS pipeline on the machines `chia`, `moon` and `vogon`, capable of handling 1, 2 and 5 observations at a time, respectively, for a total of up to 14 simultaneous BATSS observations to be processed, the maximum number of simultaneous observations that the pipeline has been tested with so far.

3.3 Data pipeline flow chart

The major stages of the BATSS data pipeline are illustrated in the flow chart of Figure 3.3. The flow chart spans all phases of slew data processing for BATSS, from the telemetry downlink from the *Swift* spacecraft, to the production of BATSS Level 3 data in the form of candidate source catalogs, both from individual and multiple observations. A general description of each of the pipeline stages is provided in Sections 3.4–3.9. In addition, a review of the intermediate and final BATSS data products resulting from both real-time and archival processing is given in Appendix A, and a user guide for the BATSS software package developed to produce them, written in the Interactive Data Language (IDL),[6] is included in Appendix B.

[6]IDL is a commercial language of wide use in the astronomy community, and it is developed, distributed and licensed by Exelis Visual Information Solutions (formerly ITT Visual Information Solutions).
Website: `http://www.exelisvis.com/language/en-us/productsservices/idl.aspx`

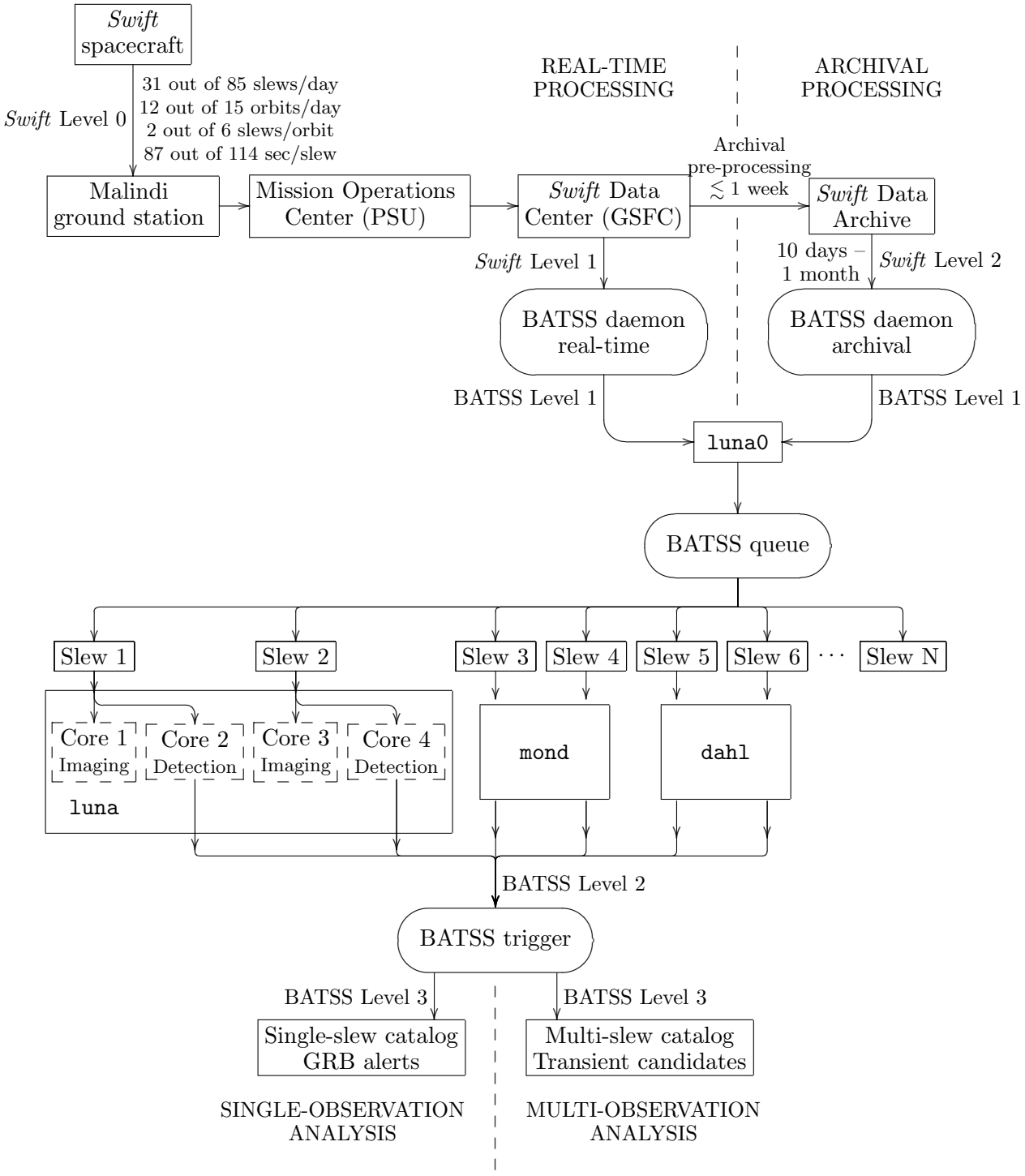

FIGURE 3.3: BATSS data pipeline flow chart

3.4 Telemetry downlink and online data transfer

As a preliminary step in the BATSS data pipeline, the required telemetry downlinks from the *Swift* spacecraft are first enabled by an event-by-event data capture command uploaded from the *Swift* Science Center at GSFC. The raw, Level 0 data are then downlinked to the Malindi ground station on each of the ∼12 daily passes the spacecraft makes,[7] and then relayed by the Mission Operations Center (MOC) to the *Swift* Data Center (SDC), where it is pre-processed into Level 1 data in a standard FITS format, without energy calibration done on the event files. From there, it is dumped into the dedicated BATSS servers at the Harvard-Smithsonian Center for Astrophysics, normally through an SSH connection to the `luna` server and the `luna0` volume, where the rest of the real-time data processing takes place offline.

On the side of the archival data, the SDC posts the final, energy-calibrated, Level 2 data products to the *Swift* Data Archive, typically within a week of the observation (*Swift* Science Center 2008). These are not transferred automatically to the BATSS servers as soon as they are posted, but they are rather pulled from the archive by the BATSS pipeline, usually within 10 days–1 month of the observation, as described in Section 3.5.

3.5 BATSS daemon

The BATSS daemon is the routine that takes the raw data products either telemetered (real-time) or downloaded (archival) from the SDC and readies them for offline processing. There are in fact two independent versions of the routine that run continuously on parallel threads (further described in Appendix B): `BATSS_daemon_realtime`,

[7] Though the spacecraft makes 15 orbits/day, in ∼3 of those orbits it does not fly close enough to the Malindi ground station to establish contact, hence there are typically only up to 12 data passes per day.

which pre-processes the real-time data as they are dumped onto the BATSS servers, and `BATSS_daemon_archival`, which regularly downloads slew data products once they have been posted to the *Swift* Data Archive, and also pre-processes them into BATSS Level 1 data.[8] The first routine iterates every time a real-time data pass is received, while the latter does so once a day, when it checks whether all the data products necessary for BATSS archival processing are available in the *Swift* Data Archive.

Given the ∼1 week delay before data are posted to the *Swift* archive by the SDC, `BATSS_daemon_archival` begins to look for archival data to download for a given date only 10 days after the original slew observations. In addition, one of the goals of archival processing is to improve the absolute timing accuracy of BATSS data products in units of Universal Time (UT) to well within the mission goal of 0.2 msec (*Swift* Science Center 2008). Times in *Swift* data products are given in units of uncorrected Mission Elapsed Time (MET), expressed in seconds after the epoch time 01/01/2001 00:00:00 UT, and the final set of corrections that account for the gradual drifting of the spacecraft clock with respect to UT are logged onto *spacecraft clock offset* files, part of the *Swift* calibration database (CALDB).[9] These files are updated by the MOC approximately only once a month, and consequently, `BATSS_daemon_archival` will not proceed until the corresponding clock offset file that includes the date to be processed has been posted to the CALDB. This results in a delay of up to ∼1 month before the results of BATSS archival data processing are available for any given date.

In addition to the spacecraft clock offset files described above, the FITS-format *Swift* Level 1 and Level 2 data products that are regularly handled by both BATSS daemon routines include:

---

[8] See Appendix A for definitions of BATSS data levels and files included in each.

[9] `http://heasarc.gsfc.nasa.gov/docs/heasarc/caldb/swift/`

Spacecraft attitude files: These standard files contain a binary table of *Swift* spacecraft attitude data records, which in turn allow determination of periods of spacecraft slewing, as well as periods of SAA passage to be excluded from downstream processing. Based on the attitude data records, BATSS single-slew observations are defined at this stage as described in Table 3.2. Also at this stage, the daemon for archival data defines a number of higher-order observations, namely the *orbital*, *daily*, *weekly*, *monthly*, *yearly* and *survey* observations. These are obtained by the addition of single slews or other higher-order observations and are also defined in Table 3.2, along with the ID nomenclature used by the BATSS pipeline for their associated data products.

Spacecraft orbital files: For the purposes of the BATSS survey, these standard files provide important information on occultation within the BAT FoV by the Earth, Sun and Moon, which in turn reduces the size of the FoV that should be considered for a given BATSS slew observation. Since orbital files are not available at the time of real-time data processing, they are only downloaded from the *Swift* archive by `BATSS_daemon_archival`. The routine then dissects these files over periods of spacecraft slewing, and creates output BATSS orbital files designated by slew observation ID, to be later used in further offline archival data processing.

Event files: One of the standard BAT raw data formats, event files contain a list of BAT detector events in the form of a binary table. In the real-time, Level 1 event files, energies are given in raw ADU (PHA) units, while the archival, Level 2 event files contain calibrated energy values in units of keV. These input event files are designated by *Swift* Observation ID in the standard form '`XXXXXXXXYYY`,' with the first 8 digits representing the ID of the target being slewed *to*, and the last 3 digits representing the Observation Segment within the *Swift* monitoring campaign of that target (Angelini 2007). In the case of BATSS, however, given that the target has no special meaning

TABLE 3.2

Definitions of BATSS observation types created by the BATSS daemon, and ID nomenclature used for their associated data products. The nomenclature for all observation types is defined in units of Universal Time (UT).

Observation type	ID nomenclature	Definitions
Slew	`YYMMDD_HHhMMmSSs+XXXs`	Single slew observation that begins at `YYMMDD_HHhMMmSSs` and lasts `XXXs`, derived from time stamps of attitude data records rounded to whole seconds[a]
Orbital	`YYMMDD_HHhMMmSSs`	Addition of all slew observations that begin during orbit that starts at `YYMMDD_HHhMMmSSs` with spacecraft at Galactic longitude $l = 0°$
Daily	`YYMMDD`	Addition of all slew observations that begin on date `YYMMDD`
Weekly	`YYMMDD`	Addition of all daily observations in the week that begins on date `YYMMDD` (Monday)
Monthly	`YYMM`	Addition of all daily observations in the month `YYMM`
Yearly	`YYYY`	Addition of all monthly observations in the year `YYYY`
Survey	`survey`	Addition of all yearly observations during the BATSS survey

[a]Since the amount of data actually captured may not necessarily span the entire slew, `XXXs` may not necessarily represent the actual exposure time contained in the observation.

in the case of a slew observation, the daemon dissects the input event files and creates a set of output BATSS event files, designated by slew observation ID. Furthermore, in the case of real-time data, the full set of data for a given slew will often come in several telemetry passes, so the daemon must also be able to update the existing BATSS event files accordingly, and flag the corresponding slew for reprocessing if necessary.

Energy calibration files: Given that raw event files in real-time processing are not energy-calibrated, standard files with maps of gain/offset setting for each BAT detector pixel must also be included as part of the telemetry passes, so the ADU-to-keV conversion for BAT events can be performed. For some of the slews in a typical day, however, it turns out that the corresponding gain/offset map may have incorrectly been assigned null values during the telemetry process, and so the daemon must scan all input energy calibration files, discard files that do not contain a full set of pixel gain/offset settings, and in that case reassign the calibration of the BATSS event file to the latest valid energy calibration file before the slew.

Furthermore, even for energy-calibrated event files, including Level 2 archival event files, it may also be necessary to re-run energy calibration. The criterion implemented in the BATSS daemon checks whether at least 50% of events in the file fall within the 10–195 keV energy range, and if not, the file is recalibrated. If several valid energy calibration files for the observation are found after downloading them from the *Swift* archive, the one closest in time before the slew is chosen. If no valid energy calibration files are found, or if the recalibrated event file still fails the criterion for valid energy calibration, the event file is discarded from further offline processing.

Detector enable/disable files: A standard BAT data product, these files are periodically produced to reflect the set of enabled and disabled pixels across the BAT

detector at a given time. The daemon relabels these files according to the BATSS nomenclature for slew observations, so they can be used in further offline processing to generate detector quality maps, which are in turn a necessary input in order to create slew sky images.

The relevant output files from the BATSS daemon stage are listed and described in Table 3.3 below, including the real-time and archival observation types for which they are created. Whether they contain event data or not, all slew observations spanned by the input spacecraft attitude files are logged into BATSS *queue files*; these are multi-extension FITS files containing one BATSS observation per file extension, and for each extension, all of the general information gathered by the BATSS daemon about the corresponding slew observation is encoded into the keywords its FITS extension header.

TABLE 3.3
Output data products from the BATSS daemon stage. The BATSS real-time and archival observation types for which they are created are included as well.

Data product	Real-time	Archival[a]	Description
Attitude files	slew	slew	Spacecraft attitude records during slew, including preceding and following pointings
Orbital files	—	slew	Spacecraft orbital records during slew (archival processing only)
Good Time Interval (GTI) files	slew	slew	Time intervals of valid science data during slew and preceding/following pointings, after excluding periods of SAA passage and *Swift* global bad time intervals
Event files	slew	slew	Energy-calibrated detector events, only for slews with captured event data
Queue files	slew	slew,O,D, W,M,Y,S	FITS files with information on every single-slew and higher-order observation spanned by attitude files. They serve as primary input for the BATSS queue stage

[a]O=orbital, D=daily, W=weekly, M=monthly, Y=yearly, S=survey

3.6 BATSS queue

As input files are pre-processed into BATSS Level 1 data products and categorized by slew observation ID, for both real-time and archival data, the queue of observations to be processed is built up and logged into BATSS queue files, which in turn serve as the primary input to the next stage of the BATSS data pipeline. The `BATSS_queue` routine then has the task of clearing the queue by assigning individual observations to BATSS machines, according to a given set of priorities. As mentioned in Section 3.2, BATSS currently runs on a set of 3 dedicated servers (`luna`, `dahl` and `mond`), each of which is able to process up to 2 slew observations at a time —whether single-slew or higher-order—, for a total of up to 6 simultaneous observations, and with the possibility of increasing the number of simultaneous observations by running in parallel on a larger number of machines.

Regarding the set of priorities implemented for assigning individual observations to machines, in the current, default operating mode, real-time slews always take priority over archival observations; among the real-time slews, those that have not been fully processed before take priority over those that have, with the latest slew (chronologically) being assigned first. Following those previously unprocessed slews, the next priority goes to slews that have already been processed at least once, but which have been modified by data from later telemetry passes. Once the queue of real-time slews has been cleared, `BATSS_queue` begins to assign the archival observations that are ready for processing; since archival data are always at least 10 days old, archival processing is not considered to be as critically time-sensitive as real-time processing is. In addition, this default set of priorities can be modified using the control routine `BATSS_queue_control`, further explained in Appendix B.

3.7 BATSS imaging thread

The imaging thread is the first of two parallel threads that run on a machine CPU once an observation from the queue has been assigned. In the case of slews (both real-time and archival), the routine `BATSS_machine_image` implements the BATSS imaging algorithm (Section 2.2) on each machine by taking several intermediate steps: first, it runs the subroutine `BATSS_evt2dpi` to create *Detector Plane Images* (DPIs) for every 0.2-sec time bin in each of the Soft (15–50 keV) and Hard (50–150 keV) energy bands. This step makes use of the the BAT software tool `batbinevt` (Markwardt et al. 2007). Then, the subroutine `BATSS_qmap_create` creates a single *detector quality map* (to screen out hot/cold/disabled pixels) for the entire slew, by applying the BAT software tool `bathotpix` and taking as inputs 1)the detector enable/disable map assigned by the BATSS deamon, and 2)a single DPI obtained by accumulating all input event data in the 15–150 keV band, from which pixels with unusually high/low number of counts can be determined. Next, the subroutine `BATSS_pcmap_create` creates a single *partial coding map* by correlating the detector quality map with the BAT mask with the help of the `batfftimage` tool. This map is later used to correct sky image counts for partial coding effects, and to determine the range of partial coding values each sky pixel is swept by the BAT FoV over the course of the slew.

In the following step, the subroutine `BATSS_img_create` creates sky images as well as variance maps by cross-correlation of each 0.2-sec DPI with the BAT mask. The FFT operation is done by the tool `batfftimage`, which takes as inputs the DPIs, the detector quality map, and BATSS attitude file for the slew. Most of the standard corrections on the output image are requested, namely those for 1)mask autocollimation effects, 2)cosine and edge projection effects, 3)FFT technique corrections, and 4)number of exposed detectors. The one remaining correction for partial coding effects is not requested at this point, however, since it is performed later after all images within the slew have been co-added.

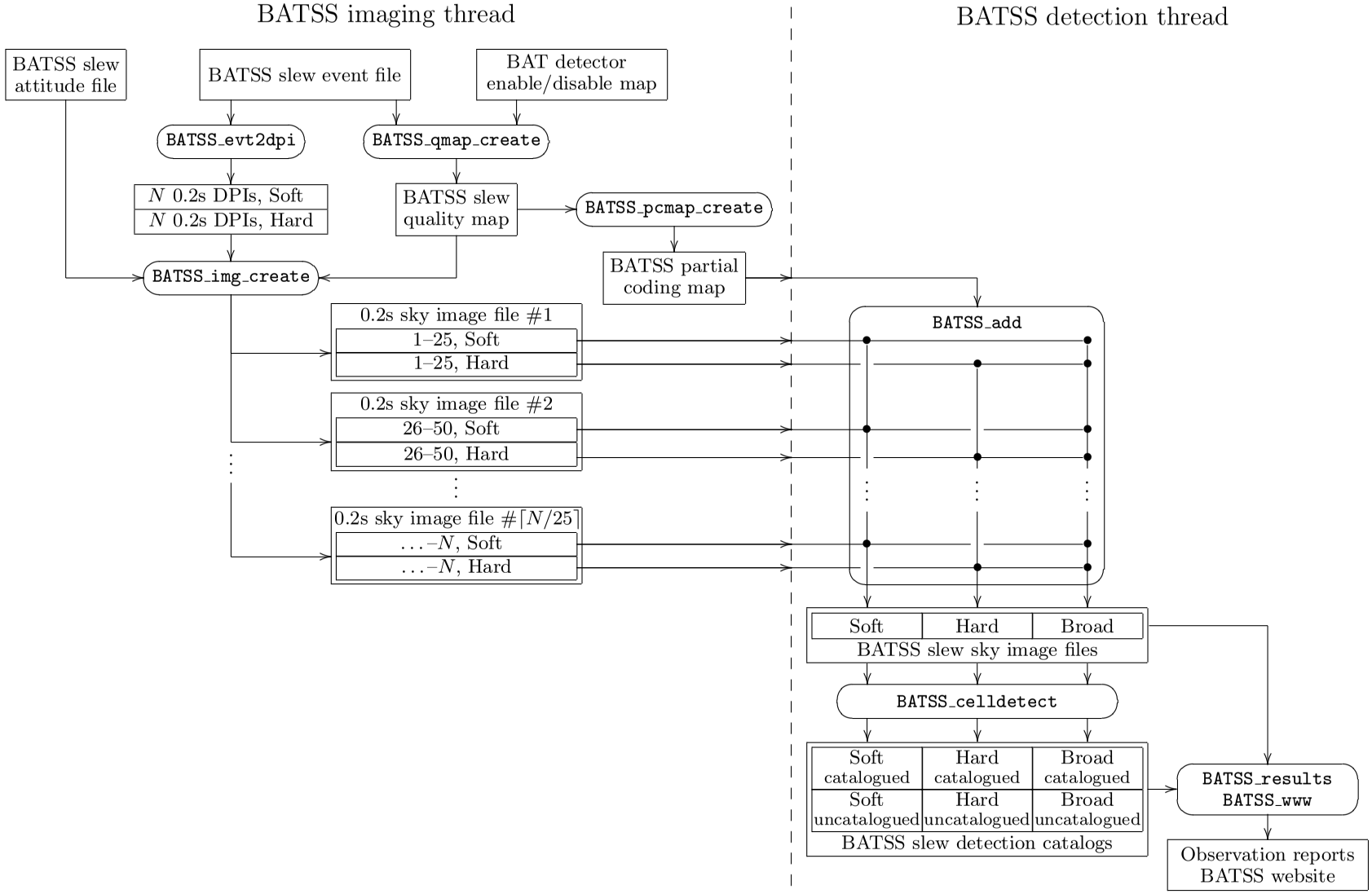

FIGURE 3.4: BATSS data pipeline: implementation of imaging and detections threads for single-slew observations (real-time and archival), showing relevant BATSS analysis tools and data products

Operationally, in order to make the detection thread for the slew proceed as quickly as possible, the sky and variance images are created in sets of 25 images (i.e. every 5 sec of instrument exposure) per energy band, per output FITS file. Once an output file is closed, it can be readily processed by the detection thread instead of waiting for the entire set of 0.2-sec sky images for the slew to be generated.

On the other hand, in the case of the archival higher-order observations (i.e. orbital through full-survey), since the FFT operation has already been conducted on the observations each of them is composed of and sky images have already been generated, `BATSS_machine_image` simply flags the observation as having been imaged and assigns it to the detection thread.

3.8 BATSS detection thread

The detection thread is the second of two parallel processing threads for an individual BATSS observation, and it is implemented in the routine `BATSS_machine_detect`, which handles single-slew and higher-order observations differently. In the case of single slews, the subroutine `BATSS_add` proceeds as soon as the first set of output 0.2-sec sky images is created by `BATSS_machine_image`, through a number of intermediate steps. First, it takes each pair of soft- and hard-band 0.2-sec sky images and co-adds them to obtain the corresponding broad-band image. Each of the 0.2-sec sky images in 3 energy bands is then projected onto the BATSS full-sky projection (quad-cube zenithal equal area) characterized in Section 2.2.2, and those in turn are co-added by variance-weighted addition. At the same time, for each pixel in the full-sky projection, additional auxiliary images are created that keep track of the accumulated exposure time as well as the time-averaged range of coding fractions the pixel sweeps through. Then, after the last of the output images from the imaging thread has been fed into the detection thread, the routine performs partial coding

correction of the 3 resulting slew images by dividing each one by the map of mean coding fractions.

In the case of higher-order observations, the input images have already been projected to the BATSS full-sky projection, so in order to produce the output sky image, it is only necessary to merge the input images by variance-weighted addition. This is done with the use of the subroutine `batss_merge`, which as in the case of single slews, also produces final output images already corrected for partial coding.

For both single-slew and higher-order observations, the subroutine `BATSS_celldetect` then performs the source detection operation itself on the BATSS full-sky images for each of 3 energy bands, by making use of the standard BAT tool `batcelldetect`; the full set of relevant input parameters used by BATSS is listed in Table 3.4. The command calls for both blind detection of unknown sources above a 3.5σ threshold, as well as detection of catalogued sources within the FoV of the observation. Current catalogs that are searched for are 1)BAT catalog of Transients (512 sources), 2)BAT ground catalog (325 sources), 3)BAT AGN catalog (153 sources), 4)INTEGRAL master catalog (1652 sources), and 5)BAT blank sky points (106 sources). The last catalog is composed by a standard set of blank sky points that are constantly monitored by BATSS for the purposes of calibrating the sky background statistics as described in Section 2.4.1. These catalogs are regularly updated by the `BATSS_daemon_archival` routine, which looks for updates in the online version of these catalogs as part of its daily operations of searching, downloading and pre-processing of new archival data.

After this first round of source detection and identification, for blind detections of sources unrecognized by `batcelldetect` a second round of source identification is done, by making a search for catalogued sources within the 90% error radius of unidentified detections, using the calibration derived in Section 2.4.4. A final catalog of unidentified

detections in all 3 energy bands of the observation is then made and fed into the next stage of the BATSS pipeline.

As a final step before further processing of unidentified detections, the subroutine `BATSS_results` is called in order to summarize the results from the imaging and detection stages into individual reports in PostScript format. As part of this script, the subroutine `BATSS_www` is called in order to post these result files to the BATSS webpage[10] and update the online list of processed observations. For each energy band, the report shows a sky image of the observation, a list of both catalogued and unidentified sources detected, as well as other general information about the observation. A sample report as currently featured on the webpage is shown in Figure 3.5, for both a single-slew and a higher-order observation (orbital observation in this example).

Once the individual machines have produced the BATSS Level 2 data, namely the sky images and detection catalogs, as well as their associated data subproducts, the individual observation is flagged as being fully processed in the corresponding BATSS queue file, and control returns to the main server (`luna`). The detection catalogs are copied to the central data volume (`luna0`) for data redundancy as well as use in the following stages of the pipeline, though the sky images must remain in the data volumes of the individual machines due to disk space constraints. If an observation was processed in a machine other than the dedicated BATSS servers, all data products are transferred to the main volume of one of the BATSS servers by calling the tool `BATSS_migrate`, and the corresponding FITS header keywords in the BATSS queue files are modified in order to indicate the new location on disk of the observation data. In consequence, after each observation is processed, no data is stored permanently on any machine other than the dedicated BATSS servers.

[10] `http://hea-www.harvard.edu/BATSS/`

TABLE 3.4
BATSS detection thread: Input parameters for `batcelldetect`

Parameter	Description	Default Value	BATSS Value
`snrthresh`	Signal-to-noise threshold for new sources	None	3.5
`incatalog`	Optional Input catalog of known sources	None	4 catalogs (see text)
`pcodefile`	Optional partial coding map file	None	Map of mean CFs over slew
`pcodethresh`	Partial coding threshold for detection	1%	35%
`bkgpcodethresh`	Partial coding threshold for background analysis	parameter `pcodethresh`	1%
`pospeaks`	Include only positive peaks in blind detection	yes	yes
`niter`	Number of iterations of source detection	2	2
`nadjpix`	Minimum number of adjacent pixels for new source detection	3	3
`nullborder`	Allow source detections at the border of the image	no	no
`bkgwindowtype`	Shape of background window	circle	circle
`bkgradius`	Radius of background window [pixels]	30	30
`srcradius`	Radius of source window (to be excluded from background window) [pixels]	6	10
`srcdetect`	Perform blind detection for new sources	yes	yes
`srcfit`	Perform source position fitting	yes	yes
`posfit`	Fit position of catalogued sources	no	no
`bkgfit`	Fit background of sources individually	no	yes
`psfshape`	Shape of point spread function	gaussian	gaussian
`psffwhm`	Width of psf (FWHM) [deg]	0.37413 (fixed)	0.37413 (fixed)
`npixthresh`	Required minimum number of pixels in background window	20	20
`posfitwindow`	Radius of window for all position fits [deg]	0	0
`possyserr`	Minimum systematic position error, to be added to radius found from position fit	0	0

BATSS Observation ID: SLEW_120625_22h38m54s+136s
Energy Band: 15-150keV (broad)

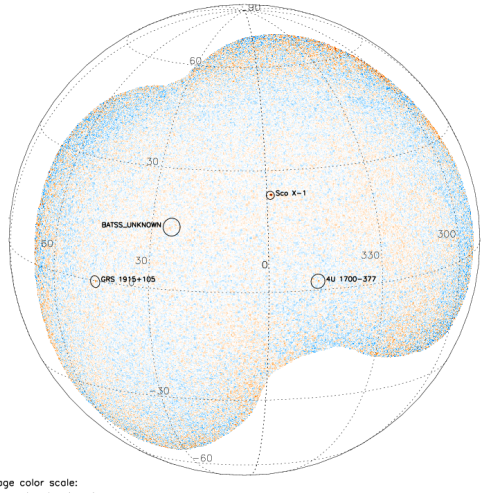

Image color scale:
cts/cm²/sec (linear)
−0.1400 0.00 0.1979

Observation start time:
2012-06-25 22:38:53.64
Observation stop time:
2012-06-25 22:38:53.64
Time in slew mode: 136.40s
Total exposure downlinked: 136.40s

Energy range: 15−150keV
Partial coding threshold: 20%
Image pixel size: 8 arcmin
FoV size: 3.575 sr (28.5% of sky)

Data type: ARCHIVAL
Data processing version: 1

Slew speed data:

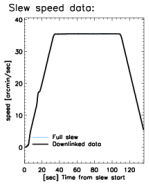

Top speed: 35.50 arcmin/sec

Aspect information:

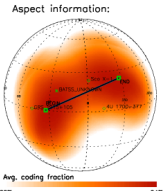

Avg. coding fraction
<20% 94%

CATALOG: BATSS
Type: Blind detection catalog
Total detections (15-150keV): 1. S/N threshold: 4.0

Source Name	RA [hms] (J2000)	Dec [dms] (J2000)	l [dms]	b [dms]	Err. rad. (90% est)	Exp. [sec]	CF [%]	S/N	Est. flux [mCrab]
BATSS_UNKNOWN	17 41 45.2	-00 05 58	24 41 53	+15 24 22	7.7'	112.8	91.3	4.8	119±25

CATALOG: BAT Transients
Type: Default reference catalog
Total detections (15-150keV): 386. Detections listed above S/N=1.0: 77

Source Name	RA [hms] (J2000)	Dec [dms] (J2000)	l [dms]	b [dms]	Exp. [sec]	CF [%]	S/N	Est. flux [mCrab]
Sco X-1	16 19 55.0	-15 38 23	359 05 38	+23 47 05	121.6	88.8	37.7	1024±27
GRS 1915+105	19 15 12.0	+10 56 24	45 21 41	-00 13 24	83.8	76.6	7.2	239±33
4U 1700-377	17 03 55.2	-37 50 38	347 45 04	+02 10 39	103.8	65.6	5.9	192±33
GX 349+2	17 05 48.0	-36 25 01	349 06 56	+02 44 33	106.2	66.8	3.4	110±32

(a)

BATSS Observation ID: ORBIT_120619_17h32m47s
Energy Band: 15-150keV (broad)

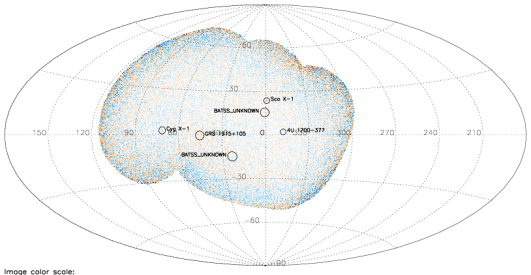

Image color scale:
cts/cm²/sec (linear)
−0.1613 0.00 >0.1613

Observation start time: 2012-06-19 17:32:46.8
Observation stop time: 2012-06-19 19:15:58.9
Time in slew mode: 17m20s
Total exposure downlinked: 03m41s

Energy range: 15−150keV
Partial coding threshold: 20%
Image pixel size: 8 arcmin
FoV size: 4.667 sr (36.7% of sky)

Data type: ARCHIVAL
Data processing version: 1

Exposure map:

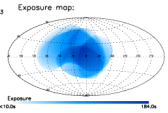

Exposure
<10.0s 186.0s

Coding fraction map:

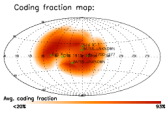

Avg. coding fraction
<20% 93%

LIST OF OBSERVATIONS:
Observations included: 9
Observations imaged: 2

Imaged

Observation ID	Start time	Slew exp[s]	Data exp[s]	
SLEW_120619_17h36m55s+144s	2012-06-19 17:36:55.1	144.00	0.00	no
SLEW_120619_17h42m54s+060s	2012-06-19 17:42:53.7	60.00	0.00	no
SLEW_120619_17h49m54s+131s	2012-06-19 17:49:53.7	131.00	131.00	yes
SLEW_120619_17h59m54s+203s	2012-06-19 17:59:53.7	203.00	0.00	no
SLEW_120619_18h26m54s+120s	2012-06-19 18:26:53.7	120.00	0.00	no
SLEW_120619_18h40m54s+142s	2012-06-19 18:40:53.7	142.00	0.00	no
SLEW_120619_18h51m53s+109s	2012-06-19 18:51:53.5	109.00	0.00	no
SLEW_120619_18h57m54s+041s	2012-06-19 18:57:53.7	41.00	0.00	no
SLEW_120619_19h07m54s+090s	2012-06-19 19:07:53.7	90.00	90.00	yes

CATALOG: BATSS
Type: Blind detection catalog
Total detections (15-150keV): 2. S/N threshold: 4.0

Source Name	RA [hms] (J2000)	Dec [dms] (J2000)	l [dms]	b [dms]	Err. rad. (90% est)	Exp. [sec]	CF [%]	S/N	Est. flux [mCrab]
BATSS_UNKNOWN	16 50 18.3	-19 38 53	00 32 49	+15 37 31	8.2'	173.4	78.3	4.6	117±25
BATSS_UNKNOWN	19 27 21.3	-14 56 48	23 22 05	-14 35 05	9.3'	127.8	81.8	4.4	143±33

CATALOG: BAT Transients
Type: Default reference catalog
Total detections (15-150keV): 469. Detections listed above S/N=1.0: 82

Source Name	RA [hms] (J2000)	Dec [dms] (J2000)	l [dms]	b [dms]	Exp. [sec]	CF [%]	S/N	Est. flux [mCrab]
Sco X-1	16 19 55.0	-15 38 23	359 05 38	+23 47 05	153.2	77.6	25.3	702±28
4U 1700-377	17 03 55.2	-37 50 38	347 45 04	+02 10 39	154.8	89.5	11.1	269±24
Cyg X-1	19 58 21.8	+35 12 07	71 20 08	+03 04 00	74.6	84.5	6.1	199±33
GRS 1915+105	19 15 12.0	+10 56 24	45 21 41	-00 13 24	133.2	52.1	4.8	162±34
Cyg X-3	20 32 25.7	+40 57 28	79 50 43	+00 42 01	65.6	84.6	3.8	141±37
EXO 1657-419	17 00 47.9	-41 40 23	344 21 13	+00 18 39	151.2	88.9	3.8	83±22
SAX J1747.0-2853	17 47 02.6	-28 52 58	00 12 26	-00 14 18	162.2	87.0	3.6	72±20
IE 1740.7-2942	17 43 56.2	-29 44 05	359 07 37	-00 06 16	161.4	87.7	3.5	69±20

(b)

FIGURE 3.5: Sample observation reports from the BATSS webpage: (a) single-slew observation and (b) orbital observation

3.9 BATSS source identification and cataloging

After each observation is flagged as processed and its detection catalog copied to the central data volume, the main server runs on a separate thread an iteration of the source triggering routine `batss_trigger`, which performs the analysis of unidentified detections within each catalog as well as across catalogs from the entire survey. As a final, BATSS Level 3 data product, it produces a *trigger database* of candidate sources according to specific criteria described in this section.

In each iteration of `BATSS_trigger`, this stage carries out two phases of analysis, in order to differentiate single-observation from multiple-observation detections. For detections identified as candidate new sources, in the case of single slews the routine calls the subroutines `BATSS_lc` and `BATSS_spectrum` in order to derive mask-tagged lightcurves and spectra, respectively, and posts a report on the candidate to the BATSS website. Furthermore, when candidate sources meet an additional set of criteria that make them highly likely to correspond to real sources, this final stage of the BATSS pipeline also issues a series of automated alert messages, including a BATSS-formatted Notice to the Gamma-ray bursts Coordinates Network[11] (GCN Notice) when applicable.

The candidate source types defined in each phase of analysis and stored in the BATSS trigger database are described in the following sections, and in section 3.9.3 all BATSS candidate types are summarized including threshold levels and other criteria used to classify them.

[11] `http://gcn.gsfc.nasa.gov`

3.9.1 Single-observation analysis

This phase matches unidentified detections above a pre-set significance threshold of 4σ across energy bands for the current slew only, with the purpose of identifying new GRBs. In all subsequent definitions, a coincidence of two detections is considered a match when the 90% error circles of such detections intersect each other. Candidate GRBs are assigned an *index number*, which ranks the likelihood of them corresponding to real bursts, and the types defined in BATSS processing are enumerated in the following table:

TABLE 3.5
Candidate types for single-slew detections

Type	Description
Index 10	Simultaneous coincidence in the two independent energy bands (Soft and Hard). Very high probability of GRB detection; always triggers automated GCN Notice
Index 9	Simultaneous coincidence in non-independent energy bands (Soft/Hard and Broad), AND Broad band detection is more significant than Soft/Hard detection. High probability of GRB detection depeding on significance
index 8	Simultaneous coincidence in non-independent energy bands (Soft/Hard and Broad), AND Soft/Hard band detection is more significant than Broad band detection. Moderate probability of GRB detection depending on significance
Index 5	High-significace detection in any single energy band

3.9.2 Multiple-observation analysis

This phase matches the unidentified detections (above a 4σ significance threshold) in the current observation against detections in all previous observations in the survey, with the purposes of identifying candidate transient sources. In addition to the index number definitions itemized above, two more index numbers are defined that apply only to transient source detections. In the current version of the BATSS pipeline, transient source detections do not trigger automated GCN alerts.

TABLE 3.6
Candidate types for multi-slew detections

Type	Description
Index 7	Non-simultaneous coincidence in any 2 energy bands, from slews that begin within 2 orbits of each other. Transient candidates with extended emission from a single flare
Index 6	Non-simultaneous coincidence in any 2 energy bands, from slews that begin over 2 orbits from each other. Transient candidates with repeated emission

3.9.3 Threshold levels

The table below summarizes the definitions of BATSS source candidate types, including the threshold levels that must be met by each of the Soft, Hard and Broad energy bands (when applicable), as well as additional constraints on coincident detection. For detections that meet the criteria for more that one candidate type, the highest applicable index number is always assigned. In addition, the threshold level to trigger an automated GCN alert is also specified.

TABLE 3.7
Summary of BATSS candidate types and criteria for classification

Index	Thresholds			Additional constraints	Simultaneous coincidence?	GCN Trigger
	S	H	B			
10	4σ	4σ	N/A	S, H coincidence	Yes	Always triggers
9	4σ	4σ	5σ	Either $B > S$ or $B > H$	Yes	$B > 6\sigma$
8	5σ	5σ	4σ	Either $S > B$ or $H > B$	Yes	$(S, H) > 6\sigma$
7	4σ	4σ	4σ	Coincidence of any 2 dets. Slews within 200 min ($\sim$2 orbits) of each other	No	Never triggers
6	4σ	4σ	4σ	Coincidence of any 2 dets. Slews over 200 min ($\sim$2 orbits) of each other	No	Never triggers
5	5.5σ	5.5σ	5.5σ	Single-band detection No coincidence	N/A	$(S, H, B) > 6.5\sigma$

3.10 Conclusions

In complementing the imaging method for processing slew images for the *Swift*-BAT instrument earlier presented in Chapter 2 and its associated systematics, we have hereby provided a detailed description of the software pipeline that has already been put in place to implement the BATSS imaging and detection algorithms. The system has been demonstrated to report positions of candidate GRBs –as well as fluxes, lightcurves and spectra– in as little as 2.5 hours from the time of the BAT observation, and longer depending mostly on the speed of the telemetry downlink to the ground station and subsequent transfer to the BATSS machines. Candidate sources from the detection stage, both from single and multiple observations, have been logged into the BATSS trigger database and ranked by index number (figure-of-merit) into 6 types according to their likelihood of corresponding to new real GRBs or Transients. Following the full implementation of the BATSS pipeline, we shift the focus to the science analysis of the candidate sources it has discovered, beginning with a study of the Gamma-Ray Burst data analyzed over the first 4.8 years of continuous survey operation.

Chapter 4

BATSS Gamma-Ray Bursts

Abstract

The prompt γ-ray emission data from GRBs detected in the *Swift*-BAT Slew Survey (BATSS) provides conclusive validation of its observational approach as a slewing coded aperture imaging survey. During its preliminary testing phase in March, 2007, BATSS detection capabilities were demonstrated with the finding of GRB 070326. Under the observational program of 4.8 years of nearly continuous real-time processing that followed, a further 18 GRBs were detected exclusively during slews, providing a meaningful contribution to the primary science goals of the *Swift* mission. Among them are a candidate short GRB with extended emission, as well as 3 GRBs with unusually soft spectra that would be classified as X-ray flashes (XRFs), both of which are rare categories of *Swift* GRBs. We further characterize the prompt timing and spectral properties of BATSS GRBs, with an emphasis on their relation to the overall population of the BAT2 GRB catalog (Sakamoto et al. 2011). We end with a discussion of the observed BATSS GRB detection rate of 5.62 GRBs/Msec of instrument exposure, a considerable increase of 45% above the equivalent detection rate in pointing mode. By verifying this result through simulation work, we reach an important set of general conclusions regarding the enhanced sensitivity of slew observations in coded aperture imaging when compared to pointings. In addition, a detailed characterization of the observational program of the BATSS survey is provided, as well as thorough description of the BATSS analysis methods for GRB prompt emission data, using GRB 070326 as a case study.

4.1 Introduction

The BAT Slew Survey (BATSS) has been developed and implemented with the purpose of contributing to the *Swift* primary science by imaging photon-by-photon data captured by the BAT instrument (Barthelmy et al. 2005) in the 15–150 keV energy band during routine spacecraft slew maneuvers. The motivation, technical features and systematic properties of the survey have already been characterized in Chapters 2 and 3 of this dissertation. The testing phase of the program concluded in November, 2007, when the spacecraft began regular capture and downlink of slew data in real time, followed immediately by processing under BATSS pipeline. Section 4.2 of this chapter begins by analyzing the main features of the slew observations processed over the 4.8-year observational program of the BATSS GRB survey, followed in Section 4.3 by a description of the data reduction and analysis methods employed in the examination of the prompt emission data from candidate GRB sources detected over the course of the survey. For the latter task, we use GRB 070326 —the first GRB detected exclusively by BATSS— as a case study in order to illustrate the analysis issues involved as well as the data products the pipeline generates along the way.

The examination of the science data from the set of GRBs detected exclusively in BATSS slews is the main subject of Section 4.4. We first present a set of data tables that summarize the detection parameters, prompt emission energetics, and follow-up afterglow observations of BATSS GRBs. Then, in the subsections that follow we proceed to expand on each of the important characteristics of the BATSS GRB population, making particular emphasis on the comparison with the analogous features in the Second *Swift*-BAT GRB Catalog (BAT2 catalog, Sakamoto et al. 2011), the most comprehensive database to date of the prompt emission data from *Swift*-BAT GRBs. That catalog in turn compares the *Swift*GRB population with that of other important GRB surveys, in particular BATSE and *HETE-2*, which allows us to assess BATSS GRB results against those surveys as well.

Section 4.5 goes on to concentrating on the specific issue of the GRB detection rates derived from the survey, by making a review of how the detection rates in pointing and slew modes evolved historically over the course of the survey, and finally arriving at the overall empirical measurement of the detection rates in both modes of operation, revealing an even larger GRB rate for slews than would have been predicted based solely on the comparison of instrument sensitivities at the local level discussed in Section 2.5. Then, as a final topic of this chapter, this result is then verified in Section 4.6 via a simulation that computes overall GRB detection probabilities in BAT pointings and slews, which not only confirms the empirical result of Section 4.5 but also reveals the main drivers behind the observed rates. This then allows us to draw a larger set of conclusions regarding the magnitude and the origin of the enhanced sensitivity of slew observations in coded aperture imaging telescopes, this time after having taken all contributing factors into consideration, and using differences in observed GRB detection rates as a proxy for the real differences in sensitivity that are intrinsic to each mode of observation.

4.2 Observational program

Up until the introduction of BATSS, the photon-by-photon data enabled by the "event" mode of the *Swift*-BAT coded aperture imaging telescope (15–150 keV, $100^\circ \times 60^\circ$ FoV) would be regularly employed only upon on-board triggering to automated targets (ATs), typically new GRBs or transient flares. Its primary use was thus to reconstruct source lightcurves during autonomous slews to new targets and before follow-up observations would be carried out by the spacecraft's narrow-field instruments (Gehrels et al. 2004). The BATSS program was proposed to enable and downlink event-mode data from every regular slew maneuver —not only when slewing to ATs—, so that every slew can be imaged as outlined in Chapter 2, thereby increasing the full-sky and temporal coverage of the BAT instrument.

The plots in Figures 4.1–4.4 illustrate the main features of the BATSS observational program carried over the 4.8 years since the start of the regular downlink of slew data from *Swift*-BAT.[1] Figure 4.1 shows on the one hand the distribution of the total number of slews over each of the 1,748 days of the survey, a nearly Gaussian distribution with a mean of 85.1 ± 9.9 slews/day, equivalent to 5.72 ± 0.67 slews/orbit given an orbital period of 96.8 minutes for the *Swift* spacecraft.[2] The figure also shows the distribution of the number of slews per day of the survey that were actually downlinked and later processed by BATSS, a wide bimodal distribution with a mean of 31.2 ± 17.9 slews/day, including 87 days where no slew data was captured and downlinked. The reason for having only a 27% overall fraction of the total number of slews per day transferred to the BATSS servers for processing was primarily a technical one, related to limitations in the bandwidth of the data link between the *Swift* spacecraft and the Malindi ground station, given the additional data load that the downlinked slew data represented. Besides the reduced number of slews, an additional constraint was imposed by *Swift* mission operations by which the amount of data captured per slew was initially limited to 120 sec per slew. On the other hand, and as discussed in Chapter 3, the BATSS dedicated servers alone were capable of processing 6 slews simultaneously, so there was no limitation on the side of the BATSS pipeline in processing the maximum possible amount of slew data per orbit without any significant data backlogs.

Figure 4.2 shows the log-normal distribution of time intervals (in clock time) between consecutive slews over the course of the survey; this gives a measure of the number of consecutive slews where a given type of astrophysical source is likely to be detected according

[1]The BATSS survey period includes the 10/25/07–07/07/12 period of continuous observation, plus the 03/01/07–03/31/07 testing phase, for a total of 1,748 days' worth of slew observations.

[2]Quoted *Swift* orbital period assumes a spacecraft altitude of 600 km in an approximately circular low-Earth orbit (Gehrels et al. 2004).

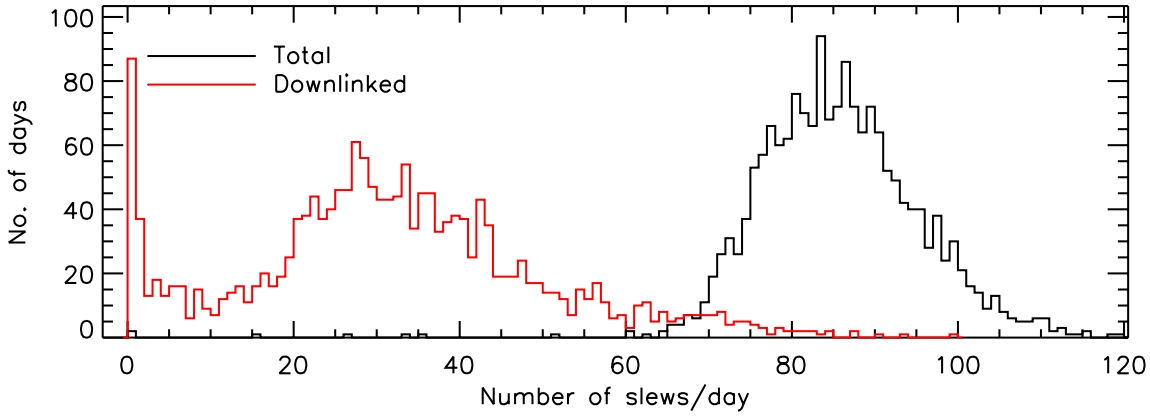

FIGURE 4.1: Distributions of daily number of slews over the 1,748 days (4.8 years) of the BATSS survey. Both the total and the actual downlinked number of slews are shown in the plot; the discrepancy is due to constraints in the amount of captured slew data imposed by *Swift* mission operations.

to its characteristic period of emission. The total number of spacecraft slewing periods spanned by the BATSS survey was 148,839, after excluding all slews shorter than 10 sec. If all of them had been downlinked and imaged, the average time interval between consecutive slews derived from the black distribution on the plot would have been $0.71^{+0.91}_{-0.40}$ ksec. Given that only 54,541 of them (37% of the total) were actually downlinked, the average time interval seen by BATSS was increased to $0.96^{+1.95}_{-0.64}$ ksec, as illustrated by the red distribution on the plot. Previous GRB surveys, including the *Swift*-BAT GRB survey itself (Sakamoto et al. 2008, 2011), coincide in observing a prompt γ-ray emission from GRBs that typically lasts from only a fraction of a second up to a few hundred seconds, which makes it highly unlikely that a GRB would be detected in otherwise uncorrelated

consecutive BATSS slews.[3] Therefore, the BATSS GRB survey is based almost exclusively on detections over single slews, and those are the types of slew observations we will be concerned with over the rest of this chapter. At the same time, however, we have conducted in parallel a deeper survey from *Swift*-BAT observations over multiple slews, in order to detect signals from other types of astrophysical sources with longer emission timespans than GRBs, and this BATSS multi-slew survey is a core subject of our ongoing work.

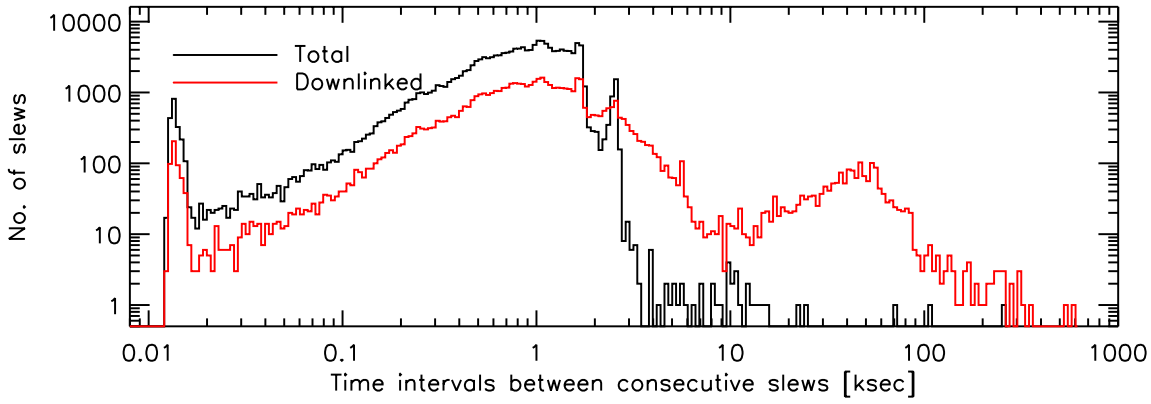

FIGURE 4.2: Distributions of time intervals (clock time) between consecutive slews, for both the total number of slews (148,839) and the actual number downlinked (54,541) over the course of the survey. The reduced number of downlinked slews causes their distribution to be shifted towards larger intervals. Given an average time interval of ∼2 ksec, it is highly unlikely that a single GRB would be detected over consecutive slews, and consequently, the BATSS GRB survey is based primarily on single-slew detections.

Continuing with the characterization of BATSS single-slew observations in this survey, the distributions of slew durations are shown in Figure 4.3. Above the threshold of 10 sec for slews to be included in the survey, the distribution of total slew durations is shown

[3]We have in fact observed cases of GRBs detected in consecutive slews, though in those cases the second slew often occurred as a result of the BAT autonomously triggering on the GRB after it came into the field-of-view during the first slew, so they would not be categorized as uncorrelated slews. What we did not observe, however, was a case of a GRB that was faint enough so as to be undetectable in the individual slews but bright enough so as to have been detected when those slews were co-added, which would have warranted the use of mosaicked (co-added) multi-slew observations for the BATSS GRB survey.

to be a single broad peak, with a mean of 114.0 ± 47.1 sec. In contrast, the distribution of downlinked slew durations shows a significant single peak at 120 sec, corresponding to 13,318 slews (24% of the total) with their amount of captured data constrained to this limit by mission operations.[4] In addition, there is a second single peak at 60 sec, corresponding to a smaller number of 960 slews (above the baseline level derived from neighboring bins) with a similarly capped amount of captured slew data; however, this limit was imposed only during the 03/01/07–03/31/07 testing period of the survey. Above the 120 sec peak lie only 3,223 (6%) of downlinked slews, even though as many as 44% of slews in the total sample are found to lie in that range of durations. The downlinked slews in this category fall into one of two main types: 1)regular slews longer than 120 sec that occurred after the exposure cap was removed on 08/08/2011, or 2)automated target (AT) slews which followed an on-board (pointing) GRB trigger. For AT slews, the entire batch of event data is always downlinked, since it is necessary in order to reconstruct the GRB prompt emission lightcurves, and therefore they are present over the entire period of the BATSS survey. Overall, the mean duration of downlinked slews was 86.7 ± 37.4 sec, 24% less than the mean of the total slew durations. Adding the BAT instrument exposure of all slews in the survey, we find a total exposure of 4.71 Msec in downlinked slews, which represent 28% of the 17.0 Msec of total time spent in the slew mode of operation over this period, after already having excluded periods of passage over the South Atlantic Anomaly (SAA).

An additional important characteristic of the single-slew observations in the survey is their total sky coverage, which enhances the GRB detection probability when compared to pointings of equal exposure, and it will be shown in Section 4.6 to play a crucial role in the overall yield of BATSS GRB detections. This quantity is of course closely related to the

[4]The 120 sec exposure cap was permanently removed as of 08/08/2011. From that point forward, the entire set of event data per downlinked slew was captured by the spacecraft and processed by BATSS.

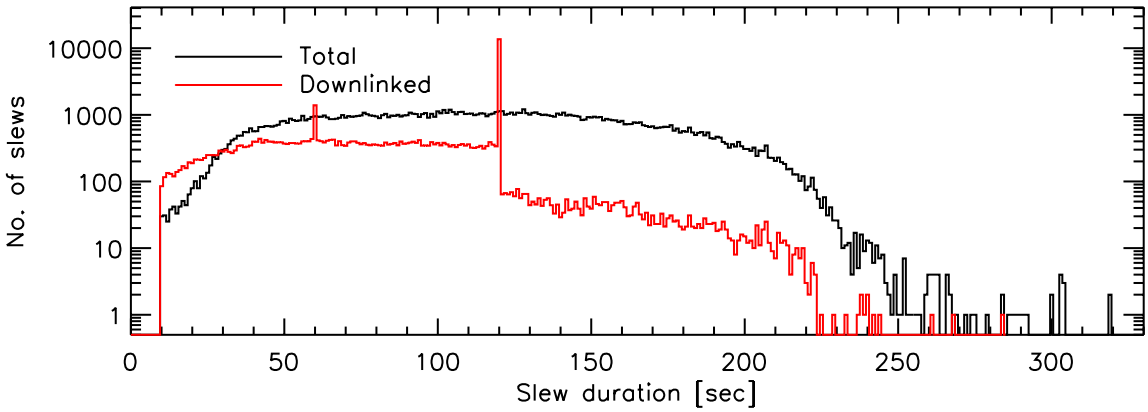

FIGURE 4.3: Distibutions of slew durations above the 10 sec threshold for both the total and downlinked slew samples. While the total sample has a single broad peak and an average of 114 sec, the downlinked sample has narrow peaks at 60 sec and 120 sec as a result of temporary caps imposed on the total amount of data captured per slew, for an average downlinked duration of 87 sec. Only 6% of downlinked slews are longer than 120 sec, as opposed to 44% in the total sample.

slew duration though not exclusively dependent on it, given the range of possible slewing speeds and BAT roll angles which also play a role in determining the net sky coverage per slew. Figure 4.4 shows the distribution of sky coverages of the downlinked slews,[5] defined as the total fraction of the sky subtended by the BAT FoV at any point over the course of the slew, above the 15% partial coding threshold we have chosen for imaging of BATSS slews, as discussed in Section 2.2.3. The distribution of solid angles is shown to be essentially confined to a broad range of 1.5–6 sr (or approximately 10–50% of the entire sky), with a mean coverage of 3.22 ± 0.68 sr ($25.6\% \pm 5.4\%$ of the sky). In addition, a significant fraction of 91% of slews are shown to cover a greater sky area than the 2.25 sr of the BAT FoV above the 1% coding fraction threshold that is employed for pointing-mode

[5]Obtaining the analogous distribution for the total slew sample is currently not possible, since BATSS pipeline imaging is performed only for downlinked slews. Despite the absence of event data for the remaining slews, it is possible in principle to calculate their sky coverage since the spacecraft attitude data, which we do have access to, is the only necessary input data product for this purpose.

detections, despite the higher coding fraction threshold employed for slews, as well as a distribution of downlinked exposures that are appreciably shorter than the actual total slew durations.

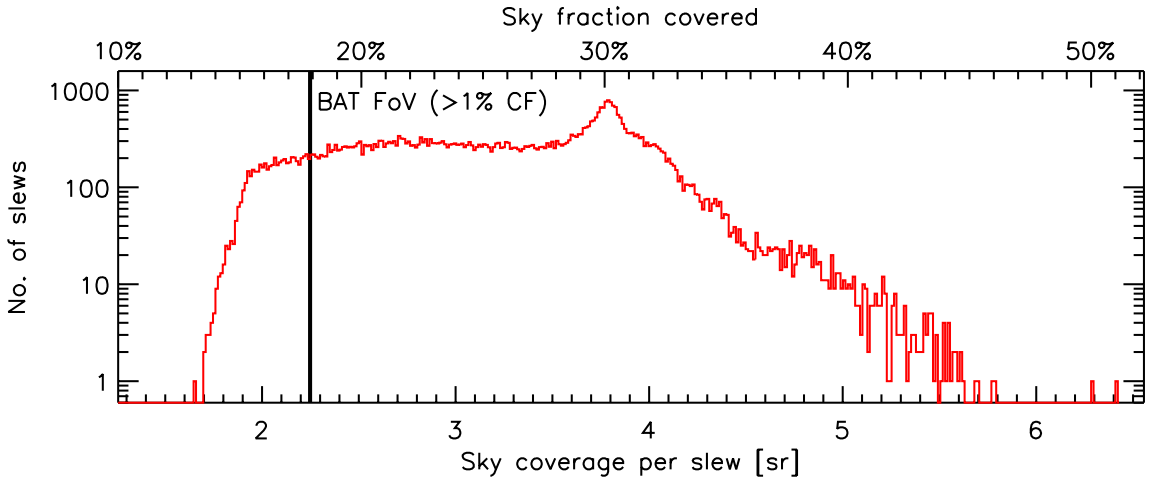

FIGURE 4.4: Distribution of sky coverages per slew (15% coding fraction threshold) for the downlinked slew sample used in the BATSS survey. A considerable fraction of slews (91%) cover a larger sky area than the BAT FoV above 1% coding fraction (CF) used in pointing-mode detections; this is despite the higher CF threshold used for slews and the shortened duration of a large fraction of downlinked slews. The particular features of the distribution are closely related to the distribution of downlinked slew durations in Figure 4.3.

As for the shape of the sky coverage distribution itself, it can be readily understood given its close association with the downlinked slew duration distribution in Figure 4.3. The prominent peak at 30% sky fraction can be directly attributed to the 120 sec slews that are overrepresented in the duration distribution, though in this case the peak has been broadened due to differences in roll angles and slewing speeds among individual slews. The sharp edge below 2 sr is mapped from the 10 sec cutoff in slew exposures that was implemented in the survey; likewise, the approximately flat distribution between this edge and the sharp peak as well as the monotonic fall above the peak are similar to the

corresponding features in the slew duration distribution. In summary, the shape of the distribution of sky coverages is a direct product of the particular sample of slews included in the survey, and not to some intrinsic distribution of sky coverages from a generic coded aperture imaging slew survey.

Lastly, the most relevant features of the single-slew observations included in the BATSS survey and presented in this section are summarized in Table 4.1.

TABLE 4.1

Overall features of the single-slew observations included in the BATSS survey. The total sample of slews spanned during the survey is compared against the sample of slews that were actually captured and downlinked.

Parameter	Total	Downlinked
Number of calendar days in survey	1,748 (4.79 years)	
Number of slews[a]	148,839	54,541
Total BAT instrument time[b]	17.0 Msec	4.71 Msec
Avg. number of slews per day	85.1 ± 9.9	31.2 ± 17.9
Avg. time interval between consecutive slews	$0.71^{+0.91}_{-0.40}$ ksec	$0.96^{+1.95}_{-0.64}$ ksec
Avg. slew duration	114.0 ± 47.1 sec	86.7 ± 37.4 sec
Fraction of slews longer than 120 sec[c]	44.5%	5.9%
Avg. sky coverage per slew[d]	n/a[e]	3.22 ± 0.68 sr ($25.6\% \pm 5.4\%$ of sky)
Fraction of slews with sky coverage above BAT FoV ($> 1\%$ CF)	n/a[e]	90.6%

[a] Excludes slews shorter than exposure threshold of 10 sec.

[b] Slew-mode exposure only. Excludes periods of SAA passage.

[c] Considerable difference in total vs. downlinked data is due to 120-sec cap imposed on downlinked slew data over most of the survey, due to bandwidth limitations.

[d] Coverage above 15% coding fraction (CF) threshold imposed on all slew images.

[e] Data not available since no imaging was done for slews that were not downlinked.

4.3 GRB data reduction and analysis

4.3.1 Detection and triggering

As outlined in the BATSS detection algorithm of Section 2.3 and the technical description of the triggering routine in Section 3.9, BATSS detection of sources such as GRBs, which flare in the timescale of individual slews, relies on coincident detection on sky images across 2 or more out of a total of 3 imaged energy bands: Soft (15–50 keV), Hard (50–150 keV) and Broad (15–150 keV). Given the specific set of coincidence criteria they fulfill, candidate sources from single slews are ranked into 4 categories (index numbers), according to the likelihood that they correspond to real sources, most likely GRBs in this case of individual observations. In practice, candidates in the highest of these categories (index 10), where a coincidence of $> 4.0\sigma$ detections in the Soft and Hard (independent) energy bands has been found, have almost always turned out to correspond to real sources. In most cases, they correspond to GRBs —either previously detected or not—, while the remaining ones are either known transient sources that were not matched to sources in the BATSS known source catalogs, or the occasional false trigger as a product of spacecraft operational errors[6].

The first demonstration of the BATSS detection method for new GRBs occurred during the testing phase of the program, when a possible new burst (GRB 070326) was found in a batch of slew data that was captured during the entire month of March, 2007, and was then processed by the BATSS pipeline. Table 4.2 summarizes the detection parameters for this burst, which was detected as a typical index-10 BATSS trigger and reported to the GRB community in the form of a GCN Circular (Copete et al. 2007).

[6]A typical instance of such errors occurs during the sporadic periods of *Swift* startracker loss-of-lock, where known sources are imaged and detected at incorrect locations due to incorrect attitude data, thereby producing a false new candidate source trigger. The SSC would normally issue a GCN Notice to alert of such occurrences, but it may come after automated alerts have already been issued.

TABLE 4.2
Detection parameters for GRB 070326, the first GRB detected by BATSS

(a) Individual detections in 3 BATSS energy bands

Parameter	15–50 keV (Soft)	50–150 keV (Hard)	15–150 keV (Broad)
S/N	8.7	6.2	10.0
RA (J2000)	02h 41m 08.8s	02h 41m 49.1s	02h 41m 25.2s
Dec (J2000)	−66° 51’ 56”	−66° 56’ 23”	−66° 53’ 17”
Gal. longitude	287° 35’ 06”	287° 34’ 24”	287° 34’ 24”
Gal. latitude	−46° 51’ 34”	−46° 45’ 37”	−46° 49’ 31”
Err. rad. (90%)	3.5’	4.3’	3.3’
Offset from centroid	2.05’	3.92’	0.17’
Image	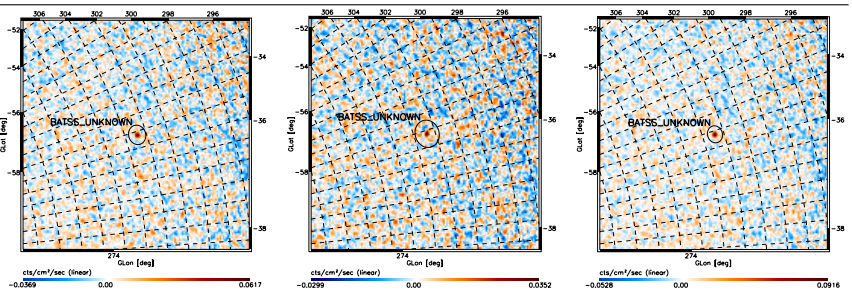		

(b) Combined position and chart of error circles

Combined GRB Position	
RA (J2000)	02h 41m 23.7s
Dec (J2000)	−66° 53’ 22”
Gal. longitude	287° 34’ 39”
Gal. latitude	−46° 49’ 32”
Err. rad. (90%)	3.25’

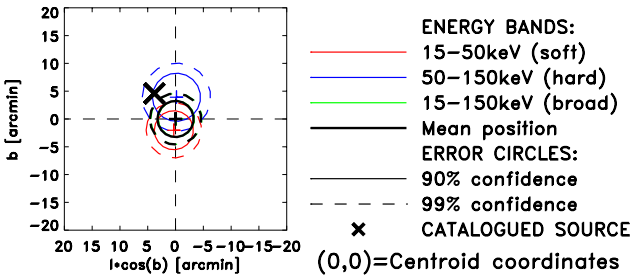

Following the initial trigger for a GRB candidate in the BATSS pipeline, an automated GCN Notice would normally be generated if the burst was detected in real time, in order to enable rapid follow-up observation of its afterglow, and subsequent confirmation of the source as a real GRB[7]. For this purpose, the specific GCN Notice type `SWIFT_BAT_SLEW_GRB_POSITION` was created, and a full description of its parameters and how they are computed by the BATSS pipeline is included in Appendix C.

Also, part of the triggering procedure includes the assignment of a unique BATSS trigger number, as outlined in the description of the `batss_trigger` tool in Section 3.9, with a trigger time associated with it as well. BATSS trigger numbers are 6-digit integers of the general form `NXXXXX`, where the first digit `N` is related to the data type the trigger was drawn from (real-time or archival) as well as the number of observations associated with the candidate source. All real-time triggers have $\mathtt{N} \equiv 0$ and are associated with only one single-slew observation, since the priority of real-time processing is the detection of GRBs over single slews. On the other hand, as we have defined them, all archival data triggers have $\mathtt{N} \geq 1$, with `N` being the number of slew observations (either single-slew or higher order) associated with the trigger.[8] In the specific case of GRBs from archival data that are the subject of this chapter, they all have $\mathtt{N} \equiv 1$, where the only observation is a single slew.[9] The description and characterization of $\mathtt{N} = 1$ triggers from single higher-

[7]Since GRB 070326 was not detected in real time, an automated GCN Notice was not generated and its afterglow was not observed. However, BATSS lightcurve and spectral information are strongly consistent with the burst's nature as a real GRB.

[8]Since `N` is constrained to be a 1-digit number, all triggers drawn from 10 or more observations have $\mathtt{N} \equiv 9$.

[9]The case of GRBs that are detected in multiple, usually consecutive slews does occur, though rarely due to the short characteristic timescales of GRB prompt γ-ray emission, as well as the case of GRBs that are bright enough to appear in orbital and even daily, weekly and monthly higher-order observations. In the case of BATSS-only GRBs, however, as it will be shown in Section 4.4, they have only been found on single slews, from which their timing and spectral properties are then derived. As of the time of this work, higher-order observations have only provided corroborative data on BATSS GRB positions, but have not yielded new GRB detections beyond those drawn from single slews, which would necessarily have to involve

order archival observations, as well as candidate sources drawn from `N` ≥ 2 observations, are the subject of our ongoing work on the results from the BATSS survey beyond GRBs. For all categories of triggers with the same first digit `N`, the remaining 5 digits `XXXXX` of the trigger number are assigned sequentially to uniquely designate candidate sources that fulfill the BATSS triggering criteria summarized in Section 3.9.3. Finally, each BATSS trigger number has an associated *version number*, corresponding to the number of times the same observation has been processed by the BATSS pipeline, which in the case of real-time data can be as high 6 or more depending on the number of data passes that include data from the same slew. The results in Section 4.4 always quote the results from the latest processing version for each trigger number, and for this reason version numbers are omitted from the data tables in that section.

As an example of the BATSS trigger number conventions for candidate GRBs, the corresponding numbers for the real-time and archival data versions of GRB 070326 are 000001 and 100042, reflecting in the first case the real-time nature of the input data and in the second case their archival, single-observation nature. In both cases, the low number in their last 5-digit sequence is directly related to the fact that the trigger was issued very early in the survey. As for BATSS trigger time definitions, they are described at the end of the next section on GRB lightcurve analysis.

4.3.2 GRB lightcurves

Following the burst detection and triggering, the automated BATSS analysis then proceeds with the computation of the lightcurve and spectral information for the candidate GRB. It begins by mask-weighting (ray-tracing) the event file by relying on the BAT tool `batmaskwtevt`, a necessary step in order to produce background-subtracted lightcurves.

---

particularly faint and long GRBs we have not yet observed.

Given the BATSS event file, spacecraft attitude and source position, `batmaskwtevt` calculates a *weight* for each event according to whether the detector pixel where it was recorded was being illuminated by the source as the telescope's mask modulated the influx of photons hitting the detector plane (Markwardt et al. 2007). The net effect is the creation of a temporal list of all photons that could have come from the GRB.

Next, by making use of the mask-weigthed event file and the BAT tool `batbinevt`, the pipeline computes background-subtracted lightcurves for the burst, in both the 3 BATSS energy channels (15–50, 50–150, and 15–150 keV), as well as the 4 BAT canonical energy channels (15–25, 25–50, 50–100, and 100–350 keV) for direct comparison with the standard data products from the BAT team. At the same time, lightcurves are accumulated for 5 different time binnings: 64ms, 200ms, 1s, 4s and 8s. In order to determine the standard timing features of the burst, a Bayesian time block analysis (Scargle 1998) implemented by the BAT tool `battblocks` is performed on the Broad band (15–150 keV) lightcurves. If a burst-like peak is found in the lightcurve data, the time blocks for the burst's 1-sec peak T_{1s} (`TPEAK`), T_{50} (`T50`), T_{90} (`T90`), full burst or T_{100} (`TTOT`), and preceding and following background intervals (`TBKG1` and `TBKG2`) are recorded and later reported in a GCN Circular on the GRB's prompt emission data.

Figure 4.5 summarizes the GRB lightcurve information computed by BATSS using the 1-sec lightcurve data for GRB 070326 as an example. As is standard in BAT data products, lightcurve units are given as *background-subtracted counts per second, per fully-illuminated detector, for an equivalent on-axis source*[10] (Markwardt et al. 2007). The Broad band lightcurve also features the calculated Bayesian time blocks, as well as the GRB's partial coding fraction as a function of time over the course of the slew.

[10]Conversion to units of ph/cm^2/sec requires fitting to a spectral model (section 4.3.3) and use of the BAT detector pixel area of 0.16 cm^2. The reduction in recorded counts due to partial coding effects has been corrected by converting to the rate of an equivalent on-axis source.

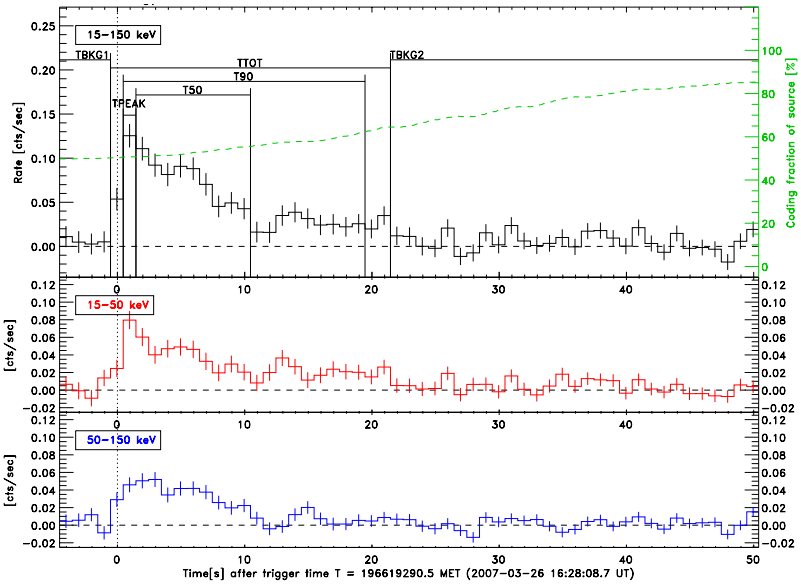

(a) BATSS energy channels

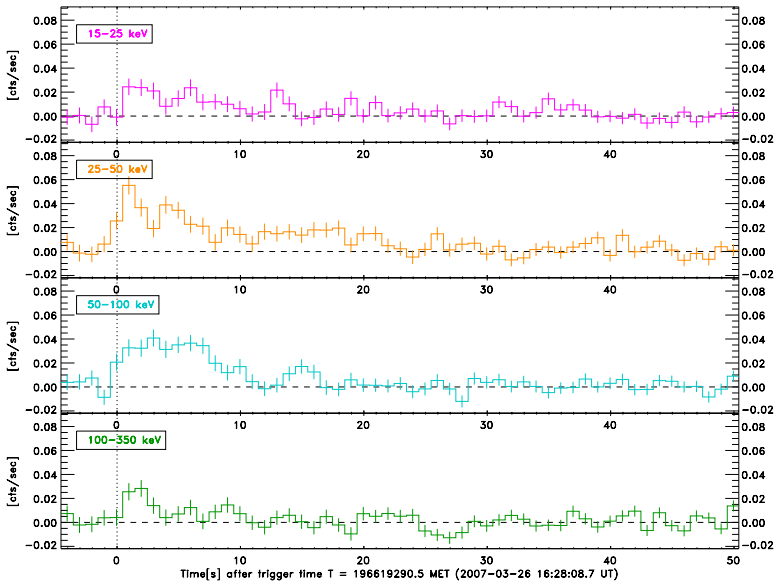

(b) BAT standard energy channels

FIGURE 4.5: GRB 070326 1-sec mask-weighted lightcurves, in BAT standard units of on-axis counts per second, per fully-illuminated detector pixel (area 0.16 cm^2). The trigger time $T = 0$ is defined in Section 4.3.2 as the start of the T_{100} interval. The BATSS Broad band (15–150 keV) lightcurve also includes Bayesian time blocks and time dependence of the GRB partial coding fraction over the course of the slew.

Finally, the lightcurve data for GRBs is also used by the BATSS pipeline in order to set the *trigger time* associated with the BATSS trigger number assigned to the candidate source upon detection. Though the specific conventions vary depending on instrument, method of detection, and time resolution of the data, the preferred general convention of the GRB community is to set the trigger time as close as possible to the start of the prompt emission of the burst (i.e. start the T_{100} interval) in some broad canonical energy band. However, by definition, BATSS detections are always drawn from triggers on images whose accumulation time may have begun long before the start of the burst itself. Since no timing information is immediately available at the time of the initial triggering, and the automated Bayesian block analysis described in this section with may not necessarily find a T_{100} interval, we define the trigger time for real-time BATSS triggers to be either the start of the batch of captured event data (usually near the start time of the slew), or the time the location of the GRB enters the BAT FoV above the 15% partial coding threshold, whichever occurs later. Both of these quantities can always be determined regardless of the profile of the GRB lightcurve. On the other hand, in the case of archival data, if an interval of prompt emission T_{100} (15–150 keV) is found from the lightcurve data analysis, the archival GRB trigger time is set at the time of this interval; otherwise, it is set the same way as the trigger time from the real-time data. These definitions are used for the BATSS GRB sample characterized in Section 4.4.

4.3.3 GRB spectra

The BATSS GRB spectral analysis begins by accumulating the mask-weighted and energy-calibrated events from the source into a BAT-standard 80-channel time-averaged raw spectrum, making use of the BAT tool `batbinevt`, and applying systematic corrections to it which the BAT team has stored in the calibration database (CALDB). If a set of

Bayesian time blocks was found in the lightcurve analysis of the burst, this is done for each of the 1-sec, T_{50}, T_{90}, and full-burst (T_{100}) time blocks, in addition to the time interval for the full slew, which is always analyzed. A spectral detector response matrix for the slew on each time block is also created through the use of the BAT tool `batdrmgen`.

Once we have a raw spectrum and response matrix, the spectral fitting itself is done in XSPEC, in all cases in the 15–150 keV energy range, since the BAT mask becomes transparent at higher energies (Barthelmy et al. 2005). By default, 2 spectral models are considered in the XSPEC fitting with the following parameterizations appropriate for BAT spectra:

1. Simple power law (PL), parameterized as

$$N_E^{\rm PL}(E) = N_{50}^{\rm PL} \cdot \left(\frac{E}{50{\rm keV}}\right)^{\alpha^{\rm PL}} \tag{4.1}$$

   where $\alpha^{\rm PL}$ is the standard spectral photon index and $N_{50}^{\rm PL}$ is the normalization factor at 50 keV, in units of ph/cm^2/sec/keV.

2. Power law with exponential high-energy cutoff (CPL), parameterized as

$$N_E^{\rm CPL}(E) = N_{50}^{\rm CPL} \cdot \left(\frac{E}{50{\rm keV}}\right)^{\alpha^{\rm CPL}} \cdot \exp\left[-\frac{E(2+\alpha^{\rm CPL})}{E_{\rm peak}}\right] \tag{4.2}$$

   again with $\alpha^{\rm CPL}$ as the spectral photon index and $N_{50}^{\rm CPL}$ as the 50 keV normalization factor. $E_{\rm peak}$, defined as the peak energy in the νF_ν spectrum (Amati et al. 2002), is the standard parameter associated with the Band GRB model (Band et al. 1993), and it is related to the cutoff energy E_0 through $E_{\rm peak} = E_0(2+\alpha^{\rm CPL})$.

A further expansion of the spectral model would include the addition of the high-energy

simple power law term $N_E(E) \propto E^{\beta}$ of the full Band model:

$$N_E^{\rm Band}(E) = \begin{cases} N_{50}^{\rm Band} \cdot \left(\frac{E}{50{\rm keV}}\right)^{\alpha} \cdot \exp\left[-\frac{E(2+\alpha)}{E_{\rm peak}}\right] & \text{if } E < E_{\rm break} \equiv \frac{(\alpha-\beta)E_{\rm peak}}{2+\alpha} \\ N_{50}^{\rm Band} \left[\frac{(\alpha-\beta)E_{\rm peak}}{(2+\alpha)50{\rm keV}}\right]^{\alpha-\beta} e^{\beta-\alpha} \cdot \left(\frac{E}{50{\rm keV}}\right)^{\beta} & \text{if } E \geq E_{\rm break} \end{cases} \tag{4.3}$$

with the high-energy spectral index β as the added parameter. However, this model has not been implemented in the analysis since BAT spectra in the 15–150 keV energy range typically do not cover a wide enough range in order to uniquely determine all Band model parameters (Markwardt et al. 2007). Sakamoto et al. (2008) in fact performed a Band model fit to all 237 GRBs in the first *Swift* BAT Gamma-Ray Burst Catalog, and found no significant improvement in any case in the χ^2 of the fit compared to the CPL model fit, thus concluding that both models generally represent the BAT 15–150 keV spectra equally well.

After XSPEC has performed the fit to the 2 models, we choose the CPL model as the best fit if its additional degree of freedom improves the χ^2 goodness-of-fit statistic of the PL model by 6.0 or more; otherwise, the PL fit is chosen. This is the same selection criterion used by the BAT team in their analysis of the prompt emission of the *Swift* GRB population (Sakamoto et al. 2008), where they show by spectral simulation in the 15–150 keV band, modeled after data from 237 *Swift* GRBs, that the chance probability that a CPL model improves the fit by $\Delta\chi^2 \equiv \chi^2_{\rm PL} - \chi^2_{\rm CPL} > 6$, when the true spectral model is a PL model, is only 0.62%. Then, along with the spectral fit in the BATSS pipeline, the time-averaged photon flux and the fluence in the 15–150 keV band are calculated as well, to be included in short order in the BATSS webpage for the burst, and also in a GCN Circular with prompt emission data from BATSS.

Figure 4.6 and Table 4.3 provide an illustration of BATSS spectral fitting results from GRB 070326 data. The figure shows the raw spectrum and folded PL and CPL models for

the full-burst T_{100} time block (interval TTOT in Figure 4.5a), quoting the χ^2 of the fits of 75.03 and 74.99, respectively, from which the PL model is chosen as the best fit. The table displays the full set of parameters derived from the spectral fitting to all Bayesian time blocks in Figure 4.5a, including a full-burst fluence of $7.95 \pm 1.01 \times 10^{-7}$ erg/cm^2, which places it at the 37% percentile of all *Swift* bursts, as will be explored in Section 4.4.5.

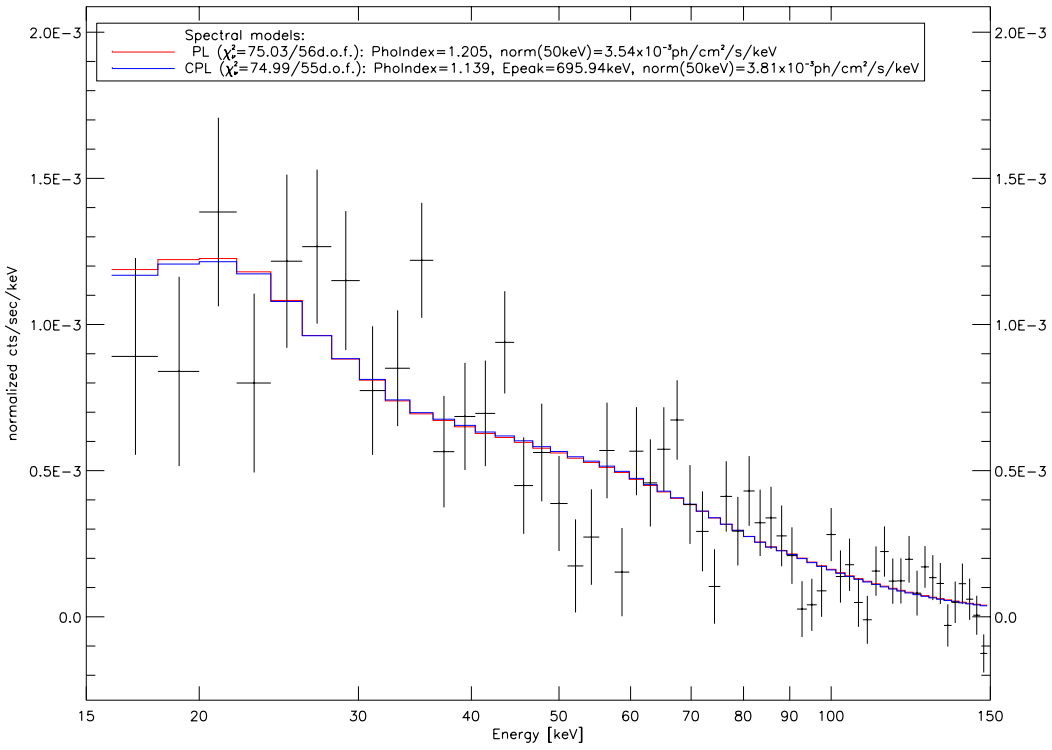

FIGURE 4.6: GRB 070326: time-averaged raw spectrum for full-burst (T_{100}) interval, and folded models simple power law (PL) and power law with high-energy exponential cutoff (CPL).

All of the spectral parameters in Table 4.3 were directly measured from the BATSS data except for the $E_{\rm peak}$ values in PL model spectra (all of the time block spectra in the case of GRB 070326), which the model does not define. Given that the $E_{\rm peak}$ parameter of the Band model (Band et al. 1993) is an intrinsic property of all GRBs, Sakamoto et al. (2009b) set out to find an empirical model that estimates $E_{\rm peak}$ for *Swift*-BAT GRB PL model spectra, which represent as much 80% of the entire *Swift*-BAT GRB population. They find that for $-2.3 \geq \alpha^{\rm PL} \geq -1.3$, $E_{\rm peak}$ is strongly dependent on $\alpha^{\rm PL}$ through a relation hereafter referred to as the $E_{\rm peak}$–$\alpha^{\rm PL}$ relation:

$$\log E_{\rm peak} = 3.258 + 0.829\ \alpha^{\rm PL} \tag{4.4}$$

This relation sets the dynamic range of estimated $E_{\rm peak}$ values at 22–151 keV, which implies that $E_{\rm peak}$ can be estimated though the $E_{\rm peak}$–$\alpha^{\rm PL}$ relation for PL model spectra whenever it falls roughly within the 15–150 keV energy band the BAT spectra are derived from.

In estimating the uncertainty $\sigma_{E_{\rm p}}$ of the $E_{\rm peak}$ value from the $E_{\rm peak}$–$\alpha^{\rm PL}$ relation, one contribution comes from the uncertainty of the empirical model itself. Sakamoto et al. (2009b) found the uncertainty $\sigma_{\rm model}$ in $\log E_{\rm peak}$ of Equation 4.4 to be the 2-sided cubic function of $\alpha^{\rm PL}$:

$$\begin{aligned}
\sigma^{+}_{\rm model} &= -\log E_{\rm peak} - \ \ 5.198 - 16.568\ \alpha^{\rm PL} - 10.630\ (\alpha^{\rm PL})^2 - 2.034\ (\alpha^{\rm PL})^3 \\
&= -8.456 - 17.397\ \alpha^{\rm PL} - 10.630\ (\alpha^{\rm PL})^2 - 2.034\ (\alpha^{\rm PL})^3 \qquad (4.5) \\
\sigma^{-}_{\rm model} &= \ \ \log E_{\rm peak} + 20.684 + 43.646\ \alpha^{\rm PL} + 26.891\ (\alpha^{\rm PL})^2 + 5.185\ (\alpha^{\rm PL})^3 \\
&= 23.942 + 44.475\ \alpha^{\rm PL} + 26.891\ (\alpha^{\rm PL})^2 + 5.185\ (\alpha^{\rm PL})^3 \qquad (4.6)
\end{aligned}$$

Since $\sigma^{+}_{\rm model}$ and $\sigma^{-}_{\rm model}$ are uncertainties in $\log E_{\rm peak}$, they would be related by error

propagation to the empirical model contribution to the uncertainty in $E_{\rm peak}$ itself through

$$\sigma^{\pm}_{E_{\rm p},{\rm model}} = \ln(10)\ E_{\rm peak}\ \sigma^{\pm}_{\rm model} \tag{4.7}$$

The second contribution to $\sigma_{E_{\rm p}}$ comes from the uncertainty of the $\alpha^{\rm PL}$ parameter obtained from the spectral fit, found from error propagation of equation 4.4 to be

$$\sigma_{E_{\rm p},\alpha} = 0.829\ \ln(10)\ E_{\rm peak}\ \sigma_{\alpha} \tag{4.8}$$

The total uncertainty in the estimated $E_{\rm peak}$ would then be found as

$$\sigma^2_{E_{\rm p}} = \sigma^2_{E_{\rm p},{\rm model}} + \sigma^2_{E_{\rm p},\alpha} \tag{4.9}$$

On Table 4.3, however, we chose to express the estimate as $E_{\rm peak} \pm \sigma_{E_{\rm p},{\rm model}} \pm \sigma_{E_{\rm p},\alpha}$, so as to distinguish between the uncertainty due to the the parameter $\alpha^{\rm PL}$ from the fit to the BATSS spectral data, and that due to the empirical $E_{\rm peak}$–$\alpha^{\rm PL}$ relation itself. We have applied the relation even to cases outside the dynamic range $-2.3 \geq \alpha^{\rm PL} \geq -1.3$ (shown as starred entries on the table) as a means of illustrating the trend in the estimated $E_{\rm peak}$ and its uncertainties when extrapolated outside its range of validity.

According the the estimate, the hard burst GRB 070326 ($\alpha^{\rm PL} = -1.21 \pm 0.15$) has an $E_{\rm peak}$ which lies near the top edge of the 15–150 keV energy band, at least as derived from its 1-sec peak spectrum, the only one with a PL spectral index $\alpha^{\rm PL}_{\rm 1s} = -1.33 \pm 0.35$ within the dynamic range of the $E_{\rm peak}$–$\alpha^{\rm PL}$ relation. However, the estimated $E_{\rm peak}$ of $143^{+219}_{-\ 52} \pm 96$ keV contains large uncertainties that prevent us to categorizing it within a narrow range.

TABLE 4.3

GRB 070326: spectral parameters derived from XSPEC fits to time-averaged spectra (15–150 keV) of Bayesian time blocks in Figure 4.5a. Bracketed values of $E_{\rm peak}$ correspond to estimates derived from the $E_{\rm peak}$–$\alpha^{\rm PL}$ empirical relation for GRB simple power law (PL) spectra (Sakamoto et al. 2009b). Starred values fall outside the dynamic range of the relation and are not regarded as valid estimates.

Time block :	Full slew	T_{100}	T_{90}	T_{50}	1-sec peak
Start time :	$T-4.5$s	$T+0.0$s	$T+0.7$s	$T+2.5$s	$T+0.8$s
Stop time :	$T+50.4$s	$T+22.1$s	$T+19.9$s	$T+11.6$s	$T+1.7$s
Duration :	54.9s	22.1s	19.2s	9.2s	1.0s
Spectral Model :	PL	PL	PL	PL	PL
Power law index (α) :	-1.20 ± 0.18	-1.21 ± 0.15	-1.22 ± 0.16	-1.01 ± 0.20	-1.33 ± 0.35
N_{50} [10^{-3} ph/cm^2/s/keV] :	1.65 ± 0.16	3.54 ± 0.29	3.70 ± 0.32	$4.35^{+0.47}_{-0.48}$	$8.94^{+1.55}_{-1.57}$
$E_{\rm peak}$ [keV] :	$[183^{+265}_{-142}\pm63]^*$	$[180^{+263}_{-130}\pm51]^*$	$[176^{+260}_{-119}\pm54]^*$	$[263^{+223}_{-674}\pm101]^*$	$[143^{+219}_{-\ 52}\pm96]$
χ^2_ν (d.o.f.) :	1.087 (56)	1.340 (56)	1.156 (56)	1.152 (56)	1.093 (56)
Flux [ph/cm^2/sec] :	$0.193^{+0.026}_{-0.033}$	$0.416^{+0.057}_{-0.040}$	$0.435^{+0.060}_{-0.056}$	$0.502^{+0.081}_{-0.070}$	$1.07^{+0.21}_{-0.22}$
Fluence [10^{-7} erg/cm^2] :	$9.16^{+1.49}_{-1.58}$	7.95 ± 1.01	$7.18^{+0.81}_{-1.11}$	4.30 ± 0.67	$0.842^{+0.164}_{-0.196}$

4.3.4 Publication and follow-up

Once the computation of the spectral parameters has been completed, the automated BATSS GRB analysis thread ends by summarizing the detection, lightcurve and spectral information for the burst on the BATSS webpage[11], on a page corresponding to its BATSS trigger number (Section 4.3.1). In the case of GRB 070326, whose 6-digit trigger number in the archival version of the slew data is 100042, the summary page for the burst is found at the URL:

`http://hea-www.harvard.edu/BATSS/data/triggers/100042/BATSS_100042.html`

The end of the BATSS automated processing for a newly discovered burst would normally be followed by the publication of a Circular to the GCN community, with the purpose of 1)confirming the initial detection earlier announced by an automated GCN Notice (see

[11] `http://hea-www.harvard.edu/BATSS/`

Appendix C), 2)providing relevant information gathered from the analysis of the prompt emission of the burst, and 3)encouraging follow-up of its afterglow emission by other observatories. A *Swift* Target of Opportunity (ToO) request would be submitted at the time to the Mission Operations Center (MOC) as well, via a web form[12], in order to enable observation by the spacecraft's narrow-field instruments (XRT and UVOT). Finally, a few weeks after the conclusion of follow-up campaign, the designated Burst Advocate (normally a SSC staff member) would publish a GCN Report (Barthelmy 2006) on the GRB, summarizing the most relevant data that was gathered by all three instruments on board *Swift*.

4.4 GRB science results

Having described the BATSS analysis thread for a candidate GRB and using GRB 070326 as a case study, in this section we begin by making a summary of the results of all confirmed and likely BATSS GRB detections and observations of prompt γ-ray emission, as well as follow-up observations of their afterglow by several telescopes including the narrow-field instruments (NFIs) on board *Swift*. We then continue with a study of the characteristics of the BATSS GRB population as derived from the BATSS analysis of the prompt emission data, with particular emphasis on how they compare with the rest of the *Swift* GRB population, which other publications (Sakamoto et al. 2008, 2011) have in turn characterized against earlier GRB survey missions such as BATSE and *BeppoSAX*.

[12] `https://www.swift.psu.edu/secure/toop/too_request.htm`

4.4.1 Data tables

Tables 4.4, 4.5 and 4.6 specify the main characteristics of 19 confirmed or likely GRBs found only from BAT slew data over the course of the BATSS survey. The data on the tables has been obtained from BATSS real-time detection and subsequent archival data processing, as well as from follow-up observations by other instruments. A description of the data contained on these tables follows below, and all relevant references for data sources are cited on the tables. In addition, Appendix D provides a further detailed description of the detection, ligthcurve and spectral properties of each GRB as derived by BATSS, along with a discussion of any additional distinguishing features for each.

Table 4.4 provides the GRB detection parameters as obtained from the BATSS pipeline, giving (where applicable) the parameters both as they were reported in real time[13], and also as computed in later analysis of the slew data after it had been posted to the *Swift* archive, which normally results in an improved GRB S/N in each of the 3 energy bands imaged by BATSS. If the GRB coordinates have been reported to the GCN system from independent data analyses, either from the BAT itself or from any other instrument which happened to observe the GRB prompt emission simultaneously, those results are included for comparison as well.

The first three columns of the table contain, respectively, the GRB number within the BATSS GRB sample, the GRB name (distinguishing those which have not been included in the official *Swift* GRB catalog[14]), and the BATSS ID of the slew where the detection

[13]Real-time reporting normally occurs in the form of an automated GCN Notice, followed by a GCN Circular once the early detection data has been reviewed, as described in Section 4.3.1.

[14]The most common reason for not including a BATSS GRB in the *Swift* catalog is that they have only been found in later analysis of archival data, after the ∼24h time window for initial afterglow observations has passed. Also in this group are detections which have been reported in real time by BATSS as likely GRBs but have not been confirmed by either 1)a BAT detection with $S/N(15\text{–}150\text{keV}) > 8.0$, the empirical threshold above which no false triggers have been found; 2)a simultaneous detection of the prompt emission

was made, including the fraction of the slew that was actually captured and imaged by BATSS (typically capped by *Swift* operations at 120.0 sec). Columns 4 and 5 contain the exposure and time-averaged partial coding fraction of the burst, both calculated above the pre-set partial coding threshold of 15%,[15] as discussed in Section 2.2.3 on the BATSS image addition method. Column 7 quotes the type of data used in making the detection (either real-time or archival), or in the case of non-BATSS detections, the corresponding observatory/instrument. Column 8 lists the BATSS trigger number (as defined in Section 4.3.1 for GRBs from both real-time and archival data), and columns 9–11 quote the signal-to-noise ratios of the detections in the Soft (15–50 keV), Hard (50–150 keV) and Broad (15–150 keV) energy bands upon which the BATSS image trigger was issued. Columns 12-14 quote the equatorial (J2000) coordinates of the burst along with its error radius (90%, including systematics), as derived in Section 2.4.4 for the specific case of BATSS slews. Finally, the numbers of the GCN Circulars where these parameters were reported are provided as reference.

Table 4.5 lists the parameters derived from observations of the GRB prompt emission, both by BATSS and by other γ-ray observatories. Columns 1-3 contain the same BATSS GRB number, GRB name and data type as defined for Table 4.4. The trigger time in column 4 is defined differently depending on the instrument, the method of detection (such as image or rate trigger), and the time resolution of the input data; in general, trigger times for rate triggers are set at the start of the leading edge of the prompt emission,

---

by another γ-ray observatory such as *Konus-Wind*, Suzaku WAM or Fermi-GBM; or 3)the confirmation of an afterglow observation.

[15]Prior to 2010, the partial coding threshold for real-time data had been set at 20%; in those cases, the exposure and mean coding fraction for real-time and archival data analysis differ from each other and are hence quoted separately on the table. From 2010 onwards, any differences between the two are only due to differences in the amount of data transferred to the BATSS server in real time versus what was later posted to the *Swift* archive.

whereas times for image triggers are set at the start of the imaging period. The trigger time definitions for the specific case of BATSS are explained in Section 4.3.2. Column 5 lists the duration of the T_{90} interval, with the only difference across instruments being the canonical energy band used to determine it. In the case of BATSS, the 15–150 keV (Broad) band was used in all cases. BAT team analysis instead uses the 15–350 keV band, though since the coded mask becomes transparent to photons at $\gtrsim$ 150 keV, the mask-weighting procedure effectively treats those counts as background (Sakamoto et al. 2008). Due to the relatively short exposure time of GRBs during slews, we may only be able to provide a lower limit on T_{90} from the BATSS data. At the same time, reports from other observatories may only quote an estimation of the full-burst (T_{100}) duration, in which case we may only be able to include an upper limit to the T_{90}. A discussion of burst durations in the BATSS GRB population is the subject of Section 4.4.3.

Column 6 of Table 4.5 indicates the high-energy range used by each instrument survey in fitting the GRB prompt emission spectra and deriving the energetics in columns 7-11.[16] In the case of BAT data, the spectral model quoted in column 9 has been chosen as the best fit according to the criterion on χ^2 described in Section 4.3.3. In all cases where the spectra have been fit to either a simple power law (PL) or a cutoff power law (CPL) model, the photon index α (column 10) and $E_{\rm peak}$ (column 11) correspond to the standard parameters defined in Equations 4.1 and 4.2. In the frequent case of PL being the best fit to the spectrum, we have provided the estimate of the corresponding Band model $E_{\rm peak}$ given the empirical $E_{\rm peak}$–$\alpha^{\rm PL}$ relation of Sakamoto et al. (2009b) and discussed in Section 4.3.3. Estimated values are quoted in the form $E_{\rm peak} \pm \sigma_{E_{\rm p},{\rm model}} \pm \sigma_{E_{\rm p},\alpha}$, using the relations in equations 4.4, 4.7 and 4.8. Entries that fall outside the dynamic range $-2.3 \geq \alpha^{\rm PL} \geq -1.3$

[16]This is not necessarily the same energy range where the initial detection was made and from which the T_{90} parameter was derived, which is usually equal to or wider than the range for spectral analysis.

are indicated by an an asterisk and disregarded from the subsequent analysis presented in this section.

Besides the PL and CPL fits, a fit to the 4-parameter Band model (Band et al. 1993) has been reported in the case of certain instruments with a wider energy range than the BAT. For those cases, the high-energy index β of the additional $\propto E^{\beta}$ simple power law term of the model is also quoted in the Comments section (column 14). For all the fits where the data was made available, the χ^2 statistic and number of degrees of freedom (d.o.f.) of the fit are quoted in column 12.[17] Having fitted the time-averaged T_{100} and T_{1s} spectra, the fluence S and 1-sec peak photon flux F_{1s}^{p} derived from the fit are quoted in columns 7 and 8, respectively, each one computed in the corresponding energy range quoted for each instrument in column 6. Finally, the relevant GCN Circular references are quoted in column 13, and any additional comments, partial conclusions and/or constraints on the spectral parameters derived from the analysis of each observation are included in column 14.

Table 4.6, the third data table, finally makes a comprehensive summary of all follow-up observations of the possible GRB afterglows by both space and ground-based observatories. Columns 1 and 2 are the same BATSS GRB number and GRB name of Tables 4.4 and 4.5. They are followed in columns 3 and 4 by the names of the observatory and instrument which performed the observation. The observation type (X-ray, optical, infrared, radio) and the corresponding energy band or filter and indicated in columns 5 and 6. Columns 6 and 7 contain the time to the observation from the GRB trigger time, which gives an indication of the typical response times that have been achieved for BATSS after the occurrence of the burst, as well as the total exposure time of said observations. Column 8 states whether

[17] In the case of a standard BAT 80-channel spectrum fitted in the 15–150 keV as was done for BATSS, the input data has 56 and 55 d.o.f. when fitting to the PL and CPL models, respectively.

a detection of a candidate afterglow has been made, and if so, the RA/Dec (J2000) and error radius of the detection are provided in columns 9–11. The accuracy of the BATSS position[18] can be assessed by measuring its offset with respect to the afterglow position, which these focusing instruments or radio antenna arrays can detect within a much smaller error radius than the BAT can, typically below $10''$ and even at the sub-arcsecond level, for instance in the case of *Swift*-XRT positions that have been enhanced in combination with *Swift*-UVOT images; the resulting offset for observations with a candidate afterglow is quoted in column 12. Lastly, the relevant GCN publications are provided for reference in column 13, and all other relevant information is logged in the final Comments column.

[18]We use the BATSS position from archival data to measure offsets throughout the table, though as can be seen in Table 4.4, the real-time and archival positions are largely consistent with each other.

TABLE 4.4
BATSS GRBs — Detection parameters

#	GRB[a]	Slew ID[b]	Exp.[c] [sec]	CF[d] [%]	Data type[e]	BATSS trigger[f]	Detection S/N Soft	Hard	Broad	RA (J2000)	Dec (J2000)	Err. rad.[g]	GCN Circulars
1	070326	16h28m00s+059s (55.0s)	58.0	65.0	R	000001	8.9	6.9	10.6	02:41:20.8	−66:59:21	n/a	6653
			55.0	68.3	A	100042	8.7	6.2	10.0	02:41:23.7	−66:53:22	3.3	
2	*071212*	03h21m00s+156s (120.0s)	57.4	27.9	A	100112	8.5	n/a	9.2	17:23:31.2	−09:11:18	3.4	
3	080130	11h12m59s+099s (43.8s)	43.8	92.2	R	000011	8.7	7.6	11.4	17:26:42	−53:11:20	2.6	7242
			43.8	94.1	A	100177	7.7	6.8	10.1	17:26:35.8	−53:11:55	3.2	
					(BAT)	n/a				17:26:31.6	−53:11:24	2.8	7248
4	080702B	01h08m59s+212s (120.0s)	65.9	61.4	R	000017	6.5	n/a	6.3	23:42:24	−05:29:23	6.4	7924
			68.6	63.7	A	100478	5.9	n/a	5.5	23:42:23.4	−05:29:25	4.5	
					(BAT)	n/a				23:42:27.8	−05:25:26	3.5	7924
5	*080806*	09h57m59s+188s (120.0s)	93.8	54.9	A	100583	9.7	7.0	10.9	04:16:18.3	−53:41:03	3.1	
6	081025	08h21m59s+175s (120.0s)	89.8	71.6	R	000021	12.9	13.7	19.1	16:21:11	+60:27:58	2.9	8409
			97.8	77.9	A	100762	9.9	10.1	14.9	16:21:11.8	+60:28:19	2.7	
7	081203B	13h51m59s+060s (44.0s)	31.0	59.4	R	000022	11.0	5.6	12.0	15:15:09	+44:25:38	3.0	8600, 8602
			36.4	65.3	A	100828	12.1	5.1	13.9	15:15:10.0	+44:25:28	2.8	
8	081211B	06h14m58s+121s (108.8s)	97.2	82.3	R	000023	7.4	n/a	8.3	11:12:55	+53:50:43	3.0	8661
			101.0	87.9	A	100851	7.7	n/a	8.8	11:12:55.0	+53:50:47	3.5	
9	090118	13h53m58s+094s (83.0s)	40.0	64.7	R	000024	6.9	n/a	8.0	03:19:28	+18:28:40	3.69	8825
10	090306B	23h06m57s+066s (55.0s)	43.4	74.9	R	000026	35.6	20.2	40.7	15:24:49	−06:57:29	2.87	8944
			50.0	82.0	A	101004	35.7	23.7	41.8	15:24:50.4	−06:57:34	1.9	
11	090418B	08:58:57s+151s (120.0s)	104.4	81.6	R	000027	86.0	41.8	92.4	15:03:38	+17:13:26	1.9	9159
			108.8	91.2	A	101098	89.1	43.3	94.9	15:03:38.2	+17:13:28	1.6	
12	090823	16h09m57s+178s (92.0s)	56.0	76.9	R	000028	6.7	n/a	6.2	08:34:41	+60:38:29	4.5	9839
			60.0	87.8	A	101320	8.4	n/a	7.8	08:34:42.8	+60:37:37	3.6	
					(BAT)	n/a				08:34:50.7	+60:39:36	4	9835, 9838

[a] GRBs which have not been included in the official *Swift* GRB catalog are highlighted in italics. See text for explanation.

[b] Slew start time [UT] + duration [s]: `[HH]h[MM]m[SS]s+[XXX]s` (data fraction captured [s] in parentheses)

[c,d] Source Exposure time and mean Coding Fraction, above the BATSS 15% partial coding fraction threshold. Real-time and Archival data up to 2009 differ in that real-time data was first processed using a higher, 20% partial coding threshold

[e] R=BATSS Real-time data, A=BATSS Archival data, (BAT)=BAT Team ground analysis, (GBM)=Fermi-GBM detection

[f] See Section 4.3.1 for BATSS GRB trigger numbering conventions

[g] [arcmin], 90% confidence, including systematics

TABLE 4.4 (continued)
BATSS GRBs — Detection parameters

#	GRB[a]	Slew ID[b]	Exp.[c] [sec]	CF[d] [%]	Data type[e]	BATSS trigger[f]	Detection S/N Soft	Hard	Broad	RA (J2000)	Dec (J2000)	Err. rad.[g]	GCN Circulars
13	090929A	04h31m57s+193s (120.0s)	87.0	90.2	A	101376	22.3	11.4	24.1	03:46:02.6	−05:57:00	2.2	
					(BAT)	n/a				03:45:57.9	−05:57:50	3	9966
					(GBM)	n/a				03:27	−07:18	(78)[h]	9962
14	*100120A*	12h51m57s+171s (120.0s)	45.2	49.0	A	101559	22.6	14.8	27.7	09:16:58.2	+37:21:54	2.1	
15	*101004A*	21h51m56s+082s (76.8s)	37.2	53.6	R	000264	10.9	5.4	11.6	14:48:31.2	+03:47:28	3.0	
					A	101962	11.3	5.5	12.0	14:48:31.4	+03:47:24	3.0	
16	110107A	21h13m55s+206s (120.1s)	117.2	77.0	R	000391	35.3	n/a	42.8	19:59:34.8	+41:54:12	1.9	
			118.4	81.9	A	102225	51.0	n/a	60.3	19:59:35.8	+41:53:32	1.8	
					(BAT)	n/a				19:59:33.6	+14:53:19	3	11545
17	110319B	19h32m55s+094s (75.0s)	74.6	84.7	R	000466	18.0	12.6	22.2	21:44:17.5	−56:46:33	2.3	
					A	102413	17.9	12.6	22.1	21:44:17.6	−56:46:33	2.3	
					(BAT)	n/a				21:44:21.1	−56:46:26	1.0	11813, 11818
18	*110906A*	12h23m55s+094s (94.0s)	13.8	23.5	R	000607	4.7	n/a	7.8	19:47:33.9	−26:12:32	3.75	12332
					A	102619	4.7	n/a	7.8	19:47:33.9	−26:12:32	3.8	
					(BAT)	n/a				19:47:39.6	−26:13:52	1	12332
19	*111011A*	06h58m55s+164s (164.0s)	110.6	88.2	R	000645	17.3	n/a	17.2	16:19:24.8	−47:48:58	2.5	
			112.6	80.8	A	102678	23.5	4.9	21.8	16:19:25.3	−47:49:32	2.2	

Table 4.4 References: Copete et al. (2007, GCN 6653); Copete et al. (2008a, GCN 7242); Cummings et al. (2008a, GCN 7248); Cummings et al. (2008c, GCN 7924); Copete et al. (2008b, GCN 8409); Copete et al. (2008c, GCN 8600); Copete et al. (2008e, GCN 8602); Copete et al. (2008d, GCN 8661); Copete et al. (2009d, GCN 8825); Copete et al. (2009a, GCN 8944); Copete et al. (2009b, GCN 9159); Copete et al. (2009c, GCN 9839); Cummings et al. (2009b, GCN 9835); Cummings (2009, GCN 9838); Cummings & Krimm (2009, GCN 9966); Rau (2009, GCN 9962); Cummings (2011, GCN 11545); Cummings et al. (2011, GCN 11813); Palmer et al. (2011, GCN 11818); Copete et al. (2011, GCN 12332)

[a] GRBs which have not been included in the official *Swift* GRB catalog are highlighted in italics. See text for explanation.

[b] Slew start time [UT] + duration [s]: `[HH]h[MM]m[SS]s+[XXX]s` (data fraction captured [s] in parenteses)

[c,d] Source Exposure time and mean Coding Fraction, above the BATSS 15% partial coding fraction threshold

[e] R=BATSS Real-time data, A=BATSS Archival data, (BAT)=BAT Team ground analysis

[f] See Section 4.3.1 for BATSS GRB trigger numbering conventions

[g] Error radius [arcmin], 90% confidence, including systematics

[h] Fermi GBM 1σ statistical error only; additional systematic error is 2°–3°

TABLE 4.5

BATSS GRBs — Prompt emission observations

#	GRB	Data type[a]	Trigger time[b] (T) [UT]	Energy range[c] [keV]	T_{90} [sec]	Fluence [10^{-7}erg/cm^2]	1-sec peak photon flux [ph/cm^2/sec]	Spectral model[d]	Photon Index (α)	$E_{\rm peak}$[e] [keV]	χ^2/d.o.f.	GCN Circulars	Comments
1	070326	R	16:28:02	15–150	19.0	3.45 ± 0.37	1.04	PL	-1.44 ± 0.17	$[116^{+167}_{-047} \pm 38]$	71.8/56	6653	
		A	16:28:08.7	15–150	19.2	$7.95^{+1.01}_{-1.01}$	$1.07^{+0.21}_{-0.22}$	PL	$-1.21^{+0.15}_{-0.15}$	$[180^{+263+51}_{-130-51}]^*$	75.0/56		
2	071212	A	03:22:36.6	15–150	10.0	$3.86^{+0.81}_{-1.00}$	$1.04^{+0.30}_{-0.36}$	PL	$-2.43^{+0.34}_{-0.39}$	$[18^{+09+11}_{-10-13}]^*$	61.7/56		
3	080130	R	11:13:59	15–150	n/a	5.0	n/a	PL	-1.46	$[112^{+158}_{-050}]$	n/a		
		A	11:13:54.5	15–150	>43.7	$>4.82^{+1.14}_{-1.26}$	n/a	PL	$-1.48^{+0.24}_{-0.24}$	$[107^{+149+49}_{-053-49}]$	47.7/56		
		(BAT)	11:13:59	15–150	65 ± 5	7.7 ± 2.8	0.2 ± 0.1	PL	-1.21 ± 0.12	$[180^{+263}_{-130} \pm 41]^*$	n/a	7248	
4	080702B	R	01:10:41	15–150	20	5.0 ± 0.9	0.5 ± 0.1	PL	-1.44 ± 0.13	$[116^{+167}_{-047} \pm 29]$	n/a		
		A	01:10:41.1	15–150	11.6	$5.04^{+0.66}_{-0.67}$	$0.70^{+0.23}_{-0.17}$	PL	$-1.35^{+0.18}_{-0.18}$	$[138^{+210+47}_{-048-47}]$	68.8/56		
		(BAT)	01:10:41	15–150	20 ± 3	5.0 ± 0.9	0.5 ± 0.1	PL	-1.44 ± 0.13	$[116^{+167}_{-047} \pm 29]$	n/a	7937	
5	080806	A	09:59:54.0	15–150	12.0	$13.5^{+0.4}_{-0.5}$	$2.52^{+0.26}_{-0.24}$	CPL	$-0.89^{+0.41}_{-0.38}$	$89.9^{+56.8}_{-17.4}$	38.5/55		
6	081025	R	08:22:02	15–150	24.0	19.4	1.51	PL	-1.04	$[249^{+245}_{-539}]^*$	50.2/56		
		A	08:23:03.4	15–150	22.8	$18.7^{+0.9}_{-0.9}$	$2.10^{+0.14}_{-0.17}$	PL	$-1.07^{+0.08}_{-0.08}$	$[235^{+260+36}_{-427-36}]^*$	53.8/56		
		(BAT)	08:22:02	15–150	23 ± 2	19 ± 2	1.3 ± 0.2	PL	-1.12 ± 0.05	$[214^{+271}_{-284} \pm 20]^*$	n/a	8415	
		(K-W)	08:23:06.316	20–1000	<25	$53.7^{+9.6}_{-8.2}$	n/a	CPL	$-0.67^{+0.43}_{-0.33}$	222^{+81}_{-46}	55.5/60	8412	Band-model $\beta < -2.07$, 256-ms peak flux $= 8.90^{+2.75}_{-2.62} \times 10^{-7}$ erg/cm^2/sec
		(WAM)	08:23:07	100–1000	22	38^{+5}_{-7}	1.5 ± 0.2	PL	$-1.93^{+0.25}_{-0.29}$	$[46^{+015+22}_{-104-25}]$	10/9	8445	
		(GBM)	08:23:05.29	8–1000	45	71 ± 5	4.50 ± 0.22	CPL	-0.35 ± 0.13	251 ± 25	736/700	8483	
								Band	-0.15 ± 0.22	200 ± 33	732/699	8483	$\beta = -2.05 \pm 0.25$
		(SPI)	08:23:04	50–100000	n/a	n/a	n/a	n/a	n/a	n/a	n/a		Reported by V. Beckmann (e-mail)
7	081203B	R	13:52:02	15–150	23.4	21.4	4.21	PL	-1.65	$[78^{+80}_{-85}]$	50.0/56	8600	
		A	13:52:15.9	15–150	29.0	$20.0^{+1.7}_{-1.9}$	$4.21^{+0.51}_{-0.55}$	PL	$-1.66^{+0.15}_{-0.16}$	$[76^{+76+22}_{-87-23}]$	56.6/56		
		(K-W)	13:51:30.368	20–2000	<80	556^{+24}_{-23}	n/a	CPL	$-1.165^{+0.057}_{-0.054}$	255^{+22}_{-19}	77.8/61	8610	256-ms peak flux $= 24.3^{+4.1}_{-4.0} \times 10^{-7}$ erg/cm^2/sec
								Band			77.7/60	8610	$\beta < -2.59$
		(WAM)	13:51:31.9	100–1000	45	290	2.9	CPL	$-1.2^{+0.2}_{-0.3}$	304^{+22}_{-20}	50.6/28	8638	Consistent with K-W detection. 1.3% coded in preceding pointing, no on-board trigger

[a] R=BATSS Real-time data, A=BATSS Archival data, (BAT)=BAT Team ground analysis (GSFC), (K-W)=Konus-Wind, (GBM)=Fermi-GBM, (WAM)=Suzaku Wide-band All-sky Monitor, (SPI)=INTEGRAL SPI Anti-Coincidence System (ACS)

[b] See Section 4.3.2 for BATSS trigger time definitions

[c] Energy range for spectral analysis, not necessarily the same as range of initial detection

[d] PL=simple power law, CPL=cutoff power law, Band=Band model (Band et al. 1993). See Section 4.3.3 for definitions of spectral model parameters.

[e] Bracketed entries correspond to estimates of $E_{\rm peak} \pm \sigma_{E_{\rm p},{\rm model}} \pm \sigma_{E_{\rm p},\alpha}$ (equations 4.4, 4.7, 4.8) for PL model spectra as a function of $\alpha^{\rm PL}$, based on the empirical relation by Sakamoto et al. (2009b) for *Swift*-BAT GRBs. Starred (*) entries fall outside of the dynamic range $-2.3 \geq \alpha^{\rm PL} \geq -1.3$ of the $E_{\rm peak}$–$\alpha^{\rm PL}$ relation, and are therefore disregarded as valid estimates in the analysis that follows in this section.

TABLE 4.5 (continued)
BATSS GRBs — Prompt emission observations

#	GRB	Data type[a]	Trigger time[b] (T) [UT]	Energy range[c] [keV]	T_{90} [sec]	Fluence [10^{-7}erg/cm^2]	1-sec peak photon flux [ph/cm^2/sec]	Spectral model[d]	Photon Index (α)	$E_{\rm peak}$[e] [keV]	χ^2/d.o.f.	GCN Circulars	Comments
8	081211B	R	06:15:02	15–150	n/a	6.1	n/a	PL	-1.73	$[67^{+55}_{-98}]$	n/a	8661	
		A	06:15:15.9	15–150	>103.5	$>5.88^{+2.86}_{-2.75}$	n/a	PL	$-1.77^{+0.45}_{-0.52}$	$[62^{+045+53}_{-102-61}]$	63.5/56		
		(K-W)	06:12:58	20–70, 70–300	$\sim$2.9	n/a	n/a	n/a	n/a	n/a	n/a	8676	BATSS detection likely to be extended emission of short GRB.
		(BAT)	06:12:55	15–150	$\sim$2.9	n/a	n/a	n/a	n/a	n/a	n/a	8676	
9	090118	R	13:54:02	15–150	16	4.0	0.45	PL	-1.35	$[138^{+210}_{-048}]$	44.1/56	8825	
10	090306B	R	23:07:02	15–150	20.4	31	2.96	CPL	-1.02	130	55.7/56	8944	
		A	23:07:19.4	15–150	21.0	$28.3^{+0.6}_{-4.0}$	$2.80^{+0.07}_{-0.92}$	CPL	$-0.98^{+0.22}_{-0.21}$	113^{+44}_{-19}	58.5/55		
		(SPI)	23:07:21.9	50–100000	<14	n/a	n/a	n/a	n/a	n/a	n/a	8968	
11	090418B	R	08:59:02	15–150	65.0	154	8.40	CPL	-1.45	196	47.7/56	9159	
		A	08:59:20.3	15–150	66.0	153^{+2}_{-3}	$10.2^{+0.3}_{-1.8}$	PL	$-1.67^{+0.03}_{-0.03}$	$[75^{+73+4}_{-89-4}]$	54.4/56		
		(K-W)	08:59:26.325	20–2000	<120	231 ± 9	n/a	CPL	$-1.23^{+0.09}_{-0.01}$	117^{+8}_{-7}	62.0/56	9171	
								Band			62.0/55	9171	$\beta < -3.18$
		(WAM)	08:54:21.299	100–1000	29	122^{+06}_{-14}	$2.13^{+0.35}_{-0.58}$	PL	$-2.09^{+0.20}_{-0.22}$	$[34^{+03+13}_{-86-14}]$	13/17	9186	
12	090823	R	16:11:28	15–150	>13.0	1.15	0.25	PL	-2.40	$[19^{+08}_{-18}]^*$	62.8/56		Data from 13.0s tail end of burst
		A	16:11:26.0	15–150	>13.0	$1.18^{+0.61}_{-0.65}$	>0.249	PL	$-2.37^{+0.48}_{-0.58}$	$[20^{+07+18}_{-25-22}]^*$	64.0/56		Data from 13.0s tail end of burst
		(BAT)	16:11:12	15–150	>10	1.0 ± 0.3	n/a	PL	-2.27 ± 0.21	$[24^{+03}_{-49} \pm 10]$	n/a	Report 241.1	Only $\sim$1% of fluence in BAT FoV. Also triggered Suzaku WAM, Agile-MCAL.
		(K-W)	16:11:10.606	20–2000	10	89^{+5}_{-3}	n/a	CPL	$-0.49^{+0.17}_{-0.15}$	188^{+18}_{-15}	56/61	9836	Band-model $\beta = -7$, 256-ms peak flux $= 28^{+2.5}_{-2.5} \times 10^{-6}$ erg/cm^2/sec
13	090929A	A	04:33:03.7	15–150	46.0	$20.7^{+0.9}_{-1.3}$	$6.27^{+0.23}_{-0.24}$	PL	$-1.26^{+0.08}_{-0.08}$	$[163^{+247+25}_{-084-25}]^*$	54.0/56		
		(BAT)	04:33:08	15–150	7 ± 2	16.9 ± 0.7	5.9 ± 0.3	PL	-0.96 ± 0.04	$[290^{+166}_{-962} \pm 22]^*$	n/a	9980	
		(GBM)	04:33:03.97	8–1000	8.5 ± 0.4	106 ± 3	10.9 ± 0.3	CPL	-0.52 ± 0.06	610.9 ± 44.5	439/393	9962	
		(K-RF)	04:33:04.747	20–3000	$\sim$6	124^{+12}_{-11}	n/a	CPL	$-0.55^{+0.11}_{-0.12}$	480^{+64}_{-54}	120.1/119	9968	16-ms peak flux $= 202 \pm 46 \times 10^{-7}$ erg/cm^2/sec
		(K-W)	04:33:07.790	20–3000	<8.4	132^{+23}_{-24}	n/a	CPL	$-0.47^{+0.25}_{-0.22}$	574^{+151}_{-100}	66.2/65	9976	16-ms peak flux $= 204^{+60}_{-61} \times 10^{-7}$ erg/cm^2/sec
								Band	$-0.36^{+0.62}_{-0.29}$	494^{+175}_{-191}	62.1/64	9976	$\beta = -2.16^{+0.43}_{-1.41}$
		(WAM)	04:33:04.634	100–1000	3.8	$49.6^{+53.2}_{-44.7}$	$5.59^{+0.53}_{-0.68}$	CPL	$-0.86^{+0.80}_{-0.36}$	557^{+117}_{-098}	125/98	9992	
		(RT-2)	04:33:04	60–1000	5	n/a	n/a	n/a	n/a	n/a	n/a	10010	

[a] R=BATSS Real-time data, A=BATSS Archival data, (BAT)=BAT Team ground analysis (GSFC), (K-W)=Konus-Wind, (GBM)=Fermi-GBM, (WAM)=Suzaku WAM, (SPI)=INTEGRAL SPI-ACS, (K-RF)=Konus-RF (CORONAS-Photon), (RT-2)=RT-2 (CORONAS-Photon)

[b] See Section 4.3.2 for BATSS trigger time definitions

[c] Energy range for spectral analysis, not necessarily the same as range of initial detection

[d] PL=simple power law, CPL=cutoff power law, Band=Band model (Band et al. 1993). See Section 4.3.3 for definitions of spectral model parameters.

[e] Bracketed entries correspond to estimates of $E_{\rm peak} \pm \sigma_{E_{\rm p},{\rm model}} \pm \sigma_{E_{\rm p},\alpha}$ (equations 4.4, 4.7, 4.8) for PL model spectra as a function of $\alpha^{\rm PL}$, based on the empirical relation by Sakamoto et al. (2009b) for *Swift*-BAT GRBs. Starred (*) entries fall outside of the dynamic range $-2.3 \geq \alpha^{\rm PL} \geq -1.3$ of the $E_{\rm peak}$–$\alpha^{\rm PL}$ relation, and are therefore disregarded as valid estimates in the analysis that follows in this section.

TABLE 4.5 (continued)
BATSS GRBs — Prompt emission observations

#	GRB	Data type[a]	Trigger time[b] (T) [UT]	Energy range[c] [keV]	T_{90} [sec]	Fluence [10^{-7}erg/cm^2]	1-sec peak photon flux [ph/cm^2/sec]	Spectral model[d]	Photon Index (α)	$E_{\rm peak}$[e] [keV]	χ^2/d.o.f.	GCN Circulars	Comments
14	100120A	A	12:52:14.9	15–150	30.8	$18.7^{+2.0}_{-1.3}$	$1.80^{+0.18}_{-0.20}$	PL	$-1.63^{+0.11}_{-0.11}$	$[81^{+87+17}_{-82-17}]$	67.1/56		
15	101004A	R	21:52:54.4	15–150	10.2	$3.66^{+0.82}_{-0.74}$	$0.615^{+0.290}_{-0.257}$	PL	$-1.65^{+0.25}_{-0.26}$	$[78^{+80+37}_{-85-39}]$	66.9/56		
		A	21:52:54.4	15–150	10.2	$3.57^{+0.88}_{-0.77}$	$0.590^{+0.302}_{-0.289}$	PL	$-1.68^{+0.26}_{-0.27}$	$[73^{+70+36}_{-90-38}]$	67.4/56		
16	110107A	R	21:14:41.1	15–150	74.8	$49.1^{+2.2}_{-2.5}$	$2.38^{+0.33}_{-0.27}$	PL	$-1.61^{+0.07}_{-0.07}$	$[84^{+94+11}_{-78-11}]$	46.3/56		
		A	21:14:41.3	15–150	78.2	$53.3^{+1.4}_{-1.7}$	$2.40^{+0.18}_{-0.20}$	PL	$-1.62^{+0.05}_{-0.05}$	$[82^{+90+8}_{-80-8}]$	50.6/56		
		(BAT)	21:15:51	15–150	n/a	$>58 \pm 5$	n/a	PL	-1.58 ± 0.03	$[89^{+106}_{-072} \pm 5]$	n/a	11546	
17	110319B	R	19:34:00.2	15–150	14.0	$9.73^{+0.56}_{-0.49}$	$1.28^{+0.16}_{-0.14}$	PL	$-1.44^{+0.09}_{-0.09}$	$[116^{+167+20}_{-047-20}]$	50.6/56		
		A	19:34:00.2	15–150	14.0	$9.72^{+0.57}_{-0.60}$	$1.28^{+0.16}_{-0.13}$	PL	$-1.44^{+0.09}_{-0.09}$	$[116^{+167+20}_{-047-20}]$	50.8/56		
		(BAT)	19:34:00.2	15–150	14.5 ± 2.0	10 ± 1	1.25 ± 0.15	PL	-1.39 ± 0.05	$[128^{+191}_{-045} \pm 12]$	n/a	11818	
18	110906A	R	12:25:13	15–150	>15.1	n/a	n/a	n/a	n/a	n/a	n/a		Moon-constrained for following 3 days; no follow-up observations
		A	12:25:13.5	15–150	>15.1	n/a	n/a	n/a	n/a	n/a	n/a		
19	111011A	R	06:58:55.6	15–150	>112.9	$>10.6^{+0.38}_{-0.53}$	n/a	PL	$-1.89^{+0.38}_{-0.40}$	$[49^{+021+36}_{-106-37}]$	63.6/56		$b = +01{:}43{:}31$
		A	06:58:54.5	15–150	>115.5	$>12.0^{+4.4}_{-4.0}$	n/a	PL	$-2.45^{+0.34}_{-0.37}$	$[17^{+11+11}_{-05-12}]^*$	62.1/56		$b = +01{:}43{:}04$

Table 4.5 References: Copete et al. (2007, GCN 6653); Cummings et al. (2008a, GCN 7248); Markwardt et al. (2008, GCN 7937); Cummings et al. (2008b, GCN 8415); Golenetskii et al. (2008b, GCN 8412); Kira et al. (2008, GCN 8445); Kienlin & Bissaldi (2008, GCN 8483); Copete et al. (2008c, GCN 8600); Golenetskii et al. (2008c, GCN 8610); Terada et al. (2008, GCN 8638); Copete et al. (2008d, GCN 8661); Golenetskii et al. (2008a, GCN 8676); Copete et al. (2009d, GCN 8825); Copete et al. (2009a, GCN 8944); Beckmann et al. (2009, GCN 8968); Copete et al. (2009b, GCN 9159); Golenetskii et al. (2009c, GCN 9171); Kono et al. (2009, GCN 9186); Golenetskii et al. (2009a, GCN 9836); Cummings et al. (2009a, GCN 9980); Rau (2009, GCN 9962); Golenetskii et al. (2009b, GCN 9968); Golenetskii et al. (2009d, GCN 9976); Ohmori et al. (2009, GCN 9992); Chakrabarti et al. (2009, GCN 10010); Cummings & Barthelmy (2011, GCN 11546); Palmer et al. (2011, GCN 11818)

[a] R=BATSS Real-time data, A=BATSS Archival data, (BAT)=BAT Team ground analysis (GSFC)

[b] See Section 4.3.2 for BATSS trigger time definitions

[c] Energy range for spectral analysis, not necessarily the same as range of initial detection

[d] PL=simple power law, CPL=cutoff power law, Band=Band model (Band et al. 1993). See Section 4.3.3 for definitions of spectral model parameters.

[e] Bracketed entries correspond to estimates of $E_{\rm peak} \pm \sigma_{E_{\rm p},{\rm model}} \pm \sigma_{E_{\rm p},\alpha}$ (equations 4.4, 4.7, 4.8) for PL model spectra as a function of $\alpha^{\rm PL}$, based on the empirical relation by Sakamoto et al. (2009b) for *Swift*-BAT GRBs. Starred (*) entries fall outside of the dynamic range $-2.3 \geq \alpha^{\rm PL} \geq -1.3$ of the $E_{\rm peak}$–$\alpha^{\rm PL}$ relation, and are therefore disregarded as valid estimates in the analysis that follows in this section.

TABLE 4.6
BATSS GRBs — Follow-up observations

#	GRB	Observatory	Instrument	Obs. type[a]	Energy range	Time to observation [ksec]	Exposure	Detected (Y/N)	RA (J2000)	Dec (J2000)	Error radius[b] [arcsec]	BATSS offset[c] [arcmin]	GCN Circulars	Comments
3	080130	*Swift*	XRT	X	0.3-10keV	40.1	1.98ks	Y	17:26:27.98	−53:11:19.6	8.7	1.31	7243	No fading
		Swift	XRT	X	0.3-10keV	122.4	4.98ks	Y	17:26:27.56	−53:11:14.7	5	1.41	7247	Fading, afterglow confirmed. Refined position.
		Swift	UVOT	O	v,u,uvw1, uvm2,uvw2	39.6		N					7245	
		La Silla (Chile)	REM 60cm	NIR	H	69.1		N					7244	
4	080702B	*Swift*	XRT	X	0.3-10keV	62.3	4ks	Y	23:42:15.95	−05:30:50.8	6.3	2.34	7931	Outside BAT circle
		Swift	XRT	X	0.3-10keV	518, 691	7ks	N					7971	Faded; afterglow confirmed
		Swift	UVOT	O	White	62.3	3.7ks	N					7931	
		Las Campanas (Chile)	LCO 100in	O	R	26.9	1.5ks	N					7933	
		La Silla (Chile)	GROND (ESO/MPI 2.2m)	O/NIR	g',r',i',z', J,H,K	115.6	53.6m(g'r'i'z'), 56.0m(JHK)	N					7943	
6	081025	*Swift*	XRT	X	0.3-10keV	74.5	2.9ks	Y	16:21:27.90	+60:28:27.4	6.7	1.99	8411	No fading
		Swift	XRT	X	0.3-10keV	1115	6.9ks	N					8514	Faded; afterglow confirmed
		Swift	UVOT	O	b,u,uvw1, uvm2	74.5	1015s(uvw1), 885s(u), 130s(b), 886s(uvm2)	N					8414	
		TUBITAK (Turkey)	RTT 1.5m	O	sdss-g	41.4	3x300s	N					8418	
		TLS Tautenburg (Germany)	Schmidt 1.34m	O	Ic,Rc		2x120s,2x600s(Ic), 600s(Rc)	N					8420	
7	081203B	*Swift*	XRT	X	0.3-10keV	16.7	1419s	Y	15:15:11.83	+44:25:42.3	1.8	0.40	8605	UVOT-enhanced position. No fading.
		Swift	XRT	X	0.3-10keV	17	3.2ks	Y	15:15:11.83	+44:25:42.3		0.40	8612	Earlier XRT position. Fading with $\alpha = -1.4^{+0.2}_{-0.1}$; afterglow confirmed.
		Swift	UVOT	O	White	16.6	154s,441s	Y	15:15:11.67	+44:25:42.9	0.5	0.39	8606	White=18.29 ± 0.04 (first observation)
		Apache Point (NM)	SDSS 2.5m	O	u,g,r,i,z			N					8607	
		Mt. Terskol (Russia)	Z-600	O	R	42.7	10x90s	Y	15:15:11.66	+44:25:42.7		0.38	8608	
		NRAO (NM)	VLA	R	8.46GHz	183		Y	15:15:11.66	+44:25:42.7		0.38	8625	Z-600 position
		Mt. Terskol (Russia)	Z-600	O	R	132	30x90s	Y	15:15:11.66	+44:25:42.7		0.38	8626	Earlier Z-600 position. R=20.9 ± 0.3
		Gemini-North (HI)	GMOS 8.19m	O	r	264		Y	15:15:11.67	+44:25:42.9		0.39	8631	UVOT position
		Gemini-North (HI)	GMOS 8.19m	O	g,r,i	352		Y	15:15:11.67	+44:25:42.9		0.39	8637	UVOT position. g=22.67 ± 0.11, r=22.41 ± 0.10, i=22.16 ± 0.20
		SAO RAS (Russia)	BTA-6	O	R	305	2x3min	Y	15:15:11.67	+44:25:42.9		0.39	8651	UVOT position. R=21.81 ± 0.10
8	081211B	*Swift*	XRT	X	0.3-10keV	81.6	1878s	Y	11:13:03.49	+53:49:48.1	2.0	1.59	8666	UVOT-enhanced position. Slight fading, no afterglow confirmation.
		Swift	XRT	X	0.3-10keV	690	2.3ks	N					8683	Faded, with $\alpha = 1.6^{+0.9}_{-0.6}$; afterglow confirmed
		Swift	UVOT	O	v,b,uvm2, uvw2,white	81.7	2318s(v),1770s(b), 478s(uvm2), 1426s(uvw2), 1770s(white)	N					8669	
		Mt. Terskol (Russia)	Z-600	O	R	158.1	85x60s	N					8727	

[a] X=X-ray, O=Optical, NIR=Near InfraRed, R=Radio

[b] 90% confidence radii

[c] Offset with respect to BATSS archival position

TABLE 4.6 (continued)
BATSS GRBs — Follow-up observations

#	GRB	Observatory	Instrument	Obs. type[a]	Energy range	Time to observation [ksec]	Exposure	Detected (Y/N)	RA (J2000)	Dec (J2000)	Error radius[b] [arcsec]	BATSS offset[c] [arcmin]	GCN Circulars	Comments
9	090118	*Swift*	XRT	X	0.3-10keV	25.3	6ks	Y	03:19:18.62	+18:24:53.3	7.1	4.38	8828	Just outside BATSS error circle. Slight fading.
		Swift	XRT	X	0.3-10keV	250	10ks	Y	03:19:18.62	+18:24:53.3		4.38	8840	Fading with $\alpha = 0.61 \pm 0.3$ afterglow confirmed.
		Swift	UVOT	O	white	25.3	1292s	N					8827	
		La Silla (Chile)	GROND (ESO/MPI 2.2m)	NIR	J,H,K	39.6	8m	N					8826, 8850	
		KPNO (AZ)	NEWFIRM 4m	IR	J,H	41.8(J), 45.0(H)	40m each	Y[d]	03:19:18.6	+18:24:54.3		4.39	8829	Variability unconfirmed. J=21.0 ± 0.5, H=20.2 ± 0.4
		GGAO (MD)	GRT 14in	O	R	37.8	1170s	N					8830	
		KPNO (AZ)	NEWFIRM 4m	NIR	J	132	80m	Y[d]	03:19:18.6	+18:24:54.3		4.39	8831	Earlier KPNO position. Constant magnitude J=21.4 ± 0.6
		Mauna Kea (HI)	IRCS/Subaru 8.2m	NIR	J	141	18m	Y[d]	03:19:18.6	+18:24:54.3		4.39	8832	Earlier KPNO position. J=21.3
		La Silla (Chile)	GROND (ESO/MPI 2.2m)	O/NIR	g',r',i',z', J,H,K	360		Y[d](g'r'i'z'), N(JHK)	03:19:18.6	+18:24:54.3		4.39	8850	$z < 3.5$. Constant nature confirmed. NOT afterglow but low-z galaxy.
10	090306B	*Swift*	XRT	X	0.3-10keV	67	5.8ks	Y	15:24:49.99	−06:58:05.6	4.0	0.54	8947	No fading
		Swift	XRT	X	0.3-10keV	484	4ks	N					8987	Faded; afterglow confirmed
		La Silla (Chile)	GROND (ESO/MPI 2.2m)	O/NIR	g',r',i',z', J,H,K	106	45m	N					8958	
11	090418B	Haleakala (HI)	Faulkes North 2m	O	i',R	100.4	6x300s	N					9176	
		La Silla (Chile)	GROND (ESO/MPI 2.2m)	O/NIR	g',r',i',z', J,H,K	64.8, 155.1	n/a	N					9178	
		RAS Mayhill (NM)	GRAS002 0.3m	O	unfiltered	68.2	4x600s	N					9181	
		TUBITAK (Turkey)	RTT 1.5m	O	Rc	57.9	3x300s	N					9191	
		TUBITAK (Turkey)	RTT 1.5m	O	Rc	141.5	4x300s	N					9191	
12	090823	*Swift*	XRT	X	0.3-10keV	108	4.7ks	Y	08:34:42.42	+60:39:06.1	5.5	1.49	9840	No fading
		Swift	XRT	X	0.3-10keV	340	9.5ks	Y	08:34:42.42	+60:39:06.1		1.49	9902	Faded w.r.t first observation
		Swift	XRT	X	0.3-10keV	1100	7.5ks	N					9902	Faded; afterglow confirmed
		Swift	UVOT	O	white,v,u	108.4	1464s(white), 1680s(v), 1597s(u)	N					9840	
13	090929A	*Swift*	XRT	X	0.3-10keV	46.8	1.4ks	N					9977	Hot target, short exposure. Upper limit $\sim 3.4 \times 10^{-13}$ erg/cm^2/sec (90%, 1-10 keV) No X-ray afterglow observed
		Swift	UVOT	O	uvm2	47.4	2252s	N					9981	No optical afterglow observed
16	110107A	*Swift*	XRT	X	0.3-10keV	64.8	2517s	Y	19:59:38.20	+41:54:50.3	3.6	1.38	11547	UVOT-enhanced position. Not fading
		Swift	XRT	X	0.3-10keV	420.7	2.1ks	N					11565	Faded with $\alpha > 0.4$; afterglow confirmed
		Swift	UVOT	O	v,u	64.4	2247s(v), 1638s(u)	N					11551	
17	110319B	*Swift*	XRT	X	0.3-10keV	27.7	4.9ks	Y	21:44:22.77	−56:46:56.6	2.4	0.81	11814	UVOT-enhanced position. Not fading
		Swift	XRT	X	0.3-10keV	340	4.9ks	N					11820	Faded with $\alpha > 0.6$; afterglow confirmed
		Swift	UVOT	O	white,v,u	27.7	1570s(white), 1678s(v), 1597s(u)	N					11817	
		La Silla (Chile)	GROND (ESO/MPI 2.2m)	O/NIR	g',r',i',z', J,H,K	46.4	25m(g'r'i'z'), 20m(JHK)	N					11815	

[a] X=X-ray, O=Optical, NIR=Near InfraRed, R=Radio
[b] 90% confidence radii
[c] Offset with respect to BATSS archival position
[d] Candidate afterglow detection, later rejected

Table 4.6 References: Starling & Stamatikos (2008, GCN 7243); Starling et al. (2008, GCN 7247); Schady & Stamatikos (2008, GCN 7245); D'Avanzo et al. (2008, GCN 7244); Evans et al. (2008, GCN 7931); Evans & Pasquale (2008, GCN 7971); Berger & Madore (2008, GCN 7933); Clemens et al. (2008, GCN 7943); Mao et al. (2008, GCN 8411); Mao (2008, GCN 8514); Schady & Mao (2008, GCN 8414); Khamitov et al. (2008, GCN 8418); Kann et al. (2008, GCN 8420); Sbarufatti et al. (2008a, GCN 8605); Sbarufatti et al. (2008b, GCN 8612); Schady et al. (2008, GCN 8606); Berger (2008, GCN 8607); Andreev et al. (2008a, GCN 8608); Chandra & Frail (2008, GCN 8625); Andreev et al. (2008b, GCN 8626); Perley & Bloom (2008, GCN 8631); Perley (2008, GCN 8637); Fatkhullin et al. (2008, GCN 8651); Page et al. (2008a, GCN 8666); Page et al. (2008b, GCN 8683); Holland (2008, GCN 8669); Andreev et al. (2008c, GCN 8727); Rowlinson & Page (2009a, GCN 8828); Rowlinson & Page (2009b, GCN 8840); Schady (2009, GCN 8827); Olivares et al. (2009, GCN 8826); Rossi et al. (2009, GCN 8850); Updike & Hartmann (2009b, GCN 8829); Sakamoto et al. (2009a, GCN 8830); Updike & Hartmann (2009a, GCN 8831); Rossi et al. (2009, GCN 8850); Minowa et al. (2009, GCN 8832); Evans (2009b, GCN 8947); Evans (2009a, GCN 8987); Updike et al. (2009, GCN 8958); Guidorzi et al. (2009, GCN 9176); Afonso et al. (2009, GCN 9178); Nissinen & Hentunen (2009, GCN 9181); Bikmaev et al. (2009, GCN 9191); Grupe et al. (2009, GCN 9840); Page (2009, GCN 9977); Grupe (2009, GCN 9902); Siegel & Page (2009, GCN 9981); Stratta et al. (2011, GCN 11547); Stratta (2011, GCN 11565); Immler & Stratta (2011, GCN 11551); Sbarufatti (2011a, GCN 11814); Sbarufatti (2011b, GCN 11820); Marshall & Sbarufatti (2011, GCN 11817); Updike et al. (2011, GCN 11815).

GCN Report References for Tables 4.4, 4.5 and 4.6: De Pasquale et al. (2008, GRB 080702B); Mao et al. (2008, GRB 081025); Holland et al. (2008, GRB 081211B); Evans et al. (2009, GRB 090306B); Grupe et al. (2009, GRB 090823); Stratta et al. (2011, GRB 110107A).

4.4.2 Locations, significances and error radii

For this section, we expand the BATSS GRB sample to include all *Swift* GRBs detected by BATSS over the 4.8-year period reported here[19], not only those that were only detected in slew data and listed in Section 4.4.1. This larger sample allows us to take a broader view of the empirical evidence these detections provide in light of the discussion of the predicted characteristics of the BATSS survey that were studied in Chapter 2.

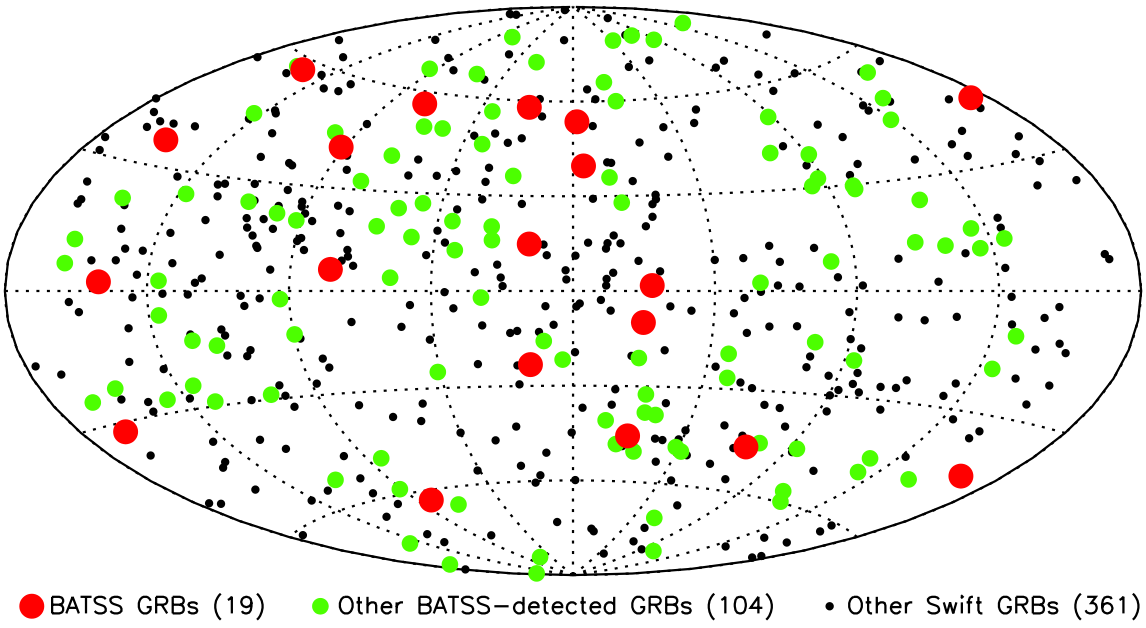

FIGURE 4.7: Sky map in Galactic coordinates of *Swift* GRBs over the 4.8-year period of the BATSS survey reported here. All BATSS-detected GRBs are shown, including those that had been detected in pointing mode as well. All other *Swift* GRBs over this period that were not detected by BATSS are displayed as well.

Figure 4.7 shows the sky distribution of all *Swift* GRBs over the survey period. In total, there were 484 GRBs detected after combining results from all modes of operation, and including both on-board and ground detections. Of those, 123 were detected by BATSS

[19]The survey period includes the 03/01/07–03/31/07 testing phase as well as the 10/25/07–07/07/12 period of full implementation.

above the S/N thresholds required to issue a GRB trigger (Section 3.9). Most of those detections were made on the Automated Target (AT) slew that immediately followed an on-board detection, however, so the seemingly large number of total BATSS GRB detections, especially when considering the large differences in total BAT instrument exposure in slew vs. pointing mode (4.7 Msec vs. 113 Msec, respectively) should not be regarded as a direct measure of the relative sensitivity in the two modes of operation.[20] The subject of GRB detection rates and their use as a proxy for measurements of BAT instrument sensitivity requires a separate discussion as is examined at length in Sections 4.5 and 4.6. Lastly, within the total sample of 123 BATSS-detected GRBs, shown in Figure 4.7 are the 19 GRBs that were found only in slew data and tabulated in Section 4.4.1.

In terms of the general distribution of BATSS GRBs across the sky, they generally follow the same isotropic distribution of the entire *Swift* GRB sample, a distribution first observed in BATSE and regarded as the first evidence of the extragalactic origin of GRBs (Hakkila et al. 1994). One noteworthy location, however, is that of the unconfirmed BATSS GRB 111011A, located in the Galactic bulge at longitude $l = 334°53'17''$ and latitude $b = 1°43'04''$ (error radius $2.3'$, 90% confidence), just above the Galactic plane. In addition, as will be discussed in Section 4.4.6, its soft spectrum makes it an X-ray flash (XRF) candidate, or possibly also an X-ray burst, and our characterization of this burst will continue in that section.

A significant number of the 123 BATSS-detected GRBs have confirmed counterpart X-ray afterglows, detected by *Swift*-XRT at arcsecond-level precision. This allows us to

[20] In fact, given that most on-board detections trigger an AT slew immediately afterwards, it could also have been expected to the contrary that most on-board detections would also have a corresponding slew detection. The fact that this is not the case either, demonstrates that the prompt γ-ray emission from most GRBs has either significantly faded by the time the slew maneuver begins, or that AT slews are not possible in a significant number of cases, typically due to observing constraints that prevent the spacecraft from slewing immediately to the target.

make an absolute assessment of the accuracy of BATSS GRB locations, and contrast them against analogous detections made in pointing mode, either immediately before or after the BATSS slew.

For the most accurate summary to date of pointing-mode BAT GRB locations, we rely on the results of the Second *Swift*-BAT GRB Catalog (BAT2 catalog, Sakamoto et al. 2011), for which the BAT data on 476 GRBs between 12/19/04–12/21/09 have been reanalyzed and refined. Within that period, a total of 68 GRBs were detected by BATSS (with 13 of them detected only during slews), and of those, 51 were found to have confirmed XRT arcsecond positions as well BAT pointing-mode positions. Figure 4.8 shows the offsets from the XRT positions of these 51 GRBs, in absolute units of arcminutes, for the BATSS detections vs. the refined positions in the BAT2 (pointing) catalog. The figure includes the error radii (90% confidence) as reported by both surveys and represented by the error bars, which already show a good degree of accuracy, having only 2 out of 51 XRT detections in each case falling just outside the BAT error circle (indicated by red error bars), a better result in both cases than the 90% confidence prediction, even though error radii in each case have been calibrated differently. At the same time, the BATSS survey has obtained a more accurate measure of the GRB location in only 13 out of 51 cases. This cannot be taken as an absolute measure of survey performance, however, since this result can be explained by the systematic fact that the slew detection almost always follows the pointing detection, and therefore the slew image is likely to have a smaller S/N ratio as the GRB prompt emission has already begun to fade at the time of the slew, sometimes significantly as evidenced by the low absolute number of BATSS GRB detections during the AT slews following the on-board detection.

To take into account the differences in location accuracy as a consequence of detection S/N, in Figure 4.9 we show the same set of offsets as in Figure 4.8, but this time in relative

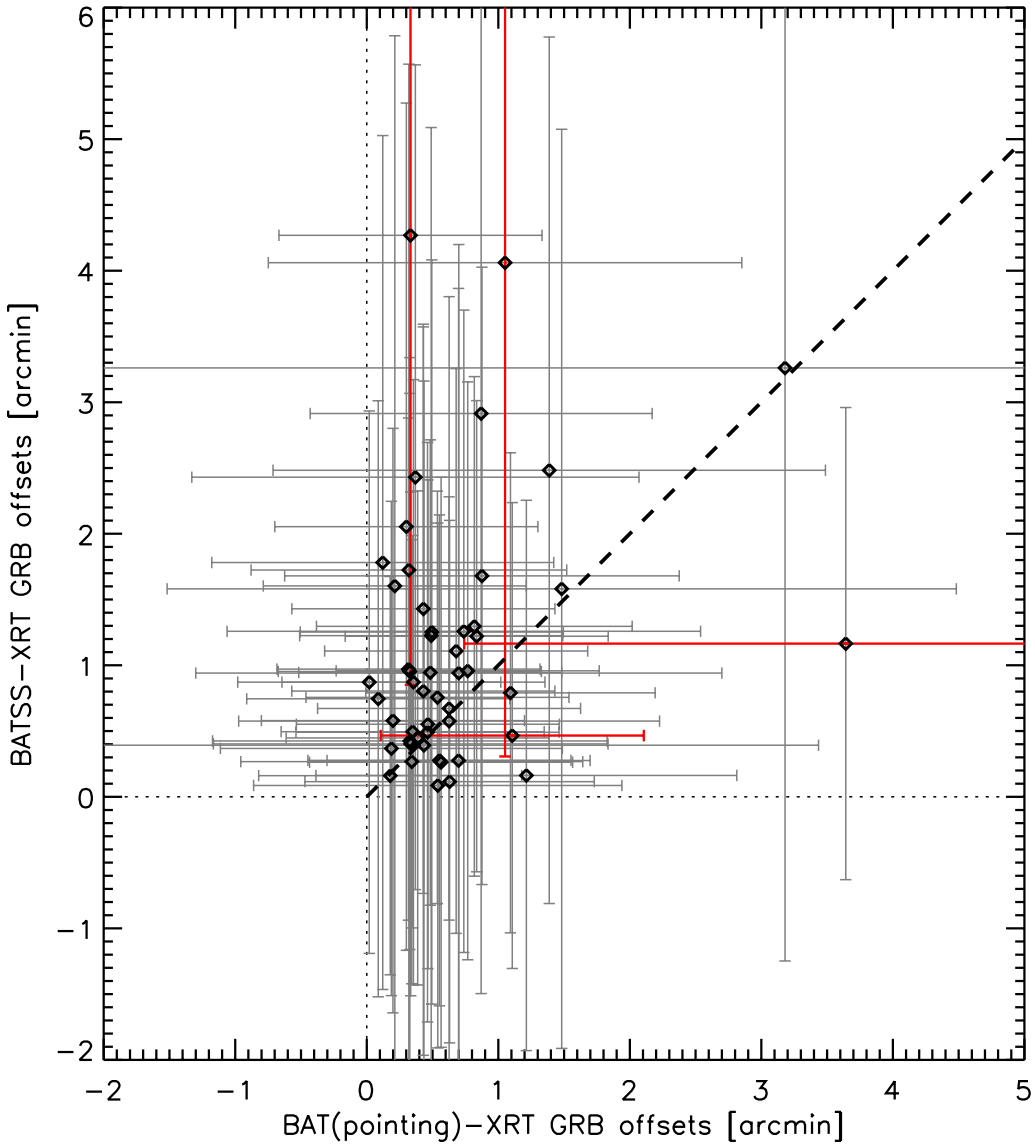

FIGURE 4.8: Absolute offsets [arcmin] of *Swift*-BAT GRBs with respect to *Swift*-XRT positions, for slew (BATSS) data vs. BAT pointing data. Data sample consists of 51 GRBs with independently derived positions from BAT pointing, BAT slew and XRT data. BAT pointing positions are drawn from the refined positions of the BAT2 GRB catalog (Sakamoto et al. 2011). Error bars for both pointings and slews are 90% confidence error radii. In both cases, error bars of BAT positions where the XRT afterglow was found outside 90% error circle are highlighted in red.

terms as a percentage of the reported 90% confidence error radii r_{90}, using the notation of Section 2.4.4. The side panels of this figure have the pointing and slew results histogrammed separately, showing a large degree of agreement between the two distributions: each has 2 XRT detections falling outside the BAT r_{90} error radius, though in each case within 130% of r_{90}; the distributions both peak just below 50% of r_{90}, with most detections contained within 80%, or even all of them in the case of BATSS except for the 2 outliers. In addition, a Kolmogorov-Smirnov (K-S) test of the two observed distributions reveals a 69% probability that they are drawn from the same parent distribution. The broad similarities between the two distributions of relative offsets, despite significantly different calibration models for the error radii themselves as will be shown next in Figure 4.10, allow us to conclude that quoted pointing and slew r_{90} values are indeed equivalent in a statistical sense, and provide empirical confirmation of the validity of the BATSS model of source position uncertainties presented in Section 2.4.4.

To make the connection between the error radii and the GRB S/N ratios in the BAT images, we plotted the corresponding $r_{90}(S/N)$ empirical relations in Figure 4.10, along with the particular distributions of S/N for the 51 GRBs in Figures 4.8 and 4.9. The data points from the pointing and slew GRB surveys were superimposed on the models they were derived from. For pointing data, the model used by Sakamoto et al. (2011) is a smoothly broken power law:

$$r_{90\%,\mathrm{point}}(S/N) = \begin{cases} 10.'92 \cdot (S/N)^{-0.7} & \text{if } S/N \leq 10.92^{\frac{1}{0.7}} = 30.42 \\ 1' & \text{if } S/N > 30.42 \end{cases} \tag{4.10}$$

where they have set the minimum systematic error at $1'$ due to limitations in the knowledge of the BAT PSF. For slew data, it is derived from our 4-parameter model of equation 2.14,

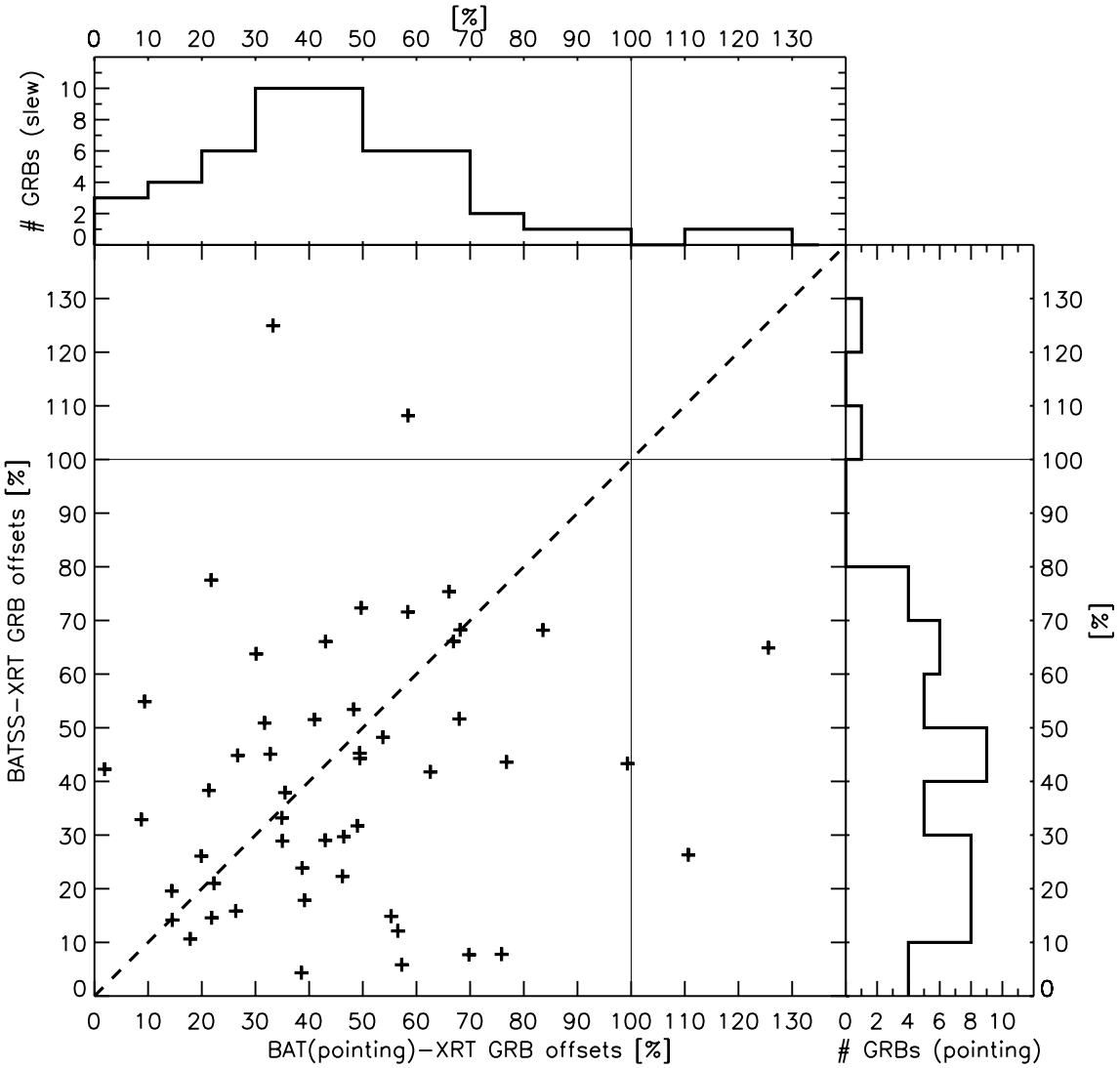

FIGURE 4.9: Relative offsets as a percentage of BAT error radius (90% confidence) for the same sample of 51 GRBs with XRT positions of Figure 4.8, for BAT slew vs. pointing observations. The results for each mode of observation are also histogrammed separately, showing a large degree of agreement in the accuracy of positions reported by both BAT GRB surveys.

with the parameters given in Table 2.2 for 90% error radii:

$$r_{90\%,\mathrm{slew}}(S/N) = \sqrt{(1.'40)^2 + \left[4.'23\left(\frac{6.0-2.2}{S/N-2.2}\right)^{0.51}\right]^2} \tag{4.11}$$

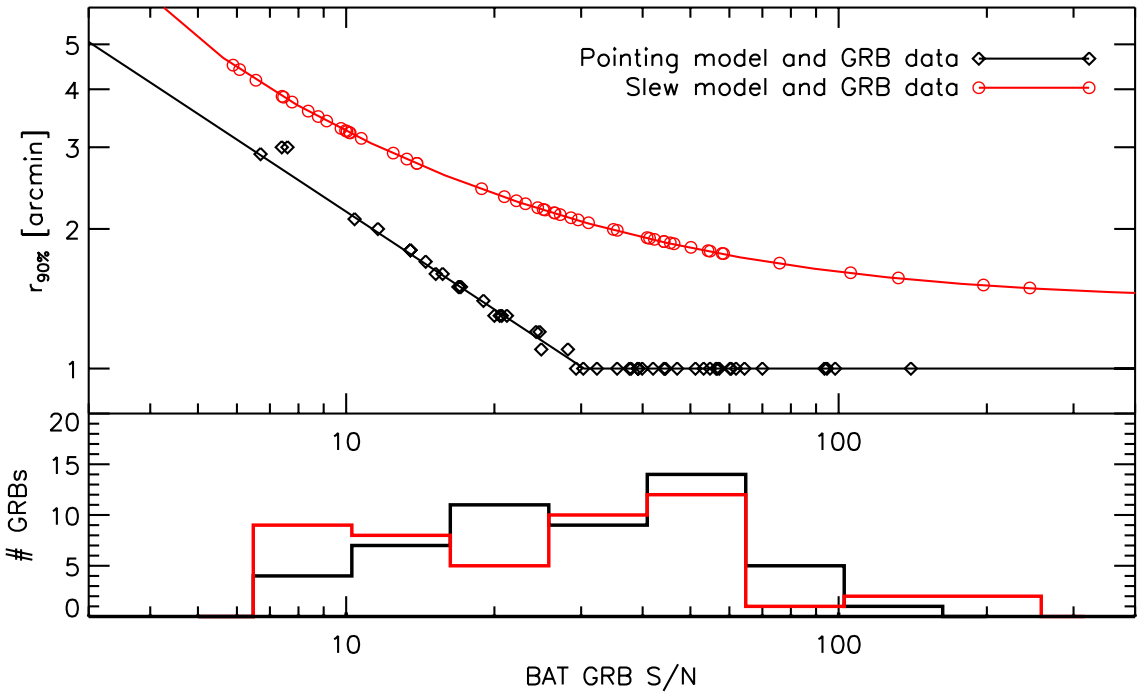

FIGURE 4.10: Top panel: 90% error radii as a function of source S/N for sample of 51 BAT GRBs, drawn from empirical relations derived separately for the BAT pointing and slew GRB surveys (equations 4.10 and 4.11). Bottom panel: log-normal distribution of S/N ratios for this sample.

Though Figure 4.10 and equations 4.10 and 4.11 make it evident that BATSS source locations are characterized by a larger degree of uncertainty than BAT pointing locations for images of equal source S/N, the important result is the fact illustrated by Figure 4.9 that BATSS 90% error radii preserve their meaning in a statistical sense and can be regarded as a reliable measure of the uncertainty of positions reported by BATSS, however large they may be. The possible ways of reducing source position uncertainty in a future implementation

of BATSS and in future slewing coded aperture missions are discussed in the Conclusions section of this work (Chapter 5).

4.4.3 Durations

Restricting the GRBs sample back to the 19 BATSS GRBs itemized in Section 4.4.1, we show the distribution of T_{90} and T_{50} intervals in Figure 4.11, and compare it to the distribution of 451 GRBs in the BAT2 catalog (Sakamoto et al. 2011) for which a measurement of those two parameters was made.[21] Ever since the finding of a bimodal distribution of GRB durations from the Burst and Transient Source Experiment (BATSE), as reported by e.g. Kouveliotou et al. (1993), GRBs have been classified in two broad categories according to their duration: long GRBs (L-GRBs), with a total duration of $T_{90} \geq 2$ sec and predominantly softer spectra, and short GRBs (S-GRBs), with $T_{90} < 2$ sec and predominantly harder spectra. In addition, a third category of so-called short GRBs with extended emission (S-GRBs with EE) has been proposed (Norris et al. 2000), which are characterized by a short, hard spike just as S-GRBs, but then followed by a long ($\gtrsim 10$ sec), softer extended γ-ray emission component (Norris et al. 2010). The proportions of the three types of GRBs in the BAT2 catalog are 89% (424) for L-GRBs, 8% (38) for S-GRBs, and 2% (10) for S-GRBs with EE, with a further 1% (4) of GRBs with incomplete data and unknown classification.

From Figure 4.11a, it is evident that most if not all of the 19 BATSS GRBs fall within the L-GRB category, since T_{90} or its lower limit for all of them is clearly above the 2-sec S-GRB/L-GRB classification threshold. This places them well within the bulk of both the T_{90} and T_{50} BAT2 distributions, though with a "hard" temporal upper limit corresponding

[21] BAT2 GRB durations are reported for the 15–350 keV band, however, whereas BATSS durations are obtained from 15–150 keV lightcurves.

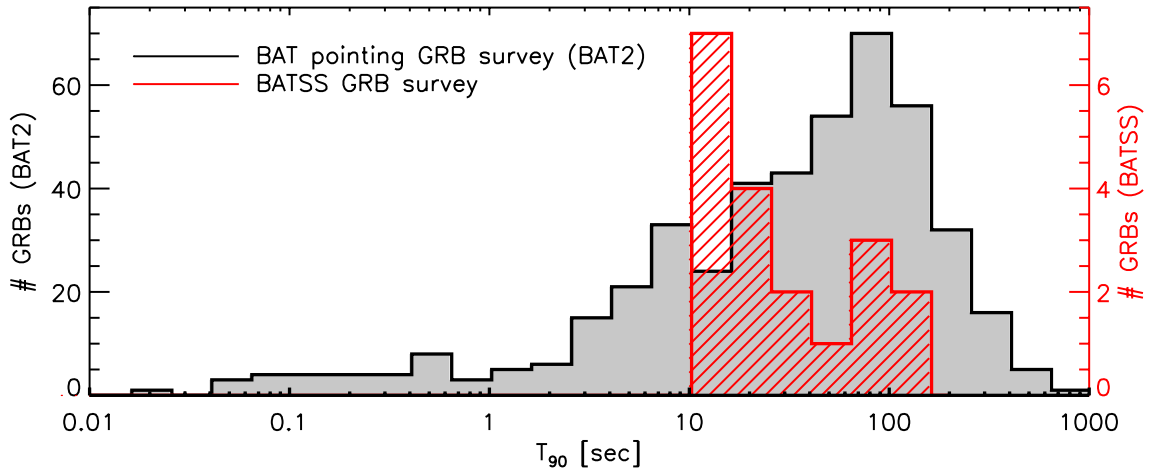

(a)

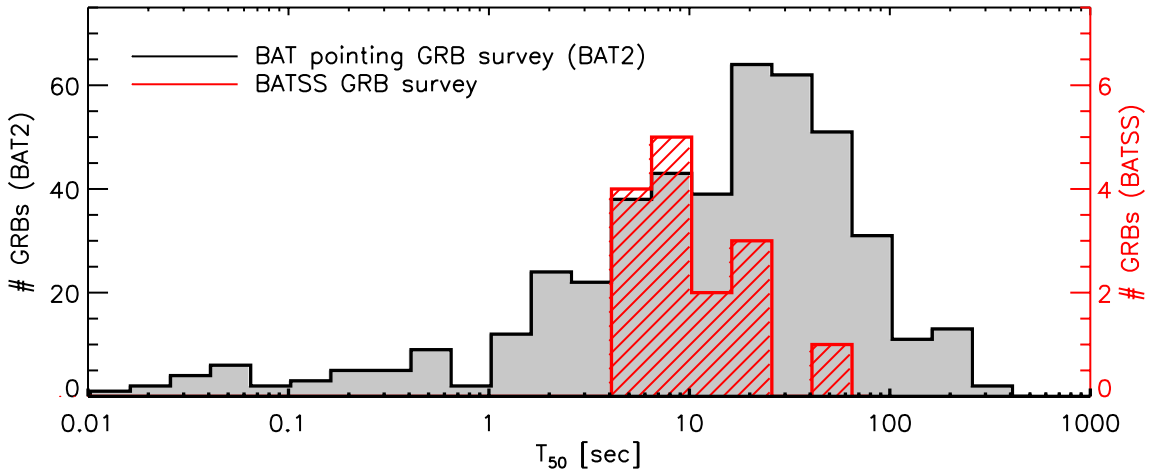

(b)

FIGURE 4.11: Distributions of GRB durations for the BAT2 survey (Sakamoto et al. 2011, left axis scale, 451 GRBs) and BATSS (right axis, scaled at 1/10 of the BAT2 axis). (a)T_{90}, including 19 BATSS GRBs, 4 of them with only lower limits; (b)T_{50}, including 15 BATSS GRBs for which a measurement was possible, 1 of them with only a lower limit.

to the 120 sec of data collection per slew that was imposed by *Swift* mission operations during the course of most of the survey, as well as a "soft" upper limit imposed by the unsteady observation of particular sky locations that is intrinsic to slews. These constraints on time and spatial coverage would be responsible for systematically skewing the BATSS GRB duration sample towards lower durations within the L-GRB category, and are likely to be primarily responsible for the result from a K-S test that the T_{90} and T_{50} distributions of the two GRB populations are only 8% and 3% likely to have been drawn from the same parent distribution, respectively. BATSS S-GRBs, if any, would be largely unaffected by these same constraints, since both limits on BATSS observations are considerably above the 2-sec GRB classification threshold.

One noteworthy possible exception within BATSS GRBs to this classification, however, is provided by GRB 081211B. When first detected by BATSS (Copete et al. 2008d), we reported that its lightcurve data suggested "the tail end of the prompt emission of a burst at that location." Shortly afterwards, the *Konus-Wind* team confirmed the simultaneous observation of the GRB's prompt emission (20–70 keV and 70-300 keV bands, Golenetskii et al. 2008a), with a 2.7-sec spike observed ∼120-sec before the reported BATSS trigger time,[22] followed by a hint of extended emission, and their lightcurve data is shown in Figure 4.12.

The combination of results from both BATSS and *Konus-Wind* then allowed Golenetskii et al. (2008a) to suggest that GRB 081211B may be classified as a S-GRB with EE, which would make it only the 11th such GRB within the BAT2 catalog. In the following subsections we will be examining this hypothesis by comparing the BATSS data from

[22]After the reanalysis of BATSS data from the *Swift* archive, we find the time gap between the *Konus-Wind* trigger of the short precursor to GRB 081211B and the beginning of BATSS observation of extended emission above the 20% partial coding threshold to be 137.9 sec, which added to the 103.5 sec of continous emission during the BATSS observation, suggest a duration of the EE component of over 240 sec. This would place it in the $\gtrsim$ 90% percentile in T_{90} of BAT2 L-GRBs.

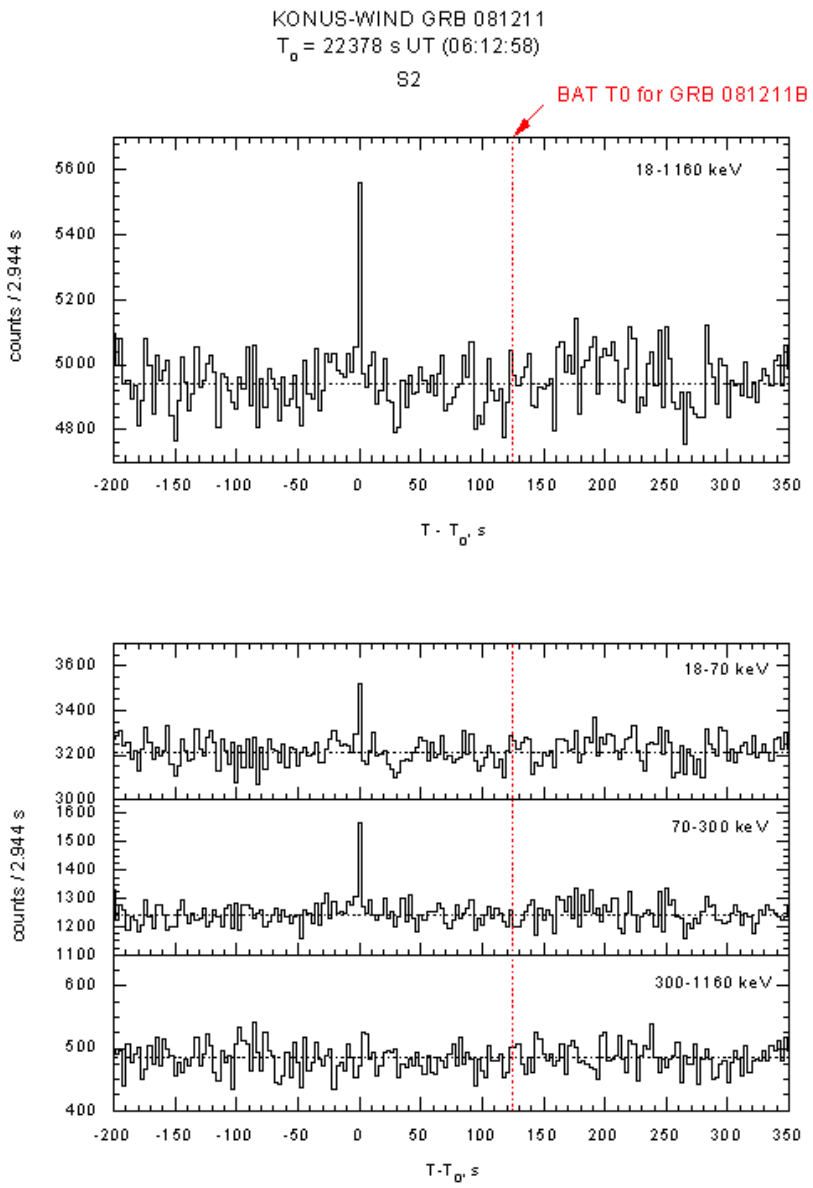

FIGURE 4.12: *Konus-Wind* lightcurves of the prompt emission from BATSS GRB 081211B (Golenetskii et al. 2008a). The short spike they find in the 18–70 keV and 70–300 keV energy bands, combined with the BATSS report by Copete et al. (2008d) of γ-ray emission after the source simultaneously enters the BAT FoV at the 15% partial coding threshold (red line), suggest the finding of a possible short GRB with extended emission (S-GRB with EE), beyond the 10 (2% of all GRBs) reported in the BAT2 catalog (Sakamoto et al. 2011).

the alleged extended emission from GRB 081211B with the spectral characteristics of the extended emission from the 10 BAT2 catalog GRBs in that category.

Regarding the general lack of S-GRBs in the BATSS sample, it is in keeping with a similar result for the overall BAT GRB population, as can be seen in Figure 4.11, where the distribution of T_{90} durations does not show the same evident bimodality as in the case of BATSE (Kouveliotou et al. 1993). This is explained by Sakamoto et al. (2011) as being driven by the fact that, unlike BATSE, the BAT is primarily an imaging instrument, and it therefore requires a larger number of photons in order to image a source at a large enough S/N level, a high threshold for the faint and short emission that is characteristic of S-GRBs. Other imaging instruments such as the *High Energy Transient Explorer 2* (*HETE-2*) or *BeppoSAX* have found a similarly low number of S-GRBs (Frontera et al. 2009; Pélangeon et al. 2008). However, the large effective area and sophisticated flight software of the BAT have allowed it to detect S-GRBs at a much higher rate than other imaging instruments (Sakamoto et al. 2011).

In the case of BATSS, it is similarly affected in its ability to detect S-GRBs by the limitations associated with being an imaging survey. However, as will be discussed in the conclusions of this dissertation (Chapter 5), we have not yet fully exploited its potential to produce finely time-resolved slew images, given that unlike in pointing mode, BATSS imaging is done using photon-by-photon ("event") data. The fact that only one image is produced per slew in each of 3 energy bands would particularly affect the detection of S-GRBs, since the integration time of the images is usually much larger than the $T_{90} < 2$ sec threshold that is used to classify BAT GRBs as S-GRBs. Hence, the significant detection that could be made in a time-resolved image drops instead below the S/N threshold when accompanied by the image background from a much larger time window.

4.4.4 Hardness

Spectral hardness is another characteristic than distinguishes S-GRBs and L-GRBs, with the latter having generally a softer spectrum (Kouveliotou et al. 1993). Figure 4.13 compares the hardness of BATSS GRBs to those in the BAT2 pointing GRB catalog (Sakamoto et al. 2011) as a function of T_{90}, with hardness defined here as the ratio of the time-averaged energy fluences in the BATSS Hard (50–150 keV) and Soft (15–50 keV) energy bands.[23] The 10 BAT2 S-GRBs with EE have been highlighted and also included in the inset plot, along with GRB 081211B, a BATSS GRBs which has been proposed to belong to this category, as discussed in Section 4.4.3.

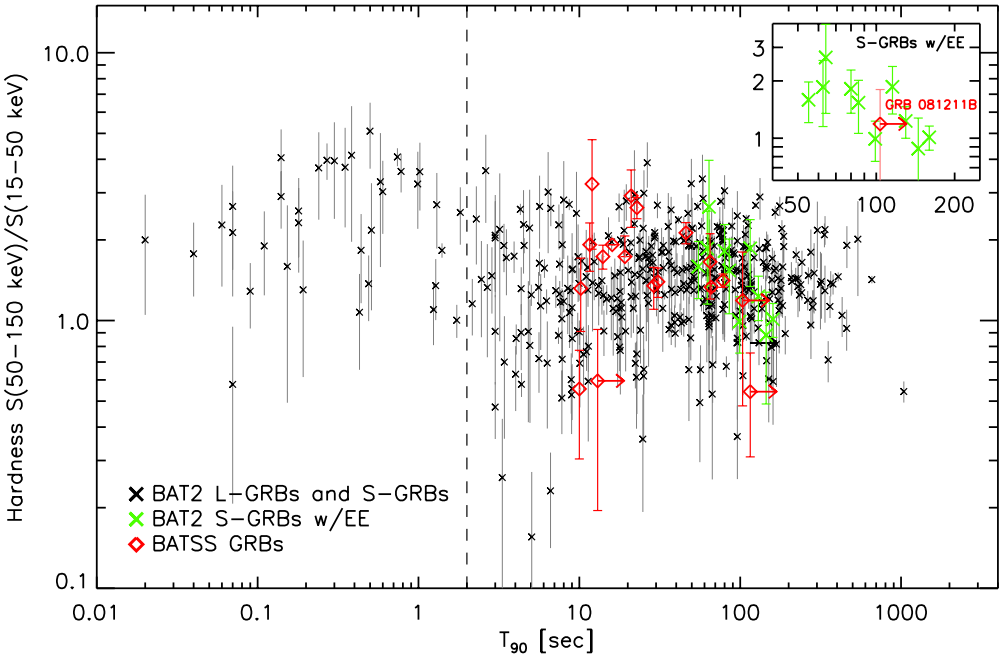

FIGURE 4.13: Spectral hardness of BATSS GRBs and BAT2 (pointing) GRBs vs. T_{90}. The dashed line separates S-GRBs (left) from L-GRBs (right). S-GRBs with extended emission are highlighted in green and also included in the inset, along with the proposed BATSS GRB in this category, GRB 081211B.

[23]BATSS fluences are calculated from the portion of the burst within the slew observation only

The hardnesses of different categories of GRBs are histogrammed separately in Figure 4.14. Though there is a large degree of overlap among all categories, BATSS GRBs are seen to fit most closely within the hardness of other L-GRBs, with a K-S probability of 48% of being drawn from the same parent distribution as the BAT2 L-GRBs, compared to 3% for BAT2 S-GRBs. As for the S-GRBs with EE, their extended emission component has been found to be most similar to L-GRBs, and both Figures 4.13 and 4.14 show the hardness of the BATSS-detected emission of GRB 081211B to lie squarely within that of the 10 BAT2 GRBs in this category. Given the overlap with L-GRBs, however, we are not able to conclusively assert through this method whether GRB 081211B is indeed an S-GRB with EE.

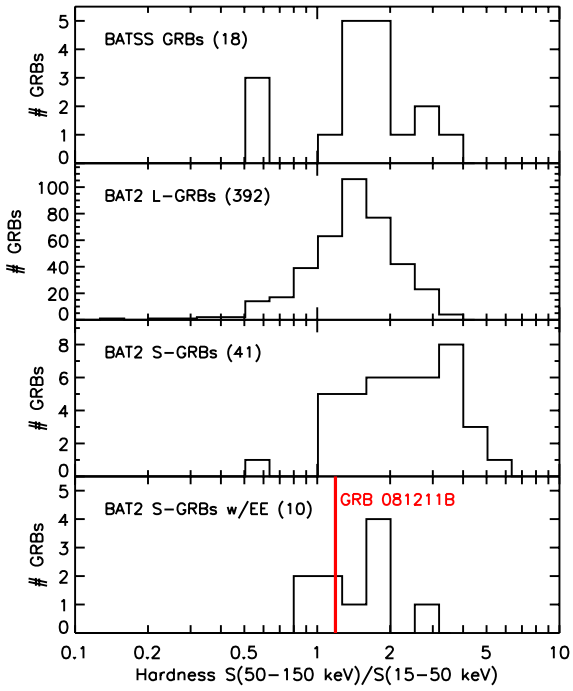

FIGURE 4.14: Distributions of spectral hardnesses in each of the GRB categories in Figure 4.13. BATSS GRBs are consistent with BAT2 L-GRBs in this measure, but 3 of them (GRB 071212, 090823, 111011A) are considerably below the mean BAT2 GRB hardness. GRB 081211B is consistent in hardness with BAT2 S-GRBs with extended emission.

Another set of BATSS GRBs does stand out in this measure, namely GRBs 071212, 090823, and 111011A. All three have a hardness in the range 0.5–0.6, considerably less than the 1.50 average for BAT2 L-GRBs, which puts them within the bottom 4% of that

population. GRB 111011A is an unconfirmed GRB occurring just above the Galactic plane; combined with the softness of its spectrum, it may be classified as either an X-ray burst or an X-ray flash (XRF).

4.4.5 Peak fluxes and fluences

The 1-sec peak flux F_{1s}^{p}(15–150 keV) and the fluence S(15–150 keV) of GRBs in the BAT2 catalogs were found by Sakamoto et al. (2008, 2011) to be positively correlated. Likewise, as illustrated in Figure 4.15, BATSS GRBs are also found to conform to such correlation over a narrow band. Also, it can be seen that BAT2 S-GRBs are localized at the higher end of this correlation; though they occupy the lower end of the BAT2 GRB fluence distribution, a larger number of photons is required in order to detect them. This is likely due to instrument selection effects, as mentioned in Section 4.4.3, which require a minimum number of photons in order to trigger detection of S-GRBs in an imaging instrument such as *Swift*-BAT, and also represent a constraint on the detection of S-GRBs by BATSS.

Reducing the BAT2 sample to the same L-GRB category of BATSS GRBs, the bottom panel of Figure 4.15 shows the log-normal distribution of fluences (15–150 keV) of the two GRB populations. The ranges of fluences are generally consistent with each other, and a K-S test gives a 45% probability that they were drawn from the same parent distribution. The lowest-fluence BATSS GRB, GRB 090823, has S(15–150 keV) = $1.18^{+0.61}_{-0.65} \times 10^{-7}$ erg/cm^2,[24] and was detected at $S/N = 7.8$ in this energy band. This places it at the bottom 2% of all BAT2 L-GRBs, which confirms BATSS' capability to detect L-GRBs at the faint end of the fluence distribution accessible to *Swift*-BAT.

[24]BATSS fluence recorded over the 13.0-sec exposure of the burst during the slew.

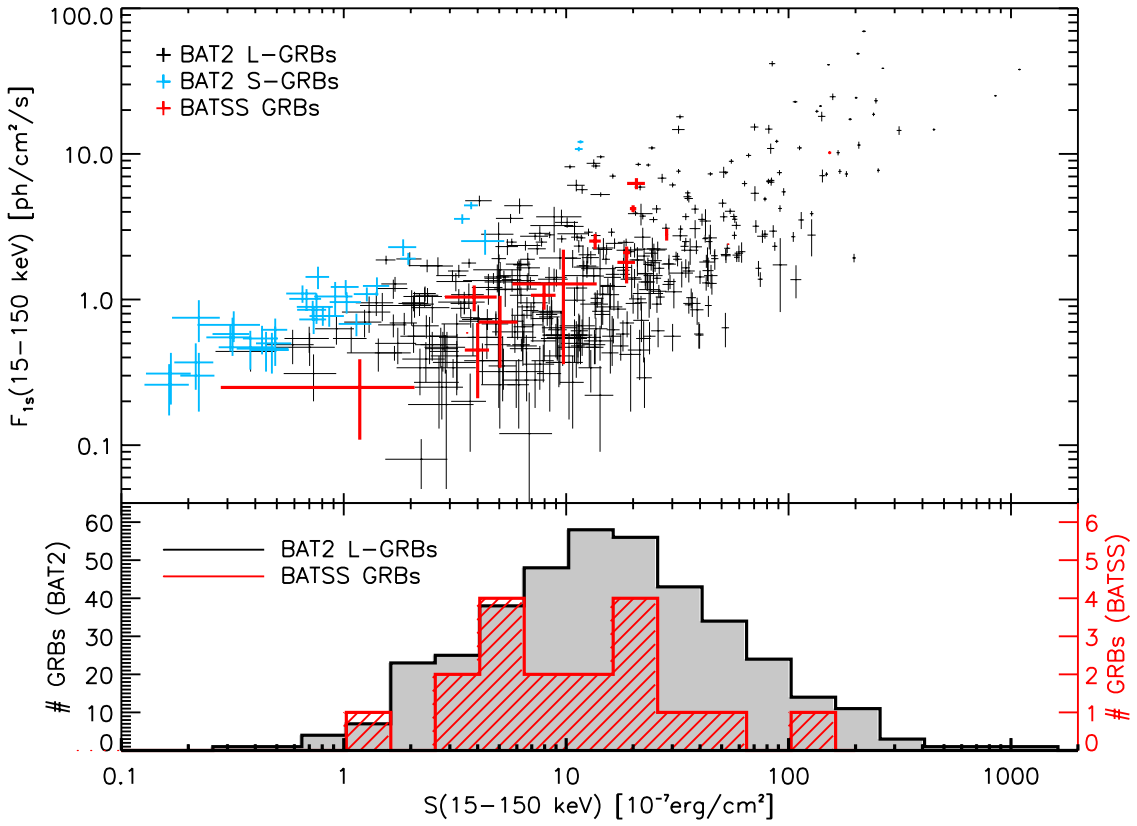

FIGURE 4.15: Top panel: Scatter plot of 1-sec peak photon flux F_{1s}^{p} vs. fluence S in the 15–150 keV energy band, for GRBs in the BAT2 catalog (Sakamoto et al. 2011) as well as BATSS. A similar correlation is found for BATSS GRBs as for BAT2 L-GRBs, with only BAT2 S-GRBs lying at the higher end of the correlation. Bottom panel: log-normal distributions of fluences for BATSS GRBs (right axis) and BAT2 L-GRBs (left axis).

4.4.6 Photon index and $E_{\mathbf{peak}}$

As discussed in Section 4.3.3, partly because of a narrow instrument energy range, BAT GRB spectra are typically best fit to either a 2-paramater simple power law (PL, equation 4.1), or a 3-parameter power law with an exponential cutoff (CPL, equation 4.2); the latter is deemed to be the best fit whenever it improves the χ^2 statistic of the fit by $\Delta\chi^2 \equiv \chi^2_{\rm PL} - \chi^2_{\rm CPL} > 6$. With this criterion, implemented for BATSS just as it was for the BAT2 (pointing) catalog, the time-averaged spectra of as many as 83% of BAT2 GRBs are found to be best fit by a PL model (Sakamoto et al. 2011). Similarly, out of 18 BATSS GRBs where spectral fits were made,[25] 16 of them (89%) were best fit to a PL model, with the remaining 2 fitted to a CPL model.

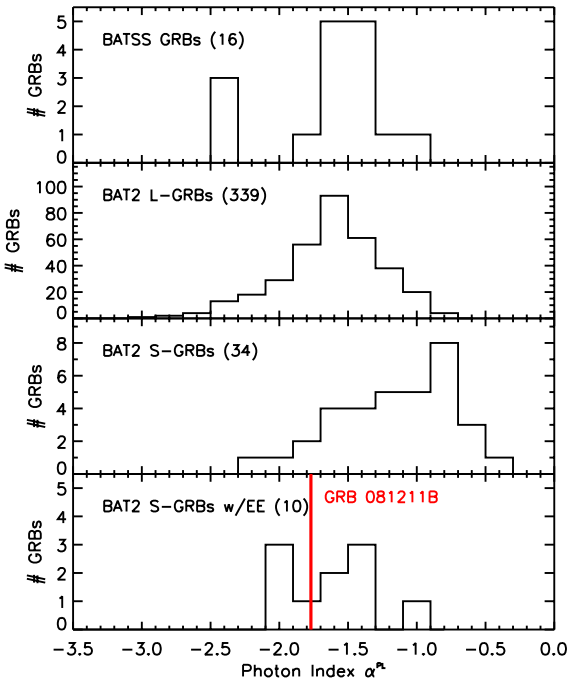

FIGURE 4.16: Distributions of photon indices $\alpha^{\rm PL}$ for GRBs best fitted by a simple power law (PL) spectral model, for BATSS GRBs as well as 3 categories of BAT2 catalog GRBs. BATSS GRBs are most consistent with the spectral indices of BAT2 L-GRBs, with a softer spectrum than BAT2 S-GRBs. Also, $\alpha^{\rm PL}$ for GRB 081211B is consistent with that of BAT2 S-GRBs with extended emission.

[25] GRB 110906A, a burst found at the edge of the BAT slew FoV (mean coding fraction 23.5%), and only 13.8-sec exposure, is the only BATSS GRB were a spectral fit with XSPEC was not possible.

Figure 4.16 shows the distributions in the photon index $\alpha^{\rm PL}$ of BATSS as well as BAT2 GRBs that were best fit to a PL model, with separate histograms of the three BAT2 GRB populations: L-GRBs, S-GRBs and S-GRBs with EE. As in the case of spectral hardness, the PL photon index of BATSS GRBs best fits the softer BAT2 L-GRB population, with a K-S probability of 85% of being drawn from the same parent distribution, compared to only 0.1% for the harder BAT2 S-GRBs. Also, the PL photon index of GRB 081211B, $\alpha^{\rm PL} = -1.77^{+0.45}_{-0.52}$ fits well within the range of spectral indices of BAT2 S-GRBs with EE. In general, spectra fit to a PL model yield a photon index $\alpha^{\rm PL}$ that is steeper than the low-energy photon index $\alpha \sim -1$ but shallower than the high-energy photon index $\beta \sim -2.5$ that characterize the time-averaged prompt emission of GRBs that are fitted to the 4-parameter Band model (Kaneko et al. 2006).

As for GRB spectra best fit to a CPL model, the $E_{\rm peak}$ and $\alpha^{\rm CPL}$ resulting from the fit are plotted against each other in Figure 4.17. The 2 BATSS GRBs that were fit to this model (GRB 080806 and GRB 090306) are included in the figure, as well the results from Sakamoto et al. (2011) of CPL fits to 68 L-GRBs and 5 S-GRBs from the BAT2 catalog; these results show again that BATSS GRBs lie well within the BAT2 L-GRB population.

Also as discussed in Section 4.3.3, since $E_{\rm peak}$ is a physical parameter for every GRB corresponding to the peak of its νF_ν spectrum, GRBs fitted to a PL model should also have an $E_{\rm peak}$ value even though the model does not define it. Based on the results of a spectral simulation by Sakamoto et al. (2009b), where they find a correlation between $\alpha^{\rm PL}$ and the Band model $E_{\rm peak}$ parameter, in Figure 4.17 we also include the $E_{\rm peak}$ estimates and photon indices of the 16 BATSS GRBs that were fitted to a PL model. Equation 4.4 gives the $E_{\rm peak}$–$\alpha^{\rm PL}$ relation the estimates are derived from, and the error bars are given by the total uncertainty $\sigma^2_{E_{\rm p}} = \sigma^2_{E_{\rm p},{\rm model}} + \sigma^2_{E_{\rm p},\alpha}$, with $\sigma_{E_{\rm p},{\rm model}}$ and $\sigma_{E_{\rm p},\alpha}$ given by equations 4.7 and 4.8, respectively. The estimation is only valid over the dynamic range $-2.3 \geq \alpha^{\rm PL} \geq -1.3$,

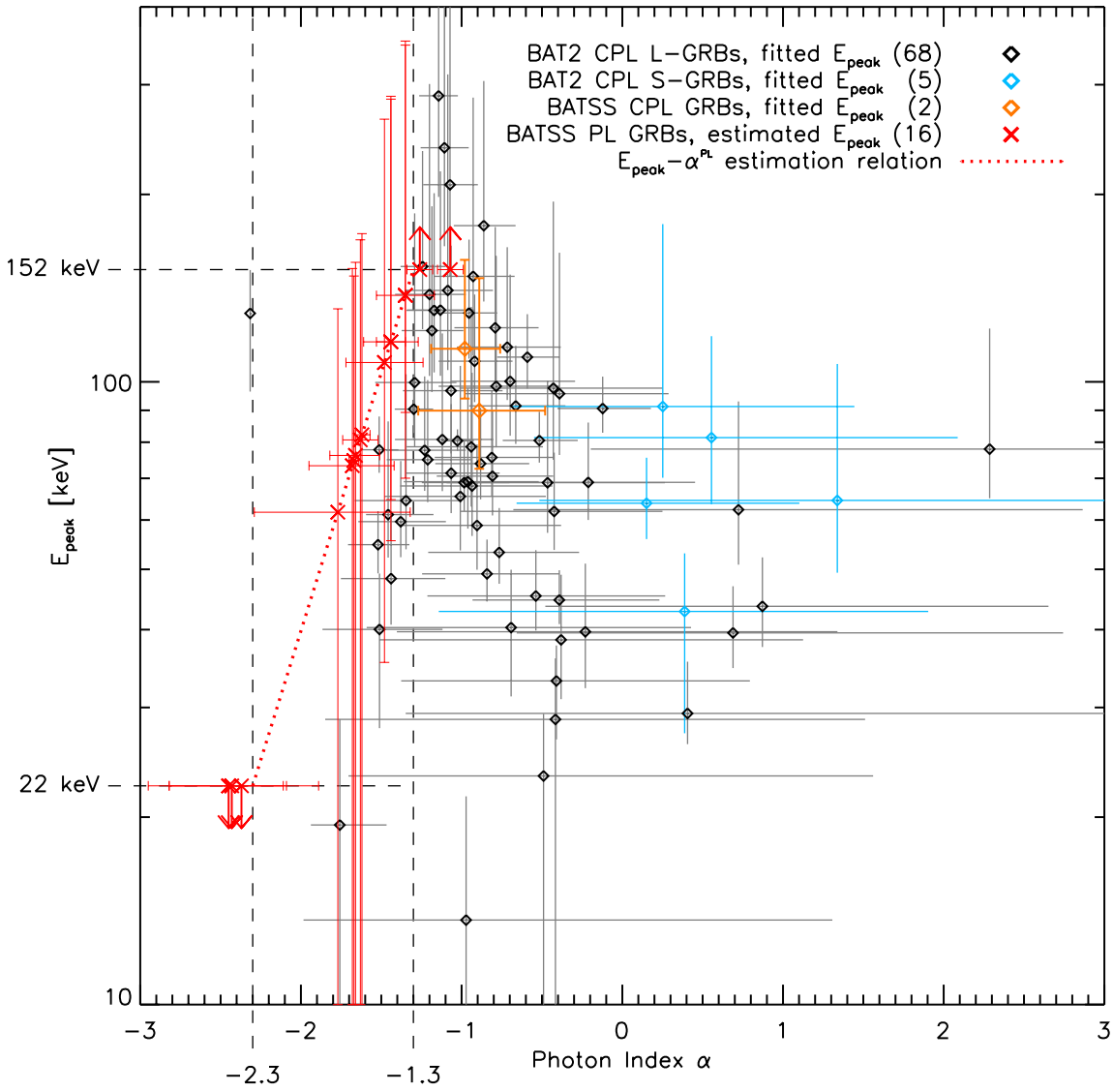

FIGURE 4.17: Peak energy $E_{\rm peak}$ of the GRB νF_ν distribution vs. photon index $\alpha^{\rm CPL}$ derived from time-averaged GRB spectra that are best fit to a cutoff power law (CPL) model, for both BATSS and BAT2 catalog GRBs. In addition, the estimated $E_{\rm peak}$ according to the $E_{\rm peak}$–$\alpha^{\rm PL}$ relation (Sakamoto et al. 2009b) is plotted against $\alpha^{\rm PL}$ for BATSS GRBs that were best fitted to a PL model. For values outside the $-2.3 \geq \alpha^{\rm PL} \geq -1.3$ dynamic range of the relation, only the estimated $E_{\rm peak}$ upper limit of 22 keV (for $\alpha^{\rm PL} < -2.3$), or its lower limit of 152 keV (for $\alpha^{\rm PL} > -1.3$) are provided.

so for values of $\alpha^{\rm PL} < -2.3$ we only indicate in the figure the estimated upper limit of $E_{\rm peak} < 22$ keV, and for values of $\alpha^{\rm PL} > -1.3$ we indicate the estimated lower limit of $E_{\rm peak} > 152$ keV.

The histograms in Figure 4.18 show the $\alpha^{\rm CPL}$ and $E_{\rm peak}$ distributions from the CPL fit results shown in Figure 4.17. The 73 GRBs from the BAT2 catalog, as well as the 2 BATSS GRBs that were best fit to a CPL model, form a distribution that is peaked at $\alpha^{\rm CPL} \sim -1$, a result which is consistent with similar results for the low-energy photon indices of GRBs detected by BATSE and *HETE-2* (Kaneko et al. 2006; Pélangeon et al. 2008). On the other hand, the log-normal $E_{\rm peak}$ distribution of BAT2 CPL GRBs is peaked at 79 keV ($\sigma = 0.18$ in $\log E_{\rm peak}$, Sakamoto et al. 2011), and the 2 BATSS CPL GRBs as well as the estimates for 11 out of 16 BATSS PL GRBs are consistent with this result. However, the same $E_{\rm peak}$ distributions for BATSE and *HETE-2* GRBs are peaked at 320 keV and 65 keV, respectively, which reveals an instrumental selection effect for the GRBs detected by each. In the case of the BAT, the $E_{\rm peak}$ values are shown to fall mostly within the 15–150 keV band that its CdZnTe (CZT) solid-state detectors are most sensitive to (Barthelmy et al. 2005). Also, because their estimated $E_{\rm peak}$ falls below the 30 keV level for classification, 3 BATSS GRBs are categorized as X-ray flashes (XRF): GRB 071212, GRB 090823 and GRB 111011A.

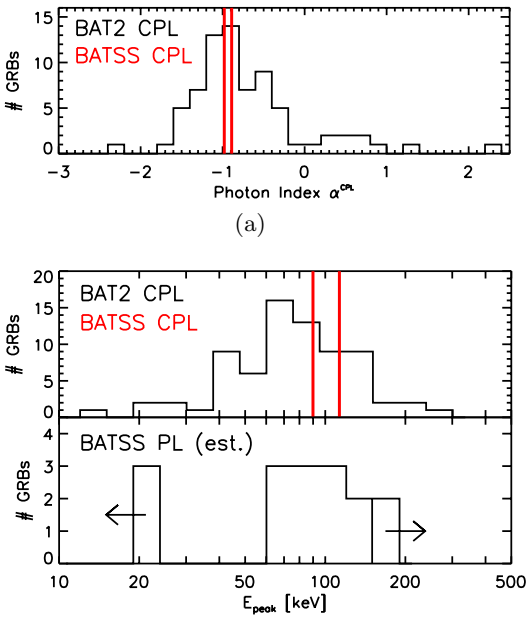

FIGURE 4.18: Distributions of (a)photon indices $\alpha^{\rm CPL}$ and (b)$E_{\rm peak}$ for 73 BAT2 and 2 BATSS GRBs that were best fitted by a cutoff power law (CPL) spectral model. The $\alpha^{\rm CPL}$ distribution is consistent with similar results for BATSE and *HETE-2*, whereas the $E_{\rm peak}$ distribution is instrument-dependent. The bottom panel of Figure (b) also shows the distribution of estimated $E_{\rm peak}$ values for 16 BATSS GRBs that were best fit by a simple power law (PL) model.

4.4.7 Afterglow data

Given the foreseeable delays in observing GRB afterglows despite our effort in making real-time data reporting as fast as possible, BATSS GRBs were knowingly at a clear disadvantage when compared to the vast majority of *Swift* GRBs which produced on-board triggers and automated target (AT) slews within ∼10 sec of the trigger time. GRB afterglow science was therefore not a main focus of the BATSS GRB survey, but for the sake of completeness, we include conclusions from the available data that was gathered by various observatories and summarized in Table 4.6:

1. Afterglow observations were attempted in only 12 of 19 BATSS GRBs. Follow-up observations on the 7 remaining GRBs were not possible due to one of the following reasons:

   - Delays in real-time reporting due to technical reasons related to the BATSS pipeline. GRB 070326, GRB 100120A, GRB 101004A, GRB 111011A fall in this category.

- Changes in the pipeline algorithm which yielded a number of new GRBs upon reprocessing of archival data. By far the most significant of these changes was the lowering of the partial coding threshold from 20% to 15% from 2010 onwards, which revealed GRBs 071212 and 080806. At the same time, GRB 090118 would not have been detected at this lower threshold due to an increase in the local image background with respect to the 20% threshold image.
- Observing constraints for follow-up instruments. The 3-day Moon constraint on GRB 110906A impeded afterglow observations by all observatories. Also, *Swift* scheduling constraints prevented a ToO observation for GRB 090418B due to a large number of recently discovered GRBs, but other observatories were able to follow up.

2. The distribution of time delays to the first *Swift*-XRT observation of the 12 BATSS GRBs,[26] along with the equivalent delay for 490 *Swift* GRBs that were triggered on-board, are shown in Figure 4.19. The figure shows a typical delay of ∼100 sec for on-board triggers, with 95% of GRBs first observed within 4 ksec of the trigger time. In contrast, BATSS GRBs are typically first observed within 10^4–10^5 sec of the original slew, equivalent to a range of ∼3–24 hr.

[26]Since GRB 090418B was not observed by the XRT, even though it was observed by other instruments, only 11 GRBs are shown.

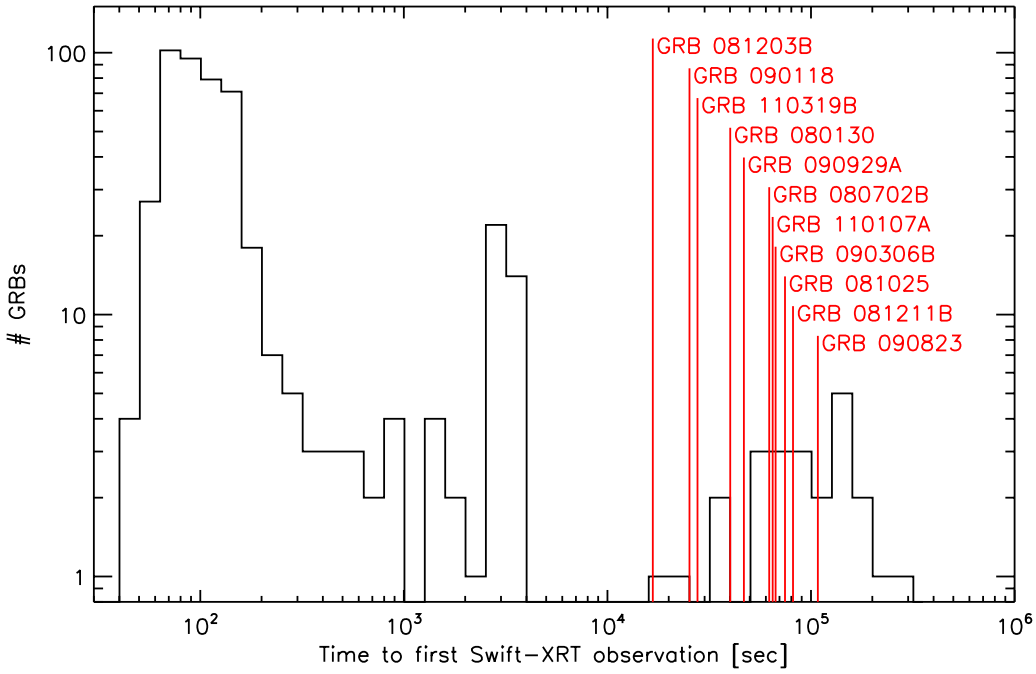

FIGURE 4.19: Distribution of time delays from BAT trigger time to start of first XRT follow-up observation for 490 *Swift* GRBs detected on board, compared to the equivalent delays for 11 BATSS GRBs (shown in red).

3. Of 12 GRBs with follow-up observations, 10 had confirmed afterglows in the following spectral ranges:

TABLE 4.7
BATSS GRBs: Spectral bands of confirmed afterglows

#	GRB	X-ray	Optical				NIR	Radio
			white	g	R	r	i	8.46GHz
3	080130	X						
4	080702B	X						
6	081025	X						
7	081203B	X	X	X	X	X	X	X
8	081211B	X						
9	090118	X						
10	090306B	X						
12	090823	X						
16	110107A	X						
17	110319B	X						

4. Of the 10 GRBs with confirmed afterglows, an X-ray counterpart was found by the *Swift*-XRT on all of them. The measurements or constraints on the decay index α were:

TABLE 4.8
BATSS GRBs: X-ray afterglow decay index α

#	GRB	X-ray α
7	081203B	$-1.4^{+0.2}_{-0.1}$
8	081211B	$-1.6^{+0.9}_{-0.6}$
9	090118	-0.61 ± 0.3
16	110107A	< -0.4
17	110319B	< -0.6

5. Only 1 of the 10 GRBs was found to be optically bright (081203B), but no redshift measurement or host galaxy determination was obtained.

4.5 GRB detection rates

The timeline of BATSS GRB detections is shown in Figure 4.20. Plotted on the figure is first of all the curve showing the cumulative exposure [Msec] of slew data captured and downlinked by *Swift*-BAT and processed by BATSS, as a function of clock time [MJD]. The curve covers the period of the first continuous BATSS test from 03/01/07 to 03/31/07, followed by a gap in slew data capture until 10/25/07, when the capture of real-time slew data for BATSS began, and ending on 07/07/12, the last day of data processing reported here. Therefore, the slope of the curve at each point is directly proportional to the amount of slew data captured per calendar day, which as it can be observed, remains approximately constant over the period of the survey, except for a period of reduced data capture during the first semester of 2010.[27]

The set of 19 GRBs detected only during *Swift* slews and listed in Table 4.4 are over-plotted on Figure 4.20 as blue lines on both axes, so as to illustrate the rate at which they have been detected, both in the domains of clock time and instrument time. For the purposes of characterizing the performance of the BATSS survey in detecting GRBs, it is this second domain (instrument time) the one that is most relevant, as it yields the total number of detected GRBs per unit of time of captured slew data, which can then be directly compared against the detection efficiency for GRBs in pointing mode as a function of the instrument exposure in that mode of operation.

Before making a direct comparison of BAT slew vs. pointing GRB detection rates, however, it is important to define the relevant sample of GRBs that should be included in each case. On the pointing side, it is clear that every on-board GRB detection reported has been made independently of the results from slew-mode detection, which has always

[27]This period coincides with the time the BATSS hardware and real-time processing system was being upgraded after a system failure in December 2009, described in Section 3.2.

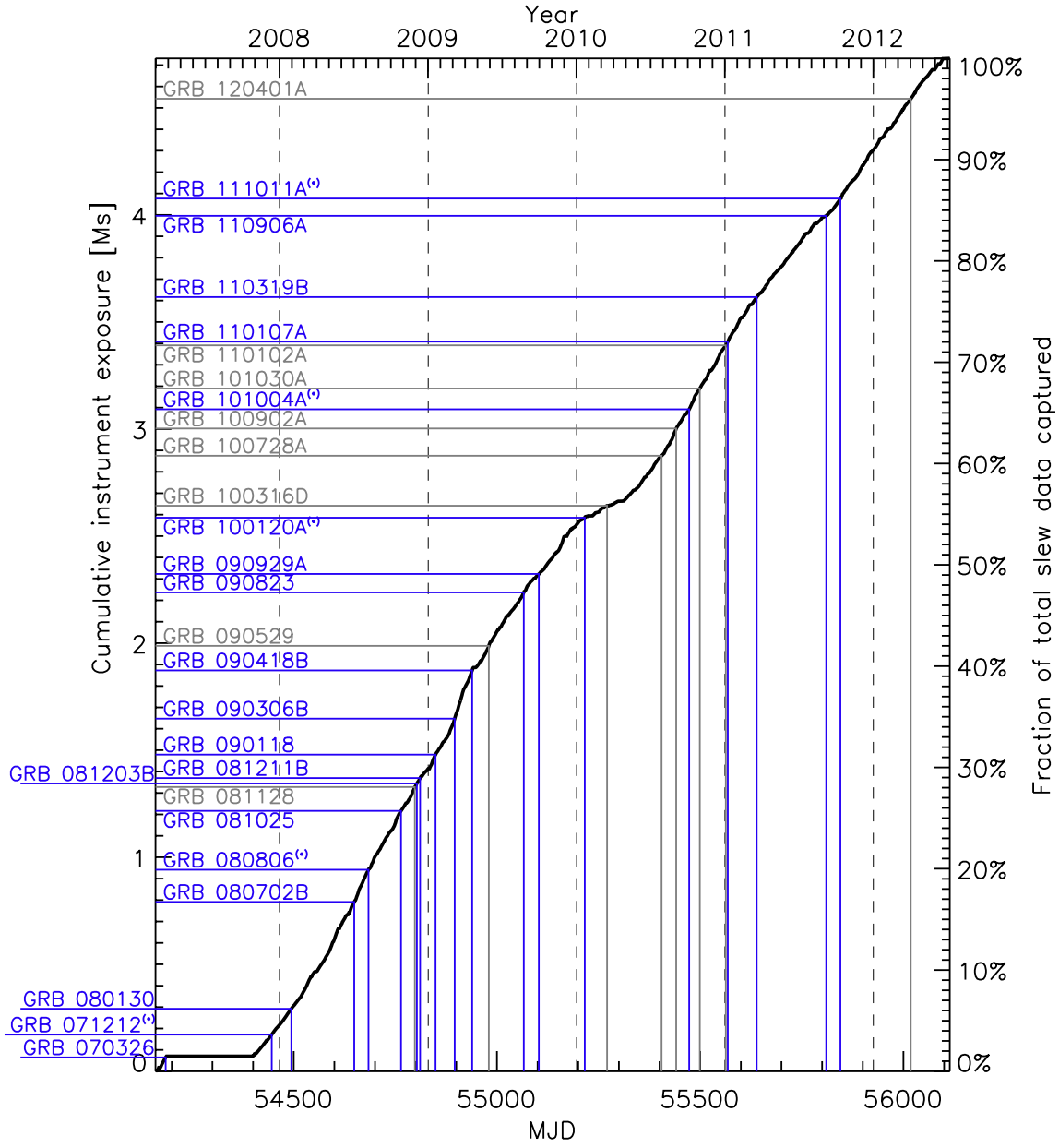

FIGURE 4.20: BATSS GRB detection timeline, shown on a plot of cumulative BAT instrument exposure in slew mode processed by BATSS, as a function of clock time. 19 GRBs detected only in slew mode are displayed in blue (Table 4.4), and an additional 9 GRBs detected independently by BATSS in slews that preceded an on-board pointing-mode detection are displayed in gray (Table 4.9).

occurred later in ground processing. Therefore, all such pointing-mode detections can be directly attributed to the performance of the instrument in this mode of operation as well as its corresponding triggering system. On the slew side, the 19 BATSS-only GRB detections have also clearly been made independently of the pointing detections, but as discussed in Section 4.4.2, a large number of the pointing-mode GRBs have been detected in slews as well (104 out of 465 GRBs in the survey period). Most of those detections have been made in the automated slew that has followed the trigger in pointing mode, so those cannot be directly attributed to the slew mode of operation or the BATSS software. The remaining detections, however, have been made in the pre-planned slew *before* the observation where the pointing-mode detection was made. Since those slews have not been prompted by a preceding pointing-mode detection, the corresponding slew detections can also be considered to have been made independently from the pointing detections, even though the GRBs themselves have been classified as pointing-mode GRBs.

That additional set of GRBs detected independently by BATSS has also been included as part of the timeline in Figure 4.20 as a set of gray lines, and they are listed in Table 4.9 along with several of their BATSS detection parameters. Over the period being analyzed in this work there were a total of 9 such GRBs, which added to the set of 19 BATSS-only GRBs yields a total of 28 GRBs detected independently in slew mode over the period of the survey. With a total instrument time of 4.71 Msec worth of slew data processed by BATSS, this yields an average slew GRB detection rate of 5.94 GRBs/Msec.

On the other hand, over the same survey period there were a total of 464 independently detected GRBs in the pointing data from 113.05 Msec of instrument exposure,[28] for an average pointing GRB detection rate of 4.10 GRBs/Msec. Consequently, we have an aver-

[28]BAT pointing instrument exposure includes only periods where the spacecraft was settled within $10'$ of its target position, and it was outside the South Atlantic Anomaly (SAA).

TABLE 4.9
Additional set of GRBs detected independently by BATSS
in the preceding slew before on-board detection

GRB	Trigger time[a] [UT]	Slew ID[b]	Detection S/N		
			S	H	B
081128	17:18:44	17h16m49s+111s (90.4s)	10.1	n/a	10.2
090529	14:12:35	14h10m57s+091s (35.8s)	15.8	n/a	14.7
100316D	12:44:50	12h43m30s+077s (76.6s)	6.8	n/a	7.5
100728A	02:18:24	02h14m56s+193s (112.4s)	42.9	35.6	54.1
100902A	19:31:54	19h30m28s+082s (72.0s)	n/a	n/a	6.4
101030A	15:56:29	15h54m56s+062s (62.2s)	18.9	9.0	20.5
110102A	18:52:25	18h49m55s+141s (121.6s)	4.7	5.5	7.7
120401A	05:24:15	05h21m54s+127s (79.6s)	9.3	4.8	10.3

[a]Reported trigger time from on-board (pointing mode) detection

[b]Slew start time [UT] + duration [s]: HHhMMmSSs+XXXs (data fraction captured [s] in parentheses)

age yield of 45% more GRBs detected per unit instrument time in slew mode compared to pointing mode, given the current detection methods.

Figure 4.21 shows how the historical average of GRB detection rates has varied over the course of the survey. The upper limit of the instrument exposure range corresponds to the total pointing-mode exposure of 113.05 Msec, which in the same observation mode yielded 464 detected GRBs, setting the scale of the secondary y-axis. If this pointing detection rate had stayed constant over the course of the survey (except for the 04/01/07–10/24/07 slew data gap), the cumulative number of GRBs as a function of clock time would have been the one represented by the dashed black line in the figure. In reality, the actual GRB yield in pointing mode is given by the solid black curve, which for the most part closely follows the dashed line for an approximately constant detection rate over time.

For the GRB yield from slew data, the dashed blue line represents the total expected GRB yield if all of the 17.01 Msec of slew data during the survey period had been down-

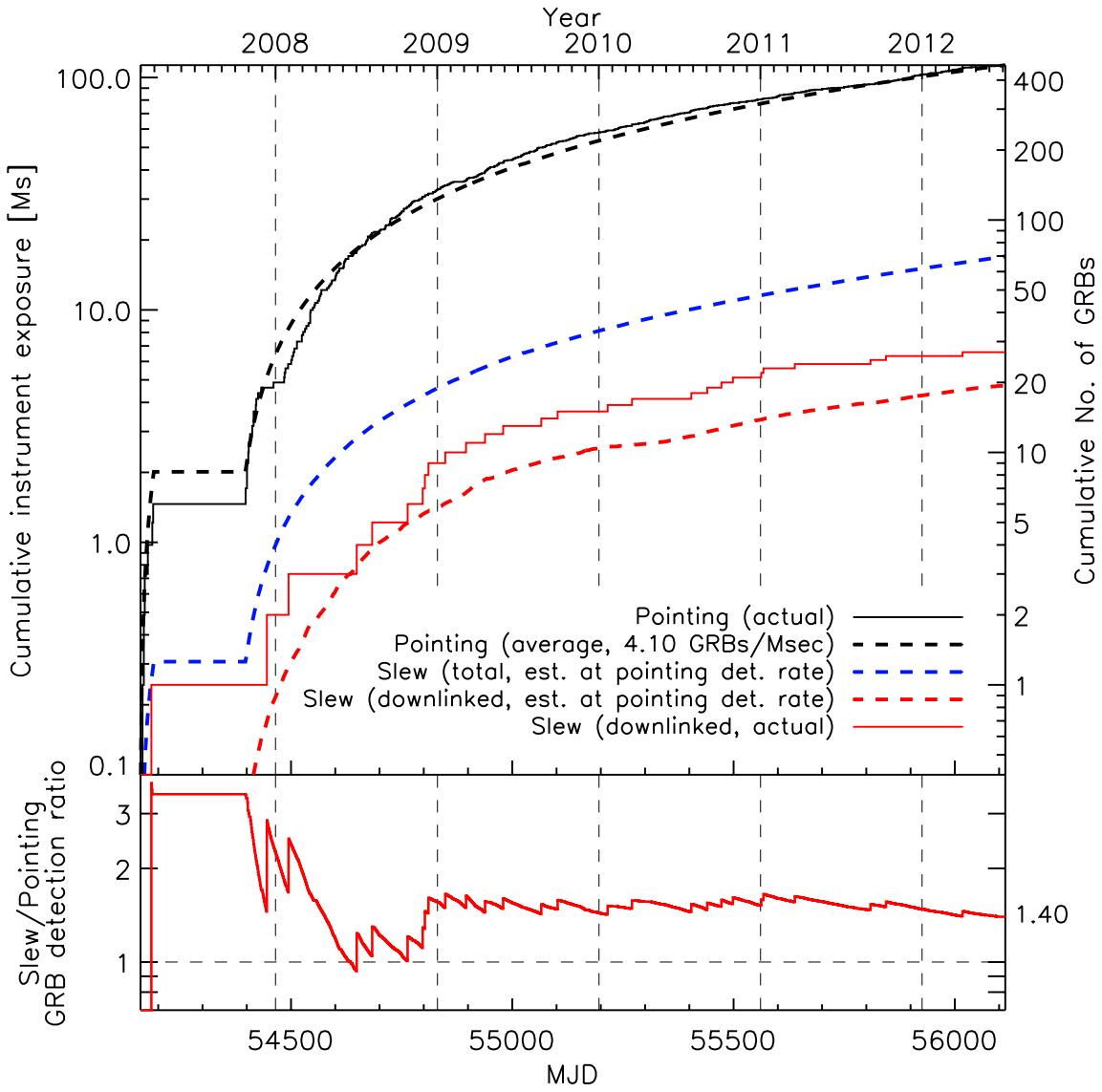

FIGURE 4.21: Top panel: cumulative GRB detection yields as a function of clock time over the course of the BATSS survey. The actual and average on-board (pointing) yields are shown as black curves, along with their corresponding *Swift*-BAT instrument exposure, for an overall rate of 4.10 GRBs/Msec. The dashed blue and red lines show the predicted yields of independent GRB detections based upon the pointing detection rate, for the total and the actual downlinked slew-mode instrument exposures, respectively; the actual yield is plotted as a solid red curve. Bottom panel: ratio of actual/predicted slew detection rates over the course of the survey (solid/dashed red lines in the top panel), showing a consistent excess above 40% over most of this period.

linked,[29] assuming the same average rate of 4.10 GRBs/Msec as in pointing mode. This would have resulted in 69.7 independent (though not necessarily unique) GRB slew detections, as the secondary y-axis of the plot shows. Given that the actual amount of slew data downlinked was 4.71 Msec (27.7% of the total), the same assumed detection rate would have yielded an expected total of 19.3 independent BATSS GRB detections, as shown by the dashed red line in Figure 4.21.[30] In contrast, the solid red curve, representing the actual yield from BATSS, is shown to be consistently above the number predicted from the pointing detection rate, and the ratio between these two quantities as a function of clock time is plotted on the bottom panel of the figure. The plot clearly shows that the excess number of detected GRBs stays above 40% for most of the survey, consistent with our overall result of 45% higher GRB detection rate for BATSS compared to the pointing mode rate.

Finally, the log-normal distributions of time intervals between consecutive GRB detections are shown in Figure 4.22, given in units of instrument time for each mode of observation (i.e. "dead" time between consecutive slews or pointing observations is excluded). The time intervals between successive on-board (pointing) triggers typically varies from a few ksec up to a Msec or longer, with an average of 243 ksec ($\sigma = 0.57$ in logarithmic units) between triggers. On the other hand, the slew distribution is shifted towards shorter time intervals, with a mean of 168 ksec ($\sigma = 0.39$ in logarithmic units) in instrument time between consecutive detections. The K-S probability that the pointing and slew distributions would have been drawn from the same parent distribution is 22.4%, which means it is unlikely that they in fact are.

---

[29]This total slew-mode instrument exposure excludes periods of SAA passage.

[30]The dashed blue and red lines are not uniformly smooth due to differences in both total and downlinked instrument exposure per day.

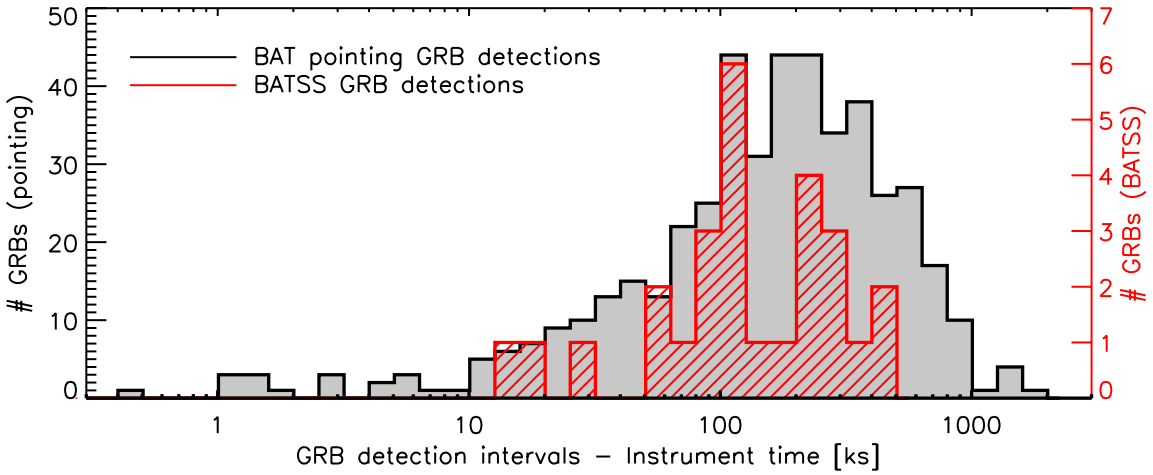

FIGURE 4.22: Log-normal distributions of time intervals (in BAT instrument time) between consecutive GRB triggers in pointing and slew modes. The slew average of 168 ksec, as well as the distribution as a whole, are shifted to the left of the pointing-mode distribution, which averages 243 ksec between triggers.

4.6 Simulation modeling of pointing vs. slew GRB detection rates

The considerable difference found in overall GRB detection rates per unit instrument time in pointing vs. slew observations implies there is a greater intrinsic sensitivity of slewing as an observational technique when compared to the default pointed mode of operation *Swift*-BAT regularly employs. In order to verify this finding given our knowledge of the BAT instrument sensitivity at the local level of sky images, as described in Section 2.5, as well as the way the *Swift* spacecraft regularly operates as reflected in its attitude data, we have carried out a simulation where we have computed detection probabilities for a sample of simulated GRBs to be observed in a representative set of BATSS slews, and then compared the equivalent results derived from BAT pointings of equal duration. In the rest of this section we describe the core set of assumptions the simulation was based on, as well its main results and the overall conclusions derived from them.

As a first consideration, on the issue of the GRB sample to be used, we first sought to define the relevant set of GRB properties we would be modeling for the purposes of this simulation. Since the BAT sensitivity results as well as the BATSS detection technique are based on image triggers on a specific set of energy bands, GRB detection significances under this technique depend only on the integrated flux of the burst over the time it remains in the instrument FoV. Therefore, it is legitimate to assume a set of simulated GRBs of constant flux in the relevant energy band and equal to the mean flux of the real GRBs over the entire period of prompt emission. The total flux integrated over this period would be given by the observed GRB fluence, and the duration of the simulated burst itself would be characterized by the T_{90} of the real sample. It is these two quantities that we set out to model in this work, with the additional empirical consideration that they are not uncorrelated quantities and hence should not be decoupled from each other. Also, since *Swift* GRB fluences are reported in the 15–150 keV energy band (equivalent to the BATSS Broad band), this was the band used to generate the fluences of the simulated GRB sample as well. As a further simplifying assumption, we based this analysis on the modeled GRB detection significances in this single energy band, so we need not be concerned about modeling the spectral properties of the GRB population, which would have been needed in order to extrapolate the detection significances to other energy bands.

Figure 4.23a shows the real distribution of detected *Swift* GRB fluences S(15–150 keV) vs. T_{90}, derived from a sample of 436 GRBs from the BAT2 catalog (Sakamoto et al. 2011) for which measurements of these parameters were available, and where the direct correlation between the two quantities can be observed. These were then used to populate a 2-D histogram with logarithmic bins which is also overplotted on the figure as a color-coded image. Then, in order to generate the model distribution for the simulated sample, this histogram was oversampled by a factor of 4 and smoothed by bilinear interpolation,

and the result is shown in Figure 4.23b. Finally, a total of 1000 points were sampled from this distribution (also shown in the figure), representing the sample of simulated GRBs to be observed. The resulting normalized distributions of simulated GRB T_{90} and fluence are displayed in Figures 4.24a and 4.24b, respectively, along with the parent (real) distributions they were derived from, all histogrammed as log-normal distributions.

With regard to the slew sample employed in the simulation, we used the full set of 2,036 slews from the month of March, 2009, a particular month in which nearly 100% of slews were downlinked and imaged by BATSS, though as in most of the survey, the amount of data captured per slew was capped at 120 sec, as can be observed in the simulated distributions of the second page of Figure 4.24. This choice was made in order to ensure the sample was representative of the entire set of slews imaged in the BATSS survey, as the figure shows it is.

Figure 4.24c shows the resulting distribution of slew durations for the chosen (simulated) sample, along with the distribution for the full (real) set of downlinked BATSS slews for comparison, both normalized. Likewise, Figure 4.24d shows the resulting normalized distributions of sky coverages per slew, which as discussed in Section 4.2 are strongly dependent on the slew duration distributions, though complicated by the ranges of possible *Swift* slewing speeds and BAT roll angles. Both plots show how closely the chosen slew sample tracks the full slew sample at least up to 120 sec duration. Given that the exposure cap was still in place on March, 2009, the slews longer than 120 sec are consequently underrepresented in the simulation, though as shown in Section 4.2 and Figure 4.3, despite the lifting of the cap on August, 2011, by *Swift* mission operations, those slews still represent only 9% of the full downlinked sample.

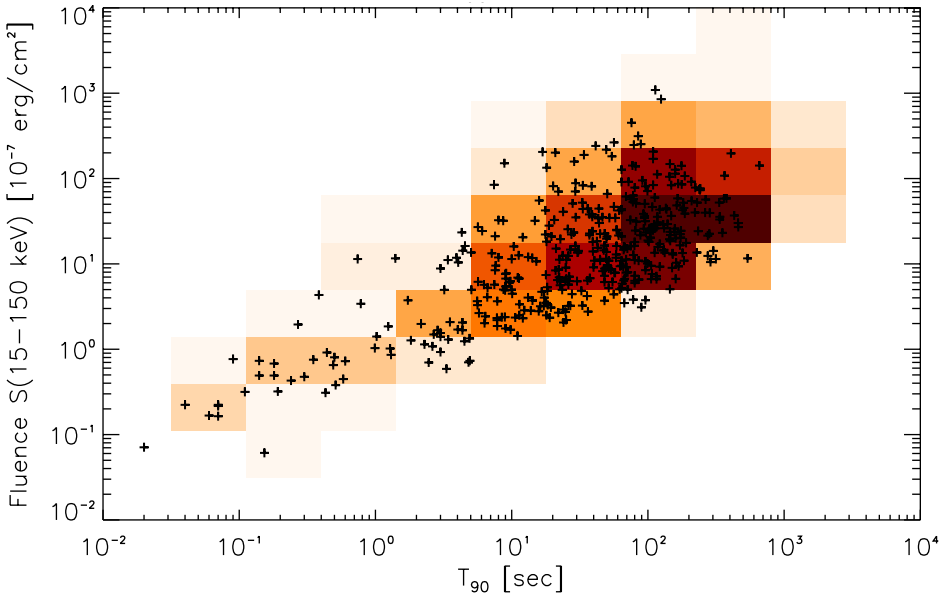

(a) Real GRB sample, from BAT2 catalog (436 sources, Sakamoto et al. 2011)

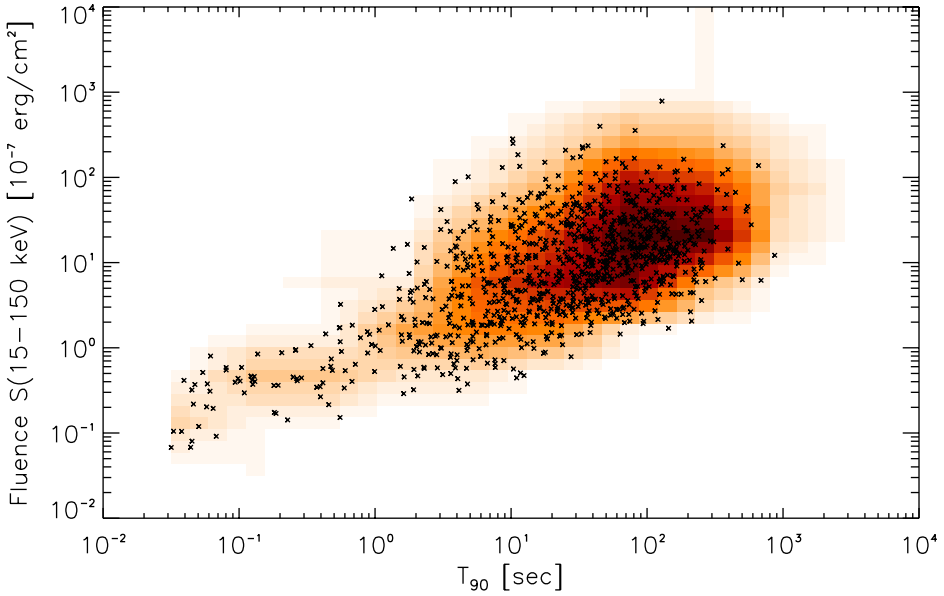

(b) Simulated GRB sample (1000 sources)

FIGURE 4.23: *Swift*-BAT GRBs: real and simulated samples, and fluence S(15–150 keV) vs. T_{90} distributions used in the modeling of BAT GRB detection rates. 436 BAT2 catalog GRBs were used to build the real distribution, and 1000 were sampled from the simulated distribution.

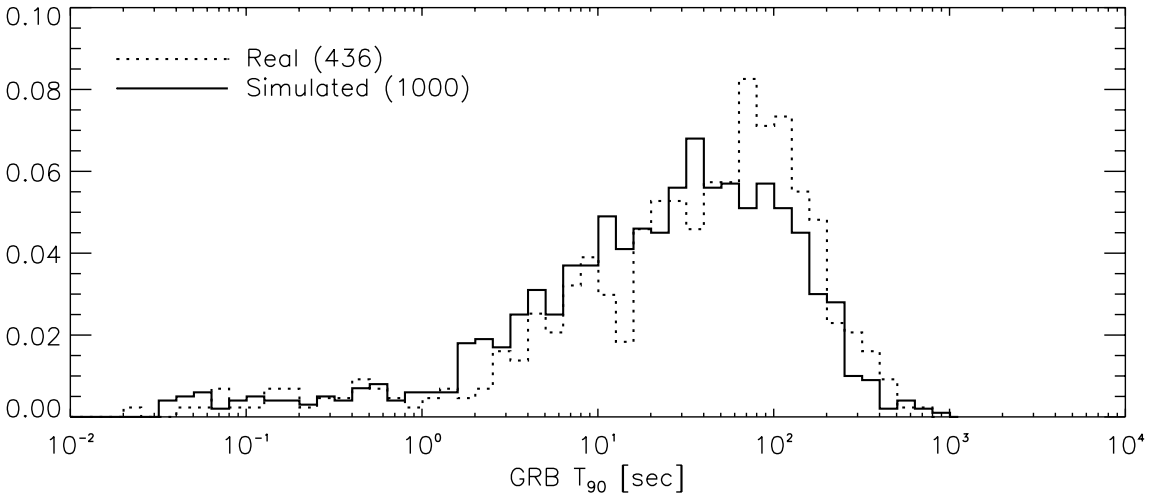

(a)

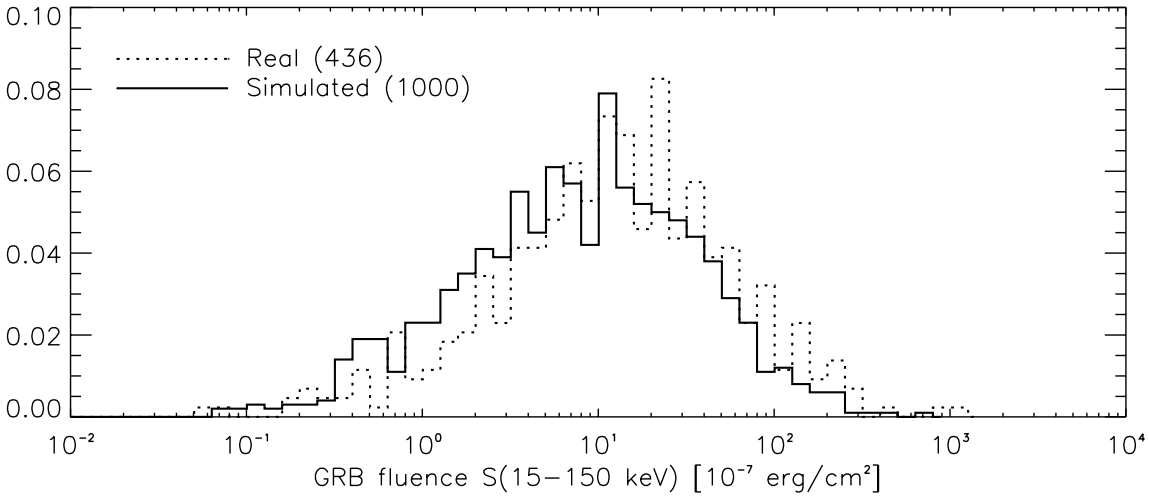

(b)

FIGURE 4.24: Normalized distributions of real and modeled parameters for BAT GRB detection rate simulation: (a) GRB T_{90}, (b) GRB fluence S(15–150 keV). Both of these distributions are derived from the scatter plots in Figure 4.23. The real sample of 436 GRBs was drawn from the BAT2 catalog (Sakamoto et al. 2011), while the simulated set of 1000 GRBs was sampled from the 2-D distribution in Figure 4.23.

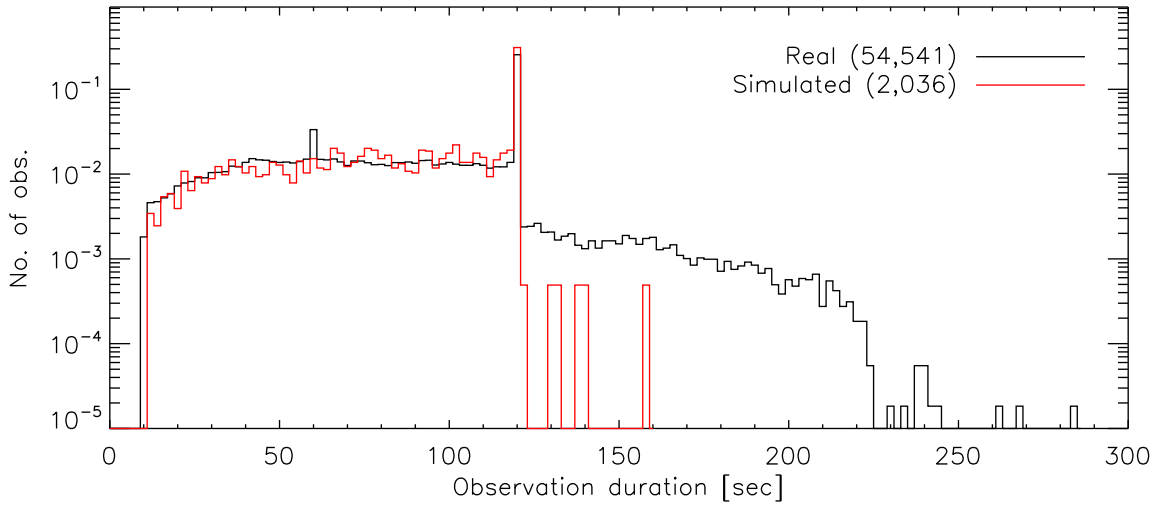

(c)

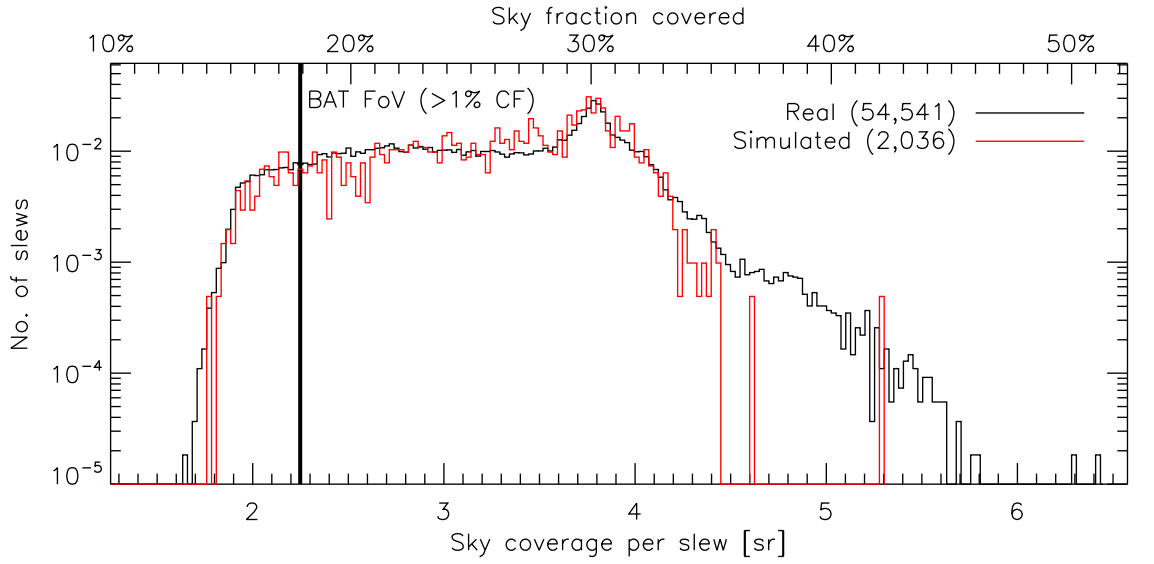

(d)

FIGURE 4.24(continued) Normalized distributions of real and modeled parameters for BAT GRB detection rate simulation: (c) slew durations, (d) sky coverage per slew. The choice of slews made for the simulation (all 2,036 slews from March, 2009) closely tracks the full real sample of downlinked slews at least up to 120 sec. Since the exposure cap had not yet been lifted at the time, the 9% of downlinked slews longer than 120 sec is underrepresented in the simulated sample, as evidenced by both of the red distributions in the figure.

Once the samples of observations and simulated GRBs were selected, we sought to calculate the 5σ detection probabilities for each GRB and each observation, assuming the burst occurs at a random location in the sky, and with its prompt emission arbitrarily chosen to start at the same time as the start of the observation. In order to replicate the partial coding and exposure threshold levels employed in the real pointing and slew surveys, we set the detection thresholds for the simulation at 1% partial coding for pointing observations, and at 20% partial coding as well as 10 sec exposure for slews. Therefore, in the case of the brightest GRBs, the maximum GRB detection probability for pointings is constrained by definition only by the 2.51-sr size of the BAT FoV above 1% partial coding, for a maximum detection probability of 19%. On the other hand, since slews generally cover a larger area of the sky than the BAT FoV alone, there is no such constraint on the slew detection probability, and the value may well fall above the pointing mode limit for a wide range of slew simulation parameters.

For the computation of the detection probability itself, we then use the full-sky projection of the exposure and partial coding maps of each observation, so we have a value for the effective exposure $T_{\mathrm{eff},x}$ for each sky location x, defined in section 2.5 as the product of the instrument exposure time $T_{0,x}$ and the time-averaged partial coding fraction p_x. We then estimate the 5σ sensitivity in slew mode from equation 2.18 as

$$S_{5\sigma,\mathrm{slew}}(15\text{–}150\ \mathrm{keV}) \approx 120\ \mathrm{mCrab} \cdot \left(\frac{T_{\mathrm{eff}}}{100\mathrm{s}}\right)^{-0.5} \tag{4.12}$$

On the pointing side, and over the entire 10 sec $< T_{\mathrm{eff}} <$ 120 sec timescale of slew observations, we found in section 2.5 a consistent sensitivity advantage for slews at the local level of approximately 20%, so we can estimate the sensitivity for pointing images on

this timescale as

$$S_{5\sigma,\mathrm{point}}(15\text{–}150\ \mathrm{keV}) \approx 1.20 \times S_{5\sigma,\mathrm{slew}} = 144\ \mathrm{mCrab} \cdot \left(\frac{T_{\mathrm{eff}}}{100\mathrm{s}}\right)^{-0.5} \tag{4.13}$$

Having computed the sky map of 5σ sensitivities for each observation, we are only left with finding the actual exposure of each GRB at each sky location x, which is constant within the entire FoV in the case of pointings but varies by location in the case of slews, and from there the mean GRB flux at each location. We then assign probability 1 to those locations above the sensitivity threshold and 0 to those below. Finally, the fraction of sky with probability 1 then gives the overall detection probability for each simulated GRB and each observation.

The scatter plot in Figure 4.25 illustrates the overall results of the simulation, where for each GRB and observation combination, we have plotted the GRB detection probability for each slew against the probability for its equivalent pointing of equal duration. The plot is color-coded according to the duration of each observation, so the strong dependence of the results on observation length can be readily observed. For each observation, it can be seen that the simulated GRB sample is mapped onto a smooth, monotonically rising sequence of points, from a probability of 0 in both cases for the faintest GRBs, to an upper end where the aforementioned upper limit on the pointing probability (19%) is reached for the brightest GRBs. Overall, the slew/pointing probability relation steepens for longer observations, with the maximum detection probability corresponding to the intuitively obvious case of the longest slews and the brightest GRBs, for which the probability is over twice the pointing upper limit. Also, in the vast majority of cases, we find that the slew detection probability is greater than the pointing detection probability, with exceptions only in two extremes illustrated in the figure: the brightest GRBs in the shortest observations, and the faintest GRBs in the longest observations.

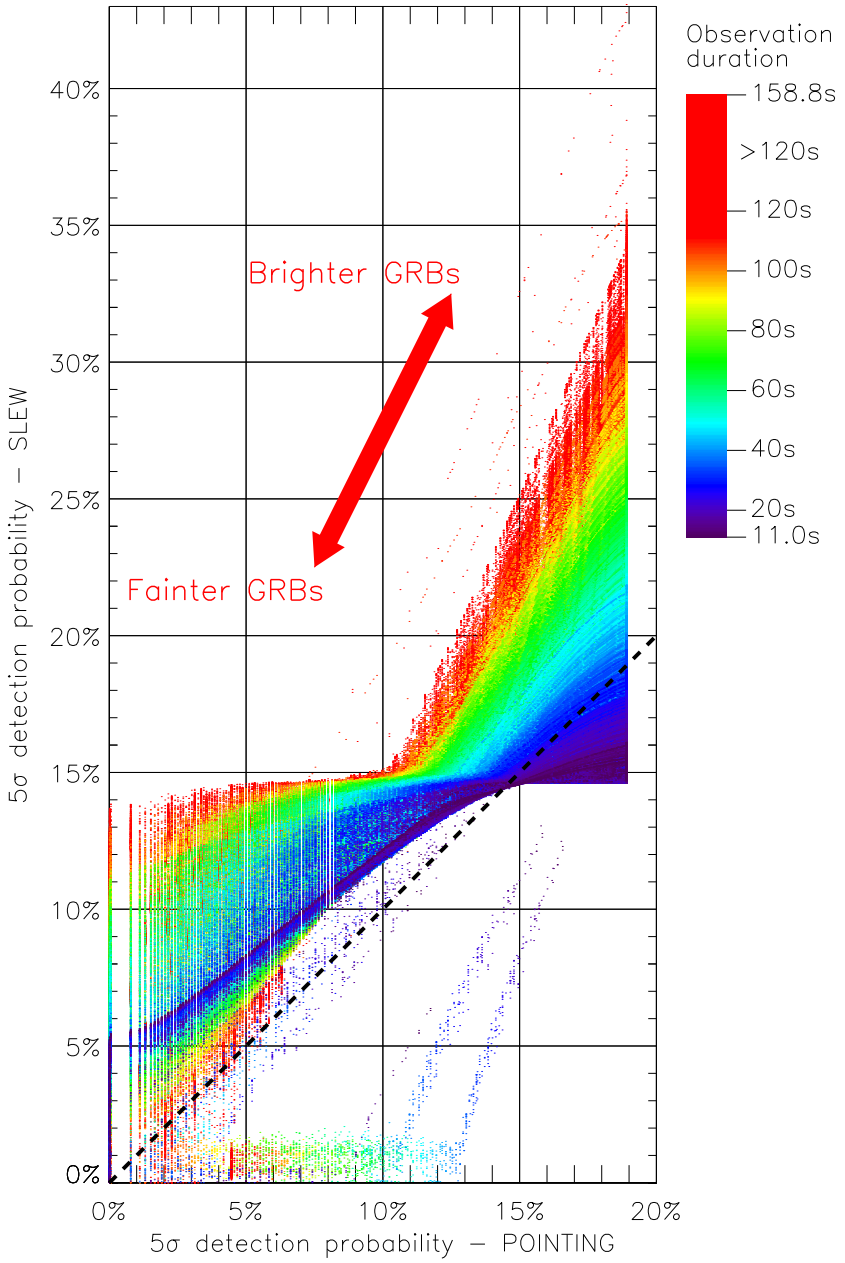

FIGURE 4.25: *Swift*-BAT slew vs. pointing 5σ detection probabilities (15–150 keV) for a simulated sample of 1000 GRBs. A sample of 2036 BATSS slews was chosen and compared against a set of pointings of equal duration. The scales on both axes have been matched to each other, and the segmented line represents the boundary of equal slew and pointing detection probabilities.

The distributions of detection probabilities are shown separately for slews and pointings in Figure 4.26, binned in sets of size 0.1% and normalized, where the relative occurrence of certain probability values can be readily observed. In particular, the frequency of cases with a detection probability of zero is a significant 36% for pointings and 33% for slews, which means that for a group of faint GRBs that are completely undetectable in pointing mode, about 10% of them are detectable in slew mode with a probability that can be as large as 6%, as the faint end of the scatter plot in Figure 4.25 shows. This relatively small slice of the GRB sample is at the same time one with a considerable potential interest, as faint, high-redshift GRBs are more likely to appear at this end of the GRB distribution.

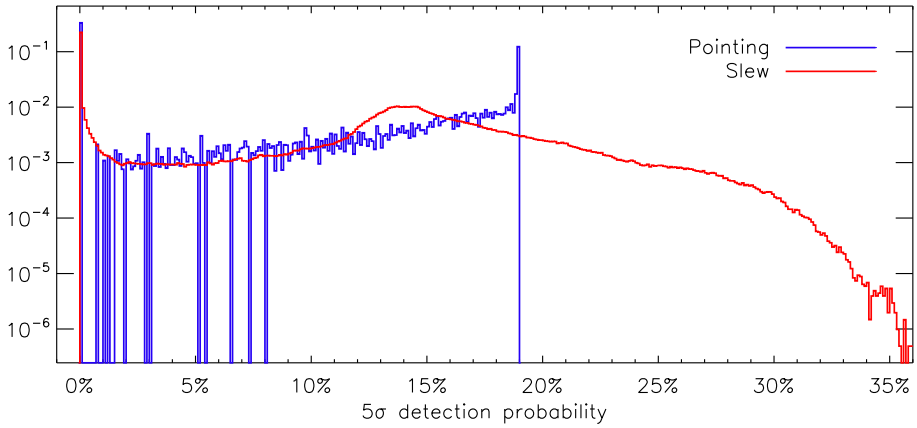

FIGURE 4.26: Normalized distributions of modeled BAT GRB detection probabilities. Pointing-mode probabilities have a well-defined upper bound due to the size of the BAT FoV, while slew-mode probabilities are not bound by this limit.

Finally, after averaging over all possible GRB/observation combinations, the mean GRB detection probability for slews in this simulation has been found to be $P_{\rm slew} = 0.122$, while the mean probability for pointings is $P_{\rm point} = 0.080$, for a predicted detectability ratio of

$$P_{\rm slew}/P_{\rm point} = 1.54 \tag{4.14}$$

This GRB detection ratio is consistent with the findings from the actual survey presented in Section 4.5, where we found an excess of 45% in detected GRBs per unit instrument time in the case of slews. Furthermore, this ratio finally gives us a quantitative measure of the overall gain in detection rates of astrophysical sources for a slewing coded aperture imaging telescope compared to operating the same instrument in pointing mode. In Chapter 1 we introduced the two features of slew-mode observations of greatest potential impact in enhancing the sensitivity of a coded aperture imaging telescope: one was the reduction of systematic effects at the local level in sky images, and a second and independent one was the greater sky coverage per unit time. In Section 2.5, we had already quantified the first of these effects for a range of timescales of up to ∼30 ksec. This result complements that BAT sensitivity analysis by deriving the combined result of both effects, and showing that the sky coverage effect is at least of equal magnitude if not greater than the systematics reduction effect. In fact, when we run the simulation while disregarding the sensitivity advantage for slews at the local level and use equation 4.13 to calculate both the slew-mode and pointing-mode sensitivities, we find the mean GRB detection probability for slews to be $P_{\rm slew} = 0.113$, for a detectability ratio of

$$P_{\rm slew}/P_{\rm point}\ (\text{sky coverage}) = 1.42 \tag{4.15}$$

This ratio is interpreted to be the increase in GRB detectability due to sky coverage effects only, which shows it is indeed the dominant effect above the increase in local sensitivity due to the reduction of systematic effects analyzed in Section 2.5.

4.7 Conclusions

The BATSS Gamma-Ray Burst survey was conducted under an observational program spanning a total of 1,748 days (4.8 years) where slew data from the Burst Alert Telescope (BAT) was regularly captured and downlinked from the *Swift* spacecraft, followed by BATSS pipeline processing in real time. The results presented in this work are derived from a refined analysis of the data after it was later posted to the *Swift* archive, which generally resulted in enhanced GRB detection significances and more accurate burst positions. A total of 54,541 downlinked single slews with a corresponding total instrument exposure of 4.71 Msec were analyzed for this survey, a 37% fraction of the total of 148,839 spacecraft slews that were spanned over the survey period, or 28% of the total of 17.0 Msec the BAT instrument spent in this mode of observation; a summary of the overall features of the slew observations processed is provided in Table 4.1. The reduced fraction of the total number of slews and the total amount of data per slew was due primarily to bandwidth limitations in the data link between the spacecraft and the Malindi ground station, though the BATSS pipeline is capable of handling the full load of slew data per orbit, were that to become a possibility in the future.

Regarding the detection of GRBs during the survey, given the timespan of up to only a few hundred seconds of the prompt γ-ray emission from GRBs, and the typical time interval of $\sim$1 ksec between consecutive downlinked BATSS slews, it is highly unlikely that a GRB would be detectable over several consecutive slews, and for this reason the BATSS GRB survey is almost exclusively restricted to detections over single slews. Though we did in fact find a few cases of GRBs that were independently detected in consecutive slews, we never observed a case of a GRB that was faint enough so as to be undetectable in the individual slews but bright enough so as to have been detected when those slews were co-added, which would have warranted the use of mosaicked multi-slew observations for the BATSS GRB survey.

Two other important considerations regarding the impact of the BATSS imaging technique presented in Chapter 2 on the GRB detection yield were: 1)the fact that BATSS detection is based on image triggers only, which would likely affect its sensitivity to certain types of GRBs —such as short GRBs— that could be more detectable in combination with a rate triggering approach. Also, 2)the lowering of the partial coding threshold for imaging from 25% to 15% in early 2010, while increasing the GRB yield overall, also rendered some GRBs undetectable under certain conditions; a prime example of that was GRB 090118, which was detected in real time with a 25% threshold but not in later archival processing with a 15% threshold. Overall, both of these effects suggest that our GRB yield as reported in Section 4.4 should only be considered to represent a lower bound to the maximum GRB yield achievable by the BATSS survey given the same input data but a more sophisticated processing pipeline. Several of the improvements to be considered in pursuing this goal are discussed in the Conclusions chapter of this dissertation (Chapter 5).

Regarding the analysis pipeline for individual GRBs, it consists of three main phases: 1)detection and triggering, following the BATSS detection algorithm discussed in Section 2.3 and the triggering criteria for single-slew detections described in Section 3.9; 2)calculation of mask-tagged, background-subtracted lightcurves for the prompt emission, preceded by a mask-weighting (ray-tracing) procedure performed on the event file, given the previously determined location of the burst; 3)spectral analysis, which in the case of the relatively narrow energy band of the BAT instrument involves fitting to either a 2-parameter simple power law (PL) spectral model or a 3-parameter cutoff power law (CPL) model, since it is generally not possible to appropriately constrain the parameter values of the more general 4-parameter Band spectral model (Band et al. 1993). For GRBs fitted to a PL model (most of both BATSS and BAT2 GRBs), it is possible to estimate the peak energy of their νF_ν spectrum, $E_{\rm peak}$, an intrinsic physical parameter that characterizes all

GRBs, using the $E_{\rm peak}$–$\alpha^{\rm PL}$ estimation relation (Sakamoto et al. 2009b), provided that their spectral index $\alpha^{\rm PL}$ lies within the $-2.3 \geq \alpha^{\rm PL} \geq -1.3$ dynamic range of the relation. Otherwise, only a simultaneous detection by a γ-ray telescope with a broader spectral range such as Fermi-GBM, *Konus-Wind*, *Suzaku*/WAM, or INTEGRAL/SPI would allow for measuring or constraining the missing parameters from the spectral fit to the BAT data. For real-time detections, this analysis would normally be followed by the publication of a Gamma-ray burst Coordinates Network (GCN) Notice and/or Circular, which then enables prompt follow-up multi-wavelength observation of the GRB afterglow by a global network of X-ray, optical, infrared and radio observatories. In the description of the analysis pipeline presented in this chapter, GRB 070326 —the first GRB detected by BATSS— was provided as a case study of the general procedure the BATSS analysis thread follows and the Level 3 data products it generates.

The overall science results of the BATSS GRB survey were presented and analyzed here in detail as well, starting with data tables (Tables 4.4, 4.5 and 4.6) which summarized the detection parameters, energetics of the prompt emission, and follow-up observations of the 19 GRBs detected exclusively in the BAT slew observations analyzed over the course of this survey. This was followed by an individual analysis of the most important physical parameters measured from the prompt emission of the BATSS GRB population, with special attention being paid to how they compared to the population of 476 GRBs reported by Sakamoto et al. (2011) as part of the Second *Swift*-BAT GRB (BAT2) Catalog, currently the most comprehensive database of prompt emission data for *Swift*-BAT GRBs.

In general, the BATSS GRB survey in its current form was found to be most sensitive to long GRBs (L-GRBs, defined as those with a 90% energy emission interval $T_{90} > 2$ sec), a category to which most if not all of the BATSS GRBs have been either confirmed or proposed to belong to. Their physical parameters as measured by BATSS, including but

not limited to their duration, spectral hardness, peak fluxes, fluences, spectral indices and $E_{\rm peak}$ values were shown to be largely consistent with analogous results for the L-GRB population in the BAT2 catalog. In addition, the properties of BATSS GRB 081211B, proposed as a member of the rare category of short GRBs with extended emission (S-GRBs with EE, comprising only 2% of GRB population in the BAT2 catalog), have also been shown to be consistent (though not conclusively so) with the properties of the 10 BAT2 S-GRBs with EE. Furthermore, 3 BATSS GRBs with unusually soft spectra and estimated $E_{\rm peak}$ values below 30 keV have also been hereby proposed to belong to the almost equally rare category of X-ray flashes (XRFs), which comprise only $\sim$10% of the overall BAT GRB population due to a low BAT instrument sensitivity to GRBs with a very soft spectrum (Band 2006). On the other hand, the absence of redshift measurements for all BATSS GRBs, due largely in part to the foreseeable delays of > 3 hours after the burst trigger time before the first set of follow-up observations would begin, have limited the amount of further conclusive science results that could have been gathered from them.

We ended the study of the BATSS GRB population by making a detailed analysis of GRB detection rates and how they provide empirical evidence of more general properties of scanning coded aperture imaging compared to the canonical pointing-mode imaging the BAT instrument regularly employs. To the set of 19 GRBs detected exclusively in slew mode and analyzed in Section 4.4, we added a set of 9 GRBs that were detected independently in slew mode as well as on board (pointing mode), for a total of 28 independently detected GRBs over the course of the BATSS survey. Given a total instrument time of 4.71 Msec worth of useable downlinked slew data, the overall BATSS GRB detection rate was found to be 5.94 GRBs/Msec = 0.49 GRBs/day. This rate is 45% greater than the overall GRB detection rate of 4.10 GRBs/Msec in pointing mode, obtained from a total of 464 detections over 113.05 Msec of instrument exposure in that mode of operation.

In order to verify this empirical result, we carried out a simulation where we used the T_{90} and fluence S(15–150 keV) of 436 GRBs in the BAT2 catalog in order to generate a set of 1000 simulated GRBs, which were then imaged in a representative set of 2036 BATSS slews as well as an equivalent set of BAT pointings of equal duration. The overall result was a detectability ratio of 1.54 in slew/pointing observations, which was in fact consistent with the observed detection rates from the BATSS GRB survey. This ratio provides a realistic quantitative measure of the overall sensitivity of slew observations with the BAT instrument, taking into account both the improvement in systematic effects at the local level that was the subject of Section 2.5, as well as the increased sky coverage that is intrinsic to slews. The latter of these effects was in fact found to be the dominant one, as it alone accounts for 1.42 of the overall GRB slew/pointing detectability ratio.

As a whole, apart from its material contribution to the primary science objectives of the *Swift* mission, the BATSS GRB survey has proven to be crucial in providing solid empirical validation for the BATSS imaging and detection method for slew-mode observations with the BAT coded aperture telescope. It has produced both new results as well as corroborating evidence of earlier findings by other surveys, which have collectively shown to be consistent with a wealth of prompt emission data gathered independently by other GRB missions and γ-ray sensitive instruments. In addition, the analysis of GRB detection rates provided quantitative confirmation of the magnitude of the enhanced sensitivity of BAT slew observations compared to pointing observations after including all contributing effects, as well as the relative magnitudes of those effects compared to each other; this can be regarded as empirical evidence, backed by simulation results, to justify the use of slewing as the primary observational technique in future coded aperture telescope missions. We regard all of these results as essential steps that provide a solid foundation for the next stage of the BATSS project, the deep multi-slew survey over a variety of observation timescales, with the capacity to detect transient flares of astrophysical sources beyond GRBs which may have gone undetected under other hard X-ray and γ-ray survey methods.

Page intentionally left blank

Chapter 5

Conclusions and future directions

In this chapter I review important results and insights derived from the previous chapters of this dissertation, with a focus on the lessons learned from them and proposals for future improvement. In addition, I provide a glance into the work left for the BATSS project in the immediate future, and how its most important results may inform the planning of future hard X-ray survey missions.

The BATSS Imaging Technique

As evidenced by the results of the study of systematic effects that characterize images in this implementation of the BAT Slew Survey (Chapter 2), the imaging method employed has been highly successful in producing images with noise characteristics as close to the theoretical Poisson limit as have been achieved by any other methods using data from the BAT coded aperture telescope. This is particularly important given the fact that, unlike the case of their focusing counterparts, the systematics of a coded aperture telescope's detector plane affect local background levels over its entire field-of-view (FoV), since every point in its FoV is projected onto the entire detector (save for closed mask element shadows),

and as a result, the relatively high background of images from a coded aperture telescope become a major disadvantage of the observational technique as a whole.

In the case of BATSS images, we showed that background distributions obtained in timescales from single slews to years essentially conform to an unbiased Gaussian distribution of width 1σ (i.e. a statistical normal distribution of truly random events), unlike pointing-mode background distributions as large as 1.23σ for 1-day mosaicked (co-added) pointings (Krimm 2006). We also showed the time dependence of image background levels to be essentially Poisson-dominated at least up to $T_{\rm eff} \sim 3$ ksec, the characteristic timescale for BATSS monthly multi-slew images, and with 5σ sensitivities at the 100-sec characteristic exposure of single slews of 116.7 ± 1.1 mCrab in the 14–50 keV band and of 119.6 ± 1.2 mCrab in the 14–195 keV band. These results compare favorably with the extrapolation from the BAT 3-month high-latitude pointing survey result by Markwardt et al. (2005), which would yield a 5σ sensitivity of 120.2 ± 21.2 mCrab (14–195 keV) at 100 sec, but which was obtained at the 30 ksec–1 Msec timescale only after co-adding many pointings over the 3 months of that survey, in an analogous way to what we routinely do over single ∼100-sec slews for BATSS. Using the BAT pointing survey's own analysis tool, however, we showed those sensitivity levels are actually not achievable for single pointings at the 100-sec timescale of single slews, as the low photon count statistics become a much more limiting systematic issue for those observations than they do for slews, which means BATSS observations are uniquely positioned within the discovery phase space of faint, high-variablity, hard X-ray transient sources such as Gamma-Ray Bursts (GRBs).

Nevertheless, several important improvements can be considered for an upgraded version of the BATSS imaging method. In an effort to further reduce background levels, the single largest improvement can be achieved by implementing a bright source cleaning procedure, a version of which is already in use for pointing observations, and which is also

generally used for coded aperture telescopes in order to reduce the additional coding noise background produced by such sources. The data for pointing observations, however, have been taken in "survey" mode, not in "event" mode (see Section 2.1.3), but event data can be mask-tagged (ray-traced) at the position of any bright source within the FoV, even during a slew. We introduced mask-tagging in Section 4.3.2 as a procedure normally employed as a preliminary step in the production of GRB lightcurves (LCs), but it can also be used to "tag" photons from a known bright source and remove them from the event list (i.e. exactly the opposite of what is done to generate LCs) before accumulating a Detector Plane Image (DPI). Other systematics reduction methods, such as large-scale modeling of the of the DPI, or the removal of individual pixels that significantly deviate from the mean detector pixel count rate (apart from the hot/cold/disabled pixels already removed when creating detector quality maps, described in Section 3.7), generally require a large amount of photon count statistics, unlike the bright source cleaning procedure described, so they are likely to be largely ineffective, in very much the same way they are ineffective for short ($\lesssim 150$ sec) pointing observations.

One more noteworthy possible improvement for the BATSS imaging technique concerns the additional systematic term found in our empirical analysis of source flux uncertainties (Section 2.4.3, equation 2.11), which we attributed to a source point-spread function (PSF) that may have appreciably deviated from the nominal Gaussian $22'$ BAT PSF (FWHM), particularly in multi-slew observations. A likely cause of this effect is the high speed of spacecraft slewing ($\lesssim 1^\circ$/sec), which would naturally alter the PSF width in the direction of the slew. This would manifest itself as well in size of the 90% error radii (r_{90}, equation 2.14), which we verified in Section 4.4.2 for a number of GRBs that were detected by BATSS, BAT pointing and *Swift*-XRT do correspond to true 90% confidence radii in the statistical sense, but at the same time were generally larger than BAT pointing error radii for equal S/N.

The most likely solution to this problem would be to further reduce the 0.2-sec time binning within slew images to 0.1 sec or less, which would minimize the slewing speed effect but on the other hand would increase computation time by the same factor. The 0.2 sec time bin was chosen because this was also the time resolution of spacecraft attitude data, but nothing prevents us from interpolating the RA, Dec, and roll angle values within the attitude file in order to increase the imaging frequency.

The BATSS Data Pipeline

As discussed in Chapter 3, the implementation of the BATSS imaging technique into the BATSS data pipeline has shown in its successive stages of development to be an effective system for the processing and analysis of event-by-event slew data from *Swift*-BAT, making appropriate use of the the computational resources at its disposal, and making high-level data products readily available for further analysis in its hierarchical internal data storage infrastructure and through the BATSS website.

Major milestones in the development of the BATSS pipeline have included:

1. The beginning of its implementation in mid-2006 when we first proposed BATSS as a research project for Cycle 3 of *Swift*'s Guest Investigator (GI) program.

2. BATSS' acceptance by the *Swift* review committee in early 2007 as an "excellent" addition to the GI program.

3. The March, 2007, month-long testing phase which included BATSS' first Gamma-Ray Burst discovery (GRB 070326).

4. The August, 2007, acquisition and installation of the dedicated BATSS servers at the Harvard-Smithsonian Center for Astrophysics' Computational Facility.

5. The beginning of real-time, continuous slew data processing from October 25, 2007 onwards.

6. The major hardware and software upgrade over the first semester of 2010, which included the first implementation of archival slew data processing along with the production of higher-order multi-slew observations: orbital, daily, weekly, monthly, yearly, and full-survey.

7. The completion of the current version of the pipeline with the full implementation of the BATSS trigger database in April, 2011.

Throughout this development process, a major advantage of the pipeline infrastructure the has been the modularity of the BATSS software package, which has allowed some basic functions to remain virtually unmodified while others have undergone major revisions. This feature should continue to allow for seamless future upgrades by other researchers and graduate students who may want to make use of the BATSS pipeline, either in its current form or in a customized version. The guide to the BATSS data products of Appendix A, and the BATSS software tool guide of Appendix B, should also be of considerable use to help achieve that goal. In addition, the pipeline has also been designed for portability to other hardware systems, a feature that has not yet been tested in a real situation, but which is not anticipated to be a major obstacle for future development.

Despite the positive attributes of the BATSS system described here, it has also been subject to some major setbacks, and some important challenges still remain. Most consequential among the setbacks was the RAID system failure of December, 2009, when we lost the main data volume of the `luna` server along with all of the Level 1-3 data products within it, including the majority of the data products from the first 2 years of the survey. However, this provided the motivation for the major system upgrade that followed in 2010,

which included a new data storage solution with considerably more redundancy built into it and which has proven to be very robust so far, as well as a thoroughly upgraded software package. The new package on the one hand makes much more efficient use of the limited storage space, to the point that no upgrades to the storage capacity have been required since its implementation, and on the other hand we finally realized the goal of implementing a parallel processing of data from the *Swift* archive, which differs in several important ways from the raw data used in real-time slew data processing. This allowed us to recover and reprocess all of the lost data since the beginning of the survey, and also provided the opportunity to begin to create high-level multi-slew data products, which we are making heavy use of in our current analysis of the BATSS Multi-slew Hard X-ray Survey.

On the side of future challenges for pipeline development, the most immediate and consequential one would be a major upgrade to the BATSS website. In its current version, it does allow users to access results from every type of BATSS observation, both real-time and archival, as well as catalog tables of candidate sources from the BATSS trigger database, but its navigation and search features need some important improvements in order to make them more useful and accessible. A transient source activity monitor, modeled after the *Swift* website's Hard X-ray Transient Source Monitor (Krimm 2006) —built with data from BAT pointed observations—, would also be a critical addition to the BATSS website and a natural complement to the *Swift*-BAT team's effort. Since our transient source monitoring campaign has already been implemented within the BATSS pipeline, all that would be needed would be an appropriate user interface for ready access to the data products we have already generated.

The BATSS GRB Survey

The BATSS Gamma-Ray Burst Survey is the first realization of our analysis of scientific data from BATSS, and our first demonstration of the properties of the survey through the discovery of new, highly-variable astrophysical sources, of which GRBs are only one example though a crucially important one, since they constitute the primary science goal for *Swift*. During the survey period of 1,748 days (4.8 years) reported here, BATSS discovered a total of 19 GRBs that had not been detected in on-board pointing observations. Though a relatively small sample compared to the total number detected on board, it is in fact the largest contribution to the *Swift* GRB catalog out of all ground-analysis efforts. Through our analysis of their detection parameters and prompt emission energetics, we found several of them to possess several unusual features, probably more than would be found in any random sample of *Swift* GRBs of the same size: Our detection of GRB 081211B, for instance, was found to likely correspond to the faint extended emission from a short GRB (S-GRB) precursor that had occurred 120 sec before, and if so, this would be only the 11th *Swift*-BAT S-GRB with extended emission detected as of December, 2009, the end of the survey period for the BAT2 GRB Catalog (Sakamoto et al. 2011). Moreover, it was found that the precursor peak in fact occurred near the edge but still within the BAT FoV, hence the fact that BATSS detected the burst's faint extended emission (recorded fluence $S(15\text{–}150\text{ keV}) \sim 6 \times 10^{-7}$ erg/cm^2), while the on-board system missed its short emission peak, attest to BATSS' ability to detect emission from faint sources. Similarly, the lowest fluence recorded for a BATSS GRB was $\sim 1.2 \times 10^{-7}$ erg/cm^2/sec (15–150 keV) for GRB 090823 ($S/N = 7.8$), which places it at the bottom 2% of all long GRBs (L-GRBs) in the BAT2 catalog, and near the faint end of the fluence distribution accessible to *Swift*-BAT.

Another set of noteworthy BATSS GRBs is made up of GRB 071212, GRB 090823 and GRB 11011A, for which we have estimated the peak of their νF_ν distribution ($E_{\rm peak}$) to lie below 30 keV, which would place them in the category of extremely soft spectrum GRBs, or X-Ray Flashes (XRFs). Though it is now believed that XRFs may make part of the same continuum as harder spectrum GRBs, instead of the product of an altogether different physical process, they still constitute a rare category within *Swift* GRBs at $\sim$10% of the overall population, even though theoretical models predict their population to be of a similar size as that of proper (hard) GRBs. Their low detection rate by *Swift* has been attributed by Band (2006) to be due to an instrumental selection effect, which makes the BAT less sensitive to soft-spectrum bursts. Thus, it is first of all noteworthy that they constitute a larger proportion of the BATSS GRB sample than they do of the overall *Swift* GRB population, and it also implies that their study, when they do occur, is of greater importance if we are to be able to characterize this population and place proper constraints on their physical parameters as well as it has been done for hard GRBs.

As discussed at length in Sections 4.5 and 4.6, one more important conclusion of the BATSS GRB survey is the remarkable GRB detection rate achieved per unit instrument time, a significant 45% above the GRB pointing-mode detection rate achieved within the same 4.8-year survey period. We then explored this result via a GRB detection simulation model, which revealed that the sky coverage effect was in fact more significant than the improved-sensitivity effect in enhancing GRB detection probabilities. It should be noted, however, that both the 45% excess figure as well as that obtained by simulation were shown to be dependent on the particular slew sample chosen. As we established in our characterization of the BATSS observational program, our sample of downlinked slews was highly biased with respect to the total *Swift* slew sample, since the slew data captured for BATSS was capped by *Swift* mission operations at 120 sec for most of the survey,

hence 120-sec slews were overrepresented in our sample, while the 41% of slews longer than 120 sec were severely underrepresented. Since the simulation results showed that there is a clear and direct correlation between the length of the slew and the increase in GRB detection probability with respect to a pointing of equal exposure, it would actually be expected for this excess to rise if an unbiased slew sample (or, in the limit, a purely scanning sample) had been used.

With respect to possible future improvements to increase the BATSS GRB detection yield, there are are two particularly important ones to consider: the first one is based on the fact that no S-GRBs (or the short precursor of a S-GRB with E.E.) were detected independently during the BATSS survey, a problem that generally affects the BAT telescope as well, as can be observed from the much lower proportion of S-GRBs it has detected compared to BATSE. This has been attributed to an instrumental selection effect related to the fact that the BAT is an imaging telescope, which would make it less suited to detecting the short (< 2 sec), faint spikes that characterize S-GRBs. On the other hand, the lack of S-GRB detections by BATSS, which arguably more severe than that of the BAT in general, is primarily due to the fact that our detection algorithm performs detection only after an entire slew has been co-added. This may not be a suitable prescription for detection of S-GRBs, which may well have been present within the BATSS FoV but would have been buried by the additional noise of an image integrated over several tens of seconds.

The remedy to this problem would be to begin performing detections over *portions* of a slew instead of only on full slews (i.e. implement *time-resolved* detection in addition to the current *time-averaged* detection). Given the well-defined duration of S-GRBs of $\lesssim 2$ sec, a reasonable prescription would be to perform detection every 3-sec (i.e. after imaging a set of 15 0.2-sec images), for instance, and then shift the time window in increments of either 1 or 2 sec in order to avoid S-GRBs to be spilt between consecutive time bins.

In terms of the required pipeline infrastructure, this would be an operation to be performed within the pipeline's detection thread (Section 3.8), while the imaging thread continues to run unchanged. Since it is imaging thread the one that takes longer to run in the current implementation, it is possible that the overall performance would not be severely affected and no additional computational resources would be required, though the detection thread would likely become the one that takes longer to run under the new implementation.

Finally, the second improvement is related to the choice of a coding fraction (CF) threshold discussed in Section 2.2.3, which we derived from a limited set of observations over the Crab. This choice has influenced the BATSS GRB survey results in two opposite ways: on the one hand, after lowering the CF threshold from 20% to 15% during the 2010 software upgrade, we found in the earlier archival data three GRBs we had not detected before: GRB 071212, GRB 080806, and GRB 100120A. On the other hand, GRB 090118, which we had detected and reported in real time when the CF threshold was 20%, was no longer found in the archival data reprocessing after lowering the threshold to 15%. Given this evidence, it is clear first of all that lowering the CF threshold to 15% was the correct choice to make, but at the same time a price was paid by covering certain faint sources with the relatively noisy 15–20% CF region, despite the gain of additional exposure time. A better compromise would be found if we were able to image the same slew at an array of $\sim$2–3 different CF thresholds, which would be certain to make a further improvement in the BATSS GRB detection rate with respect to a pipeline with a single CF imaging threshold, whatever that threshold may be. However, this is not seen to be as critical an improvement as the aforementioned implementation of time-resolved detection, which would be certain to broaden the science discovery space for BATSS to include at least S-GRBs and possibly also other low-duty cycle astrophysical sources at the $\sim$1-sec timescale.

Current work and future prospects

Concerning the immediate prospects for BATSS, we are currently in the process of summarizing results from the BATSS Multi-slew Hard X-ray Survey, which we plan to include in a forthcoming publication. As mentioned in the Introduction (Chapter 1), performing an all-sky, hard X-ray (15–150 keV) slew survey is the ultimate goal for BATSS, since it is the first slew survey ever with a coded aperture imaging telescope, the type of instrument that is necessary in order to locate sources in the hard X-ray sky with arcminute-level precision. As mentioned in Section 2.1.2, such a precision, in the order of the FoV of most focusing telescopes, would readily enable those instruments to perform follow-up observation and multi-wavelength analysis. As discussed in Chapter 4, since GRBs are the type of transient most likely to be observed over individual slews, and those single-slew observations have been the exclusive focus of that chapter, the focus for the full survey is the multi-slew observations, particularly those in the orbital through monthly timescales, which is where the prime time-domain discovery phase space lies for BATSS. Given that the BAT pointing survey has been exclusively focused in performing as deep a survey as possible —currently 70-months long as of the BAT team's latest published result (Baumgartner et al. 2011)—, instead of performing a time-resolved analysis of the type we have done with BATSS, the goal of providing a fitting complement to the BAT pointing survey would be achieved by our multi-slew survey work.

Regarding the long-term prospects, our observed GRB detection rate of 5.62 GRBs/Msec of instrument time, or 0.49 GRBs/day, is undoubtedly the most consequential result for the planning of future hard X-ray missions, since it constitutes an empirical demonstration of the potential for an all-slewing coded aperture telescope mission to push the boundary for discovery compared to an otherwise equal pointing-based mission such as *Swift*. The most immediate realization of such a mission would be provided by the Brazilian-US

MIRAX Hard X-ray Imager mission (*MIRAX-HXI*, Grindlay 2012), projected to be launched in 2017, with a significant participation from our research group. The payload consists of an array of four (4) coded aperture telescopes, laid out in a fixed, upward-pointing position within the spacecraft. As the satellite orbits the Earth every 96 minutes, the telescopes scan the entire southern sky, essentially playing the role of an all-slewing, hard X-ray coded aperture imager. Since the equivalent "slewing" speed in this case would be $360^\circ/96$ min $= 3.75'$/sec —much lower than the $\sim 60'$/sec top slewing speed of *Swift*—, the appreciable systematic effects that affected BATSS images as a consequence of *Swift*'s fast slewing speeds would be largely eliminated. This would place *MIRAX-HXI* at an ideal position to demonstrate the capabilities of an all-slewing coded aperture mission, and enhance its prospects of achieving its stated goal of increasing the high-redshift-GRB and short-GRB samples, a goal which *Swift* has achieved with only modest success.

Appendix A

BATSS data products

This appendix makes a review of the data products generated by the BATSS data pipeline presented in Chapter 3 and stored on the BATSS servers at the computational facility at Harvard-Smithsonian Center for Astrophysics. After an introduction on the system infrastructure necessary to access and manipulate the data, and on the definitions of BATSS data levels, the BATSS data products are categorized and presented according to their rank within the data level hierarchy.

A.1 System Infrastructure

This section presents the basic requirements necessary to access and manipulate BATSS data products. Section A.1 states the prerequisites for access to the data volumes of the BATSS dedicated servers. Section A.1 introduces the root directories for BATSS data product storage, including the BATSS central data volume and the individual machine data volumes, and gives an overview of the type of products stored in each. Section A.1 then presents the common data formats used for BATSS data products and defines the basic terms to be later referenced in the description of the individual products.

A.1.1 System Access

As introduced in Section 3.2, the data products from the BATSS pipeline are stored on the volumes of the three (3) dedicated BATSS servers: "`luna`" (`luna.cfa.harvard.edu`), "`mond`" (`mond.cfa.harvard.edu`), and "`dahl`" (`dahl.cfa.harvard.edu`). They are part of the IT network of the High Energy Astrophysics Division (HEAD) of the Harvard-Smithsonian Center for Astrophysics (CfA),[1] and maintained by the staff of the HEAD Systems Group. All issues regarding user access to the CfA HEAD network are handled by the help desk of the HEAD Systems Group (`syshelp@head.cfa.harvard.edu`), and a comprehensive list of the services they provide can be found on their website.[2] Access to the data volumes on these machines can be gained after login into any server on the CfA HEAD network.

A.1.2 Root Directory

The data products presented in this Appendix are spread among four (4) data volumes in the three dedicated BATSS servers listed on Table 3.1. As indicated in Section 3.2, `luna0` is the central data volume where both the raw (BATSS Level 0–1) and high-level (BATSS Level 3) data products are stored, whereas the intermediate (BATSS Level 2), observation-level products are stored in the volumes `luna1`, `mond1` and `dahl1` of their corresponding servers. BATSS data levels are defined in Section A.2 of this appendix.

All data products in the central volume `luna0` reside in *BATSS products* root directory, whose name as a UNIX environment variable and fully qualified path are:

`$BATSS_PRODUCTS` ≡ `luna.cfa.harvard.edu:/data/luna0/acopete/BATSS/products/`

---

[1] `http://www.cfa.harvard.edu/hea/`

[2] `http://hea-www.harvard.edu/HEAD-info/syshelp/help.html`

On the other hand, the observation-level data in the volumes `luna1`, `mond1` and `dahl1` are stored in their *BATSS data* root directories:

$$\texttt{\$BATSS\_DATA} \equiv \begin{cases} \texttt{luna.cfa.harvard.edu:/data/luna1/acopete/BATSS/data/} \\ \texttt{mond.cfa.harvard.edu:/data/mond1/acopete/BATSS/data/} \\ \texttt{dahl.cfa.harvard.edu:/data/dahl1/acopete/BATSS/data/} \end{cases}$$

The individual data products described in the rest of this appendix should therefore be assumed to reside within the substructure of these directories, unless otherwise indicated.

A.1.3 Data Formats

Most of the data products described here are files in the astronomy standard FITS format[3], each of them composed of one or more file *extensions* or data units. Each FITS file extension is in turn composed first of a FITS *header*, which is a text file containing information on the extension encoded as a number of header *keywords*, each with a unique name, a value, and a description (optional), complemented by *comment* and *history* fields which provide further general information on the file and/or the extension. In addition, each file extension may have an *extension data product* attached to it; in the case of BATSS, the FITS extension data is always either a 2-D *image* or a *binary table* of varying size.

FITS files, including all of the BATSS FITS-format data products, can be read and manipulated in a number of software platforms of the user's choice, though the BATSS pipeline has generally produced them with a combination of tools from either the UNIX-based HEASoft/FTOOLS software package[4], or analysis tools written in the Interactive Data

[3] `http://heasarc.gsfc.nasa.gov/docs/heasarc/fits.html`

[4] `http://ftools.gsfc.nasa.gov/`

Language (IDL), including the BATSS software tools themselves. Further information on these software packages and analysis tools can be found in Appendix B.

In addition to FITS data files, other formats for BATSS data products include:

Text files which normally contain data logs from the BATSS pipeline and can be used for diagnostics purposes.

PostScript files which contain reports and summaries from the various stages of the BATSS data pipeline.

HTML files which contain summaries of BATSS results for publication to the BATSS webpage.[5]

A.2 BATSS data levels

BATSS data level definitions are analogous to the standards of the High Energy Astrophysics Science Archive Research Center (HEASARC)[6] and of the *Swift* mission, which are specified in the *Swift* Technical Handbook (*Swift* Science Center 2008). Certain variations to the *Swift* standards have been introduced within the context of the BATSS pipeline (illustrated in the flow chart of Figure 3.3), however, with the purpose of more closely reflecting the hierarchy of the BATSS data structure. This section serves as an introduction to the full set of BATSS data products as a whole, while the rest of this appendix presents the details of the specific products within each category organized into individual sections.

[5] `http://hea-www.harvard.edu/BATSS/`

[6] `http://heasarc.gsfc.nasa.gov/`

The four (4) levels of the BATSS data structure, further described in the following sections of this appendix, are defined as follows:

BATSS Level 0 — Input data: These are the *Swift* data products as generated in their original form at the *Swift* Data Center (SDC), prior to any BATSS pipeline processing. They have been either received in real time by the BATSS servers, or downloaded directly from the *Swift* Data Archive. As such, the files follow the conventions laid out in the *Guide to the Swift Archive* (Angelini 2007), though their location within the BATSS directory structure may not necessarily match that of the *Swift* archive. These are all FITS files which, as categorized within the structure of *Swift* data levels, correspond to either raw, uncalibrated *Swift* Level 1 data, or to pre-processed *Swift* Level 2 data. All BATSS Level 0 products are kept in the BATSS central data volume (`luna0`) in order to remain available for re-processing by future, updated versions of the BATSS data pipeline.

BATSS Level 1 — Pre-processed data: These files are the main output of the pre-processing (BATSS daemon) stage of the BATSS pipeline (Section 3.5), in both its real-time and archival implementations. In general, these files are the result of parsing the input BATSS Level 0 files, determining the periods of spacecraft slewing that define BATSS observations, selecting the relevant intervals for further processing of individual observations, and organizing the data by BATSS Observation ID rather than by *Swift* Observation ID. As discussed in Section 3.5, a different nomenclature has been adopted for BATSS observations, since the convention for *Swift* observations bears no special meaning in the case of BATSS slews. BATSS Level 1 files are created and stored in the central data volume, though they are later copied to the individual machines and modified over the course of processing of individual observations.

BATSS Level 2 — Observation-level data: These files are the end result of the imaging and detection stages of the BATSS pipeline (Sections 3.7 and 3.8), whose main results are sky images and detection catalogs for individual observations in each of 3 energy bands: Soft (15–50 keV), Hard (50–150 keV) and Broad (15–150 keV). Because of their large size, sky image files are kept in the data volumes of the individual machines where they were created, while the detection catalogs are copied to the BATSS central data volume for further processing by the BATSS trigger stage (Section 3.9).

BATSS Level 3 — Source-level data: These high-level data products are the result of analyzing the detection catalogs from individual observations, after comparing them against themselves as well as to catalogs of known sources. While matches to known transients are set apart for purposes of individual source monitoring, unidentified detections are further categorized according to their likelihood of corresponding to real sources and catalogued in the BATSS trigger database, according to the criteria described in Section 3.9. All BATSS Level 3 data products are generated and stored in the BATSS central data volume.

The following sections expand on the data products on this list. The directories listed on the tables are referenced with respect to the root directories presented Section A.1; they are represented by the environment variables `$BATSS_PRODUCTS`, which is the root of the central data volume `luna0`, and `$BATSS_DATA`, which is any of the individual BATSS machine data directories, whichever applies to the observation in question. As for the files, they are referenced within the subdirectories indicated above each of them. In each case, the tables specify: the item number of each data product within its category (column 1), the data product format (column 2) and its corresponding file name (column 3), as well as a short description of their format and contents (column 4).

A.3 BATSS Level 0 products

The BATSS Level 0 products (input data products) are listed in Table A.1. These are created by the *Swift* Data Center and their characteristics are described in detail by Angelini (2007). They are divided into the following categories as shown in the table:

a. Original real-time data products: These are the files transferred directly into the BATSS central data volume from the SDC in real time, using the local user account `sbarthel`. The root directory for these files is:

   `luna.cfa.harvard.edu:/data/luna0/sbarthel/batss/`

   Transferred files in this category include *Swift* spacecraft attitude files, uncalibrated BAT event files, BAT detector enable files, and energy calibration files. The way they are manipulated at the BATSS daemon stage is described in Section 3.5.

b. As-Flown Science Timeline (AFST) files: These files are posted in HTML format to the *Swift* webpage to indicate the actual observation schedule for each completed day of the mission. This schedule differs from the Pre-Planned Science Timeline (PPST) whenever on-board triggers have taken place, followed by Automated Target (AT) observations. AFST files are downloaded and parsed as a preliminary step to the downloading of archival data by the tool `BATSS_daemon_archival`.

c. Original archival data products: These are the files downloaded directly from the *Swift* archive after determining the actual observation schedule for each day of the mission. As in the case of real-time data, the relevant files include *Swift* spacecraft attitude files, BAT event files, and BAT detector enable files. Unlike real-time event files, however, archival event files are energy calibrated (*Swift* Level 2) files, thus energy calibration files are in principle not necessary. In addition, spacecraft orbital files, which are not made available in real time, are downloaded in order to identify regions of Earth/Sun/Moon occultation at the imaging stage.

TABLE A.1
Section A.4: BATSS Level 0 products — Input data

#	Product type	Format	File name	Description
a. Original real-time data				
1	Real-time data pass directory	Directory	`/data/luna0/sbarthel/batss/pass_[YYYYDDDHHMM]/bat2fits6_[YYYYMMDD][_hhmm]/`	Real-time data from date-time `YYYYDDDHHMM` (year-DOY-hour-minute format), with the observation taken on `YYYYMMDD` (year-month-day format). A time string `hhmm` is included only in case of several data passes per observation.
2	*Swift* real-time attitude file	FITS	`./sw99999999000b1e5x001.att`	One real-time spacecraft attitude file per data pass directory. All are given the same file name, and are only distinguished by the directory they are located in.
3	BAT real-time event file	FITS	`./sw[XXXXXXXXYYY]bevshto_uf[_NN].evt.gz`	Uncalibrated (*Swift* Level 1) real-time BAT event file from *Swift* Observation ID `XXXXXXXXYYY`, which may include both pointing and slew data. The `NN` string differentiates event files in the same data pass.
4	BAT real-time detector enable file	FITS	`./swt[TTTTTTTTTT]bdecb.fits.gz`	Real-time file of BAT enabled/disabled detector pixels, designated by Mission Elapsed Time `TTTTTTTTTT` (MET, defined as seconds since epoch 01/01/2001 UT) .
5	BAT real-time energy calibration file	FITS	`./sw[XXXXXXXXYYY]bcbo[OOOO]g[GGGG].fits.gz`	Real-time energy calibration file for BAT detector events from *Swift* Observation ID `XXXXXXXXYYY`, designated by offset setting `OOOO` and gain setting `GGGG`, expressed as hexadecimal (HEX) numbers.
b. As-Flown Science Timeline (AFST) data				
6	*Swift* as-flown science timeline data directory	Directory	`$BATSS_PRODUCTS/afst/`	Directory of as-flown timeline data used for retrieval of archival data.
7	*Swift* as-flown science timeline file	HTML	`./afst_[YYMMDD].html`	HTML table with as-flown science timeline for date `YYMMDD`, as posted to the *Swift* website.
c. Original archival data[a]				
8	Archival *Swift* observation directory	Directory	`$BATSS_PRODUCTS/[YYYY_MM]/obs/[XXXXXXXXYYY]/`	Directory of *Swift* observation data from month `YYYY_MM` and *Swift* Observation ID `XXXXXXXXYYY`, as downloaded from the *Swift* archive.
9	*Swift* archival attitude file	FITS	`./auxil/sw[XXXXXXXXYYY]sat.fits.gz`	Spacecraft attitude file for *Swift* observation.
10	*Swift* archival orbital file	FITS	`./auxil/sw[XXXXXXXXYYY]sao.fits.gz`	Spacecraft orbital file for *Swift* observation.
11	BAT archival detector enable file	FITS	`./hk/sw[XXXXXXXXYYY]bdecb.hk.gz`	BAT detector enable/disable data for *Swift* observation.
12	BAT archival event file	FITS	`./bat/event/sw[XXXXXXXXYYY]bevshsl.evt.gz`	BAT event file for *Swift* observation.

[a]Files deleted upon completion of the BATSS daemon stage

A.4 BATSS Level 1 products

The BATSS Level 1 (pre-processed) data products are listed in Table A.2. They are divided into the following categories as shown on the table:

a. Daily attitude data: Consolidated spacecraft attitude data files after parsing input attitude files. One consolidated attitude file is created per day (UT), for both real-time and archival data. These files are created prior to identifying and defining the individual BATSS slew observations for each day.

b. Consolidated BAT real-time data by *Swift* observation: Input BAT real-time data products, organized by *Swift* Observation ID, after parsing input BAT event, energy calibration, and detector enable files. Consolidated BAT event files, unlike input real-time event files, have also been energy-calibrated.

c. BATSS real-time queue files: FITS-formatted files with queue of all real-time BATSS observations, as identified from the daily attitude data files. Only *single-slew* observations are logged into real-time queue files. Queue files are organized as one file per day and one observation per file extension, with the extension header containing all relevant information on the observation logged as header keywords, and no additional data product attached to the extension. Observations with captured event data are flagged for further processing.

d. BATSS archival queue files: Queue files for archival BATSS observations, as identified from the corresponding daily attitude data files. Archival observation types logged into queue files include *single-slew*, *orbital*, *daily*, *weekly*, *monthly*, *yearly* and *survey*, as defined in Section 3.5. Individual observations are logged as FITS file extensions of their corresponding queue files, and those with captured event data are flagged for further processing.

e. BATSS single-slew observation input data: Every single-slew observation, whether real-time or archival, has a data directory associated with it within the `$BATSS_PRODUCTS` root directory of the BATSS central data volume `luna0`. Within its directory, every slew observation also includes a BATSS spacecraft attitude file and a Good Time Interval (GTI) file, which cover both the slewing interval as well as the preceding and following pointing intervals. In addition, archival slew observations also include a spacecraft orbital file. Finally, in the case of slews with captured BAT event data, an energy-calibrated event file is included as well.

f. BATSS control data: The BATSS control data directory contains a number of FITS-format housekeeping files used by the control routines of the BATSS software package, further discussed in Section B.7 of Appendix B. In addition, each of the machine threads for individual observation processing also has a machine control file associated with it, which tracks the flow of its imaging and detection threads, and those files are stored within this directory as well.

TABLE A.2
Section A.4: BATSS Level 1 products — Pre-processed data

#	Product type	Format	File name	Description
a. Daily attitude data				
1	*Swift* daily attitude data directory	Directory	`$BATSS_PRODUCTS/[YYYY_MM]/attitude/`	Directory of *Swift* daily attitude data (both real-time and archival) from month `YYYY_MM`.
2	*Swift* real-time daily attitude files	FITS	`./attitude_[YYMMDD]_realtime.fits.gz`	*Swift* spacecraft attitude file for date `YYMMDD` after consolidating all real-time data.
3	*Swift* archival daily attitude files	FITS	`./attitude_[YYMMDD].fits`	*Swift* spacecraft attitude file for date `YYMMDD` after consolidating all archival data.
b. Consolidated BAT real-time data by *Swift* observation				
4	Consolidated BAT real-time data directory	Directory	`$BATSS_PRODUCTS/[YYYY_MM]/obs_realtime/`	Directory of BAT real-time data from month `YYYY_MM` after consolidating input BATSS Level 0 data products.
5	Consolidated BAT real-time event files	FITS	`./[XXXXXXXXYYY]/sw[XXXXXXXXYYY]bevshto.evt.gz`	BAT real-time event file after consolidating all data for *Swift* observation `XXXXXXXXYYY` and performing energy calibration.
6	Consolidated BAT real-time detector enable files	FITS	`./detmap/swt[TTTTTTTTTT]bdecb.fits.gz`	Real-time file of BAT enabled/disabled detector pixels at MET time `TTTTTTTTTT`, copied unmodified from original data pass directory.
7	Consolidated BAT real-time energy calibration files	FITS	`./gainoffs/sw[XXXXXXXXYYY]bcbo[OOOO]g[GGGG].fits.gz`	Real-time energy calibration file for BAT detector events from *Swift* Observation ID `XXXXXXXXYYY` and offset/gain settings `OOOO`/`GGGG` (HEX). Copied unmodified from original data pass directory.
c. BATSS real-time queue files				
8	BATSS real-time queue file directory	Directory	`$BATSS_PRODUCTS/[YYYY_MM]/queue_realtime/`	Directory of BATSS real-time queue files from month `YYYY_MM`.
9	BATSS real-time single-slew queue files	FITS	`./queue_[YYMMDD]_slew.fits.gz`	Queue file of all BATSS real-time single-slew observations from date `YYMMDD`, one observation per file extension.
d. BATSS archival queue files				
10	BATSS archival queue file directory	Directory	`$BATSS_PRODUCTS/[YYYY_MM]/queue/`	Directory of BATSS archival queue files from month `YYYY_MM`.
11	BATSS archival single-slew queue files	FITS	`./queue_[YYMMDD]_slew.fits`	Queue file of all BATSS archival single-slew observations from date `YYMMDD`, one observation per file extension.
12	BATSS archival orbital queue files	FITS	`./queue_[YYMMDD]_orbital.fits`	Queue file of all BATSS archival orbital observations from date `YYMMDD`, one observation per file extension.

TABLE A.2 (continued)
Section A.4: BATSS Level 1 products — Pre-processed data

#	Product type	Format	File name	Description
13	BATSS archival daily queue files	FITS	`./queue_[YYMMDD]_daily.fits`	Queue file of BATSS archival daily observation `YYMMDD` (one file extension).
14	BATSS archival weekly queue files	FITS	`./queue_[YYMMDD]_weekly.fits`	Queue file of BATSS archival weekly observation `YYMMDD` (one file extension).
15	BATSS archival monthly queue files	FITS	`./queue_[YYMM]_monthly.fits`	Queue file of BATSS archival monthly observation `YYMM` (one file extension).
16	BATSS archival yearly queue files	FITS	`$BATSS_PRODUCTS/yearly/queue_[YYYY]_yearly.fits`	Queue file of BATSS archival yearly observation `YYYY` (one file extension).
17	BATSS archival survey queue file	FITS	`$BATSS_PRODUCTS/survey/queue_BATSS_survey.fits`	Queue file of BATSS archival survey observation (one observation, one file extension).
e. BATSS single-slew observation input data				
18	BATSS single-slew observation input data directory	Directory	`$BATSS_PRODUCTS/[YYYY_MM]/slew[_realtime]/[YYMMDD]/[YYMMDD_HHhMMmSSs+XXXs]/`	Directory of input data products for single-slew observation `YYMMDD_HHhMMmSSs+XXXs`. Real-time data products are stored in `slew_realtime` subdirectories, while archival data products are stored in `slew` subdirectories.
19	BATSS single-slew spacecraft attitude files	FITS	`./slew_[YYMMDD_HHhMMmSSs+XXXs].att.gz`	Spacecraft attitude file for BATSS single-slew observation `YYMMDD_HHhMMmSSs+XXXs`.
20	BATSS single-slew spacecraft orbital files	FITS	`./slew_[YYMMDD_HHhMMmSSs+XXXs].sao.gz`	Spacecraft orbital file for BATSS single-slew observation (archival data only).
21	BATSS single-slew Good Time Interval (GTI) files	FITS	`./slew_[YYMMDD_HHhMMmSSs+XXXs].gti.gz`	Good Time Interval file for BATSS single-slew observation.
22	BATSS single-slew event files[a]	FITS	`./slew_[YYMMDD_HHhMMmSSs+XXXs].evt.gz`	Event file for BATSS single-slew observation.
f. BATSS control data				
23	BATSS control data directory	Directory	`$BATSS_PRODUCTS/control/`	Directory of BATSS control files.
24	BATSS software tool control files	FITS	`./[BATSS_control_tool].fits`	Housekeeping files used by the control routines of the BATSS software package (Section B.7)
25	BATSS machine control files	FITS	`./machines/[machine_disk]_[thread].fits`	Housekeeping file to track the status of observation processing thread `[thread]` on individual machine disk `[machine_disk]`. Machine disk strings for the corresponding data volumes of the BATSS dedicated servers (Section 3.2) are `luna1`, `mond1` and `dahl1`.

[a] Only for observations with captured event data

A.5 BATSS Level 2 products

Once an individual BATSS observation with captured event data has been assigned to an individual machine at the BATSS queue stage of the data pipeline (Section 3.6), the BATSS imaging and detection stages take place locally on the machine, generating a number of BATSS Level 2, observation-level data products. The product types are listed in Table A.3, which shows them divided in the following categories:

a. BATSS single-slew observation imaging data: single-slew observation imaging (both real-time and archival) begins with the creation of a local data directory for the observation on the machine it was assigned to, as well as an *observation FITS file* initialized using the FITS header of the corresponding extension for the observation in its BATSS queue file. This file then centralizes all of the processing data for the observation, by keeping a log of the results of the pipeline stages that follow in the header of its primary file extension. The spacecraft attitude, spacecraft orbit (for archival observations), good time interval (GTI), and event files are copied from the BATSS central data volume and serve as inputs for the BATSS imaging stage (Section 3.7). Output products include the detector quality map file, BAT partial coding map file, as well as the 6 sky image files of the co-added slew, representing the Zenithal Equal Area (ZEA) sub-projections of the quad-cube full-sky projection that has been implemented for BATSS observations (Section 2.2.2).

b. BATSS single-slew observation detection data: residing in the same local data directory as the single-slew imaging data products, the output files of the BATSS detection stage (Section 3.8) include the detection catalog file as well as a number of files in various formats that present the results of BATSS processing at the observation level. The detection catalog file contains the lists of individual detections made as FITS binary

table extensions: the uncatalogued BATSS detections are listed in the first file extension, while each of the following extensions contains the matches to each of the known source catalogs that were searched. These detections are also logged in text format as *region files* which can be then be read by interactive analysis applications such as DS9[7]. The `BATSS_results` tool also generates observation-level output in the form of full-sky Cartesian (CAR) projection FITS files, PostScript-format reports (at both the local and global levels), and HTML-format summaries for the BATSS webpage.

c. BATSS higher-order observation imaging data: since sky images of BATSS higher-order observations are obtained from image files already projected onto the BATSS full-sky projection, imaging data products for these observations are limited to only the local data directory, the observation FITS file which centralizes the processing information in the same way as for slew observations, and the output set of 6 ZEA sub-projection files of the quad-cube, full-sky projection.

d. BATSS higher-order observation detection data: This is a similar set of output data products as for the single-slew observations. The detection catalog file lists the catalogued and uncatalogued detections in all energy bands as FITS binary tables, and they are logged into detection region files as well. As in the case of single-slew observations, other observation-level output files include the CAR-projection FITS file —which shows the 6 ZEA sub-projection images merged into a single full-sky image— , PostScript local and global observation reports, and HTML summary report for the BATSS webpage. Because of the larger FoV of higher-order observations, with the monthly, yearly, and survey observations normally covering the entire sky, images in higher-order observation reports are shown in the full-sky Aitoff projection.

---

[7] `http://hea-www.harvard.edu/RD/ds9/site/Home.html`

TABLE A.3
Section A.5: BATSS Level 2 products — Observation-level data

#	Product type	Format	File name	Description
a. BATSS single-slew observation imaging data				
1	BATSS single-slew obs. machine data directory	Directory	`$BATSS_DATA/[YYYY_MM]/slew[_realtime]/[YYMMDD]/[YYMMDD_HHhMMmSSs+XXXs]/`	Directory of imaging data products for single-slew observation `YYMMDD_HHhMMmSSs+XXXs`, in root data directory `$BATSS_DATA` of the BATSS machine the observation was assigned to. Real-time data products are stored in `slew_realtime` subdirectories, while archival data products are stored in `slew` subdirectories.
2	BATSS single-slew observation FITS files	FITS	`./[slew_fileroot].fits`	FITS file log with all processing information on BATSS single-slew observation. For this and following data products, `[slew_fileroot]` corresponds to string `slew_[YYMMDD_HHhMMmSSs+XXXs]`.
3	BATSS single-slew spacecraft attitude files	FITS	`./[slew_fileroot].att.gz`	Spacecraft attitude file for BATSS single-slew observation, copied unmodified from input data directory in BATSS central data volume.
4	BATSS single-slew spacecraft orbital files	FITS	`./[slew_fileroot].sao.gz`	Spacecraft orbital file for BATSS single-slew observation, copied unmodified from input data directory in BATSS central data volume (archival data only).
5	BATSS single-slew Good Time Interval (GTI) files	FITS	`./[slew_fileroot].gti.gz`	Good Time Interval file for BATSS single-slew observation, copied unmodified from input data directory in BATSS central data volume.
6	BATSS single-slew event files	FITS	`./[slew_fileroot].evt.gz`	Event file for BATSS single-slew observation, copied unmodified from input data directory in BATSS central data volume.
7	BATSS single-slew detector quality map files	FITS	`./[slew_fileroot].mask.gz`	Detector quality map for BATSS single-slew observation, created by `BATSS_qmap_create`.
8	BATSS single-slew partial coding map files	FITS	`./[slew_fileroot].img.pc.gz`	Partial coding map of BAT FoV for BATSS single-slew observation, created by `BATSS_pcmap_create`.
9	BATSS single-slew sky image files (ZEA projection)	FITS	`./[slew_fileroot].ZEA_[1-6]of6.fits.gz`	Sky image files for BATSS single-slew observation, one file for each of 6 individual Zenithal Equal Area (ZEA) sub-projections of full-sky, quad-cube projection. Created by `BATSS_add`.

TABLE A.3 (continued)
Section A.5: BATSS Level 2 products — Observation-level data

#	Product type	Format	File name	Description
b. BATSS single-slew observation detection data				
10	BATSS single-slew obs. machine data directory	Directory	`$BATSS_DATA/[YYYY_MM]/slew[_realtime]/[YYMMDD]/[YYMMDD_HHhMMmSSs+XXXs]/`	Directory of detection data products for single-slew observation `YYMMDD_HHhMMmSSs+XXXs`. Same as directory of imaging data products.
11	BATSS single-slew detection catalog files	FITS	`./[slew_fileroot].catalog.fits.gz`	Catalog file of BATSS single-slew detections, both catalogued and uncatalogued. Created by `BATSS_celldetect`
12	BATSS single-slew detection region files	TXT	`./regfiles/[slew_fileroot].ZEA_[1-6]of6.[catalog-eband].reg`	Region files of BATSS single-slew detections, one file for each catalog-energy band combination (string `[catalog-eband]`). Created by `BATSS_celldetect`.
13	BATSS single-slew sky image files (CAR projection)	FITS	`./[slew_fileroot].CAR.fits.gz`	Sky image file for BATSS single-slew observation, with each image in a single full-sky Cartesian (CAR) projection. Created by `BATSS_results`.
14	BATSS single-slew detection reports (local)	PS	`./[slew_fileroot].[eband].local.ps`	Report files of BATSS single-slew detections, one file per energy band, one page per detection. Created by `BATSS_results`.
15	BATSS single-slew observation reports (global)	PS	`./[slew_fileroot].[eband].global.ps`	Report files of global results from BATSS single-slew observations, one file per energy band. Created by `BATSS_results`.
16	BATSS single-slew full-sky images (Orthographic projection)	PNG	`./html/[slew_fileroot].[eband].png`	Full-sky images (Orthographic projection) and detections from BATSS single-slew observation, one image per energy band, for publication on BATSS website. Created by `BATSS_results`.
17	BATSS single-slew HTML report files	HTML	`./html/[slew_fileroot].[eband].html`	HTML report files from BATSS single-slew observation, one file per energy band, for publication on BATSS website. Created by `BATSS_results`.

TABLE A.3 (continued)
Section A.5: BATSS Level 2 products — Observation-level data

#	Product type	Format	File name	Description
c. BATSS higher-order observation imaging data				
18	BATSS higher-order obs. machine data directory	Directory	`$BATSS_DATA/[obs_dir]/`	Directory of imaging data products for higher-order observation, in root data directory `$BATSS_DATA` of the BATSS machine the observation was assigned to. `obs_dir` corresponds to the subdirectory strings: Orbital: `[YYYY_MM]/orbital/[YYMMDD_HHhMMmSSs]/` Daily: `[YYYY_MM]/daily/[YYMMDD]/` Weekly: `[YYYY_MM]/weekly/[YYMMDD]/` Monthly: `[YYYY_MM]/monthly/` Yearly: `yearly/[YYYY]/` Survey: `survey/`
19	BATSS higher-order observation FITS files	FITS	`./[obs_fileroot].fits`	FITS file log with all processing information on BATSS higher-order observation. For this and following data products, `obs_fileroot` corresponds to the file root strings: Orbital: `orbit_YYMMDD_HHhMMmSSs` Daily: `day_YYMMDD` Weekly: `week_YYMMDD` Monthly: `month_YYMM` Yearly: `year_YYYY` Survey: `BATSS_survey`
20	BATSS higher-order obs. sky image files (ZEA projection)	FITS	`./[obs_fileroot].ZEA_[1-6]of6.fits.gz`	Sky image files for BATSS higher-order observation, one file for each of 6 individual Zenithal Equal Area (ZEA) sub-projections of full-sky, quad-cube projection. Created by `BATSS_merge`.

TABLE A.3 (continued)
Section A.5: BATSS Level 2 products — Observation-level data

#	Product type	Format	File name	Description
d. BATSS higher-order observation detection data				
21	BATSS higher-order obs. machine data directory	Directory	`$BATSS_DATA/[obs_dir]/`	Directory of detection data products for higher-order obs. Same as directory of imaging data products.
22	BATSS higher-order obs. detection catalog files	FITS	`./[obs_fileroot].catalog.fits.gz`	Catalog file of BATSS higher-order observation detections, both catalogued and uncatalogued. Created by `BATSS_celldetect`.
23	BATSS higher-order obs. detection region files	TXT	`./regfiles/[obs_fileroot].ZEA_[1-6]of6.[catalog-eband].reg`	Region files of BATSS higher-order observation detections, one file for each catalog-energy band combination (string `[catalog-eband]`). Created by `BATSS_celldetect`.
24	BATSS higher-order obs. sky image files (CAR projection)	FITS	`./[obs_fileroot].CAR.fits.gz`	Sky image file for BATSS higher-order observation, with each image in a single full-sky Cartesian (CAR) projection. Created by `BATSS_results`.
25	BATSS higher-order obs. detection reports (local)	PS	`./[obs_fileroot].[eband].local.ps`	Report files of BATSS higher-order observation detections, one file per energy band, one page per detection. Created by `BATSS_results`.
26	BATSS higher-order observation reports (global)	PS	`./[obs_fileroot].[eband].global.ps`	Report files of global results from BATSS higher-order observations, one file per energy band. Created by `BATSS_results`.
27	BATSS higher-order obs. full-sky images (Aitoff projection)	PNG	`./html/[obs_fileroot].[eband].png`	Full-sky images (Aitoff projection) and detections for BATSS higher-order observation, one image per energy band, for publication on BATSS website. Created by `BATSS_results`.
28	BATSS higher-order obs. HTML report files	HTML	`./html/[obs_fileroot].[eband].html`	HTML report files for BATSS higher-order observation, one file per energy band, for publication on BATSS website. Created by `BATSS_results`.

A.6 BATSS Level 3 products

BATSS Level 3 data products, or source-level products, are created at the BATSS trigger stage of the data pipeline (Section 3.9) and stored in the BATSS central data volume, once detection catalogs for individual observations have been created and copied over from the data volumes of the individual machines. These products are listed in Table A.4, and they are categorized as follows:

a. BATSS observation-level detection results: In addition to the BATSS Level 1 input data products at the observation level (Section A.4, item e.), the data directory for each observation within the BATSS central data volume also stores a copy of the detection catalog files created in the individual machines, as well as a link to the FITS file containing all relevant processing information on the BATSS observation. The information on these FITS files can be later use to locate and retrieve other BATSS Level 2 (observation-level) data products from the individual machine data volumes.

b. BATSS source-level detection catalogs: The source-level detection root directory (#4) stores BATSS detection catalog data categorized by source as opposed to by BATSS observation. Each catalog of known sources searched at the detection stage has its own subdirectory (including a separate one for BATSS unidentified detections), as well as each source within each catalog. These files are the core data products to be used in the monitoring of transient activity of known hard X-ray sources, as detected during BATSS observations.

c. BATSS trigger catalog: Uncatalogued BATSS detections are processed by the analysis tool `BATSS_trigger`, which creates as its core data product the *BATSS trigger database* of candidate sources. Candidate source data in the database are stored and handled in a three-level hierarchy:

Individual detections are drawn from individual sky image in one of the 3 BATSS energy bands from an individual BATSS observation of any type.

Observation-level detections are found after applying spatial and time coincidence criteria on individual detections within the same observation across energy bands. They are therefore composed of 1–3 individual detections, whose positions are then variance-weighted to obtain the position and error radius of the observation-level detection.

Candidate source detections are found after applying spatial coincidence and significance criteria across the entire database of observation-level detections. A set of observation-level detections that matches the criteria is then classified as a *BATSS candidate source* and assigned a *BATSS trigger number* of the form `NXXXXX`, where `N` corresponds to the number of coincident observation-level detections, and the 5-digit number `XXXXX` is assigned sequentially. The candidate source detection for an "unmatched" observation-level detection is the single observation-level detection itself, though without a BATSS trigger number assigned to it.

The full database of matched and unmatched BATSS candidate sources is stored in the BATSS central data volume as Level 3 FITS and IDL binary files, and they are continuously updated by the `BATSS_trigger` tool by matching them against new catalogs of unidentified BATSS detections.

d. BATSS candidate source data: Once a candidate source has been identified and assigned a BATSS trigger number, a subdirectory within the BATSS central data volume is created in order to store all subsequent BATSS Level 3 data products related to the candidate source. These products can be subcategorized as follows, including references to Table A.4 entry numbers:

Detection data (#15–16): These include the FITS file with the candidate source detection parameters, organized in the same 3-level hierarchy as the full BATSS trigger database, as well as a PostScript candidate source detection report.

Lightcurve data (#17–23): For candidate sources with single-slew observation-level detections, lightcurve files for each slew are produced after mask-weighting (ray-tracing) its corresponding BATSS event file at the position of the candidate source. The Bayesian block algorithm in the BAT tool `battblocks` is then applied to identify periods of high source variability and store them in the form of Good Time Interval (GTI) and burst duration FITS files. The latter contain the standard set of burst time blocks: T_{100}, T_{90}, T_{50}, T_{1s}, as well as pre- and post-burst background intervals. These results are summarized in a PostScript lightcurve report file.

Spectral data (#24–29): For each of the burst time blocks of single-slew observations identified in the lightcurve analysis, spectral analysis is then performed by executing an XSPEC script which is generated dynamically by the tool `BATSS_spectrum`. The script takes as inputs the FITS files with the raw, 80-channel, count-based spectrum (PHA) of the candidate source, as well as the spectral response matrix of the BAT instrument over the course of the slew. It then computes a photon-based source spectrum which it attempts to fit with the spectral models presented in Section 4.3.3. The overall results of the XSPEC analysis are saved to an IDL binary file, and are displayed in the form of a PostScript spectrum report file.

In addition, the BATSS candidate source analysis results are summarized into an HTML report file (#30) and its associated image files, which are then published to the BATSS webpage[8].

[8] `http://hea-www.harvard.edu/BATSS/`

TABLE A.4
Section A.6: BATSS Level 3 products — Source-level data

#	Product type	Format	File name	Description
a. BATSS observation-level detection results				
1	BATSS observation central data directory	Directory	`$BATSS_PRODUCTS/[obs_dir]/`	Observation directory within BATSS central data volume. Stores both BATSS Level 1 and Level 3 data products for observation. `[obs_dir]` corresponds to the subdirectory strings: Slew: `[YYYY_MM]/slew[_realtime]/[YYMMDD]/[YYMMDD_HHhMMmSSs+XXXs]/` Orbital: `[YYYY_MM]/orbital/[YYMMDD_HHhMMmSSs]/` Daily: `[YYYY_MM]/daily/[YYMMDD]/` Weekly: `[YYYY_MM]/weekly/[YYMMDD]/` Monthly: `[YYYY_MM]/monthly/` Yearly: `yearly/[YYYY]/` Survey: `survey/`
2	BATSS observation FITS file link	FITS (link)	`./[obs_fileroot].fits`	Symbolic link to the observation FITS file in the machine data directory where it was processed (Table A.3, #2 and #19). For this and following data products, `[obs_fileroot]` corresponds to the file root strings: Slew: `slew_[YYMMDD_HHhMMmSSs+XXXs]` Orbital: `orbit_[YYMMDD_HHhMMmSSs]` Daily: `day_[YYMMDD]` Weekly: `week_[YYMMDD]` Monthly: `month_[YYMM]` Yearly: `year_[YYYY]` Survey: `BATSS_survey`
3	BATSS observation detection catalog file	FITS	`./[obs_fileroot].catalog.fits.gz`	Catalog file of BATSS observation detections, copied unmodified from machine data directory.

TABLE A.4 (continued)
Section A.6: BATSS Level 3 products — Source-level data

#	Product type	Format	File name	Description
b. BATSS source-level detection catalogs				
4	BATSS source-level detection root directory	Directory	`$BATSS_PRODUCTS/detections/`	Root directory for source-level detection catalogs.
5	Catalog detection subdirectory	Directory	`./[catalog]/`	Subdirectiory for specific known source catalog. `[catalog]` corresponds to the following default catalog strings: `BATSS`: Uncatalogued BATSS detections `bat_gcn_ground`: BAT GCN ground catalog `bat_survey`: BAT 22-month survey catalog `bat_transients`: BAT Hard X-ray Transient catalog `bat_transients_blind`: BAT Hard X-ray Transient catalog (blind detection) `bat_blank`: BAT blank sky (calibration) points
6	Source detection subdirectory	Directory	`./[source]/`	Subdirectory for individual sources in catalog, with `[source]` corresponding to the source name string. Uncatalogued detections within the catalog subdirectory `BATSS` are logged under generic source name `BATSS_UNKNOWN`.
7	BATSS observation subdirectory	Directory	`./[obs_dir]/`	Subdirectory for BATSS observation where source detection was made. `[obs_dir]` corresponds to the following observation subdirectory strings: Slew: `[YYYY_MM]/slew[_realtime]/[YYMMDD]/` Orbital: `[YYYY_MM]/orbital/` Daily: `[YYYY_MM]/daily/` Weekly: `[YYYY_MM]/weekly/` Monthly: `[YYYY_MM]/monthly/` Yearly: `yearly/` Survey: `survey/`
8	BATSS source-level detection catalog	FITS	`./[obs_fileroot].det.fits.gz`	FITS detection catalog file with a single binary table extension, corresponding to the catalog entry for the specific catalog/source/BATSS observation combination considered. `[obs_fileroot]` corresponds to the same observation file root strings listed on #2.

TABLE A.4 (continued)
Section A.6: BATSS Level 3 products — Source-level data

#	Product type	Format	File name	Description
c. BATSS trigger catalog				
9	BATSS trigger catalog root directory	Directory	`$BATSS_PRODUCTS/triggers/`	Root directory for the BATSS trigger database of uncatalogued candidate sources.
10	BATSS matched FITS file	FITS	`./hk/BATSS_matched.fits`	BATSS trigger database FITS file, containing 3 binary table extensions: 1. `CANDIDATES`: Candidate source list, after matching detections across individual observations. 2. `OBSERVATIONS`: Observation-level detections, after matching spatially coincident detections across energy bands. 3. `DETECTIONS`: Individual detections that make up observation-level detections.
11	BATSS matched IDL file	IDL binary	`./hk/BATSS_matched.idl`	BATSS trigger database, with data saved as IDL structures in an IDL binary file.
12	BATSS unmatched FITS file	FITS	`./hk/BATSS_unmatched.fits`	Database of uncatalogued BATSS detections that have not yet matched any of the criteria for BATSS candidate sources. FITS file has the same 3 extensions as candidate source catalog file: 1. `CANDIDATES`, 2. `OBSERVATIONS`, 3. `DETECTIONS`. However, since no candidate source matching has been found, the candidate source list is the same size as the observation-level detection list.
13	BATSS unmatched IDL file	IDL binary	`./hk/BATSS_unmatched.idl`	Database of unmatched, uncatalogued BATSS detections, with data saved as IDL structures in an IDL binary file.
d. BATSS candidate source data				
14	BATSS candidate source subdirectory	Directory	`$BATSS_PRODUCTS/triggers/[NXXXXX]/`	Directory of data products for individual candidate source, characterized by BATSS *trigger number* `NXXXXX`. `N` is the number of contributing observation-level detections, while the 5-digit number `XXXXX` is assigned sequentially.
15	BATSS candidate source FITS file	FITS	`./BATSS_[NXXXXX].fits`	FITS file with detection parameters for BATSS candidate source with trigger number `NXXXXX`. 3 file extensions are: 0. `TRIGGER`: Trigger information in primary header 1. `OBSERVATIONS`: Binary table of observation-level dets. 2. `DETECTIONS`: Binary table of individual detections

TABLE A.4 (continued)
Section A.6: BATSS Level 3 products — Source-level data

#	Product type	Format	File name	Description
16	BATSS candidate source detection report	PS	`./BATSS_[NXXXXX]_det.ps`	Report with candidate source detection chart, trigger information and individual detection parameters.
17	Mask-weighted event files	FITS	`./[slew_fileroot]_[src_pos].evt.gz`	Mask-weighted (ray-traced) event files at position of candidate source, for triggers derived from single-slew detections, one event file per slew observation. For this and following data products, `[slew_fileroot]` corresponds to the string `slew_[YYMMDD_HHhMMmSSs+XXXs]`, while `[src_pos]` is the string `J[AAAA±DDD]`, expressed as a function of the candidate source position in J2000 equatorial coordinates RA (`AAAA`) and Dec (`±DDD`).
18	Auxiliary raytracing files	FITS	`./[slew_fileroot]_[src_pos].evaux.gz`	Auxiliary raytracing files with candidate source position data within the BAT FoV over the course of the slew. One file is created for each single-slew observation of candidate source.
19	BATSS candidate source lightcurve files	FITS	`./lc/[slew_fileroot]_[src_pos]_[N]chan_[tbin].lc`	Lightcurve files derived from mask-tagged event file, for a set of time binnings and energy channels. Time binning settings `[tbin]` used are: `64ms`, `200ms`, `1s`, `4s`, `8s`. Energy channel settings `[N]chan` used are: `1chan`: 15–150keV (Broad) `2chan`: 15–50keV (Soft), 50–150keV (Hard) `4chan`: 15–25keV, 25–50keV, 50–100keV, 100–350keV (standard BAT energy channels)
20	Lightcurve GTI files	FITS	`./lc/[slew_fileroot]_[src_pos]_1chan_[tbin]_bb.gti`	File of "interesting," high-variability time intervals (GTIs) derived from the Broad band `1chan` lightcurves, using Bayesian Block (`bb`) algorithm. GTIs are saved in single binary table extension `STDGTI`. Computed by `battblocks` within `BATSS_lc` routine.
21	Lightcurve duration files	FITS	`./lc/[slew_fileroot]_[src_pos]_1chan_[tbin]_bbdur.gti`	File of standard time blocks for burst detection, derived from the Broad band `1chan` lightcurves. Extensions: 1. `GTI_T90` (T_{90}): 5% to 95% of source counts 2. `GTI_T50` (T_{50}): 25% to 75% of source counts 3. `GTI_PEAK` (T_{1s}): 1-second peak counts 4. `GTI_TTOT` (T_{100}): total burst duration 5. `GTI_BKG1`: Pre-burst background interval 6. `GTI_BKG2`: Post-burst background interval

TABLE A.4 (continued)
Section A.6: BATSS Level 3 products — Source-level data

#	Product type	Format	File name	Description
22	Burst duration file	FITS	`./[slew_fileroot]_[src_pos]_dur.gti`	Duration file with selected time blocks for burst, chosen among the lightcurve duration files (#21) as the one with the longest T_{90} interval.
23	BATSS candidate source lightcurve report file	PS	`./BATSS_[NXXXXX]_lc.ps`	Report with lightcurve plots for all selected time and energy binnings. If burst time blocks are found, they are overplotted on the corresponding Broad band lightcurve.
24	Raw time-averaged burst spectrum files	FITS	`./spec/[slew_fileroot]_[src_pos]_[tblock].pha`	80-channel raw spectrum (PHA) of candidate source at `[src_pos]` over single-slew observation, accumulated from mask-weighted event file, and time-averaged over a set of standard burst time blocks. For this and following data products, `[tblock]` corresponds to the following time block strings: `obs`: full single-slew observation `burst`: full-burst interval (T_{100}) `t90`: 90% burst count interval (T_{90}) `t50`: 50% burst count interval (T_{50}) `peak`: 1-second peak count interval (T_{1s})
25	Spectral response matrix files	FITS	`./spec/slew_[slew_fileroot]_[src_pos]_[tblock].rsp`	Spectral response matrix over slew observation, for a set of time blocks `[tblock]`.
26	Burst spectral analysis scripts	XSPEC script	`./spec/slew_[slew_fileroot]_[src_pos]_[tblock].xcm`	XSPEC script for burst spectral analysis, time-averaged over a set of time blocks `[tblock]`. Script is generated and run dynamically as part of `BATSS_spectrum` analysis routine.
27	Burst spectral data output file	IDL script	`./spec/[slew_fileroot]_[src_pos]_XSPEC_[tblock].dat.pro`	Output file from XSPEC spectral analysis, formatted as IDL script for declaration of output data arrays as IDL variables for further analysis.
28	Burst time-averaged spectrum file	IDL binary	`./slew_[slew_fileroot]_[src_pos]_spec.idl`	IDL binary file with burst spectral analysis data. Results for each time block are saved as an element of the IDL structure `TBLOCKS`.
29	BATSS candidate source spectrum report file	PS	`./BATSS_[NXXXXX]_spec.ps`	Report with results of spectral analysis for each burst time block of candidate source with BATSS trigger number `[NXXXXX]`.
30	BATSS candidate source HTML report file	HTML	`./html/BATSS_[NXXXXX].html`	HTML report for BATSS candidate source trigger `[NXXXXX]`, for publication on BATSS website. All image files referenced on report file are located in the same `html/` subdirectory.

Appendix B

BATSS software tool guide

This appendix serves as a technical reference guide to the BATSS software package presented in Chapter 3 on the BATSS data pipeline, as of its most current implementation at the time of submission of this dissertation. After an introduction regarding the IT system infrastructure the package is built upon, the individual BATSS software tools are hereby presented and categorized according to their function within the BATSS pipeline. For each tool, a general description is provided, along with its input and output arguments and data products, and a short description of how they are calculated.

B.1 System Requirements

This section describes the requirements of the system the BATSS software package has relied upon in order to process the *Swift*-BAT data used for this work. It provides information that should be useful for the purposes of running the software package in its current form, and also to modify it and/or port it to a different computer system if desired.

B.1.1 System Access

As was the case for the Level 0, 1 and 3 BATSS data products presented in Appendix A, the BATSS software package is found on the central data volume "`luna0`" of the server "`luna`" (`luna.cfa.harvard.edu`), housed at the computational facility of the High Energy Astrophysics Division (HEAD) at the Harvard-Smithsonian Center for Astrophysics (CfA),[1] and maintained by the staff of the HEAD Systems Group. Access to the root directory `\data\luna0\` of the `luna0` volume can be gained after login into any server in the CfA HEAD network.

B.1.2 Root Directory

The root directory for read-only access to all of the software tools of the BATSS pipeline is the subdirectory `/acopete/BATSS/pipeline/` of the `luna0` volume. Its fully qualified path, hereafter referred to by the environment variable `$BATSS_PIPELINE`, is therefore:

`$BATSS_PIPELINE` ≡ `luna.cfa.harvard.edu:/data/luna0/acopete/BATSS/pipeline/`

The current version of the individual tools described in this guide should hence be assumed to reside in this directory, unless otherwise indicated.

B.1.3 Software Requirements

The BATSS software package is written entirely in the Interactive Data Language (IDL), a commercial language of wide use in the astronomy community. IDL is developed by Exelis Visual Information Solutions (formerly ITT Visual Information Solutions), and information on distribution and licensing can be found on the company website.[2] The

[1] `http://www.cfa.harvard.edu/hea/`

[2] `http://www.exelisvis.com/language/en-us/productsservices/idl.aspx`

BATSS pipeline has been operating under the CfA HEAD's IDL license, with IDL v7.0.6 as the most current version used.

Aside from the functions and procedures in the regular IDL distribution, BATSS software also relies on the use of the IDL Astronomy User's Library,[3] which contains a repository of basic procedures of common use in astronomy. User access to the tools in this library is assumed, and the BATSS software has been most recently used with the May, 2011, distribution installed by the HEAD Systems Group.

Lastly, the BATSS pipeline requires use of the procedures in the *Swift*-BAT software package, as well as the data in the *Swift* calibration database (CALDB), which are developed and maintained by the *Swift* Science Center. This mission-specific software is distributed as part of the larger HEASoft software package —also known as FTOOLS— for the general manipulation of files in the FITS format,[4] including those related to the *Swift* mission and the BAT instrument in particular. The most current version of the package as of the time of submission of this work is HEASoft 6.12 (14 March 2012), which was installed and run locally on the BATSS servers in order to optimize for processing speed. The *Swift* CALDB,[5] on the other hand, is accessed remotely at run time in order to always make use of the most current version of the calibration data files for the mission.

[3] `http://idlastro.gsfc.nasa.gov/`

[4] `http://ftools.gsfc.nasa.gov/`

[5] `http://heasarc.nasa.gov/docs/heasarc/caldb/swift/`

B.2 BATSS software tools overview

The full list of IDL functions and procedures included as part of the BATSS software package is shown in Table B.1, where they are categorized according to their function within the BATSS data pipeline presented in Chapter 3. A short description of each category and the analysis tools included in each are presented in this section, followed by a full description of the individual tools in the sections that follow.

a. Pre-processing routines — Section B.3: These routines encompass all the analysis steps up to the start of the processing of individual slew observations by the BATSS servers. The routines that implement the *BATSS daemon* stage of the pipeline (Section 3.5), in both its real-time and archival forms, are the core components of this category, as they parse the input data products (BATSS Level 0, Section A.3) that are either transferred into the servers (real-time) or downloaded from the *Swift* archive (archival), and identify the new slew observations to be processed. This functionality is complemented by the implementation of the *BATSS queue* stage of the pipeline (Section 3.6), which then follows by making the individual assignments of observations to machines.

b. Imaging routines — Section B.4: These tools implement the *BATSS imaging thread* (Section 3.7), which runs on every machine tasked with processing individual BATSS observations. They take the pre-processed data products (BATSS Level 1, Section A.4) stored in the BATSS central data volume, and further process them locally to generate the sky images in the BATSS full-sky projection (Section 2.2.2) to be then co-added to produce the final images for each observation.

c. Detection routines — Section B.5: These tools implement the *BATSS detection thread* (Section 3.8), which runs on every machine in parallel with the imaging thread. They produce the final set of observation-level data products (BATSS Level 2, Section A.5),

which include the final sky images for every type of observation, as well as detection catalogs and observation reports.

d. Source-level processing routines — Section B.6: Once observation-level processing has taken place and control has returned to the BATSS main server, the tools in this category perform further analysis of the observation-level detection catalogs in order to generate source-level data products (BATSS Level 3, Section A.6). While source-level detection catalogs for known sources are created in order to monitor their transient activity during BATSS observations, unidentified detections are processed at the *BATSS trigger* stage of the pipeline (Section 3.9) to produce a database of BATSS candidate sources. Lightcurve and spectral analyses of individual candidate sources are performed automatically by tools in this category as well, followed by the summary and publication to the BATSS webpage of the source-level results produced by the pipeline.

e. Control routines — Section B.7: For those tools that run continuously on the BATSS servers, several control routines have been implemented in order to provide an interactive method to modify their runtime behavior, from changing preferences and priorities in their handling of BATSS data products, to halting their execution at a time when it is safe to do so.

For each to the BATSS software tools enumerated in Table B.1, the reference number for their full description in Sections B.3–B.7 is provided in column 1, and the name of the IDL routine associated with each is given in column 2.[6] Column 3 indicates whether they correspond to IDL Functions (F) or Procedures (P),[7] while column 4 gives the names of

[6]Names of IDL functions and procedures are case-insensitive.

[7]IDL functions and procedures differ only in that the latter do not have a return value associated with them. Procedures use the general syntax `[procedure_name],[arg1],[arg2],...`, while functions use the general syntax `[return_value]=[function_name]([arg1],[arg2],...)`. Depending on the definition of

the files (with the IDL-standard `.pro` extension) where they are located on disk within the `$BATSS_PIPELINE` root directory. Column 5 states the tools' runtime mode: non-interactive tools can be either "Continuous" if the tool is meant to run continuously in its own thread, or they can instead be called by another BATSS routine as part of its own execution; in the latter case, the name of the calling routine is given. Interactive tools, i.e. those that are meant to be called directly by the user at any point along the execution of the pipeline, are explicitly labeled as "Interactive;" the BATSS control routines described above would typically fall within this category. Finally, column 6 provides a short description of the tool's characteristics.

The individual BATSS software tool descriptions in the Sections B.3–B.7 elaborate further on the features and functionality of each, and also indicate the essential characteristics of their corresponding IDL routines: IDL type (either Function or Procedure), input/output arguments (both parameters and keywords), and return values (applicable to IDL functions only). In addition, a list of the input and output data products they handle is included, in order to provide the link with the individual BATSS products described in Appendix A. Within this structure, input data products that are modified in place by BATSS tools are listed separately as "Input/Output data products."

---

the specific procedure/function, arguments `[argN]` can be either *parameters* (syntax `[value]`) or *keywords* (syntax `[keyword_name]=[value]`), and in each case they can be either required or optional.

TABLE B.1
Section B.2: BATSS software tools overview

#	Tool name	IDL F/P	File name	Runtime mode/ Called by	Description
a. Pre-processing routines — Section B.3					
1	BATSS_daemon_realtime	P	BATSS_daemon_realtime.pro	Continuous	BATSS daemon for parsing new real-time data. Controlled by BATSS_daemon_realtime_control.
2	BATSS_daemon_archival	P	BATSS_daemon_archival.pro	Continuous	BATSS daemon for parsing new archival data. Controlled by BATSS_daemon_archival_control.
3	BATSS_queue	P	BATSS_queue.pro	Continuous	Prioritizes and assigns observations from the BATSS queue to individual machines. Controlled by BATSS_queue_control.
b. Imaging routines — Section B.4					
4	BATSS_machine_image	P	BATSS_machine.pro	Continuous	Directs imaging thread on individual BATSS machines. Controlled by BATSS_machine_control.
5	BATSS_evt2img	F	BATSS_imaging.pro	BATSS_machine_image	Executes BATSS imaging routines for single-slew observations.
6	BATSS_evt2dpi	F	BATSS_imaging.pro	BATSS_evt2img	Creates DPIs from event files on single-slew observations.
6	BATSS_qmap_create	F	BATSS_imaging.pro	BATSS_evt2img	Creates detector quality map for single-slew observations.
8	BATSS_pcmap_create	F	BATSS_imaging.pro	BATSS_evt2img	Creates partial coding map of BAT FoV for single-slew observations.
9	BATSS_img_create	F	BATSS_imaging.pro	BATSS_evt2img	Creates 0.2sec sky images, uncorrected for partial coding effects, for single-slew observations.
c. Detection routines — Section B.5					
10	BATSS_machine_detect	P	BATSS_machine.pro	Continuous	Directs detection thread on individual BATSS machines. Controlled by BATSS_machine_control.
11	BATSS_detection	F	BATSS_detection.pro	BATSS_machine_image	Executes BATSS detection routines for all observations.
12	BATSS_add	F	BATSS_add.pro	BATSS_detection	Co-adds 0.2sec sky images to create full-sky images, corrected for partial coding, for single-slew observations.
13	BATSS_merge	F	BATSS_merge.pro	BATSS_detection	Co-adds full-sky images to create BATSS higher-order observation sky images.
14	BATSS_celldetect	F	BATSS_celldetect.pro	BATSS_detection	Performs detection on BATSS sky images for all observations, creates detection catalogs.
15	BATSS_results	F	BATSS_results.pro	BATSS_detection	Creates PostScript and HTML observation reports for BATSS webpage.

TABLE B.1 (continued)
Section B.2: BATSS tools overview

#	Tool name	IDL F/P	File name	Runtime mode/ Called by	Description
d. Source-level processing routines — Section B.6					
16	BATSS_trigger	P	BATSS_trigger.pro	Continuous	Creates and updates databases of BATSS candidate sources from unidentified detections. Executes analysis routines for new BATSS candidate sources.
17	BATSS_lc	F	BATSS_lc.pro	BATSS_trigger	Performs lightcurve analysis on single-slew observations of BATSS candidate sources.
18	BATSS_spectrum	F	BATSS_spectrum.pro	BATSS_trigger	Performs spectral analysis on single-slew observations of BATSS candidate sources.
19	BATSS_www	P	BATSS_www.pro	Continuous	Publishes observation and candidate source reports to BATSS webpage.
e. Control routines — Section B.7					
20	BATSS_daemon_realtime_control	P	BATSS_daemon_realtime.pro	Interactive	Controls running of BATSS_daemon_realtime
21	BATSS_daemon_archival_control	P	BATSS_daemon_archival.pro	Interactive	Controls running of BATSS_daemon_archival
22	BATSS_queue_control	P	BATSS_queue.pro	Interactive	Controls running of BATSS_queue
23	BATSS_machine_control	P	BATSS_machine.pro	Interactive	Controls running of BATSS_machine_image and BATSS_machine_detect
24	BATSS_trigger_control	P	BATSS_trigger.pro	Interactive	Controls running of BATSS_trigger

B.3 Pre-processing routines

The three IDL procedures `BATSS_daemon_realtime`, `BATSS_daemon_archival` and `BATSS_queue` implement the processing of BATSS Level 0 (input) data products into BATSS Level 1 (pre-processed) data products. These non-interactive tools must run continuously and on stand-alone parallel threads, which enables the pipeline to proceed into individual observation processing shortly after new input data products are made available. Their default behavior can be modified at run time by the control routines (Section B.7) `BATSS_daemon_realtime_control`, `BATSS_daemon_archival_control` and `BATSS_queue_control`, respectively.

1. `BATSS_daemon_realtime`: IDL procedure that implements the BATSS daemon stage (Section 3.5) for real-time slew data. Though it takes no input/output arguments, it accepts the arguments of its control routine `BATSS_daemon_realtime_control` (#20) as IDL *extra keywords* in order to modify its default behavior.

   File: `BATSS_daemon_realtime.pro`
   IDL type: Procedure. Return value: N/A
   Required input arguments: None
   Optional input arguments: Arguments of `BATSS_daemon_realtime_control`
   Output arguments: None

   Input/Output data products:

Type	BATSS data level	Product	Table reference
I	0	*Swift* real-time attitude file	A.1.2
I	0	BAT real-time event file	A.1.3
I	0	BAT real-time detector enable file	A.1.4
I	0	BAT real-time energy calibration file	A.1.5
O	1	*Swift* real-time daily attitude files	A.2.2
O	1	Consolidated BAT real-time event files	A.2.5
O	1	Consolidated BAT real-time detector enable files	A.2.6
O	1	Consolidated BAT real-time energy calibration files	A.2.7
O	1	BATSS real-time single-slew queue files	A.2.9
O	1	BATSS single-slew spacecraft attitude files	A.2.19
O	1	BATSS single-slew Good Time Interval (GTI) files	A.2.21
O	1	BATSS single-slew event files	A.2.22

2. `BATSS_daemon_archival`: IDL procedure that implements the BATSS daemon stage (Section 3.5) for archival slew data. Though it takes no input/output arguments, it accepts the arguments of its control routine `BATSS_daemon_archival_control` (#21) as IDL extra keywords in order to modify its default behavior.

   File: `BATSS_daemon_archival.pro`
   IDL type: Procedure. Return value: N/A
   Required input arguments: None
   Optional input arguments: Arguments of `BATSS_daemon_archival_control`
   Output arguments: None

   Input/Output data products:

Type	BATSS data level	Product	Table reference
I	0	*Swift* as-flown science timeline file	A.1.7
I	0	*Swift* archival attitude file	A.1.9
I	0	*Swift* archival orbital file	A.1.10
I	0	BAT archival detector enable file	A.1.11
I	0	BAT archival event file	A.1.12
O	1	*Swift* archival daily attitude file	A.2.3
O	1	BATSS archival single-slew queue file	A.2.11
O	1	BATSS archival orbital queue file	A.2.12
O	1	BATSS archival daily queue file	A.2.13
O	1	BATSS archival weekly queue file	A.2.14
O	1	BATSS archival monthly queue file	A.2.15
O	1	BATSS archival yearly queue file	A.2.16
O	1	BATSS archival survey queue file	A.2.17
O	1	BATSS single-slew spacecraft attitude file	A.2.19
O	1	BATSS single-slew spacecraft orbital file	A.2.20
O	1	BATSS single-slew Good Time Interval (GTI) file	A.2.21
O	1	BATSS single-slew event file	A.2.22

3. `BATSS_queue`: Non-interactive procedure that implements the BATSS queue stage (Section 3.6) for all observation types. Identifies BATSS observations with captured slew data and assigns them to individual machines according to a set of priorities, which can be modified by the control routine `BATSS_queue_control` (#22).

File: `BATSS_queue.pro`
IDL type: Procedure. Return value: N/A
Required input arguments: None
Optional input arguments: Arguments of `BATSS_queue_control`
Output arguments: None

Input/Output data products:

Type	BATSS data level	Product	Table reference
I	1	BATSS real-time single-slew queue files	A.2.9
I	1	BATSS archival single-slew queue file	A.2.11
I	1	BATSS archival orbital queue file	A.2.12
I	1	BATSS archival daily queue file	A.2.13
I	1	BATSS archival weekly queue file	A.2.14
I	1	BATSS archival monthly queue file	A.2.15
I	1	BATSS archival yearly queue file	A.2.16
I	1	BATSS archival survey queue file	A.2.17
O	2	BATSS single-slew observation FITS file	A.3.2
O	2	BATSS single-slew spacecraft attitude file	A.3.3
O	2	BATSS single-slew spacecraft orbital file	A.3.4
O	2	BATSS single-slew Good Time Interval (GTI) file	A.2.5
O	2	BATSS single-slew event file	A.2.6
O	2	BATSS higher-order observation FITS file	A.3.19

B.4 Imaging routines

Imaging routines take the BATSS Level 1 (pre-processed) data products and process them into BATSS Level 2 (observation-level) intermediate and final imaging data products. The non-interactive IDL procedure `BATSS_machine_image` directs the imaging thread on each machine and executes the other BATSS imaging routines in this category as needed. It must run continuously on each machine to be used for processing of individual observations, and on as many threads as observations to be processed simultaneously per machine.

4. `BATSS_machine_image`: Non-interactive IDL procedure that implements the BATSS imaging thread (Section 3.7) on each machine. Its only required argument is the parameter `MACHINE`, a scalar string of the form `'[machine_disk]_[thread]'`. The

string [machine_disk] stands for the name of the corresponding machine data volume (e.g. 'luna1', 'mond1' or 'dahl1' for the BATSS dedicated servers), while [thread] is any string that uniquely identifies the observation processing thread within the machine disk (e.g. 'A', 'B', 'C', etc.). Each combination has a corresponding *machine control file* associated with it of the form [machine_disk]_[thread].fits, a housekeeping file used for tracking the status of each observation processing thread, introduced in Section A.4, item f. In addition, the procedure also accepts the arguments of the control routine BATSS_machine_control (#20) as IDL extra keywords, in order to modify its runtime behavior.

File: BATSS_machine.pro
IDL type: Procedure. Return value: N/A

Required input arguments:

Argument type	Name	Variable type	Description
Paramater	MACHINE	String (scalar)	'[machine_disk]_[thread]'

Optional input arguments: Arguments of BATSS_machine_control
Output arguments: None

Input/Output data products:

Type	BATSS data level	Product	Table reference
I/O	1	BATSS machine control file	A.2.25
I/O	2	BATSS single-slew observation FITS file	A.3.2
I/O	2	BATSS higher-order observation FITS file	A.3.19

5. BATSS_evt2img: IDL function called by BATSS_machine_image to execute imaging routines for BATSS single-slew observations. The only required parameter is the name of the observation FITS file (Table A.3, #2), while optional arguments define the energy bands for imaging (15–50 keV and 50–150 keV by default), whether partial coding correction should be performed on the output 0.2-sec sky images (no partial coding correction by default), and whether sky image units should be COUNTS or RATE (per fully-illuminated detector pixel, by definition; RATE units used by default). The return variable STATUS has a value of 1 if executed successfully or 0 if failed.

File: `BATSS_imaging.pro`
IDL type: Function
Return value: `STATUS` ≡ 1 (success) or 0 (failure)

Required input arguments:

Argument type	Name	Variable type	Description
Paramater	`FITSFILE`	String (scalar)	`'[obs_dir]/slew_[YYMMDD_HHhMMmSSs].fits'`

Optional input arguments: See script file for full list
Output arguments: None
Input/Output data products: None

6. `BATSS_evt2dpi`: IDL function called by `BATSS_evt2img` (#5) to create 0.2-sec Detector Plane Images (DPIs) from event files of single-slew observations.

Input/Output data products:

Type	BATSS data level	Product	Table reference
I/O	2	BATSS single-slew observation FITS file	A.3.2
I	2	BATSS single-slew Good Time Interval (GTI) file	A.3.5
I	2	BATSS single-slew event file	A.3.6

7. `BATSS_qmap_create`: IDL function called by `BATSS_evt2img` (#5) to create detector quality map for single-slew observations, given an input detector enable/disable map, and a single observation DPI accumulated from slew event data and screened for hot/cold detector pixels.

File: `BATSS_imaging.pro`
IDL type: Function
Return value: `STATUS` ≡ 1 (success) or 0 (failure)
Required input arguments: `FITSFILE` (described in #5)
Optional input arguments: See script file for full list
Output arguments: None

Input/Output data products:

Type	BATSS data level	Product	Table reference
I/O	2	BATSS single-slew observation FITS file	A.3.2
I	1	Consolidated BAT real-time detector enable file	A.2.6
I	2	BATSS single-slew event file	A.3.6
O	2	BATSS single-slew detector quality map file	A.3.7

8. `BATSS_pcmap_create`: IDL function called by `BATSS_evt2img` (#5) to create partial coding map of the BAT FoV during single-slew observation.

File: `BATSS_imaging.pro`
IDL type: Function
Return value: `STATUS` ≡ 1 (success) or 0 (failure)
Required input arguments: `FITSFILE` (described in #5)
Optional input arguments: See script file for full list
Output arguments: None

Input/Output data products:

Type	BATSS data level	Product	Table reference
I/O	2	BATSS single-slew observation FITS file	A.3.2
I	2	BATSS single-slew detector quality map file	A.3.7
O	2	BATSS single-slew partial coding map file	A.3.8

9. `BATSS_img_create`: IDL function called by `BATSS_evt2img` (#5) to create individual 0.2-sec sky images and variance maps for single-slew observation. Output images are saved as temporary files of 25 images (5 sec of exposure) each.

File: `BATSS_imaging.pro`
IDL type: Function
Return value: `STATUS` ≡ 1 (success) or 0 (failure)
Required input arguments: `FITSFILE` (described in #5)
Optional input arguments: See script file for full list
Output arguments: None

Input/Output data products:

Type	BATSS data level	Product	Table reference
I/O	2	BATSS single-slew observation FITS file	A.3.2
I	2	BATSS single-slew spacecraft attitude file	A.3.3
I	2	BATSS single-slew spacecraft orbital file	A.3.4
I	2	BATSS single-slew event file	A.3.6
I	2	BATSS single-slew detector quality map file	A.3.7

B.5 Detection routines

Detection routines take the output intermediate imaging data products from the BATSS imaging routines, and produce the final set of BATSS Level 2 (observation-level) data products, in the form of full-sky images, observation-level detection catalogs, and associated report files. The non-interactive IDL procedure `BATSS_machine_detect` directs the detection thread on each machine and executes the other BATSS detection routines for all observation types. It must run continuously on each machine to be used for processing of individual observations, and on as many threads as observations to be processed simultaneously per machine, in parallel with `BATSS_machine_image` (#4).

10. `BATSS_machine_detect`: Non-interactive IDL procedure that implements the BATSS detection thread (Section 3.8) on each machine. As with `BATSS_machine_image` (#4), it takes the required parameter `MACHINE` = `'[machine_disk]_[thread]'`, and accepts as optional keywords the arguments of its control routine `BATSS_machine_control` (#20), in order to modify its runtime behavior.

File: `BATSS_machine.pro`
IDL type: Procedure. Return value: N/A

Required input arguments:

Argument type	Name	Variable type	Description
Paramater	`MACHINE`	String (scalar)	`'[machine_disk]_[thread]'`

Optional input arguments: Arguments of `BATSS_machine_control`
Output arguments: None

Input/Output data products:

Type	BATSS data level	Product	Table reference
I/O	1	BATSS machine control file	A.2.25
I/O	2	BATSS single-slew observation FITS file	A.3.2
I/O	2	BATSS higher-order observation FITS file	A.3.19

11. `BATSS_detection`: IDL function called by `BATSS_machine_detect` to execute the BATSS image addition routines, for both single-slew and higher-order observations, followed by the detection and observation-level result analysis routines. Its only required parameter `FITSFILE` is the scalar string with the name of the observation FITS file (Table A.3, #2 and #19) containing the processing information of the assigned observation.

File: `BATSS_detection.pro`
IDL type: Function
Return value: `STATUS` $\equiv$ 1 (success) or 0 (failure)

Required input arguments:

Argument type	Name	Variable type	Description
Paramater	`FITSFILE`	String (scalar)	`'[obs_dir]/[obs_fileroot].fits'`

Optional input arguments: See script file for full list
Output arguments: None
Input/Output data products: None

12. `BATSS_add`: IDL function called by `BATSS_detection` (#11) to perform the addition operation on the intermediate 0.2-sec sky images from BATSS single-slew observations, previously created by `BATSS_img_create` (#9). The co-added output images are corrected for partial coding, projected onto the the BATSS quad-cube full-sky projection (Section 2.2.2), and saved as a set of 6 output files, one for each its Zenithal Equal Area (ZEA) sub-projections.

File: `BATSS_add.pro`
IDL type: Function
Return value: `STATUS` $\equiv$ 1 (success) or 0 (failure)
Required input arguments: `FITSFILE` (described in #11)
Optional input/output arguments: See script file for full list

Input/Output data products:

Type	BATSS data level	Product	Table reference
I/O	2	BATSS single-slew observation FITS file	A.3.2
I	2	BATSS single-slew spacecraft orbital file (archival only)	A.3.4
I	2	BATSS single-slew partial coding map file	A.3.8
O	2	BATSS single-slew sky image files (ZEA projection)	A.3.9

13. `BATSS_merge`: IDL function called by `BATSS_detection` (#11) to perform the addition operation on images already in the BATSS full-sky projection, in order to obtain higher-order observation images. Apart from the observation FITS file of the output image set, the IDL keyword `FILEARR`, a string array containing the input observation FITS files, is a required input argument as well.

File: `BATSS_merge.pro`
IDL type: Function
Return value: `STATUS` $\equiv$ 1 (success) or 0 (failure)

Required input arguments:

Argument type	Name	Variable type	Description
Paramater	`FITSFILE`	String (scalar)	`'[obs_dir]/[obs_fileroot].fits'`
Keyword	`FILEARR`	String (array)	`['[obs_dirN]/[obs_filerootN].fits',[...]]`

Optional input/output arguments: See script file for full list

Input/Output data products:

Type	BATSS data level	Product	Table reference
I/O	2	BATSS higher-order observation FITS file	A.3.19
I	2	BATSS single-slew observation FITS file	A.3.2
I	2	BATSS single-slew sky image files (ZEA projection)	A.3.9
I/O	2	BATSS higher-order obs. sky image files (ZEA projection)	A.3.20

14. `BATSS_celldetect`: IDL function called by `BATSS_detection` (#11) to perform detection on BATSS full-sky images from all observation types. Output products from this routine include observation-level detection catalogs (both catalogued and uncatalogued detections), their associated detection region files (for use with interactive analysis tools such as DS9), as well as full-sky images in the Cartesian (CAR) projection for observation display in a single image (for each energy band).

File: `BATSS_celldetect.pro`
IDL type: Function
Return value: `STATUS` $\equiv$ 1 (success) or 0 (failure)
Required input arguments: `FITSFILE` (described in #11)
Optional input/output arguments: See script file for full list

Input/Output data products:

Type	BATSS data level	Product	Table reference
I/O	2	BATSS single-slew observation FITS file	A.3.2
I/O	2	BATSS higher-order observation FITS file	A.3.19
I	2	BATSS single-slew sky image files (ZEA projection)	A.3.9
I	2	BATSS higher-order obs. sky image files (ZEA projection)	A.3.20
O	2	BATSS single-slew detection catalog files	A.3.11
O	2	BATSS higher-order obs. detection catalog files	A.3.22
O	2	BATSS single-slew detection region files	A.3.12
O	2	BATSS higher-order obs. detection region files	A.3.23
O	2	BATSS single-slew sky image files (CAR projection)	A.3.12
O	2	BATSS higher-order obs. sky image files (CAR projection)	A.3.24
O	3	BATSS observation detection catalog file	A.4.3
O	3	BATSS source-level detection catalog	A.4.8

15. `BATSS_results`: IDL function called by `BATSS_detection` (#11) to analyze and display observation-level results. For each energy band, PostScript-format reports are created at both the global (full-sky) and local (detection region) levels, as well as HTML observation summary report files for publication to the BATSS webpage.

File: `BATSS_celldetect.pro`
IDL type: Function
Return value: `STATUS` $\equiv$ 1 (success) or 0 (failure)
Required input arguments: `FITSFILE` (described in #11)
Optional input/output arguments: See script file for full list

Input/Output data products:

Type	BATSS data level	Product	Table reference
I/O	2	BATSS single-slew observation FITS file	A.3.2
I/O	2	BATSS higher-order observation FITS file	A.3.19
I	2	BATSS single-slew detection catalog files	A.3.11
I	2	BATSS higher-order obs. detection catalog files	A.3.22
I	2	BATSS single-slew sky image files (CAR projection)	A.3.12
I	2	BATSS higher-order obs. sky image files (CAR projection)	A.3.24

Type	BATSS data level	Product	Table reference
O	2	BATSS single-slew detection reports (local)	A.3.14
O	2	BATSS single-slew observation reports (global)	A.3.15
O	2	BATSS higher-order observation detection reports (local)	A.3.25
O	2	BATSS higher-order observation reports (global)	A.3.26
O	2	BATSS single-slew full-sky images (Orthographic proj.)	A.3.16
O	2	BATSS higher-order obs. full-sky images (Aitoff projection)	A.3.27
O	2	BATSS single-slew HTML report files	A.3.17
O	2	BATSS higher-order observation HTML report files	A.3.28

B.6 Source-level processing routines

The processing of BATSS Level 2 (observation-level) data products into BATSS Level 3 (source-level) products is done primarily by the software tool `BATSS_trigger`, which analyzes uncatalogued detections to build a database of BATSS candidate sources (each having a 6-digit BATSS trigger number assigned to it), while keeping a separate database of detections that do not match the candidate source criteria. New candidate sources are also subject to lightcurve and spectral analysis, also done by tools in this category, and the overall results are summarized and displayed on the BATSS webpage. `BATSS_trigger` is a non-interactive tool which must run continuously on a stand-alone thread in the BATSS central data volume, which allows it to promptly issue automated alert messages related to new candidate sources of interest.

16. `BATSS_trigger`: Non-interactive IDL procedure that implements the BATSS trigger stage of the data pipeline (Section 3.9), and executes all other source-level analysis routines as needed. Though it takes no required input/output arguments, it accepts the arguments of its control routine `BATSS_trigger_control` (#24) as IDL extra keywords in order to modify its default behavior.

File: `BATSS_trigger.pro`
IDL type: Procedure. Return value: N/A
Required input arguments: None

Optional input/output arguments: See script file for full list
Arguments of `BATSS_trigger_control`

Input/Output data products:

Type	BATSS data level	Product	Table reference
I	3	BATSS source-level detection catalog	A.4.8
I/O	3	BATSS matched FITS file	A.4.10
I/O	3	BATSS matched IDL file	A.4.11
I/O	3	BATSS unmatched FITS file	A.4.12
I/O	3	BATSS unmatched IDL file	A.4.13
O	3	BATSS candidate source FITS file	A.4.15
O	3	BATSS candidate source detection report	A.4.16
O	3	BATSS candidate source HTML report file	A.4.30

17. `BATSS_lc`: IDL function called by `BATSS_trigger` (#16) to perform lightcurve analysis on single-slew observations of BATSS candidate sources. The required input keyword `FITSFILE` can be a scalar or array of single-slew observation FITS files (Table A.3, #2), each of which will have its event data mask-tagged (ray-traced) at the position `[[RA],[DEC]]` of the candidate source as a preliminary step to the lightcurve analysis itself.

File: `BATSS_lc.pro`
IDL type: Function
Return value: `STATUS` $\equiv$ 1 (success) or 0 (failure)

Required input arguments:

Argument type	Name	Variable type	Description
Keyword	`FITSFILE`	String (array)	`['[slew_dirN]/[slew_filerootN].fits',[...]]`
Keyword	`EQUATORIAL`	Double (array)	`[[RA],[DEC]]` (deg, J2000)

Optional input/output arguments: See script file for full list

Input/Output data products:

Type	BATSS data level	Product	Table reference
I	3	BATSS candidate source FITS file	A.4.15
I	2	BATSS single-slew observation FITS files	A.3.2
I	2	BATSS single-slew event files	A.3.6
O	3	Mask-weighted event files	A.4.17

Type	BATSS data level	Product	Table reference
O	3	Auxiliary raytracing files	A.4.18
O	3	BATSS candidate source lightcurve files	A.4.19
O	3	Lightcurve GTI files	A.4.20
O	3	Lightcurve duration files	A.4.21
O	3	Burst duration file	A.4.22
O	3	BATSS candidate source lightcurve report file	A.4.23

18. `BATSS_spectrum`: IDL function called by `BATSS_trigger` (#16) to perform spectral analysis on single-slew observations of BATSS candidate sources, time-averaged over a set of selected time blocks computed as part of the lightcurve analysis. As with `BATSS_lc` (#17), an array of single-slew observation FITS files as well as the coordinates of the BATSS candidate source are required input arguments.

File: `BATSS_spectrum.pro`
IDL type: Function
Return value: `STATUS` $\equiv 1$ (success) or 0 (failure)

Required input arguments:

Argument type	Name	Variable type	Description
Keyword	`FITSFILE`	String (array)	`['[slew_dirN]/[slew_filerootN].fits',[...]]`
Keyword	`EQUATORIAL`	Double (array)	`[[RA],[DEC]]` (deg, J2000)

Optional input/output arguments: See script file for full list

Input/Output data products:

Type	BATSS data level	Product	Table reference
I	3	BATSS candidate source FITS file	A.4.15
I	2	BATSS single-slew observation FITS file	A.3.2
I	3	Mask-weighted event file	A.4.17
I	3	Burst duration file	A.4.22
O	3	Raw time-averaged burst spectrum files	A.4.24
O	3	Spectral response matrix files	A.4.25
O	3	Burst spectral analysis scripts	A.4.26
O	3	Burst spectral data output file	A.4.27
O	3	Burst time-averaged spectrum file	A.4.28
O	3	BATSS candidate source spectrum report file	A.4.29

19. `BATSS_www`: As an addition to the BATSS data pipeline, this IDL procedure continuously scans for HTML-format report files created along its execution, both at the observation level and at the source level, and adds them to the BATSS web directory for public access via the BATSS website. The procedure takes no required input arguments and is run on an independent, stand-alone thread on the BATSS central data volume.

File: `BATSS_www.pro`
IDL type: Procedure. Return value: N/A
Required input arguments: None
Optional input/output arguments: See script file for full list

Input/Output data products:

Type	BATSS data level	Product	Table reference
I	2	BATSS single-slew HTML report files	A.3.17
I	2	BATSS higher-order observation HTML report files	A.3.28
I	3	BATSS candidate source HTML report file	A.4.15

B.7 Control routines

As mentioned in the previous sections, BATSS control routines are a separate category of software tools whose purpose is to modify the runtime behavior of several continuously-running, non-interactive BATSS tools. In all cases, these are interactive routines that can be executed from the IDL command line after compilation of their respective script files. Their input/output arguments are all optional IDL *keywords* (i.e. entered in the form `[keyword_name]=[value]`), and they are also accepted as extra keywords in the call to the IDL routine they control.

20. `BATSS_daemon_realtime_control`: Controls the running of the BATSS software tool `BATSS_daemon_realtime` (#1).

File: `BATSS_daemon_realtime.pro`
IDL type: Procedure. Return value: N/A

Input/Output keywords:

I/O type	Name	Variable type	Description
I	RESET	Boolean	Set to restore default settings
I	HALT	Boolean	Set to halt execution of routine
I	WAIT	Float	[sec] Time to wait before checking on new data passes (10 sec by default)
I	START	String	'[YYMMDD]' Date (UT) to begin looking for new data ('071025' by default)
I	CLOBBER	Boolean	Set to reset and re-read data passes already read
O	CONTROLFILE	String	Returns name of FITS control file for routine

Input/Output data products:

Type	BATSS data level	Product	Table reference
I/O	1	BATSS software tool control file	A.2.24

21. `BATSS_daemon_archival_control`: Controls the running of the BATSS software tool `BATSS_daemon_archival` (#2).

File: `BATSS_daemon_archival.pro`
IDL type: Procedure. Return value: N/A

Input/Output keywords:

I/O type	Name	Variable type	Description
I	RESET	Boolean	Set to restore default settings
I	HALT	Boolean	Set to halt execution of routine
I	WAIT	Float	[sec] Time to wait before checking on new data passes (10 sec by default)
I	START	String	'[YYMMDD]' Date (UT) to begin looking for new data ('071025' by default)
I	CLOBBER	Boolean	Set to reset and re-read data passes already read
O	CONTROLFILE	String	Returns name of FITS control file for routine

Input/Output data products:

Type	BATSS data level	Product	Table reference
I/O	1	BATSS software tool control file	A.2.24

22. `BATSS_queue_control`: Controls the running of the BATSS tool `BATSS_queue` (#3).

File: `BATSS_queue.pro`
IDL type: Procedure. Return value: N/A

Input/Output keywords:

I/O type	Name	Variable type	Description
I	RESET	Boolean	Set to restore default settings
I	HALT	Boolean	Set to halt execution of routine
I	WAIT	Float	[sec] Time to wait before checking on new observations to be assigned (10 sec by default)
I	CHRONOLOGICAL	Boolean	Set to read observations chronologically
I	NEW_ONLY	Boolean	Set to read new observations only
I	LAST	Boolean	Set to assign last slew first (new slews only)
I	IDLE	Boolean	Assign new slews only when machine is idle
O	CONTROLFILE	String	Returns name of FITS control file for routine

Input/Output data products:

Type	BATSS data level	Product	Table reference
I/O	1	BATSS software tool control file	A.2.24

23. `BATSS_machine_control`: Controls the runtime behavior of the BATSS software tools `BATSS_machine_image` (#4) and `BATSS_machine_detect` (#10). As with the tools themselves, the parameter `MACHINE` is required in order to identify the machine thread being addressed by the function call.

File: `BATSS_machine.pro`
IDL type: Procedure. Return value: N/A

Required input arguments:

Argument type	Name	Variable type	Description
Paramater	MACHINE	String (scalar)	'[machine_disk]_[thread]'

Input/Output keywords: (see script file for full list)

I/O type	Name	Variable type	Description
O	MACHINEFILE	String	Returns name of machine control file
I	INITIALIZE	Boolean	Set to initialize machine control file and use default settings
I	ACTIVE	Boolean	Set to label machine as active
I	PRIORITY	Integer	Set priority among machines (1=highest)
I	HALT_IMG	Boolean	Set to halt execution of imaging thread
I	HALT_DET	Boolean	Set to halt execution of detection thread
I	WAIT	Float	[sec] Time to wait before checking on new assigned observations (10 sec by default)

Input/Output data products:

Type	BATSS data level	Product	Table reference
I/O	1	BATSS machine control file	A.2.25

24. `BATSS_trigger_control`: Controls the runtime behavior of the BATSS software tool `BATSS_trigger` (#16).

File: `BATSS_queue.pro`
IDL type: Procedure. Return value: N/A

Input/Output keywords:

I/O type	Name	Variable type	Description
I	`RESET`	Boolean	Set to restore default settings
I	`HALT`	Boolean	Set to halt execution of routine
I	`REFRESH`	Boolean	Set to refresh entire trigger catalog
I	`WAIT`	Float	[sec] Time to wait before checking on new observations to be assigned (10 sec by default)
I	`CHRONOLOGICAL`	Boolean	Set to read observation-level detection catalogs chronologically
I	`LAST`	Boolean	Set to read last observation-level detection catalog first
O	`CONTROLFILE`	String	Returns name of FITS control file for routine

Input/Output data products:

Type	BATSS data level	Product	Table reference
I/O	1	BATSS software tool control file	A.2.24

Page intentionally left blank

Appendix C

BATSS GCNs

The Gamma-ray Coordinates Network (GCN, Barthelmy et al. 1998), operating out of NASA's Goddard Space Flight Center (GSFC), is the primary alert system for information on detection and follow-up observation of GRBs and other Transients.[1] After a short introduction on the three major types of communications defined within the system (Notices, Circulars and Reports), this appendix provides a description of the generic GCN Notice type `SWIFT_BAT_SLEW_GRB_POSITION`, designed in collaboration with S. Barthelmy and C. Markwardt from the *Swift*-BAT team (GSFC) for the exclusive purpose of reporting BATSS GRB and Transient detections in real time. The BATSS data pipeline (Chapter 3) incorporates the automated generation of BATSS GCN Notices upon detection and triggering on candidate GRBs, and the description of the fields ("tokens") included in the Notices, along with the data reduction method to generate their corresponding token values, are included in this appendix as well.

[1] In fact, the system is currently undergoing a period of transition towards becoming the Transient Astronomy Network (TAN), in order to encompass within its core mission the reporting of a larger set of transient activity phenomena beyond GRBs.

C.1 Definitions

This section provides a brief introduction to the GCN/TAN system with a focus on its relation to the reports of observations from the BATSS survey; further background information can be found on the GCN website.[2] The GCN system distinguishes three (3) main types of alerts:

Notices serve as the early alerts of detections of possible new GRBs and Transients. They are generally sent by observers as real-time automated messages, formatted as machine-readable *packets* populated by a set of *tokens* (fields), which as a whole characterize the detection being reported. The BATSS GCN Notice type (packet) `SWIFT_BAT_SLEW_GRB_POSITION`, the main subject of this Appendix, belongs under this alert category.

Circulars[3] are brief prose-style summaries of observations, normally sent by ground observers in short order after the automated Notices, with the purpose of describing the details of a confirmed detection or a set of ongoing follow-up observations. Most of the communications related to BATSS-detected GRBs that have been distributed via the GCN system have been sent in the form of GCN Circulars, and their specific references and results have been quoted within the Chapter 4 analysis of the BATSS GRB survey.

Reports[4] are the final, comprehensive summaries of all observations of a particular object, where all the available data for the object from various observatories is synthesized. In the case of *Swift* GRBs, these are normally prepared by the designated Burst

[2] `http://gcn.gsfc.nasa.gov`

[3] `http://gcn.gsfc.nasa.gov/gcn_circulars.html`

[4] `http://gcn.gsfc.nasa.gov/reports.html`

Advocate from the mission's science team, and published several weeks after the original observations have been carried out. Available GCN Reports on BATSS-detected GRBs have been quoted and referenced within the discussion of Chapter 4 as well.

C.2 The GCN Notice type SWIFT_BAT_SLEW_GRB_POSITION

The *Swift* science team has created a large library of standard GCN Notice types for the automated reporting of detections of GRBs and Transients by all three of the mission's on-board instruments. These Notice types are listed and briefly described in the GCN/*Swift* GRB and Transient Notices webpage.[5] In addition, the technical description of the contents of these and all other Notice types defined for the GCN/TAN system is provided by the GCN/TAN Internet Socket Packet Definition Document[6], where each type is identified by a *packet type number* in the range 60–99.

For the specific purpose of reporting new burst positions from BATSS slew observations, we —in collaboration with the *Swift*-BAT team— developed the GCN Notice type SWIFT_BAT_SLEW_GRB_POSITION, identified by the packet type #99. In its generic form, the packet consists of a set of 40 four-byte quantities, and it was modeled after the GCN Notice BAT_POS (type=61), which had been previously developed to announce BAT on-board triggers, usually within 10–20 sec of the trigger time.

Table C.1 lists the contents of the packet SWIFT_BAT_SLEW_GRB_POSITION as currently listed in the GCN/TAN Internet Socket Packet Definition Document, which provides further information on the individual tokens (fields) as originally defined by the system. Section C.3 then discusses the implementation of this packet within the BATSS pipeline for reporting of candidate GRB positions in real time.

---

[5] http://gcn.gsfc.nasa.gov/gcn/swift.html

[6] http://gcn.gsfc.nasa.gov/gcn/sock_pkt_def_doc.html

TABLE C.1
GCN Notice SWIFT_BAT_SLEW_GRB_POSITION: Generic list of tokens (fields) and their formats as originally defined by the GCN system

Index	Item name	Units	Comments
0	pkt_type	integer	Packet type number (=99)
1	pkt_sernum	integer	1 thru infinity
2	pkt_hop_cnt	integer	Incremented by each node
3	pkt_sod	[centi-sec]	(int)(sssss.sss *100)
4	id_num	integer	ID number
5	burst_tjd	[days]	Truncated Julian Day
6	burst_sod	[centi-sec]	(int)(sssss.sss *100)
7	burst_ra	[0.0001-deg]	(int)(0.0 to 359.9999 *10000)
8	burst_dec	[0.0001-deg]	(int)(-90.0 to +90.0 *10000)
9	burst_flue	[counts]	Num events during image window, 0 to inf
10	burst_ipeak	[cnts/sec]	Counts in image-plane peak, 0 to infinity
11	burst_error	[0.0001-deg]	(int)(0.0 to 180.0 *10000)
12	spare	integer	4 bytes for the future
13	spare	integer	4 bytes for the future
14	integ_time	[4mSec]	Duration of the trigger interval, 1 to inf
15	spare	integer	4 bytes for the future
16	spare	integer	4 bytes for the future
17	trig_index	integer	Trigger criterion index
18	soln_status	bits	Type of source/trigger found
19	misc	bits	Misc stuff packed in here
20	image_signif	[centi-sigma]	(int)(sig2noise *100)
21–38	spare[18]	integer	72 bytes for the future
39	pkt_term	integer	Pkt Termination (always = \n)

C.3 BATSS GCN Notices for GRB detections

The BATSS data pipeline (Chapter 3) includes an implementation of the generic GCN Notice type `SWIFT_BAT_SLEW_GRB_POSITION` for the specific purpose of the reporting candidate GRB detections from real-time BATSS observations. The tokens (fields) of these BATSS GCN Notices are calculated by the routine `BATSS_trigger` (Section B.6, item #16) as part of its analysis of individual candidate sources, and then passed as an IDL structure array to the subroutine `BATSS_GCN`, which in turn does the proper formatting of the data fields and drafts the GCN Notice to be sent as output.

The original BATSS GCN Notices are issued by the pipeline as e-mail messages with the subject field "`SWIFT_BAT_SLEW_POS_IMPORT`," and sent to the e-mail address for the GCN system `vxw@capella.gsfc.nasa.gov` for their automated parsing and distribution to the worldwide GCN Network. The official GCN Notice distributed includes the subject field "`GCN/SWIFT_BAT_SLEW_POSITION`," and adds a number of tokens and comments based on the data provided in the original BATSS GCN Notice. An example of an original BATSS GCN Notice and its corresponding distributed GCN Notice (as originally sent/received) are shown in Figure C.1. These correspond to the real-time detection of candidate GRB 110906A, which was assigned the BATSS trigger number 000607.

For the rest of this section, we provide a detailed description of the individual tokens (fields) in the input BATSS GCN Notices (subject "`SWIFT_BAT_SLEW_POS_IMPORT`") for real-time GRB detections. Table C.2 contains the list of tokens defined, along with the units and format of their corresponding token values. The description and computation method for the token values employed by the BATSS pipeline follows below.

Antonio Copete <acopete@head.cfa.harvard.edu>
To: vxw@capella.gsfc.nasa.gov
Cc: craigm@milkyway.gsfc.nasa.gov, scott@milkyway.gsfc.nasa.gov, acopete@head.cfa.harvard.edu
SWIFT_BAT_SLEW_POS_IMPORT

```
TITLE:          GCN/SWIFT NOTICE
NOTICE_DATE:    Tue Sep  6 16:15:18 2011 UT
NOTICE_TYPE:    Swift/BAT Slew GRB Position
ID_NUM:         000607
GRB_RA:         296.89d {19h 47m 33.9s} (J2000)
GRB_DEC:        -26.21d {-26d 12' 32"} (J2000)
GRB_ERROR:      3.75 [arcmin radius, stat+sys(90%)]
GRB_INTEN:      214306 [cnts]   Peak=      0 [cnts/sec]
TRIGGER_DUR:    13.8 [sec]
BKG_INTEN:      0 [cnts]
BKG_TIME:       0.00 SOD
BKG_DUR:        0.0 [sec]
GRB_DATE:       15810 TJD
GRB_TIME:       44713.49 SOD
GRB_PHI:        85.59 -  78.29 [deg]
GRB_THETA:      37.17 -  32.34 [deg]
TRIGGER_INDEX:  9
SOLN_STATUS:    0x00000011
RATE_SIGNIF:    0.00 [sigma]
IMAGE_SIGNIF:   5.53 [sigma]
ENERGY_RANGE:   0x5
PAGE_URL:   triggers/000607/BATSS_000607.html
TEST_FLAG:      0
COMMENTS:
```

(a) Original BATSS GCN Notice `SWIFT_BAT_SLEW_POS_IMPORT`

Bacodine <vxw@capella2.gsfc.nasa.gov> September 6, 2011 12:15 PM
To: josh@head.cfa.harvard.edu, acopete@head.cfa.harvard.edu
GCN/SWIFT_BAT_SLEW_POSITION

```
TITLE:          GCN/SWIFT NOTICE
NOTICE_DATE:    Tue 06 Sep 11 16:15:23 UT
NOTICE_TYPE:    Swift-BAT Slew GRB Position
ID_NUM:         607
GRB_RA:         296.890d {+19h 47m 34s} (J2000),
                297.068d {+19h 48m 16s} (current),
                296.126d {+19h 44m 30s} (1950)
GRB_DEC:        -26.210d {-26d 12' 35"} (J2000),
                -26.181d {-26d 10' 49"} (current),
                -26.334d {-26d 20' 02"} (1950)
GRB_ERROR:      3.75 [arcmin radius, statistical only]
GRB_INTEN:      214306 [cnts]    Image_Peak=0 [image_cnts]
TRIGGER_DUR:    13.800 [sec]
TRIGGER_INDEX:  9    Criteria: (S(15-50) OR H(50-150)) > 4.0 sigma  AND  B(15-150) > 6.0 sigma
ENERGY_RANGE:   15-150 keV
BKG_INTEN:      0 [cnts]
BKG_TIME:       0.00 SOD {00:00:00.00} UT
BKG_DUR:        0 [sec]
GRB_DATE:       15810 TJD;  249 DOY;  11/09/06
GRB_TIME:       44713.48 SOD {12:25:13.48} UT
SOLN_STATUS:    0x4011
RATE_SIGNIF:    0.00 [sigma]
IMAGE_SIGNIF:   5.53 [sigma]
SUN_POSTN:      165.01d {+11h 00m 01s}   +6.40d {+06d 23' 56"}
SUN_DIST:       130.29 [deg]   Sun_angle= -8.8 [hr] (East of Sun)
MOON_POSTN:     278.50d {+18h 33m 59s}  -21.67d {-21d 40' 14"}
MOON_DIST:      17.55 [deg]
MOON_ILLUM:     71 [%]
GAL_COORDS:     14.27,-23.26 [deg] galactic lon,lat of the burst (or transient)
ECL_COORDS:     294.04, -4.99 [deg] ecliptic lon,lat of the burst (or transient)
COMMENTS:       SWIFT-BAT Slew GRB Coordinates.
COMMENTS:       A point_source was found.
COMMENTS:       This does not match any source in the ground catalog.
COMMENTS:       This is probably a GRB.
COMMENTS:       High confidence of reality (silver-plated).
COMMENTS:       This Notice was ground-processed from flight-data.
COMMENTS:
```

(b) Distributed GCN Notice `GCN/SWIFT_BAT_SLEW_POSITION`

FIGURE C.1: Examples of original GCN Notices for the reporting of BATSS real-time GRB detections: (a) Original created and submitted automatically by the BATSS system; (b) Official Notice distributed worldwide by the GCN system. The candidate GRB for this example is GRB 110906A, which was assigned the BATSS trigger number 000607.

TABLE C.2
BATSS GCN Notice for GRB detections: List of tokens (fields) and their formats

#	Token Name	Units	Format
1.	TITLE	string	GCN/SWIFT NOTICE
2.	NOTICE_DATE	string	[DOW MMM DOM HH:MM:SS YYYY] UT
3.	NOTICE_TYPE	string	Swift/BAT Slew GRB Position
4.	ID_NUM	6-digit integer	[NXXXXX]
5.	GRB_RA	[degrees]	[DDD.DD]d {[HH]h [MM]m [SS.S]s} (J2000)
6.	GRB_DEC	[degrees]	[±DD.DD]d {[±DD]d [MM]′ [SS]″} (J2000)
7.	GRB_ERROR	[arcminutes]	[F.FF] [arcmin, stat+sys(90%)]
8.	GRB_INTEN	[counts]	[N_1] [cnts] Peak= [N_2] [cnts/sec]
9.	TRIGGER_DUR	[seconds]	[F.F] [sec]
10.	BKG_INTEN	[counts]	[N] [cnts]
11.	BKG_TIME	[seconds-of-day]	[F.FF] SOD
12.	BKG_DUR	[seconds]	[F.F] [sec]
13.	GRB_DATE	[Truncated Julian Day]	[DDDDD] TJD
14.	GRB_TIME	[seconds-of-day]	[SSSSS.SS] SOD
15.	GRB_PHI	[degrees]	[$DD.DD_i$] - [$DD.DD_f$] [deg]
16.	GRB_THETA	[degrees]	[$DD.DD_i$] - [$DD.DD_f$] [deg]
17.	TRIGGER_INDEX	integer	[N]
18.	SOLN_STATUS	32-bit HEX	0x[HHHHHHHH]
19.	RATE_SIGNIF	[sigma]	[F.FF] [sigma]
20.	IMAGE_SIGNIF	[sigma]	[F.FF] [sigma]
21.	ENERGY_RANGE	4-bit HEX	0x[H]
22.	PAGE_URL	HTML file	triggers/[NXXXXX]/BATSS_[NXXXXX].html
23.	NOT_A_GRB	string	Not a real GRB
24.	NOT_A_TRANS	string	Not a real Transient
25.	UPDATE_FLAG	boolean	[B]
26.	TEST_FLAG	boolean	[B]
27.	COMMENTS	string (array)	[COMMENTS]

1. TITLE: Always set to default string 'GCN/SWIFT NOTICE'.

2. NOTICE_DATE: Set to time (UT) of issuing Notice, in the form of a long-format string (e.g. 'Tue Sep 6 16:15:18 2011 UT')

3. NOTICE_TYPE: Always set to default string 'Swift/BAT Slew GRB Position'

4. ID_NUM: BATSS trigger number assigned by the routine BATSS_trigger (Section B.6, item #16). The trigger number NXXXXX is a 6-digit integer, with N $\equiv$ 0 for real-time, single-slew detections, as is the case for real-time BATSS candidate GRBs. The 5-digit integer XXXXX is assigned sequentially.

5. GRB_RA: Right Ascension (J2000) of the BATSS candidate GRB, quoted in decimal degrees, as computed by BATSS_trigger after weighing the positions of the contributing individual detections by their significance. GRB_RA also quotes the R.A. in h-m-s format.

6. GRB_DEC: Declination (J2000) of the BATSS candidate GRB, computed in an analogous way to GRB_RA, and quoted in both decimal degrees and d-m-s format.

7. GRB_ERROR: Candidate GRB error radius (90%), including both statistical and systematic errors. BATSS_trigger computes it as the largest error radius of the contributing individual detections, which have in turn been computed by BATSS_celldetect (Section B.5, item #14) using the calibration prescription for BATSS position uncertainties of Section 2.4.4.

8. GRB_INTEN: Candidate GRB intensity, computed by BATSS_trigger as the total number N_1 of detector counts recorded over the total exposure of the source during the slew, or, if a smaller burst duration (T_{100}) is found by BATSS_lc (Section B.6, item #17), the detector counts over that smaller time window. In addition, if a 1-sec peak

count interval (T_{1s}) is found, the number of detector counts `N2` over that interval are quoted within the same token value as well; otherwise, 0 [cnts/sec] is quoted.

9. `TRIGGER_DUR`: Image accumulation time at the position of the candidate GRB, quoted in seconds. Computed as part of the BATSS detection stage (Section 3.8) by the tool `BATSS_celldetect`.

10. `BKG_INTEN`: Background intensity of candidate GRB, computed as the total number of detector counts recorded over the background interval preceding the GRB outburst (`T_BKG1`) found earlier by `BATSS_lc`. If no pre-burst background interval was found, the token value is set to `0 [cnts]` by default.

11. `BKG_TIME`: Background interval time, computed as the start time in seconds-of-day (SOD) of the pre-burst background interval `T_BKG1`. If no interval found, the token value defaults to `0.00 SOD`.

12. `BKG_DUR`: Duration of background interval of candidate GRB, quoted in seconds. If no background interval found, the token value defaults to `0.0 [sec]`.

13. `GRB_DATE`: GRB date, computed as date of BATSS trigger time, in units of Truncated Julian Date (TJD). If a full-burst time interval (T_{100}) is found by `BATSS_lc`, the BATSS trigger time is set to the start time of the burst. If no T_{100} interval is found, the quoted value is the start of the integration time interval at the position of the source.

14. `GRB_TIME`: GRB time, quoted as seconds-of-day (SOD) after `GRB_DATE`, based on BATSS trigger time as defined in item #13.

15. `GRB_PHI`: Azimuthal angle (ϕ) of GRB candidate position in BAT instrument coordinates. Because the source's position shifts across the BAT FoV during a slew, this is given as a range ϕ_i – ϕ_f between the initial and final source positions while in the

BAT FoV. The range is calculated by `BATSS_lc`, and the angles are quoted in decimal degrees.

16. `GRB_THETA`: Polar angle (θ) of GRB candidate position in BAT instrument coordinates, quoted as a range $\theta_{\rm i}$ – $\theta_{\rm f}$ in decimal degrees, and calculated by `BATSS_lc`.

17. `TRIGGER_INDEX`: BATSS trigger index of GRB candidate, assigned by `BATSS_trigger` according to the single-slew coincidence criteria quoted in Table 3.5. Currently defined BATSS trigger indices for single-slew candidate sources are 5, 8, 9, and 10, listed in increasing order of likelihood of corresponding to a real source.

18. `SOLN_STATUS`: 32-bit (8-digit) HEX number, quoted as `0x[HHHHHHHH]`, which encodes a set of binary attributes related to the BATSS GRB detection. The individual bits and their values as assigned by `BATSS_trigger` are summarized in Table C.3.

19. `RATE_SIGNIF`: Significance (S/N) of rate-trigger detection, quoted in sigma units. Because rate triggers are currently not implemented for BATSS sources, the token value is always set to `0.00 [sigma]`.

20. `IMAGE_SIGNIF`: Significance (S/N) of image-trigger detection, quoted in sigma units. Because all BATSS triggers are image triggers, this token always applies to BATSS GRB candidates, and is quoted as the source's S/N in the Broad (15–150 keV) energy band, regardless of the energy channels of the individual detections.

TABLE C.3
BATSS GCN Notice: Flag bits for token SOLN_STATUS (#18.)

Bit	F/G[a]	Name	Description	Value	Explanation
0	F	point_src	Point source was found	1	Flight-assigned, but bit is always set by convention
1	F	grb	It is a GRB	0	Flight-assigned bits are normally unset
2	F	interesting	It is an interesting source (i.e. a flaring known source)	0	Flight-assigned bits are normally unset
3	F	flt_cat_src	It is in the flight catalog	0	Flight-assigned bits are normally unset
4	F	image trigger	It is an image trigger (else rate trigger)	0	Flight-assigned, but always set by convention since all BATSS triggers are image triggers
5	G	def_not_grb	It is definitely not a GRB (i.e. a retraction)	0	Retraction Notices are not sent automatically
6	G	uncert_grb	It is probably not a GRB or Transient (hi bkg level, near SAA)	0	Retraction Notices are not sent automatically
7	G	uncert_grb	It is probably not a GRB or Transient (low image significance; < 5.0 sigma)	1|0	Set if token IMAGE_SIGNIF (#20.) < 5.0
8	G	gnd_cat_src	It is in the ground catalog	0	BATSS candidate GRBs are always uncatalogued
9	G	uncert_grb	It is probably not a GRB or Transient (negative bkg slope, exit SAA)	0	Retraction Notices are not sent automatically
10	G	st_loss_lock	Bad attitude data during slew, so trigger probably bogus	0	Retraction Notices are not sent automatically
11	G	uncert_grb	It is really probably not a GRB or Transient (VERY low image significance; < 4.0 sigma)	1|0	Set if token IMAGE_SIGNIF (#20.) < 4.0
12	G	blk_cat_src	It is in the catalog of sources to be blocked (internal use only)	0	No source blocking by BATSS
13	G	near_brt_star	There is a nearby bright star (mag < 6.5)	0	No bright star tracking by BATSS
14–29	G	spare	Spare for future use	0	Spare bits are always unset
30	G	test_submit	This is a test submission (internal use only)	1|0	Set if token TEST_FLAG (#26.) $= 0$
31	G	spare	Spare for future use	0	Spare bits are always unset

[a]F = flight-assigned, G = ground-assigned

21. ENERGY_RANGE: 4-bit (1-digit) HEX number, quoted as 0x[H], which encodes the set of energy bands of the contributing detections as follows:

Bit	Value	Condition
0	1|0	Set for Soft-band (15–50 keV) detection
1	1|0	Set for Hard-band (50–150 keV) detection
2	1|0	Set for Broad-band (15–150 keV) detection
3	0	Unassigned

22. PAGE_URL: URL of the candidate GRB within the data directory of the BATSS webpage. The fully qualified path to the candidate GRB webpage would then be:

    `http://hea-www.harvard.edu/BATSS/data/[PAGE_URL]`

    PAGE_URL is computed by BATSS_trigger as a function of the BATSS trigger number [NXXXXX] (token ID_NUM). This token allows for the BATSS candidate GRB webpage to be automatically copied to the BAT Wiki page for public access as soon as the Notice is received by the GCN system.

23. NOT_A_GRB: Binary token set to indicate a retraction of an earlier GRB detection Notice. When true, the token value is set to the string 'Not a real GRB'; otherwise, the token is suppressed altogether. Because retraction Notices are not sent automatically by BATSS_trigger, it does not include this token as part of its output.

24. NOT_A_TRANS: Binary token set to indicate a retraction of an earlier Transient detection Notice. When true, the token value is set to the string 'Not a real Transient'; otherwise, the token is suppressed altogether. Because retraction Notices are not sent automatically by BATSS_trigger, it does not include this token as part of its output.

25. UPDATE_FLAG: Binary flag ([B] = 1|0), set when issuing an update to a detection already reported on a previous GCN Notice.

26. `TEST_FLAG`: Binary flag (`[B]` = 1|0), set to prevent the GCN Notice from being distributed to the world. Setting input keyword `TEST` of `BATSS_trigger` procedure sets this flag.

27. `COMMENTS`: String with additional comments to the added to the end of the Notice, with the character '`\`' separating individual lines. Comments beyond those generated automatically by `BATSS_trigger` can be passed as a string array value to the input keyword `GCN_COMMENTS`.

Page intentionally left blank

Appendix D

BATSS GRB catalog

This appendix summarizes all of the available BATSS detection and prompt emission data from each of the nineteen (19) GRBs detected exclusively by BATSS and introduced in Chapter 4 on the BATSS GRB survey. As a complement to the analysis of Section 4.4, where they were analyzed globally as a population, this appendix lists them individually in order to focus on the particular characteristics of each one. The description is made both from the anecdotal perspective of when and how their discovery was made, and from the scientific perspective of the distinguishing features that may make them a subject of further study in the future.

In the list that follows, the BATSS mode of detection for each GRB is included, along with a list of relevant references in the form of GCN Circulars and Reports (defined in Appendix C, Section C.1), and a reference to a figure with relevant reduced detection and prompt emission data from the BATSS pipeline (Section 4.3). The figure includes the results from the latest archival data processing of the corresponding BATSS single-slew observation, including subfigures with detection, lightcurve and spectral analysis results.

GRB 070326 (Figure D.1): First BATSS-detected GRB, found in the preliminary testing phase of March, 2007.

References: Copete et al. (2007, GCN 6653)

GRB 071212 (Figure D.2): Detected in archival processing only, at the edge of the BAT FoV (27.9% mean coding fraction). Categorized as a BATSS index 9 candidate, from coincidence of Soft (8.5σ) and Broad (9.2σ) band detections only.

GRB 080130 (Figure D.3): First BATSS GRB detected in real time. No Bayesian time blocks were derived from the burst lightcurve, but the GRB afterglow was confirmed in follow-up *Swift*-XRT observations.

References: Copete et al. (2008a); Cummings et al. (2008a); D'Avanzo et al. (2008); Schady & Stamatikos (2008); Starling et al. (2008); Starling & Stamatikos (2008)

GRB 080702B (Figure D.4): Detected in real time, with the GRB afterglow being confirmed in follow-up *Swift*-XRT observations. Categorized as Index 8, from coincidence of Soft (6.5σ) and Broad (6.3σ) band detections only.

GRB 080806 (Figure D.5): Detected in archival processing only, at a high detection significance of 10.9σ in the Broad band. Slew `080806_09h57m59s+188s` had not been processed in real time.

GRB 081025 (Figure D.6): Detected and reported in real time, with the GRB afterglow being confirmed in follow-up *Swift*-XRT observations. GRB prompt emission was also observed by Konus-Wind, Suzaku WAM, Fermi GBM, and INTEGRAL SPI-ACS.

References: Copete et al. (2008b, GCN 8409); Mao et al. (2008, GCN 8411); Golenetskii et al. (2008b, GCN 8412); Schady & Mao (2008, GCN 8414); Cummings et al. (2008b, GCN 8415); Khamitov et al. (2008, GCN 8418); Kann et al. (2008, GCN 8420); Kira et al. (2008, GCN 8445); Kienlin & Bissaldi (2008, GCN 8483).

GRB 081203B (Figure D.7): Detected and reported in real time, with the GRB afterglow being confirmed in follow-up *Swift*-XRT observations.

References: Copete et al. (2008c, GCN 8600); Copete et al. (2008e, GCN 8602); Sbarufatti et al. (2008a, GCN 8605); Schady et al. (2008, GCN 8606); Berger (2008, GCN 8607); Andreev et al. (2008a, GCN 8608); Golenetskii et al. (2008c, GCN 8610); Sbarufatti et al. (2008b, GCN 8612); Chandra & Frail (2008, GCN 8625); Andreev et al. (2008b, GCN 8626); Perley & Bloom (2008, GCN 8631); Perley (2008, GCN 8637); Terada et al. (2008, GCN 8638); Fatkhullin et al. (2008, GCN 8651).

GRB 081211B (Figure D.8): Detected and reported in real time. No Bayesian time blocks found in lightcurve analysis, but GRB afterglow was confirmed in follow-up *Swift*-XRT observations. Konus-Wind found a short 2.9-sec spike ∼120 sec before start of slew (Golenetskii et al., GCN Circ. 8676), which indicates this is probably a short GRB with extended emission (S-GRB with E.E.). These make up only 2% of the overall *Swift* GRB population, numbering only 10 up to the end of 2009 (Sakamoto et al. 2011).

References: Copete et al. (2008d, GCN 8661); Page et al. (2008a, GCN 8666); Holland (2008, GCN 8669); Golenetskii et al. (2008a, GCN 8676); Page et al. (2008b, GCN 8683); Andreev et al. (2008c, GCN 8727); GCN Report 189.1 (Holland et al. 2008).

GRB 090118 (Figure D.9): Detected in real time only, under the previous implementation of the BATSS imaging and detection algorithms (25% partial coding threshold). Not detected in archival data, under current data pipeline implementation (15% partial coding threshold). GRB afterglow confirmed in follow-up *Swift*-XRT observations.

References: Copete et al. (2009d, GCN 8825); Olivares et al. (2009, GCN 8826); Schady (2009, GCN 8827); Rowlinson & Page (2009a, GCN 8828); Updike & Hart-

mann (2009b, GCN 8829); Sakamoto et al. (2009a, GCN 8830); Updike & Hartmann (2009a, GCN 8831); Minowa et al. (2009, GCN 8832); Rowlinson & Page (2009b, GCN 8840); Rossi et al. (2009, GCN 8850).

GRB 090306B (Figure D.10): Detected and reported in real time, with the GRB afterglow being confirmed in follow-up *Swift*-XRT observations.

References: Copete et al. (2009a, GCN 8944); Evans (2009b, GCN 8947); Updike et al. (2009, GCN 8958); Beckmann et al. (2009, GCN 8968); Evans (2009a, GCN 8987).

GRB 090418B (Figure D.11): Detected and reported in real time, but *Swift*-XRT was unable to follow up due *Swift* ToO schedule overload. Brightest BATSS-detected GRB, with a 94.9σ significance in the Broad band.

References: Copete et al. (2009b, GCN 9159); Golenetskii et al. (2009c, GCN 9171); Guidorzi et al. (2009, GCN 9176); Afonso et al. (2009, GCN 9178); Nissinen & Hentunen (2009, GCN 9181); Kono et al. (2009, GCN 9186); Bikmaev et al. (2009, GCN 9191).

GRB 090823 (Figure D.12): Detected in real time, and categorized as a BATSS index 8 candidate due to coincidence of Soft (8.4σ) and Broad (7.8σ) band detections. GRB afterglow was confirmed in follow-up *Swift*-XRT observations.

References: Cummings et al. (2009b, GCN 9835); Golenetskii et al. (2009a, GCN 9836); Cummings (2009, GCN 9838); Copete et al. (2009c, GCN 9839); Grupe et al. (2009, GCN 9840); Grupe (2009, GCN 9902), Grupe et al. (2009).

GRB 090929A (Figure D.13): Detected in archival data only. No BATSS real-time detection was made in any band, possibly due to a detection run-time error related to the position being near edge of its corresponding ZEA full-sky sub-projection.

Reported in real time by J. Cummings et al (GSFC). A follow-up *Swift*-XRT observation was carried out, but no point source was found due to the presence of a 9th magnitude star 45″ from the reported BAT position.

References: Rau (2009, GCN 9962); Cummings & Krimm (2009, GCN 9966); Golenetskii et al. (2009b, GCN 9968); Golenetskii et al. (2009d, GCN 9976); Page (2009, GCN 9977); Cummings et al. (2009a, GCN 9980); Siegel & Page (2009, GCN 9981); Ohmori et al. (2009, GCN 9992); Chakrabarti et al. (2009, GCN 10010).

GRB 100120A (Figure D.14): Detected in archival data only, due to BATSS real-time processing being offline at the time of a major software and hardware upgrade (Section 3.2. No follow-up observations were made, but Broad band detection had very high significance (27.7σ), and a lightcurve profile consistent with that of a real GRB.

GRB 101004A (Figure D.15): Detected in archival data only. BATSS real-time processing was online but triggering routine was in the process of being upgraded. No follow-up observations were made, but Broad band detection had very high significance (12.0σ), and a lightcurve profile consistent with that of a real GRB.

GRB 110107A (Figure D.16): Detected in archival data only, and categorized as a BATSS index 9 candidate due to coincidence of high-significance Soft (51.0σ) and Broad (60.3σ) band detections. BATSS real-time detection was online but triggering routine was in the process of being upgraded. Reported in real time by J. Cummings (GSFC), with GRB prompt emission also detected by Fermi GBM. GRB afterglow was confirmed in follow-up *Swift*-XRT observations.

References: Cummings (2011, GCN 11545); Cummings & Barthelmy (2011, GCN 11546); Stratta et al. (2011, GCN 11547); Immler & Stratta (2011, GCN 11551); Stratta (2011, GCN 11565).

GRB 110319B (Figure D.17): Detected in archival data only. BATSS real-time detection was online but triggering routine was in the process of being upgraded. First detected and reported in real time by Fermi GBM, followed by a report from the *Swift*-BAT team by J. Cummings (GSFC). GRB afterglow confirmed in follow-up *Swift*-XRT observations.

References: Cummings et al. (2011, GCN 11813); Sbarufatti (2011a, GCN 11814); Updike et al. (2011, GCN 11815); Marshall & Sbarufatti (2011, GCN 11817); Palmer et al. (2011, GCN 11818); Sbarufatti (2011b, GCN 11820).

GRB 110906A (Figure D.18): Detected and reported in real time. Categorized as a BATSS index 9 candidate, due to coincidence of Soft (4.7σ) and Broad (7.8σ) band detections. Source position was near the edge of the BAT FoV (23.7% mean coding fraction). No follow-up observations were scheduled due to a Moon constraint, hence no GRB afterglow confirmation was made. However, a point source consistent with the position of the BATSS candidate GRB was also found from an independent analysis of the BAT data by J. Cummings (GSFC).

References: Copete et al. (2011, GCN 12332).

GRB 111011A (Figure D.19): Detected in real time as a BATSS index 8 candidate (trigger 000645), and in archival data as an index 10 candidate (trigger 102678). No GCN alert was issued due to position being at Galactic latitude $|b| < 10^{\circ}$, raising the possibility of a Galactic origin. No follow-up observations were made, but Broad band detection had very high significance (21.8σ), and a rapidly fading lightcurve profile consistent with that of a real GRB.

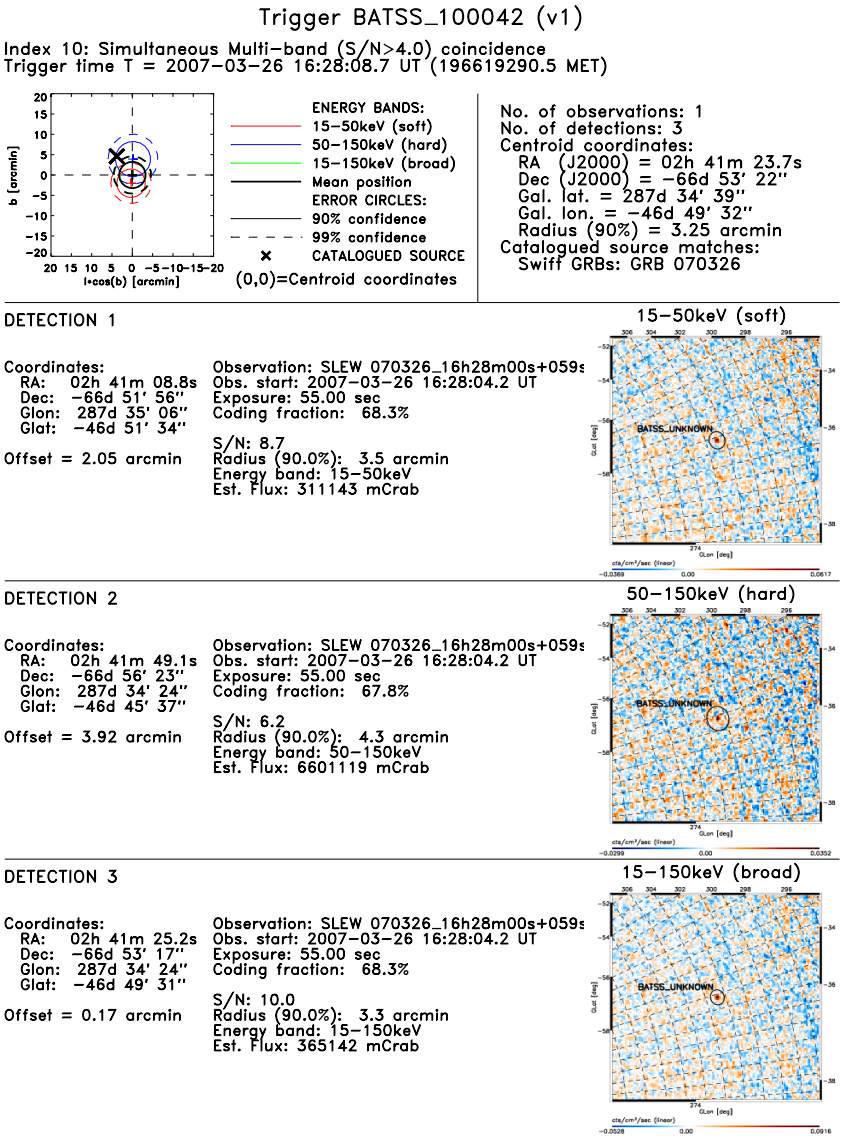

(a) BATSS detection parameters

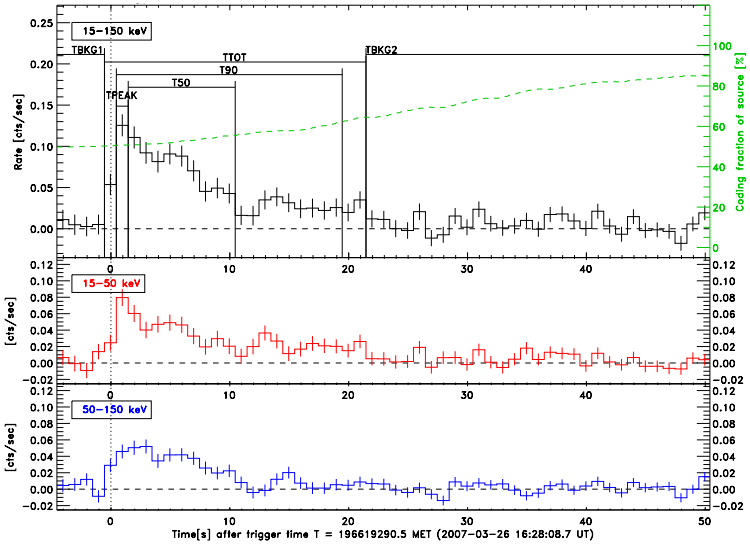

(b) BAT lightcurves (1-sec binning) and burst time blocks

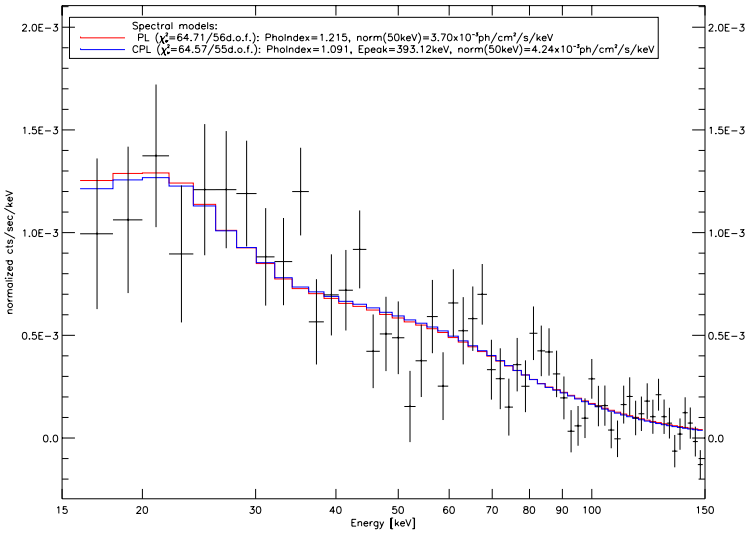

(c) BAT raw spectrum and folded models PL/CPL — time block T_{90}

FIGURE D.1: GRB 070326: BATSS detection and prompt emission data

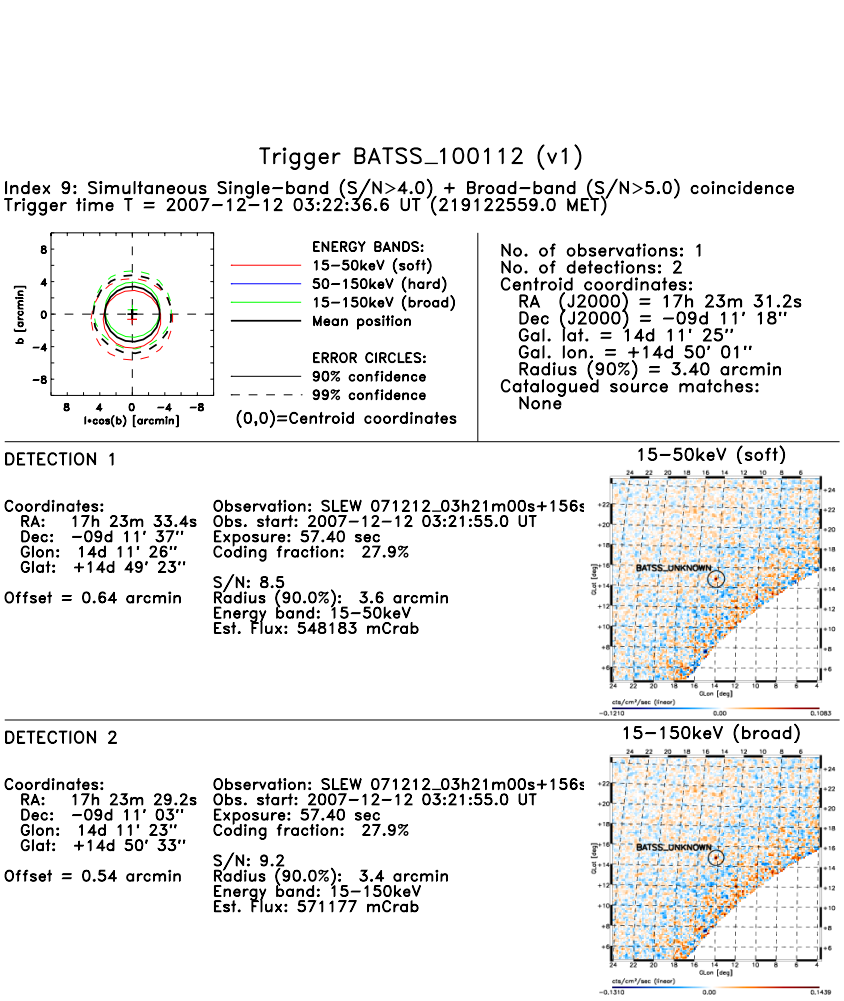

(a) BATSS detection parameters

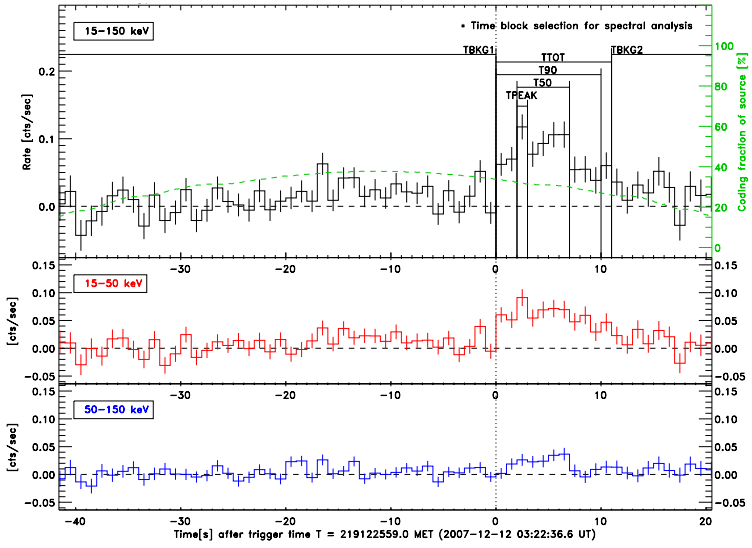

(b) BAT lightcurves (1-sec binning) and burst time blocks

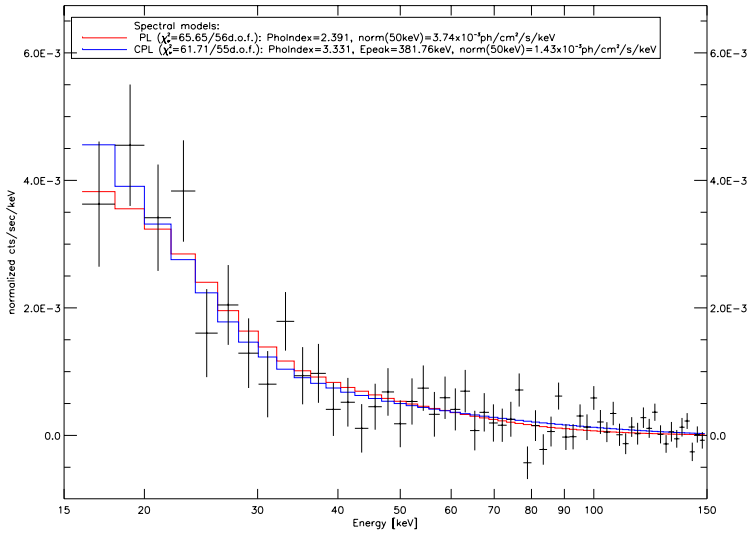

(c) BAT raw spectra and folded models PL/CPL — time block T_{90}

FIGURE D.2: GRB 071212: BATSS detection and prompt emission data

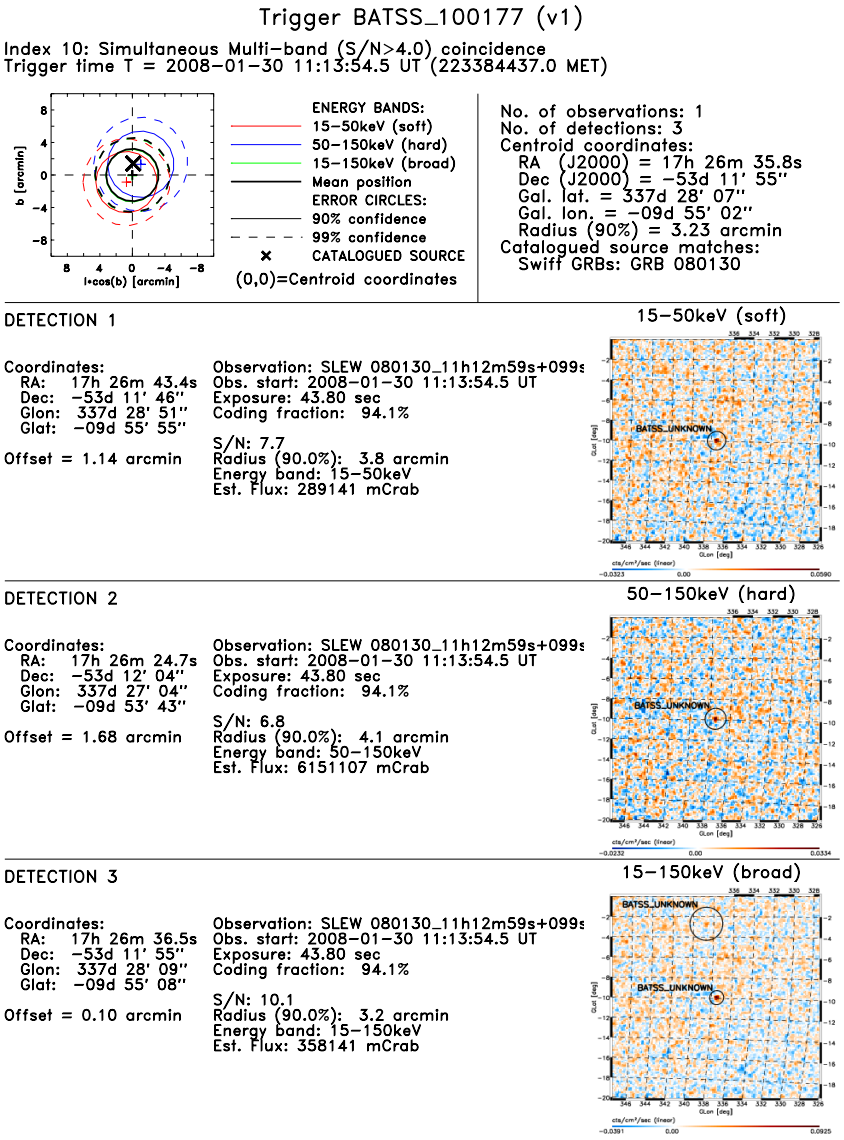

(a) BATSS detection parameters

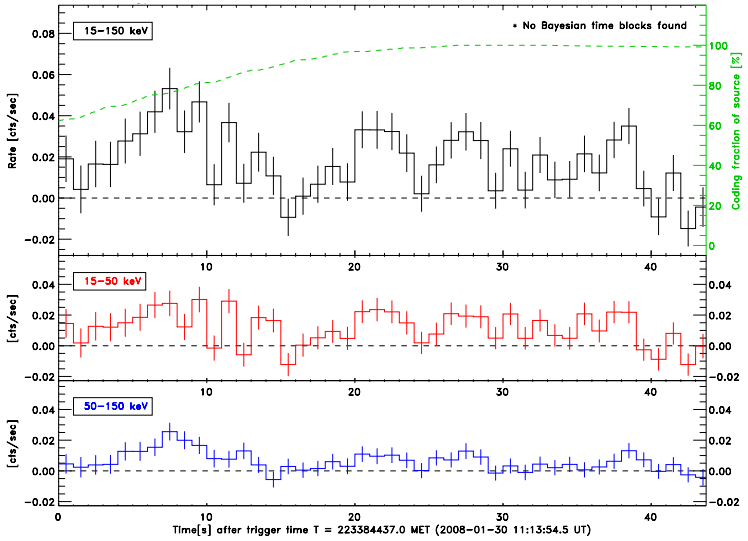

(b) BAT lightcurves (1-sec binning). No Bayesian time blocks found

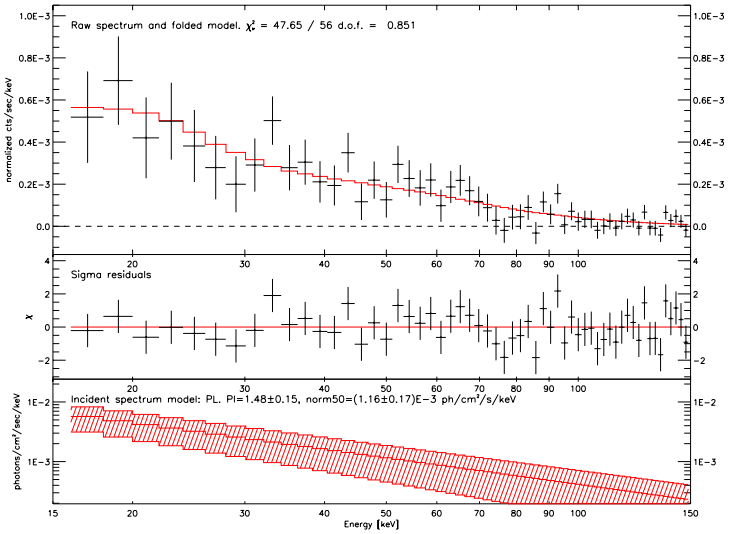

(c) BAT raw spectrum and folded model — full observation

FIGURE D.3: GRB 080130: BATSS detection and prompt emission data

Trigger BATSS_100478 (v1)

Index 8: Simultaneous Single−band (S/N>5.0) + Broad−band (S/N>4.0) coincidence
Trigger time T = 2008−07−02 01:10:41.1 UT (236653844.0 MET)

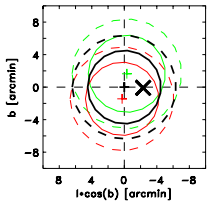

ENERGY BANDS:
15−50keV (soft)
50−150keV (hard)
15−150keV (broad)
Mean position
ERROR CIRCLES:
90% confidence
99% confidence
CATALOGUED SOURCE
(0,0)=Centroid coordinates

No. of observations: 1
No. of detections: 2
Centroid coordinates:
RA (J2000) = 23h 42m 23.4s
Dec (J2000) = −05d 29' 25"
Gal. lat. = 82d 37' 51"
Gal. lon. = −62d 49' 36"
Radius (90%) = 4.51 arcmin
Catalogued source matches:
Swift GRBs: GRB 080702B

DETECTION 1

Coordinates:
RA: 23h 42m 27.6s
Dec: −05d 30' 26"
Glon: 82d 38' 27"
Glat: −62d 51' 02"

Offset = 1.46 arcmin

Observation: SLEW 080702_01h08m59s+212s
Obs. start: 2008−07−02 01:10:07.2 UT
Exposure: 69.60 sec
Coding fraction: 63.7%

S/N: 5.9
Radius (90.0%): 4.5 arcmin
Energy band: 15−50keV
Est. Flux: 202134 mCrab

15−50keV (soft)

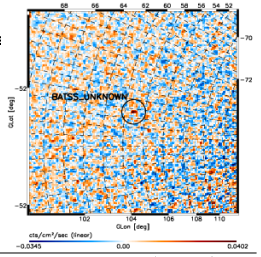

DETECTION 2

Coordinates:
RA: 23h 42m 18.5s
Dec: −05d 28' 15"
Glon: 82d 37' 10"
Glat: −62d 47' 57"

Offset = 1.68 arcmin

Observation: SLEW 080702_01h08m59s+212s
Obs. start: 2008−07−02 01:10:07.2 UT
Exposure: 69.60 sec
Coding fraction: 63.7%

S/N: 5.5
Radius (90.0%): 4.7 arcmin
Energy band: 15−150keV
Est. Flux: 191131 mCrab

15−150keV (broad)

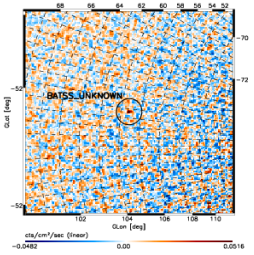

(a) BATSS detection parameters

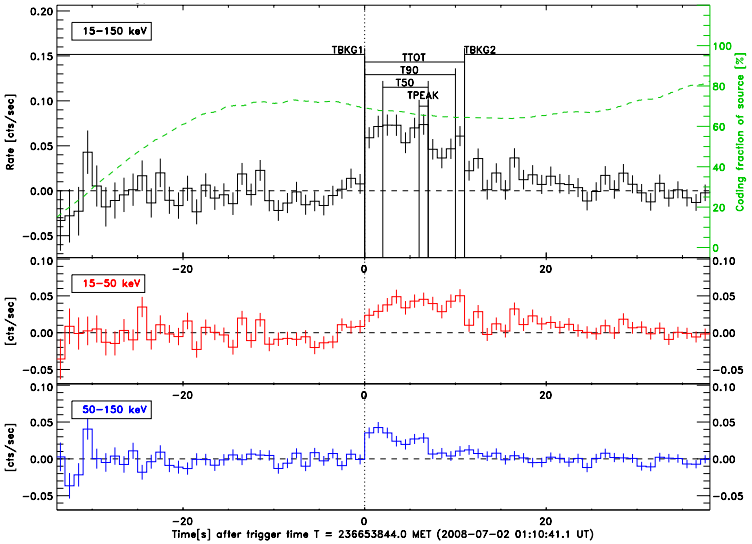

(b) BAT lightcurves (1-sec binning) and burst time blocks

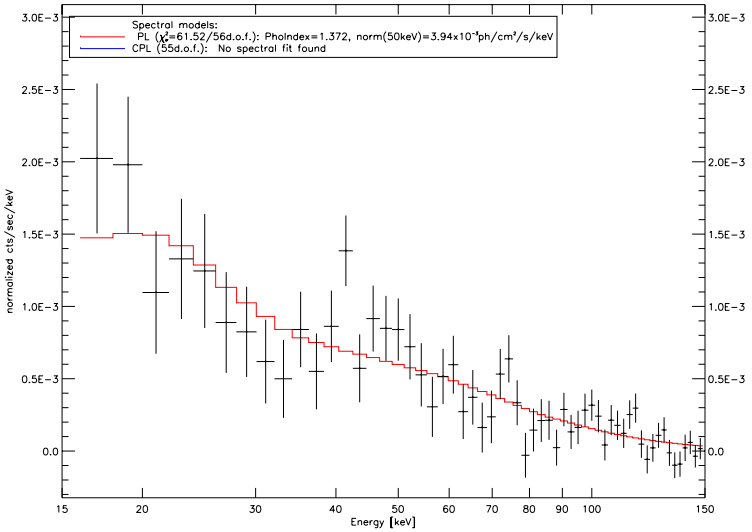

(c) BAT raw spectrum and folded model PL — time block T_{90}

FIGURE D.4: GRB 080702B: BATSS detection and prompt emission data

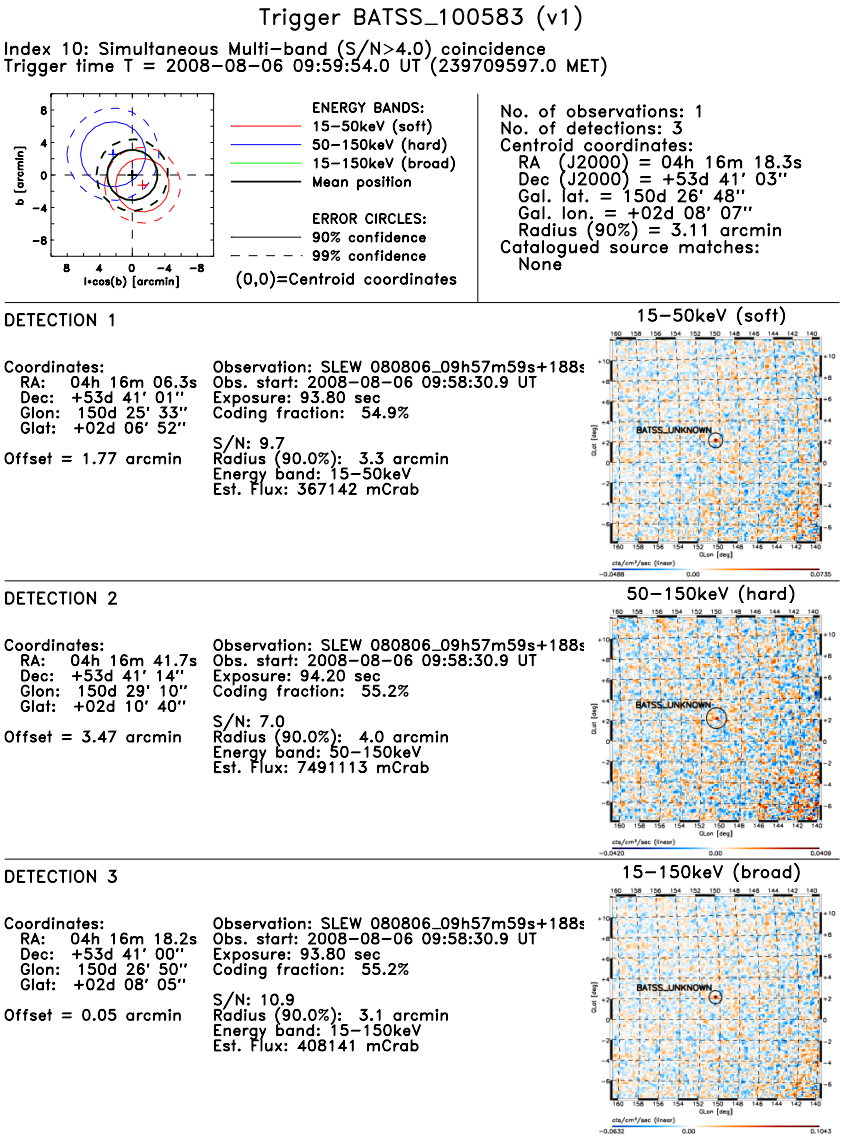

(a) BATSS detection parameters

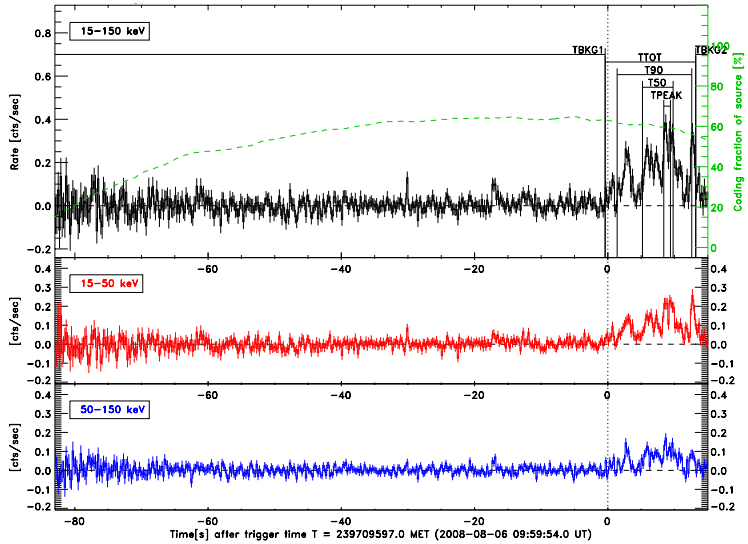

(b) BAT lightcurves (200-msec binning) and burst time blocks

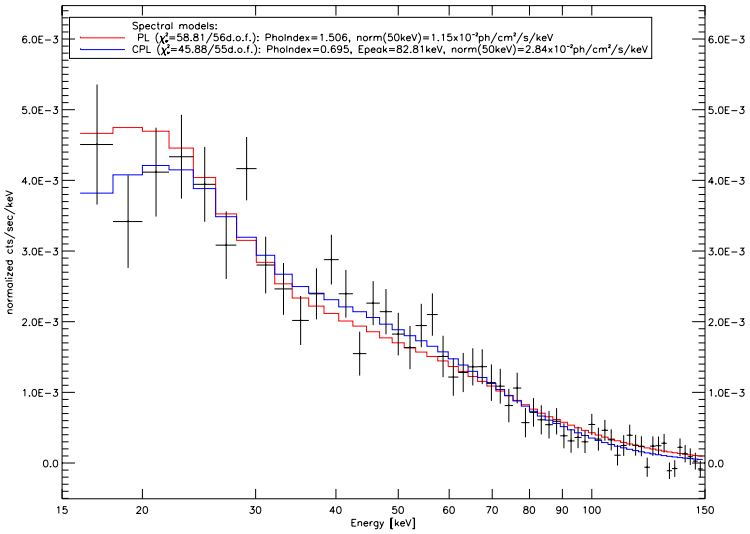

(c) BAT raw spectrum and folded models PL/CPL — time block T_{90}

FIGURE D.5: GRB 080806: BATSS detection and prompt emission data

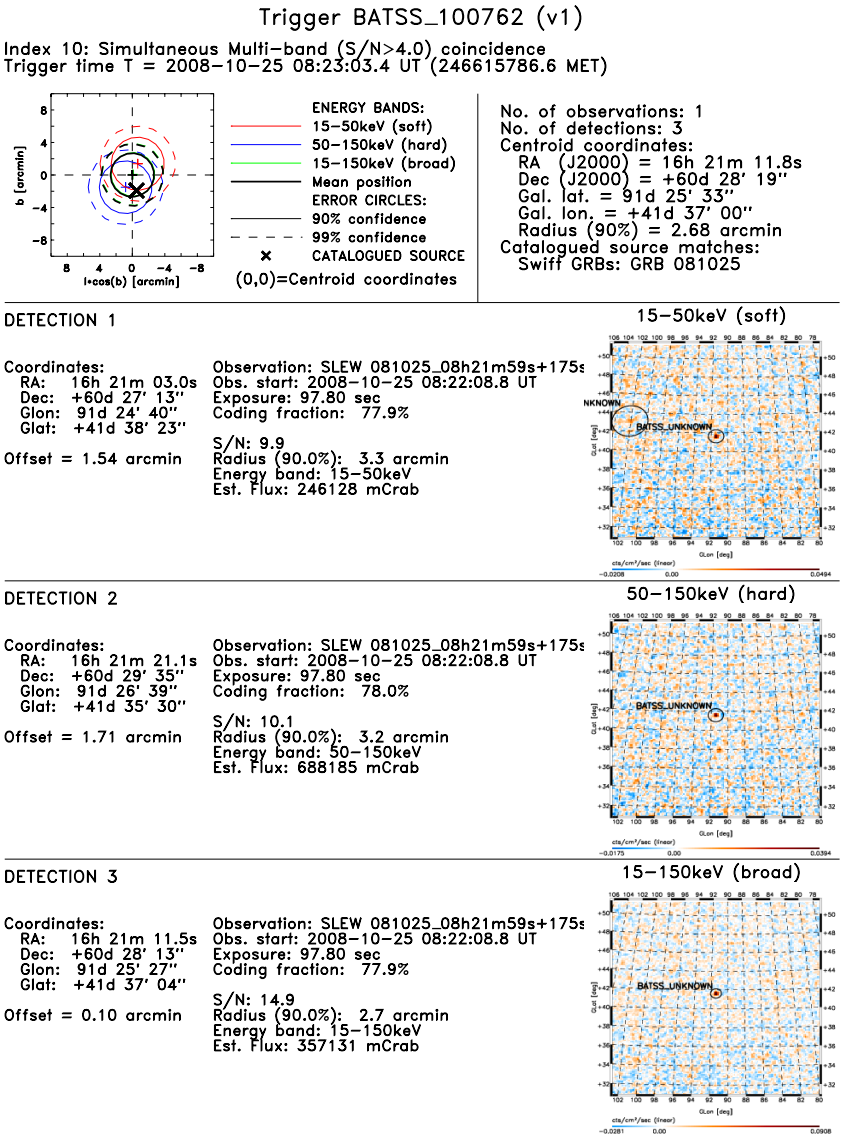

(a) BATSS detection parameters

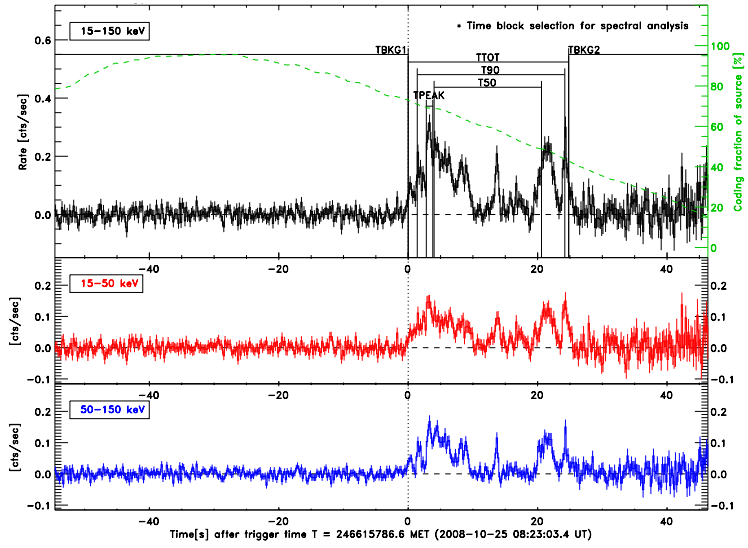

(b) BAT lightcurves (200-msec binning) and burst time blocks

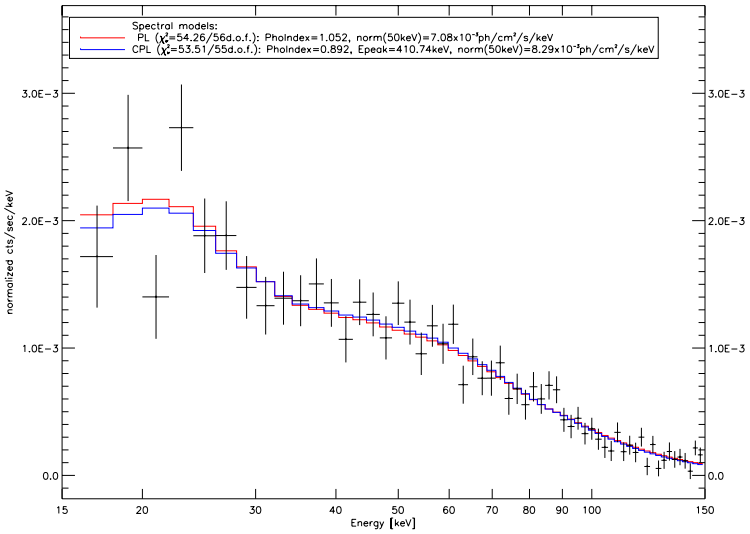

(c) BAT raw spectrum and folded models PL/CPL — time block T_{90}

FIGURE D.6: GRB 081025: BATSS detection and prompt emission data

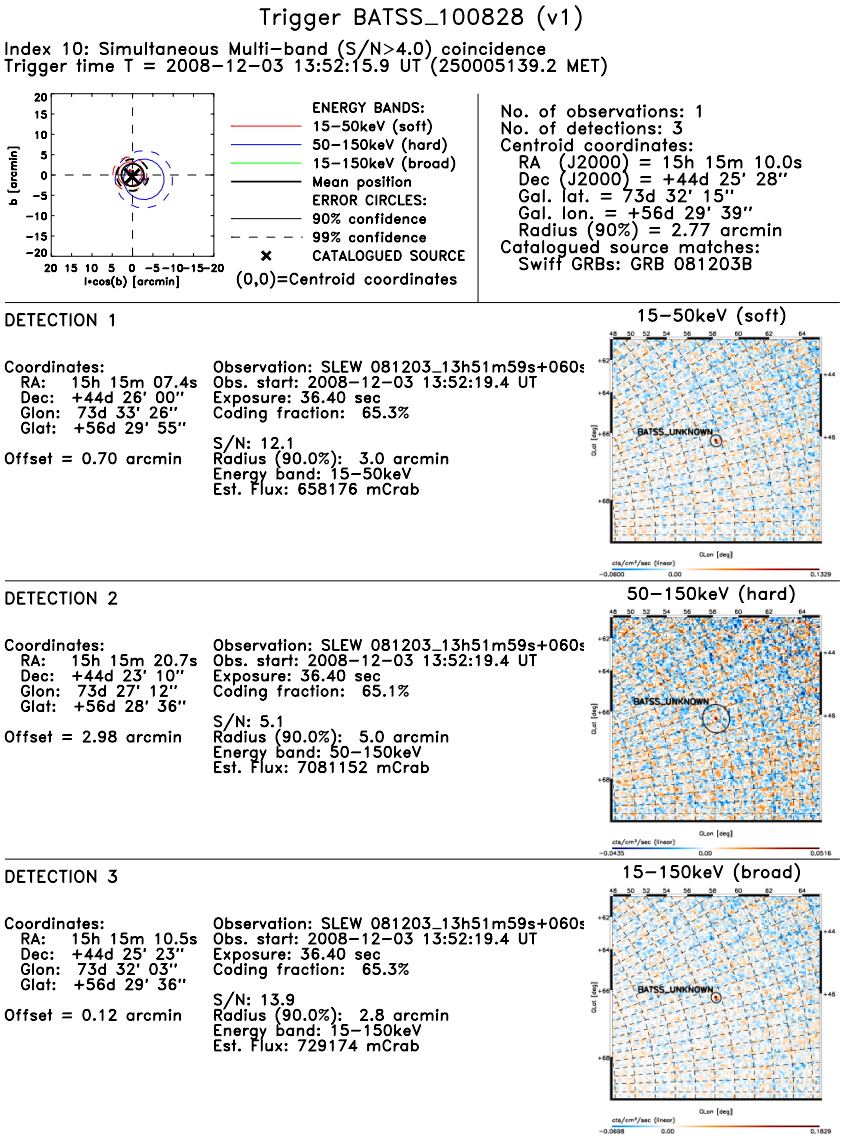

(a) BATSS detection parameters

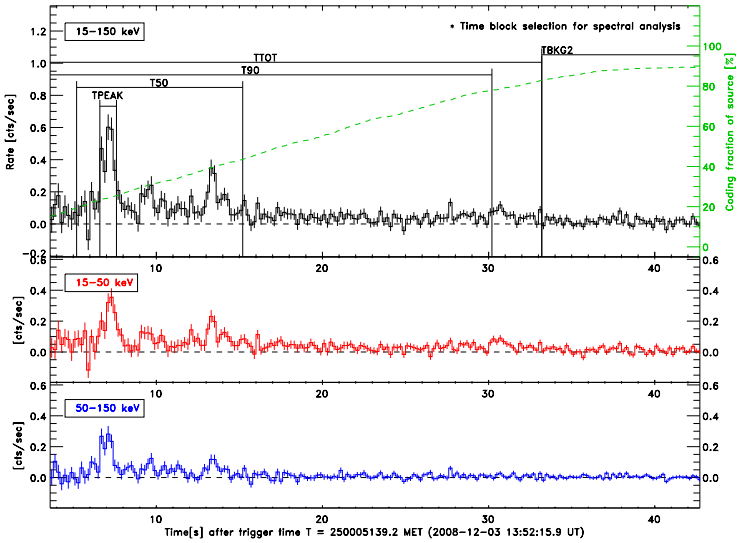

(b) BAT lightcurves (200-msec binning) and burst time blocks

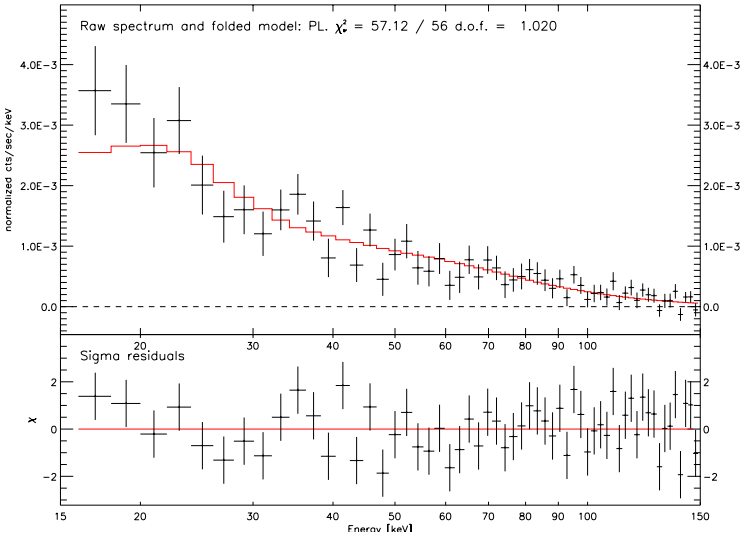

(c) BAT raw spectrum and folded model PL — time block T_{90}

FIGURE D.7: GRB 081203B: BATSS detection and prompt emission data

Trigger BATSS_100851 (v1)

Index 9: Simultaneous Single−band (S/N>4.0) + Broad−band (S/N>5.0) coincidence
Trigger time T = 2008−12−11 06:15:15.9 UT (250668919.2 MET)

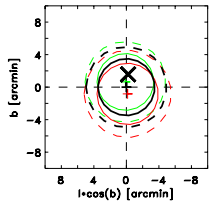

ENERGY BANDS:
15−50keV (soft)
50−150keV (hard)
15−150keV (broad)
Mean position
ERROR CIRCLES:
90% confidence
99% confidence
CATALOGUED SOURCE
(0,0)=Centroid coordinates

No. of observations: 1
No. of detections: 2
Centroid coordinates:
RA (J2000) = 11h 12m 55.0s
Dec (J2000) = +53d 50' 47"
Gal. lat. = 150d 20' 39"
Gal. lon. = +57d 43' 15"
Radius (90%) = 3.49 arcmin
Catalogued source matches:
Swift GRBs: GRB 081211B

DETECTION 1

Coordinates:
RA: 11h 12m 51.9s
Dec: +53d 51' 29"
Glon: 150d 20' 22"
Glat: +57d 42' 25"

Offset = 0.85 arcmin

Observation: SLEW 081211_06h14m58s+121s
Obs. start: 2008−12−11 06:15:15.9 UT
Exposure: 101.00 sec
Coding fraction: 87.9%

S/N: 7.7
Radius (90.0%): 3.8 arcmin
Energy band: 15−50keV
Est. Flux: 186124 mCrab

15−50keV (soft)

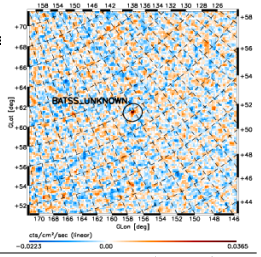

DETECTION 2

Coordinates:
RA: 11h 12m 57.5s
Dec: +53d 50' 14"
Glon: 150d 20' 52"
Glat: +57d 43' 54"

Offset = 0.65 arcmin

Observation: SLEW 081211_06h14m58s+121s
Obs. start: 2008−12−11 06:15:15.9 UT
Exposure: 101.00 sec
Coding fraction: 87.9%

S/N: 8.8
Radius (90.0%): 3.5 arcmin
Energy band: 15−150keV
Est. Flux: 209123 mCrab

15−150keV (broad)

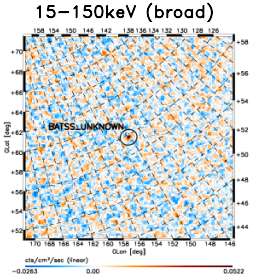

(a) BATSS detection parameters

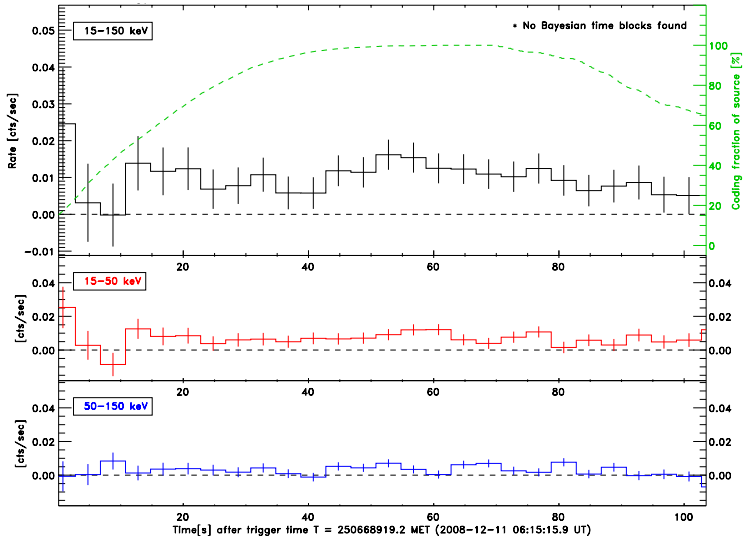

(b) BAT lightcurves (4-sec binning). No Bayesian time blocks found

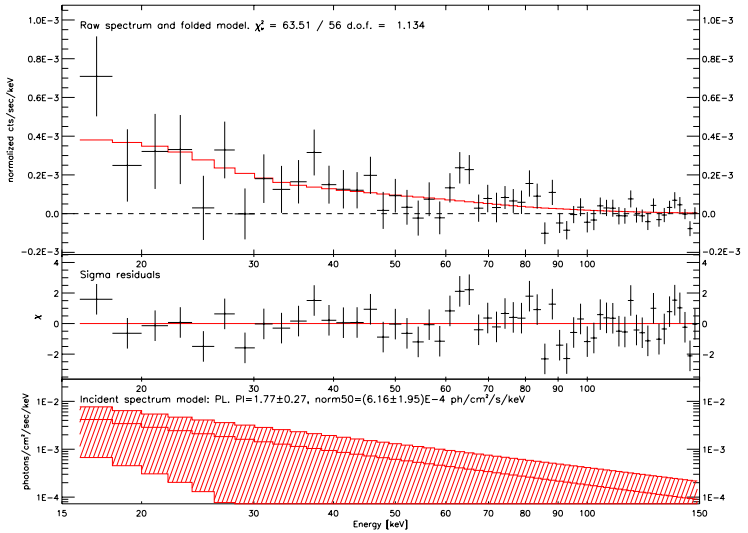

(c) BAT raw spectrum and folded model PL — full observation

FIGURE D.8: GRB 081211B: BATSS detection and prompt emission data

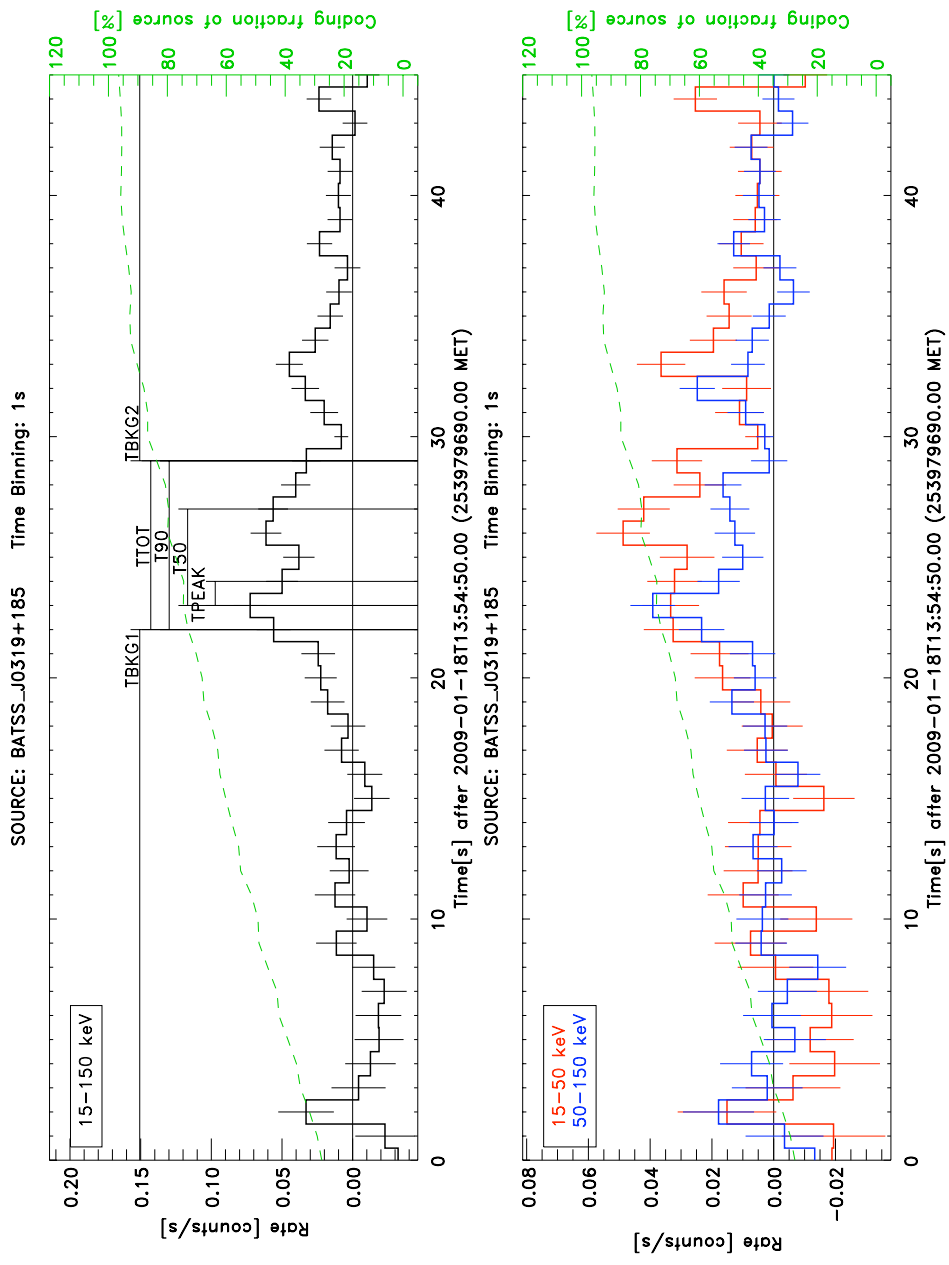

FIGURE D.9: GRB 090118: BATSS lightcurves (1-sec binning, real-time data) and burst time blocks

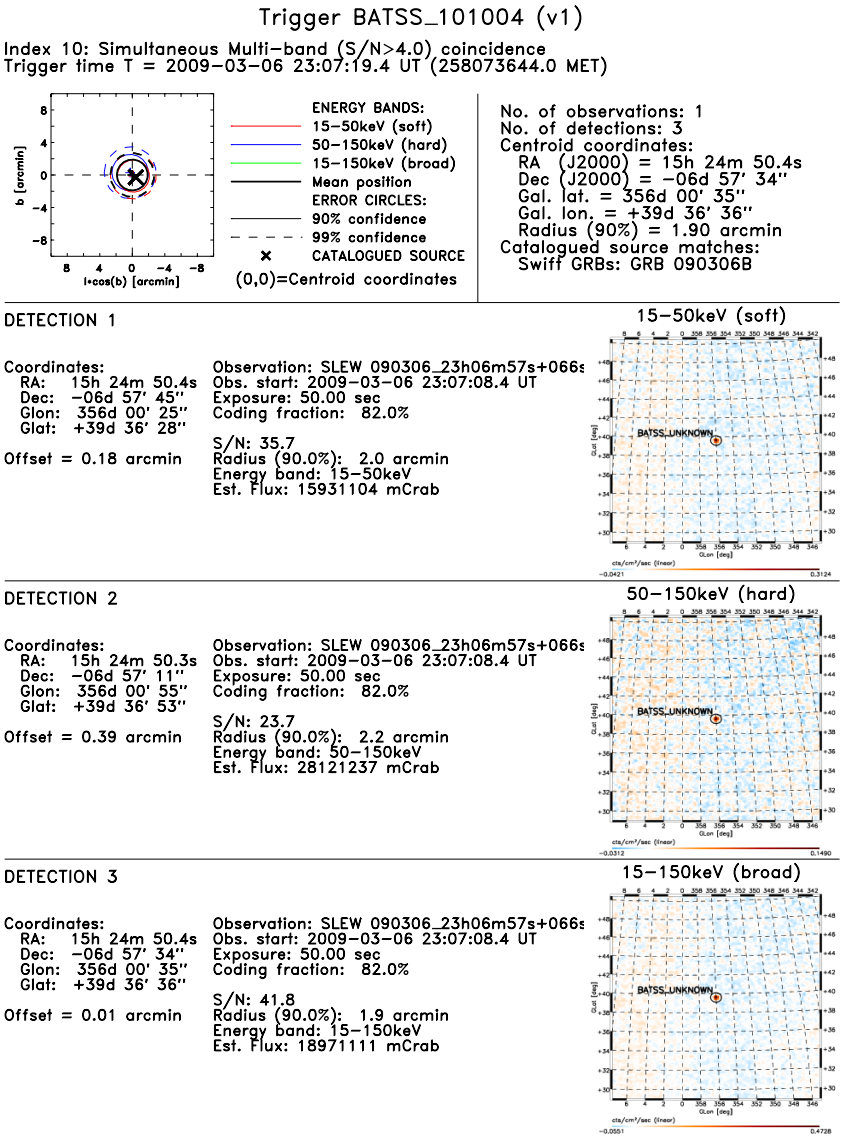

(a) BATSS detection parameters

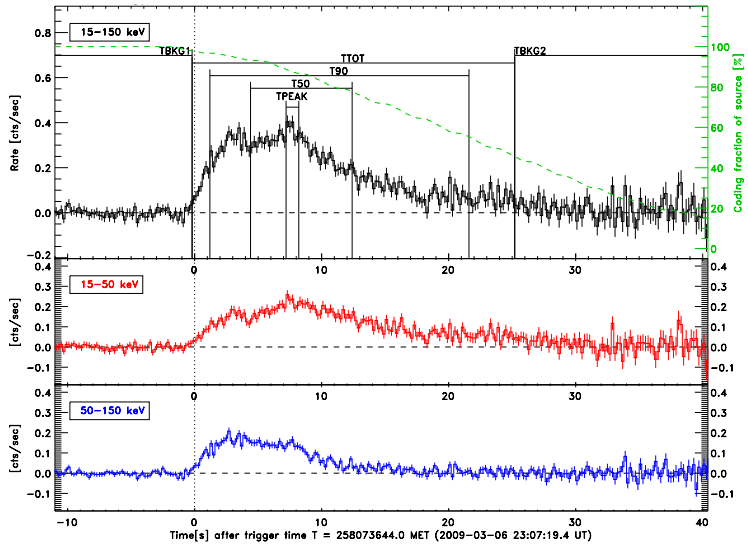

(b) BAT lightcurves (200-msec binning) and burst time blocks

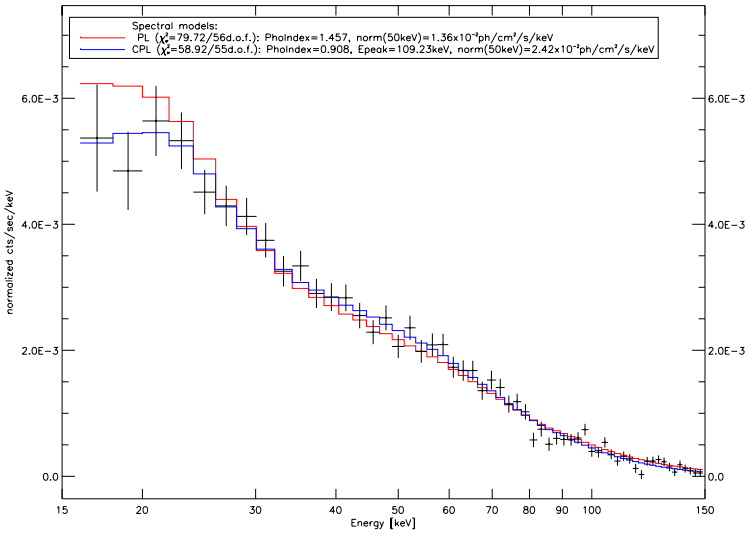

(c) BAT raw spectrum and folded models PL/CPL — time block T_{90}

FIGURE D.10: GRB 090306B: BATSS detection and prompt emission data

Trigger BATSS_101098 (v1)

Index 10: Simultaneous Multi-band (S/N>4.0) coincidence
Trigger time T = 2009-04-18 08:59:20.3 UT (261737965.0 MET)

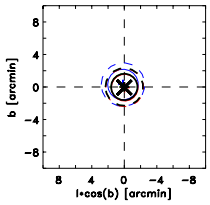

ENERGY BANDS:
15-50keV (soft)
50-150keV (hard)
15-150keV (broad)
Mean position
ERROR CIRCLES:
90% confidence
99% confidence
CATALOGUED SOURCE
(0,0)=Centroid coordinates

No. of observations: 1
No. of detections: 3
Centroid coordinates:
RA (J2000) = 15h 03m 38.2s
Dec (J2000) = +17d 13' 28"
Gal. lat. = 21d 54' 11"
Gal. lon. = +57d 56' 48"
Radius (90%) = 1.63 arcmin
Catalogued source matches:
Swift GRBs: GRB 090418B

DETECTION 1

Coordinates:
RA: 15h 03m 38.4s
Dec: +17d 13' 23"
Glon: 21d 54' 06"
Glat: +57d 56' 43"

Offset = 0.10 arcmin

Observation: SLEW 090418_08h58m57s+151s
Obs. start: 2009-04-18 08:59:22.0 UT
Exposure: 108.80 sec
Coding fraction: 91.2%

S/N: 89.1
Radius (90.0%): 1.6 arcmin
Energy band: 15-50keV
Est. Flux: 25341124 mCrab

15-50keV (soft)

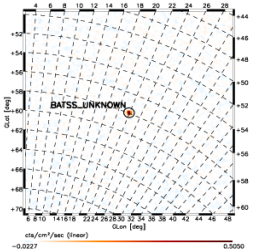

DETECTION 2

Coordinates:
RA: 15h 03m 37.3s
Dec: +17d 13' 44"
Glon: 21d 54' 29"
Glat: +57d 57' 06"

Offset = 0.34 arcmin

Observation: SLEW 090418_08h58m57s+151s
Obs. start: 2009-04-18 08:59:22.0 UT
Exposure: 108.80 sec
Coding fraction: 91.2%

S/N: 43.3
Radius (90.0%): 1.9 arcmin
Energy band: 50-150keV
Est. Flux: 29631183 mCrab

50-150keV (hard)

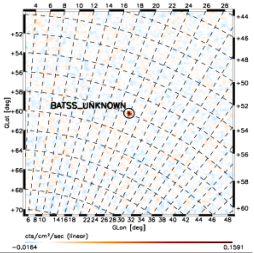

DETECTION 3

Coordinates:
RA: 15h 03m 38.1s
Dec: +17d 13' 28"
Glon: 21d 54' 12"
Glat: +57d 56' 49"

Offset = 0.01 arcmin

Observation: SLEW 090418_08h58m57s+151s
Obs. start: 2009-04-18 08:59:22.0 UT
Exposure: 108.80 sec
Coding fraction: 91.2%

S/N: 94.9
Radius (90.0%): 1.6 arcmin
Energy band: 15-150keV
Est. Flux: 26431125 mCrab

15-150keV (broad)

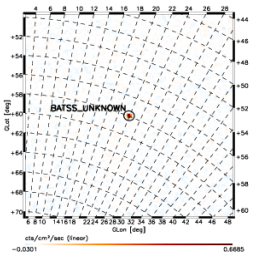

(a) BATSS detection parameters

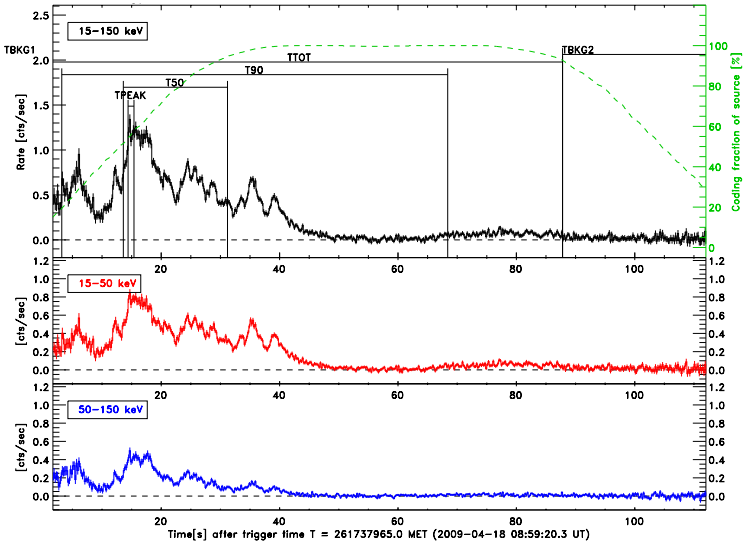

(b) BAT lightcurves (200-msec binning) and burst time blocks

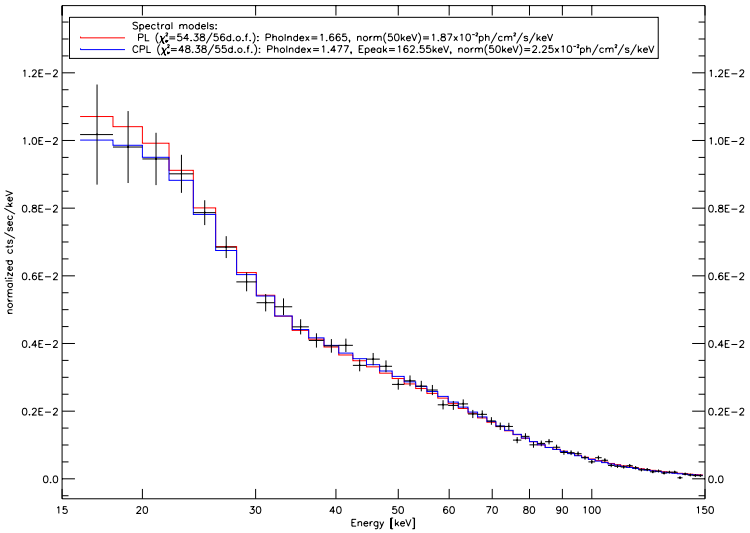

(c) BAT raw spectra and folded models PL/CPL — time block T_{100}

FIGURE D.11: GRB 090418B: BATSS detection and prompt emission data

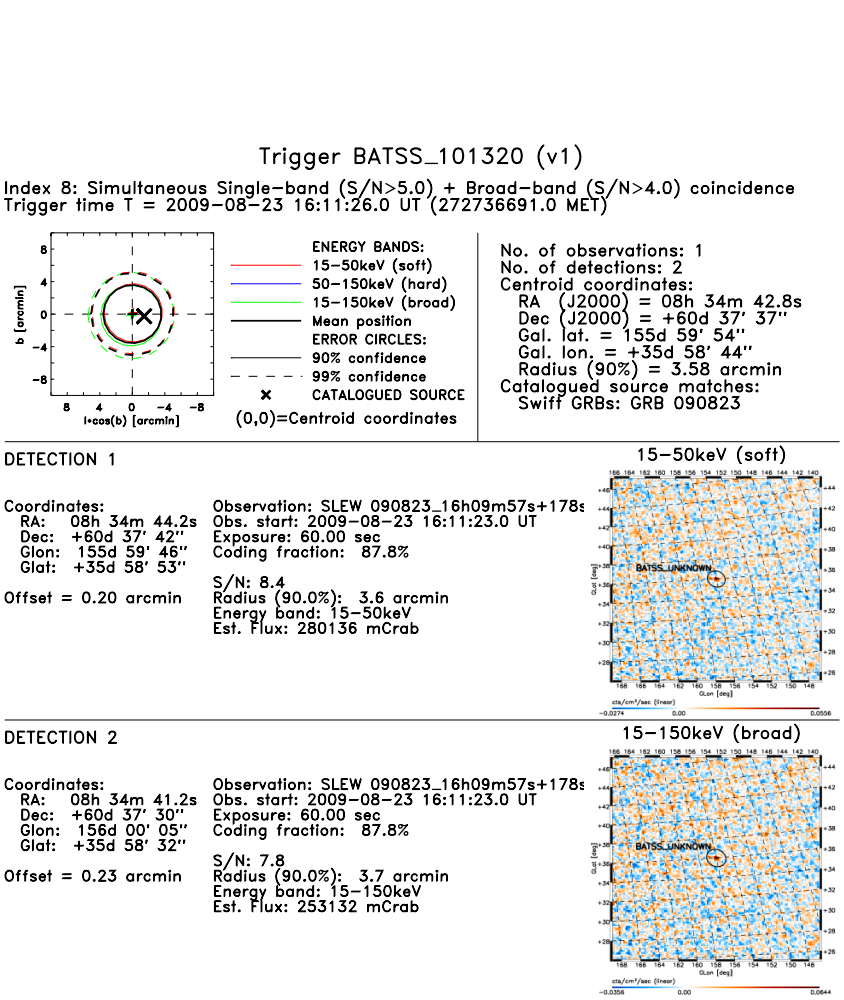

(a) BATSS detection parameters

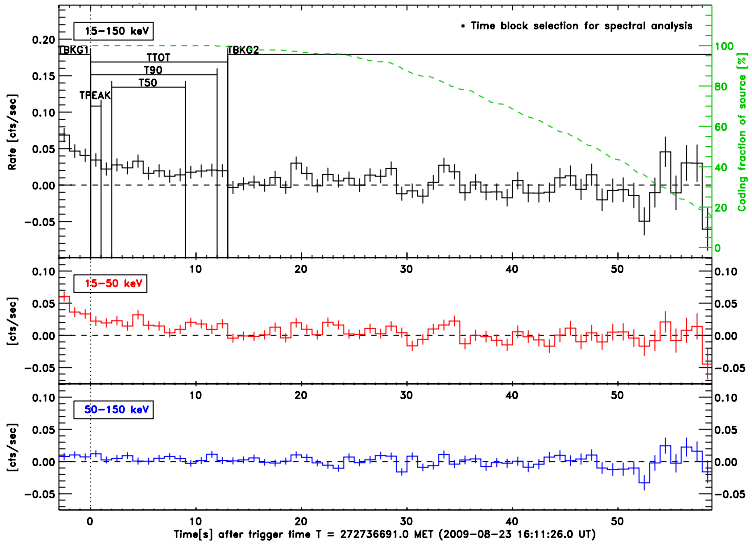

(b) BAT lightcurves (1-sec binning) and burst time blocks

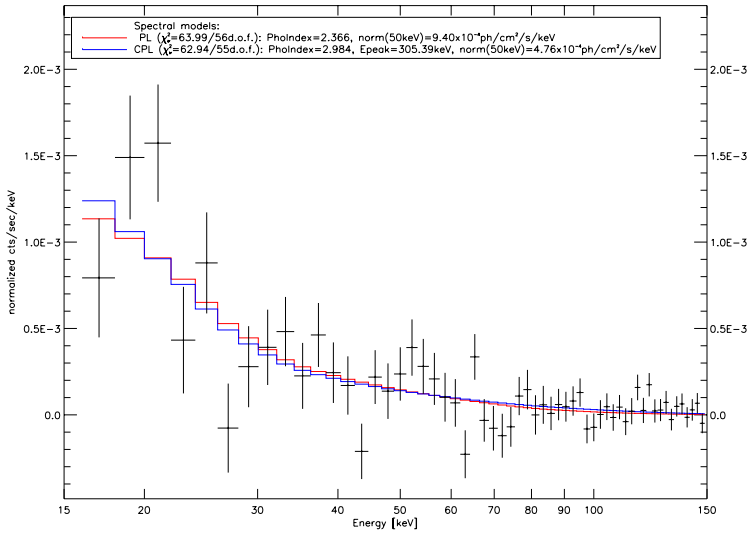

(c) BAT raw spectrum and folded models PL/CPL—time block T_{100}

FIGURE D.12: GRB 090823: BATSS detection and prompt emission data

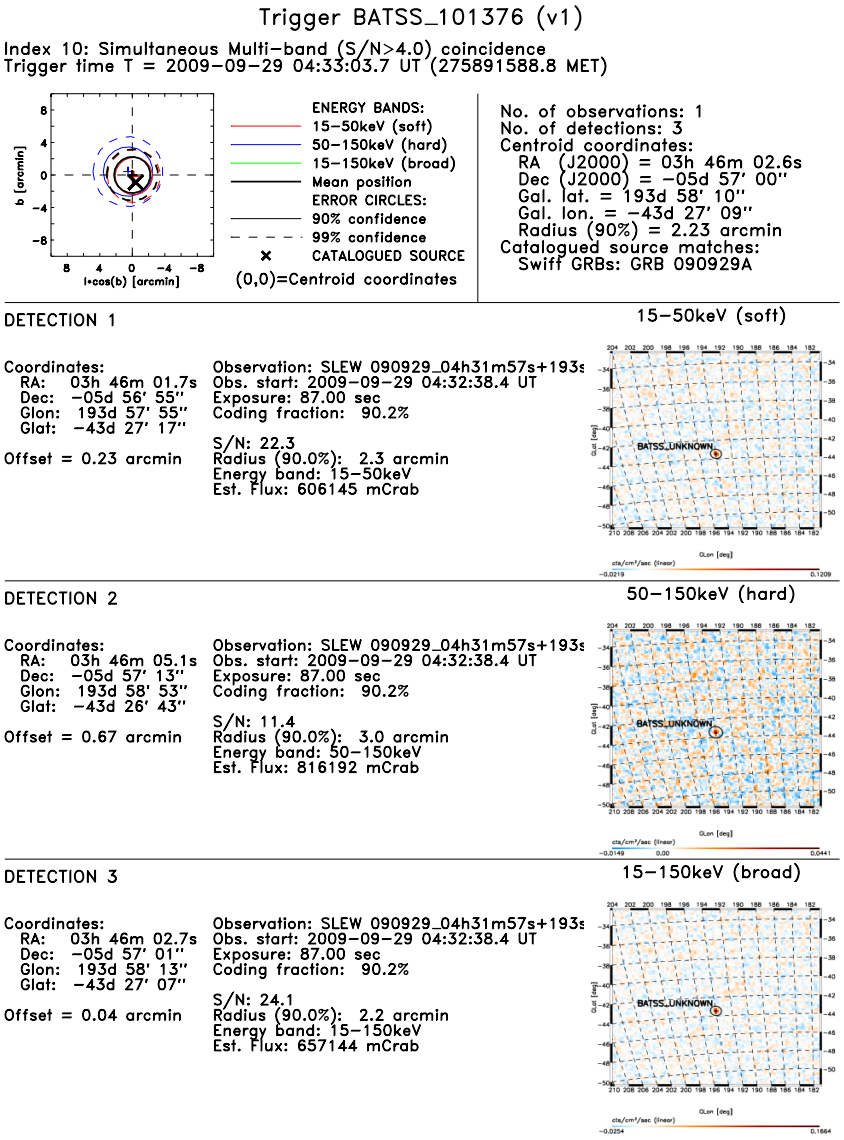

(a) BATSS detection parameters

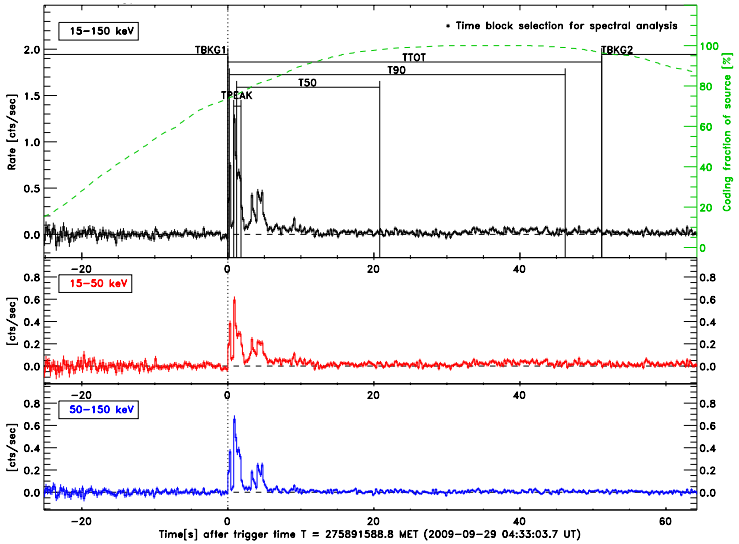

(b) BAT lightcurves (200-msec binning) and burst time blocks

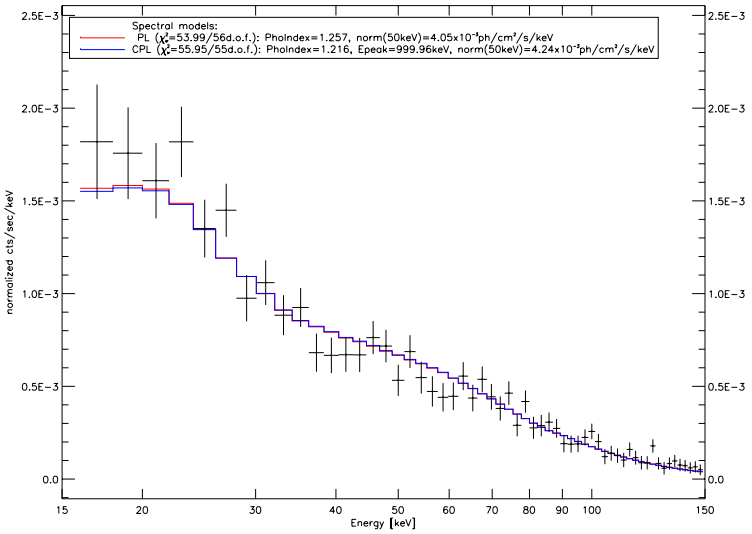

(c) BAT raw spectrum and folded models PL/CPL—time block T_{100}

FIGURE D.13: GRB 090929A: BATSS detection and prompt emission data

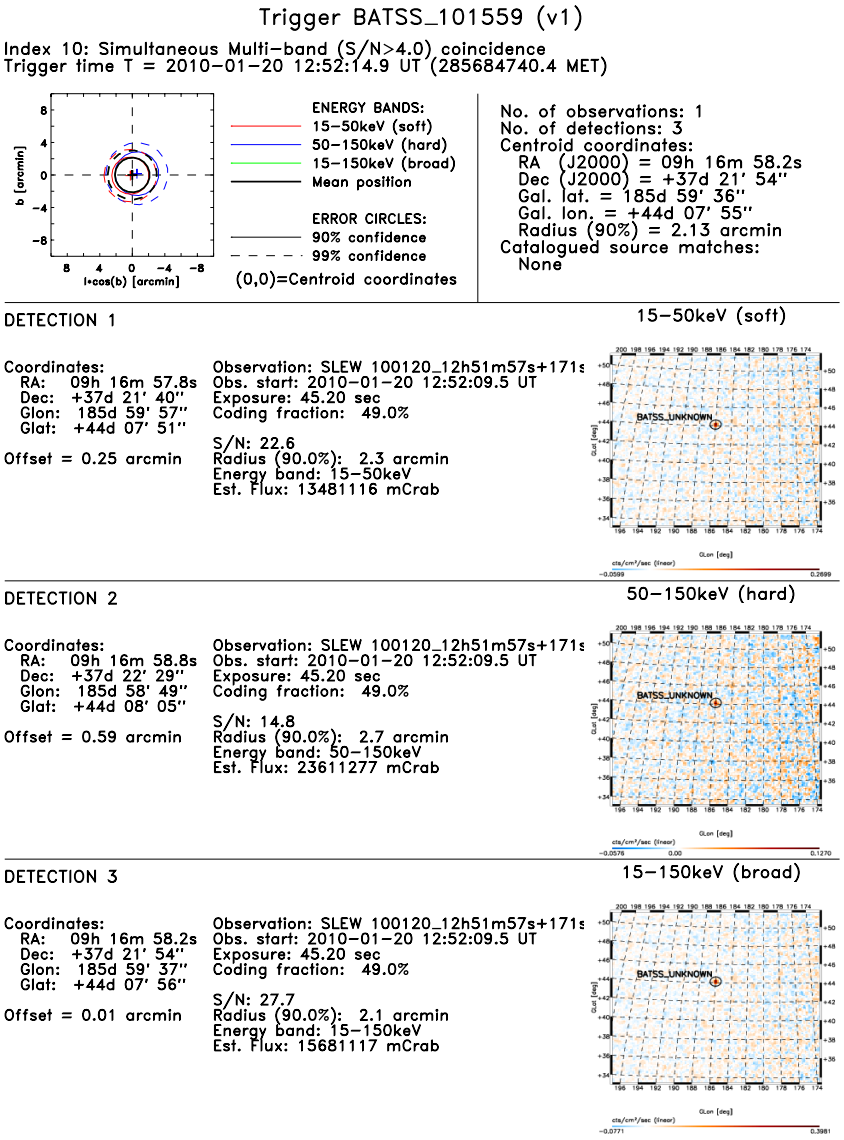

(a) BATSS detection parameters

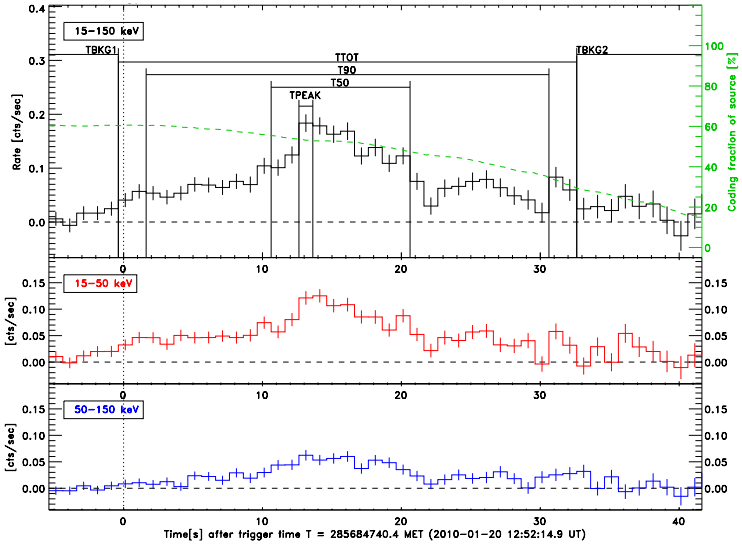

(b) BAT lightcurves (1-sec binning) and burst time blocks

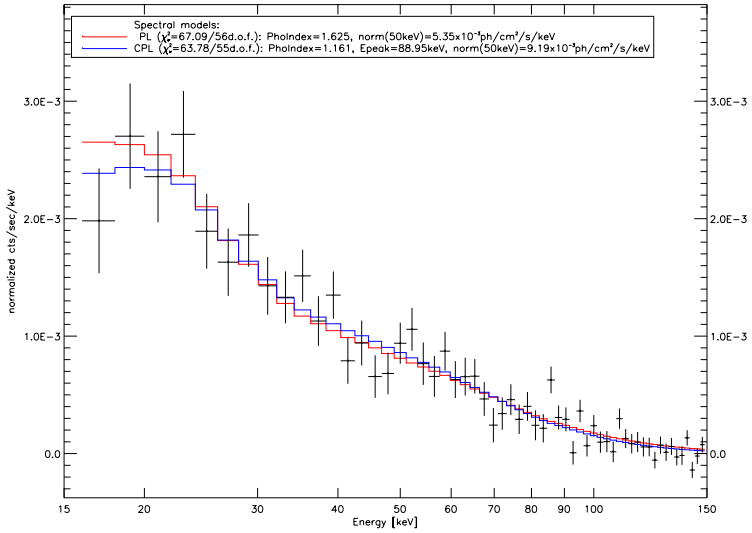

(c) BAT raw spectra and folded models PL/CPL — time block T_{100}

FIGURE D.14: GRB 100120A: BATSS detection and prompt emission data

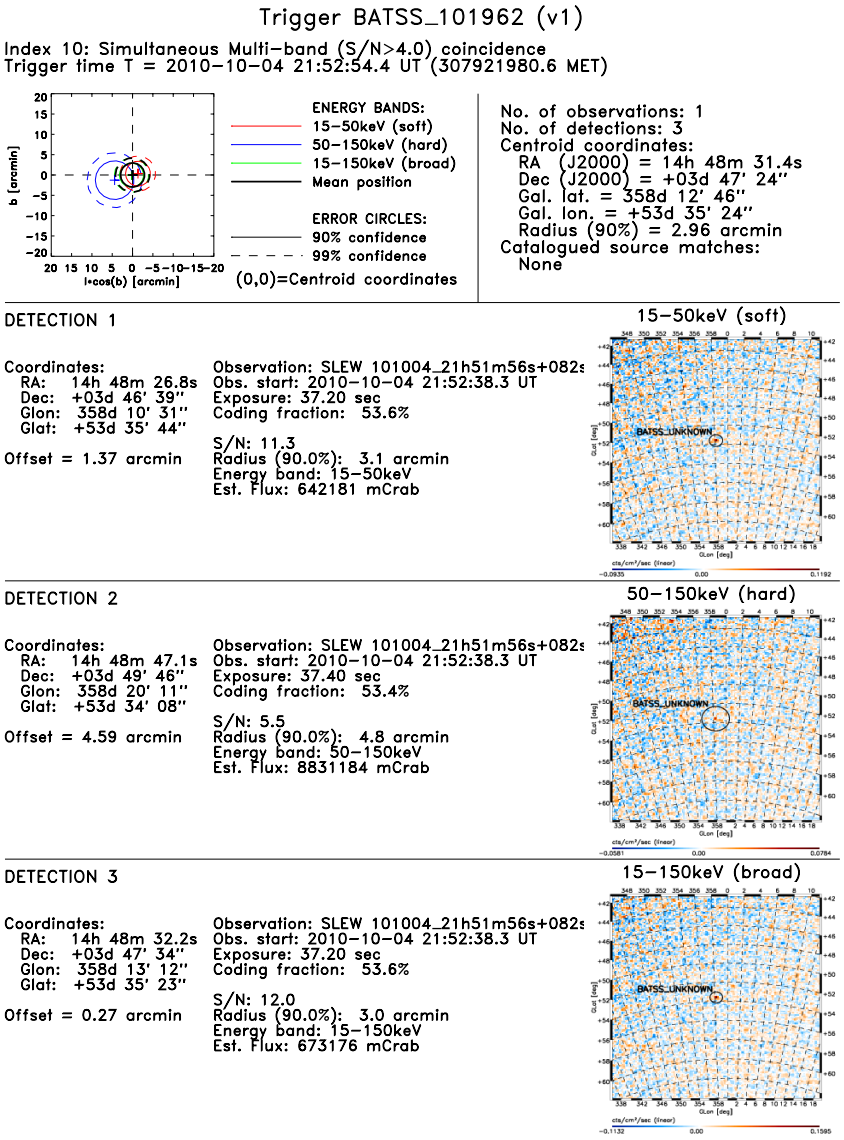

(a) BATSS detection parameters

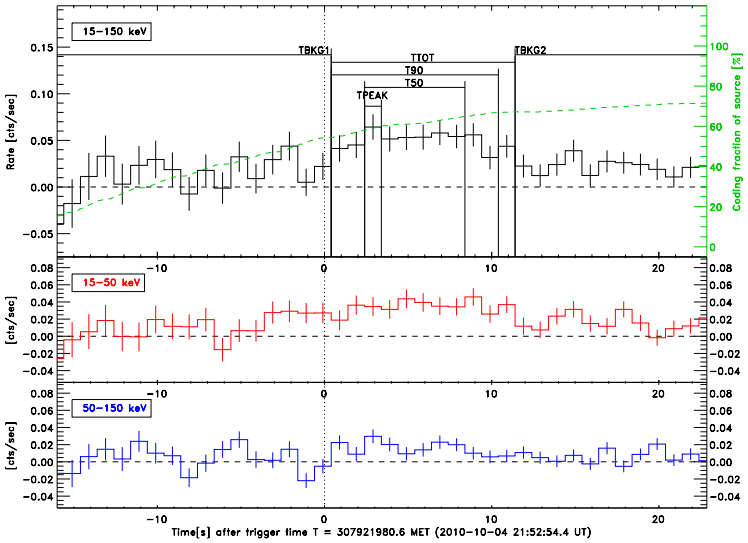

(b) BAT lightcurves (1-sec binning) and burst time blocks

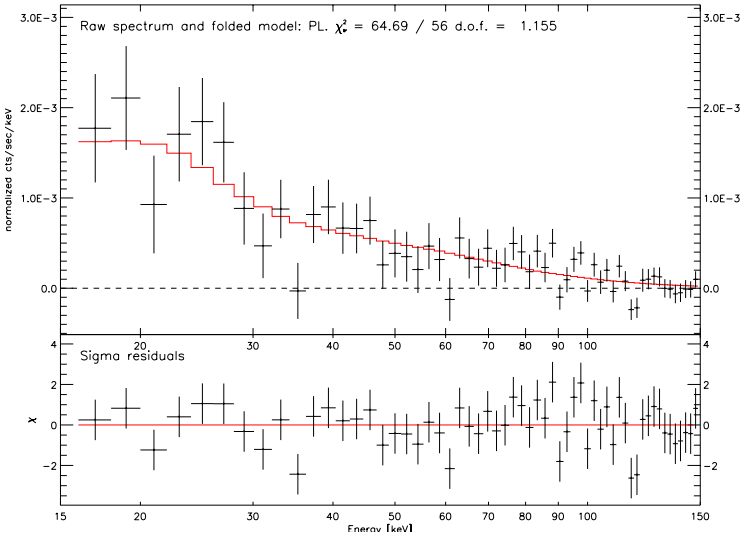

(c) BAT raw spectrum and folded model PL — time block T_{90}

FIGURE D.15: GRB 101004A: BATSS detection and prompt emission data

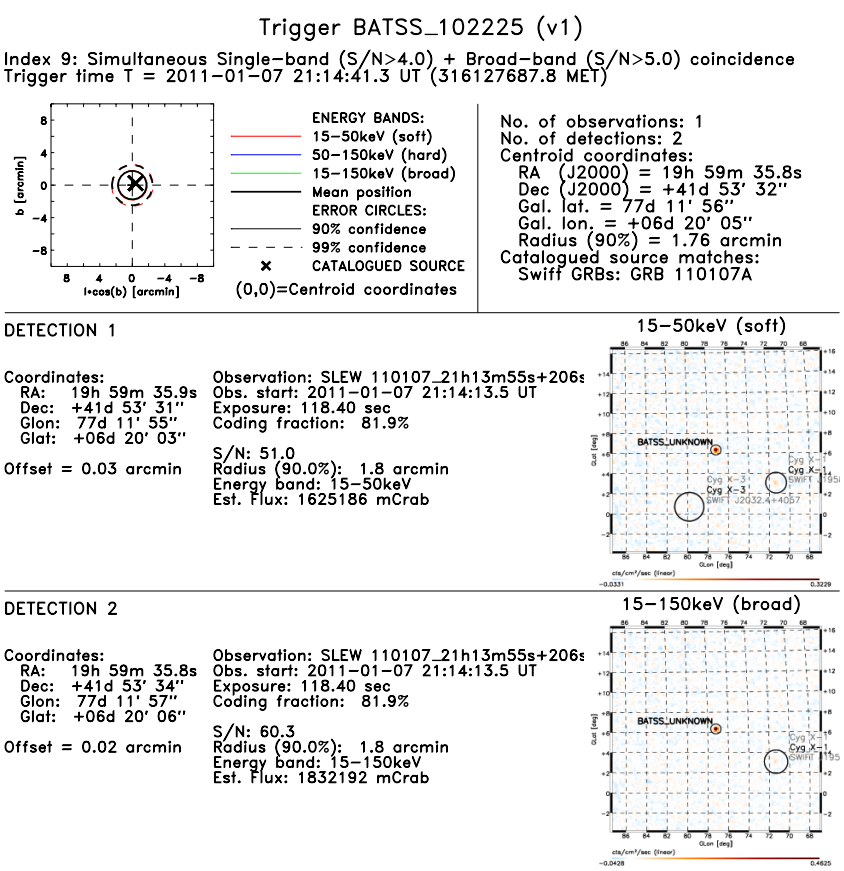

(a) BATSS detection parameters

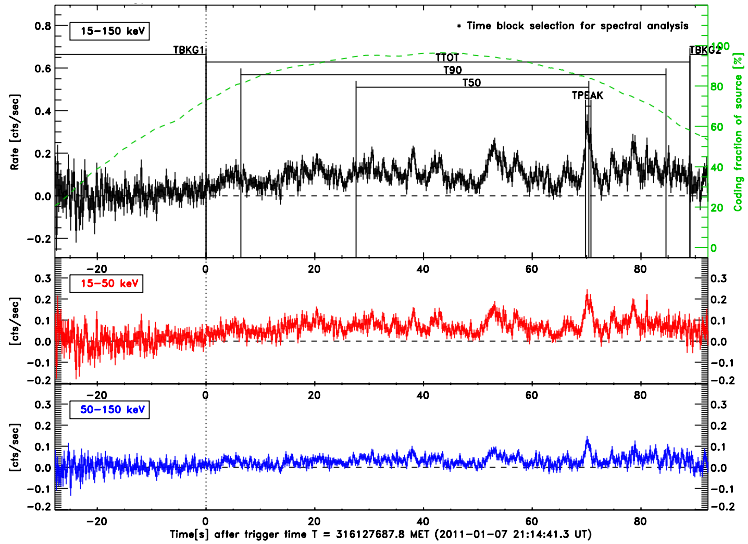

(b) BAT lightcurves (200-msec binning) and burst time blocks

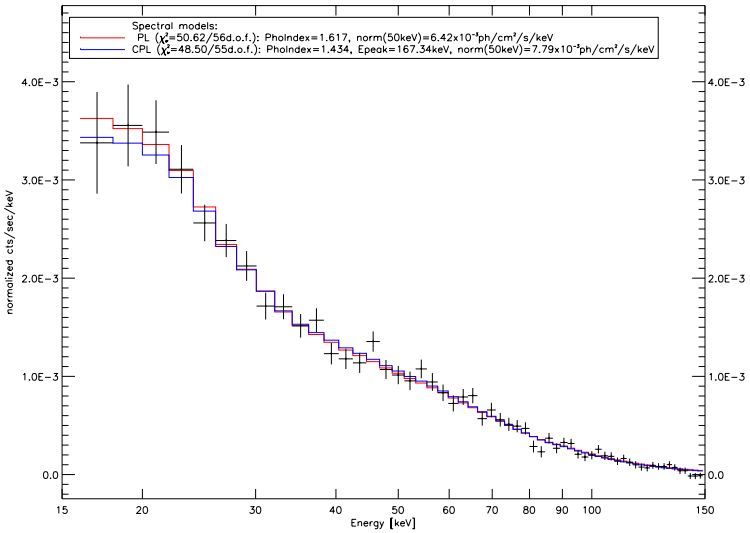

(c) BAT raw spectra and folded models PL/CPL — time block T_{100}

FIGURE D.16: GRB 110107A: BATSS detection and prompt emission data

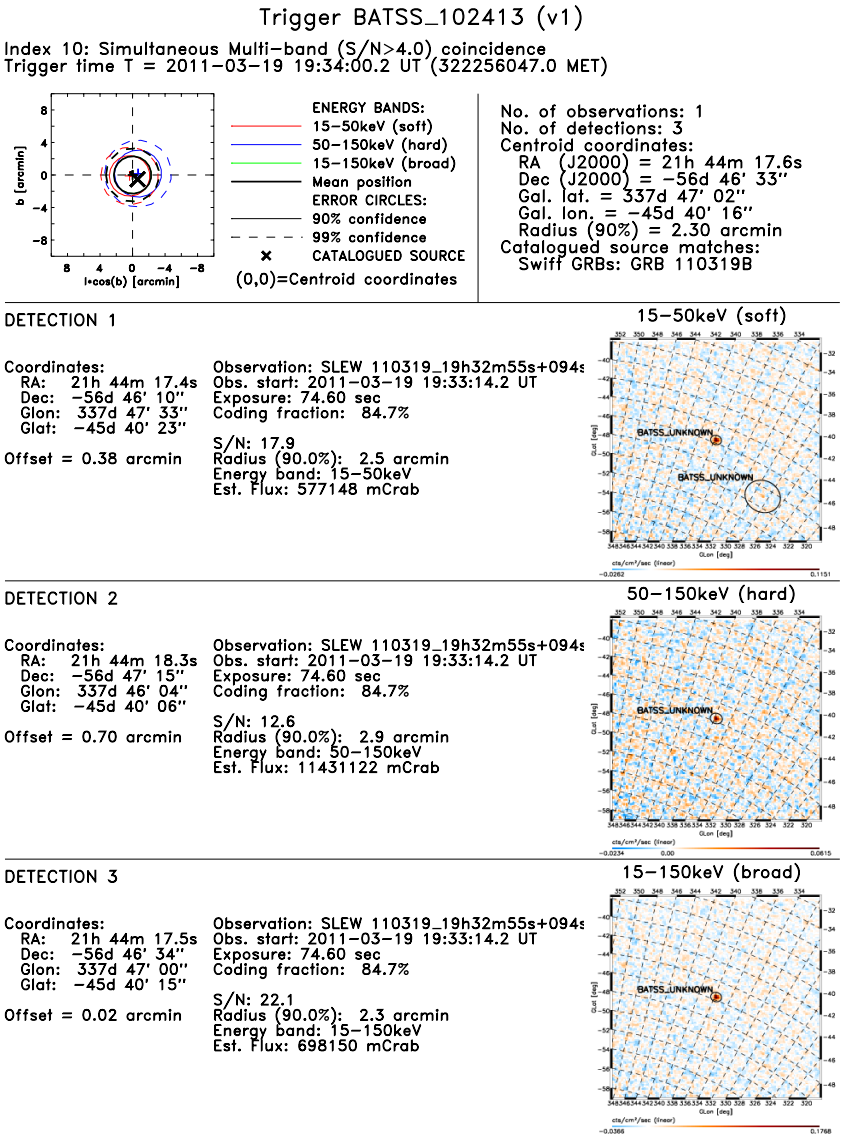

(a) BATSS detection parameters

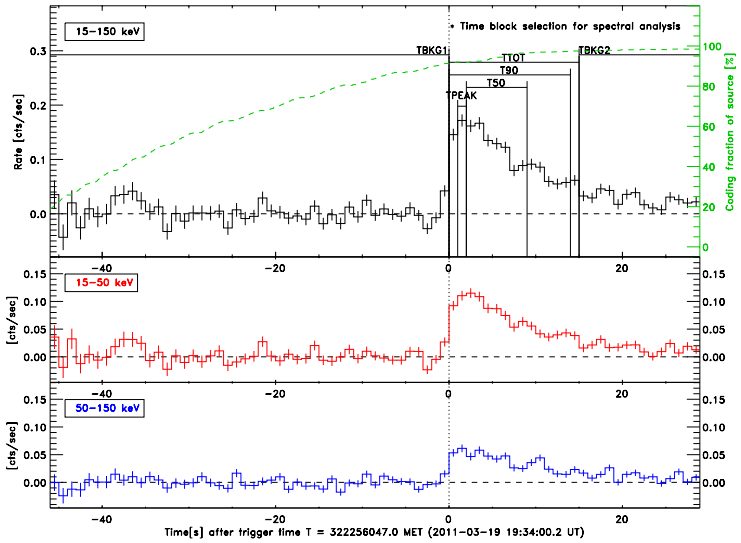

(b) BAT lightcurves (1-sec binning) and burst time blocks

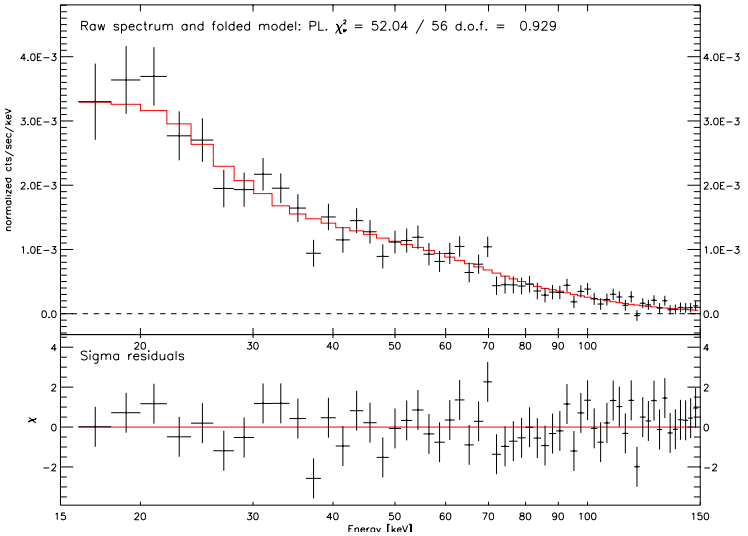

(c) BAT raw spectrum and folded model PL — time block T_{90}

FIGURE D.17: GRB 110319B: BATSS detection and prompt emission data

Trigger BATSS_102619 (v1)

Index 9: Simultaneous Single−band (S/N>4.0) + Broad−band (S/N>5.0) coincidence
Trigger time T = 2011−09−06 12:25:13.5 UT (337004720.8 MET)

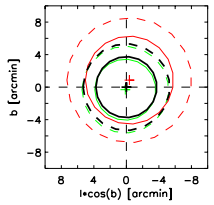

ENERGY BANDS:
15−50keV (soft)
50−150keV (hard)
15−150keV (broad)
Mean position

ERROR CIRCLES:
90% confidence
99% confidence

(0,0)=Centroid coordinates

No. of observations: 1
No. of detections: 2
Centroid coordinates:
RA (J2000) = 19h 47m 33.9s
Dec (J2000) = −26d 12' 32"
Gal. lat. = 14d 16' 34"
Gal. lon. = −23d 15' 54"
Radius (90%) = 3.75 arcmin
Catalogued source matches:
None

DETECTION 1

Coordinates:
RA: 19h 47m 29.7s
Dec: −26d 12' 36"
Glon: 14d 16' 09"
Glat: −23d 15' 02"

Offset = 0.94 arcmin

Observation: SLEW 110906_12h23m55s+094s
Obs. start: 2011−09−06 12:25:13.5 UT
Exposure: 13.80 sec
Coding fraction: 23.7%

S/N: 4.7
Radius (90.0%): 5.4 arcmin
Energy band: 15−50keV
Est. Flux: 692±198 mCrab

15−50keV (soft)

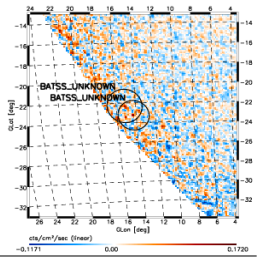

DETECTION 2

Coordinates:
RA: 19h 47m 35.4s
Dec: −26d 12' 31"
Glon: 14d 16' 42"
Glat: −23d 15' 13"

Offset = 0.34 arcmin

Observation: SLEW 110906_12h23m55s+094s
Obs. start: 2011−09−06 12:25:13.5 UT
Exposure: 13.80 sec
Coding fraction: 23.5%

S/N: 7.8
Radius (90.0%): 3.8 arcmin
Energy band: 15−150keV
Est. Flux: 1019±210 mCrab

15−150keV (broad)

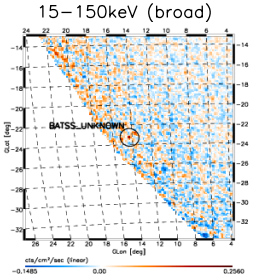

(a) BATSS detection parameters

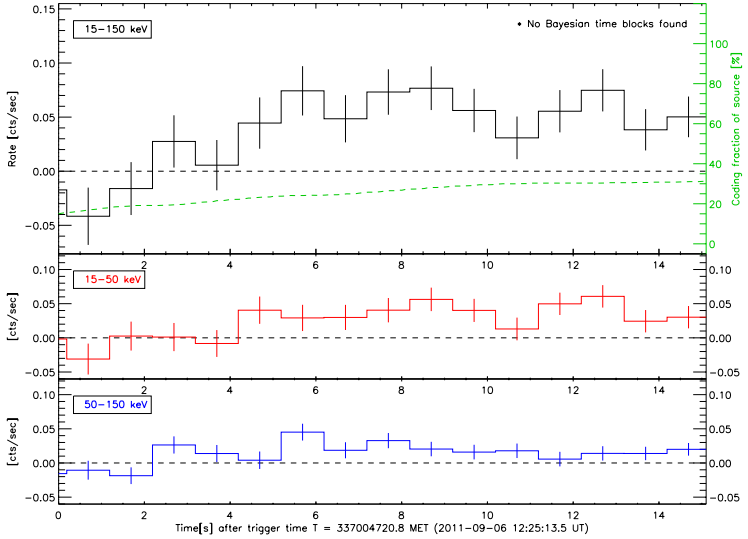

(b) BAT lightcurves (1-sec binning). No Bayesian time blocks found

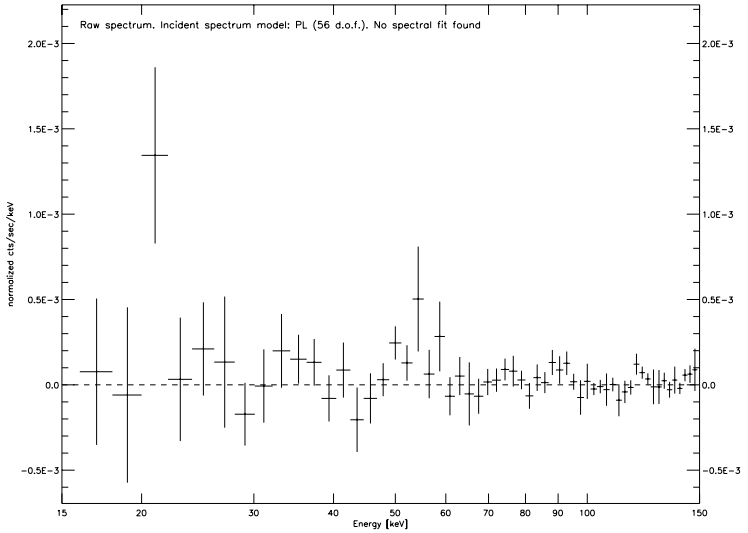

(c) BAT raw spectrum — full observation (no fit found)

FIGURE D.18: GRB 110906A: BATSS detection and prompt emission data

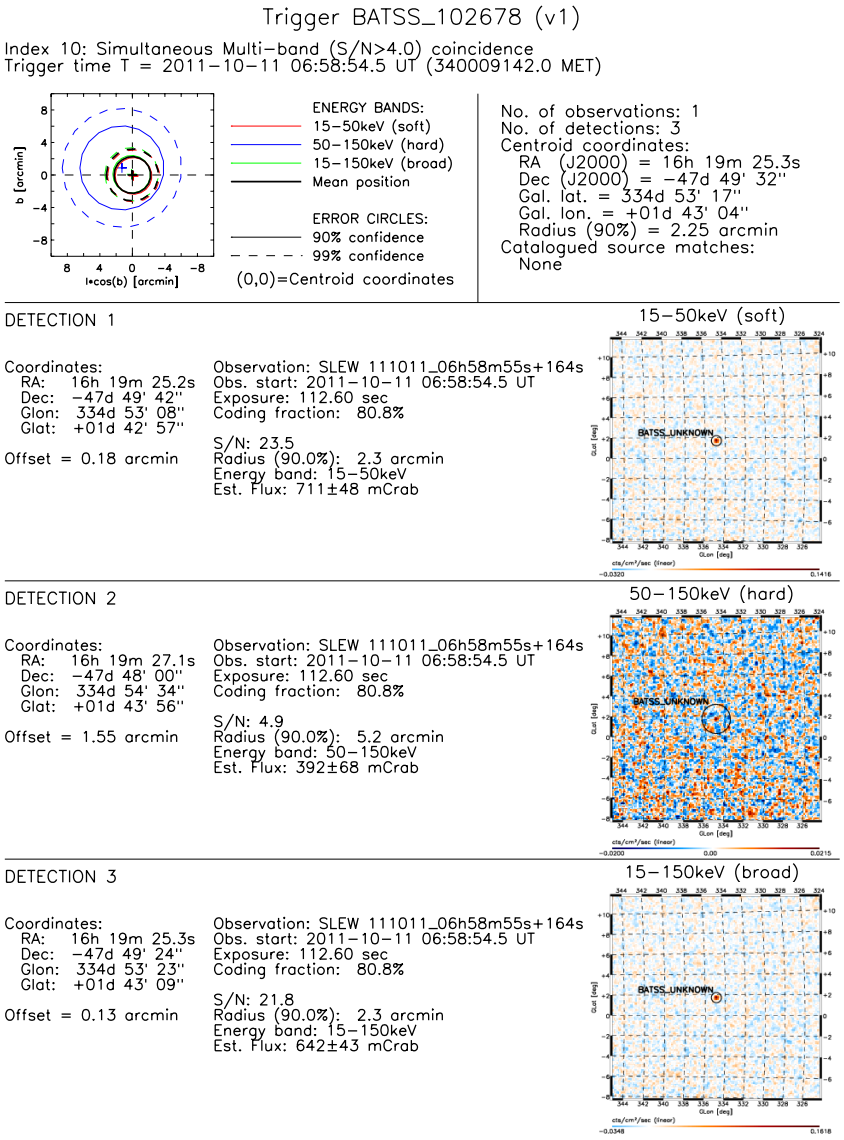

(a) BATSS detection parameters

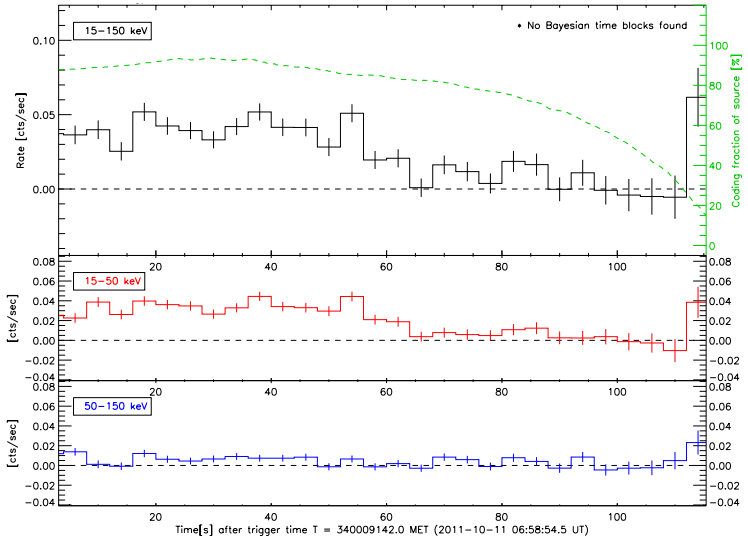

(b) BAT lightcurves (4-sec binning). No Bayesian time blocks found

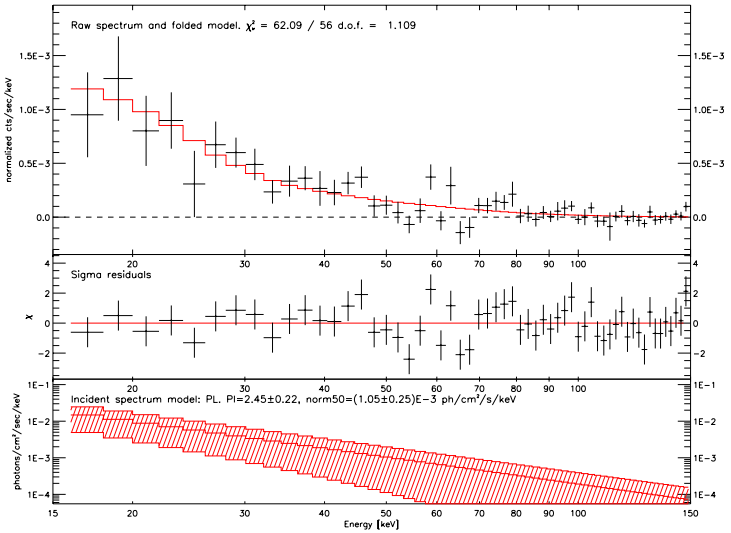

(c) BAT raw spectrum and folded model PL — full observation

FIGURE D.19: GRB 111011A: BATSS detection and prompt emission data

Page intentionally left blank

Bibliography

Afonso, P., Klose, S., Kruehler, T., & Greiner, J. 2009, GCN Circ., 9178 [LINK]

Allen, B., Hong, J., Grindlay, J., Barthelmy, S. D., Baker, R. G., Gehrels, N. A., Garson, T., Krawczynski, H. S., Cook, W. R., Harrison, F. A., Apple, J. A., & Ramsey, B. D. 2010, in Society of Photo-Optical Instrumentation Engineers (SPIE) Conference Series, Vol. 7732 [ADS]

Amati, L., Frontera, F., Tavani, M., in't Zand, J. J. M., Antonelli, A., Costa, E., Feroci, M., Guidorzi, C., Heise, J., Masetti, N., Montanari, E., Nicastro, L., Palazzi, E., Pian, E., Piro, L., & Soffitta, P. 2002, A&A, 390, 81

Andreev, M., Sergeev, A., & Babina, J. 2008a, GCN Circ., 8608 [LINK]

—. 2008b, GCN Circ., 8626 [LINK]

Andreev, M., Sergeev, A., Babina, J., & Pozanenko, A. 2008c, GCN Circ., 8727 [LINK]

Angelini, L. 2007, Guide to the Swift Archive, v2. edn., HEASARC [LINK]

Band, D., Matteson, J., Ford, L., Schaefer, B., Palmer, D., Teegarden, B., Cline, T., Briggs, M., Paciesas, W., Pendleton, G., Fishman, G., Kouveliotou, C., Meegan, C., Wilson, R., & Lestrade, P. 1993, ApJ, 413, 281

Band, D. L. 2006, ApJ, 644, 378 [ADS]

Barthelmy, S. D. 2006, The GCN Reports [LINK]

Barthelmy, S. D., Barbier, L. M., Cummings, J. R., Fenimore, E. E., Gehrels, N., Hullinger, D., Krimm, H. A., Markwardt, C. B., Palmer, D. M., Parsons, A., Sato, G., Suzuki, M., Takahashi, T., Tashiro, M., & Tueller, J. 2005, Space Sci. Rev., 120, 143

Barthelmy, S. D., Butterworth, P., Cline, T. L., Gehrels, N., Marshall, F., Takeshima, T., Connaughton, V., Kippen, R. M., Kouveliotou, C., & Robinson, C. R. 1998, in American Institute of Physics Conference Series, Vol. 428, Gamma-Ray Bursts, 4th Hunstville Symposium, ed. C. A. Meegan, 99–103 [ADS]

Baumgartner, W. H., Tueller, J., Markwardt, C., & Skinner, G. 2010, in Bulletin of the American Astronomical Society, Vol. 42, AAS/High Energy Astrophysics Division #11, 675 [ADS]

Baumgartner, W. H., Tueller, J., Markwardt, C., Skinner, G., Mushotzky, R., Evans, P., & Gehrels, N. 2011, in AAS/High Energy Astrophysics Division, Vol. 12, AAS/High Energy Astrophysics Division, 07.29 [ADS]

Beckmann, V., Beck, M., Ferrigno, C., Produit, N., Savchenko, V., Borkowski, J., Gotz, D., Mereghetti, S., & Kienlin, A. v. 2009, GCN Circ., 8968 [LINK]

Berger, E. 2008, GCN Circ., 8607 [LINK]

Berger, E. & Madore, B. 2008, GCN Circ., 7933 [LINK]

Bikmaev, I., Zhuchkov, R., Sakhibullin, N., Khamitov, I., Eker, Z., Kiziloglu, U., Gogus, E., Burenin, R., Pavlinsky, M., & Sunyaev, R. 2009, GCN Circ., 9191 [LINK]

Burrows, D. N., Hill, J. E., Nousek, J. A., Kennea, J. A., Wells, A., Osborne, J. P., Abbey, A. F., Beardmore, A., Mukerjee, K., Short, A. D. T., Chincarini, G., Campana, S., Citterio, O., Moretti, A., Pagani, C., Tagliaferri, G., Giommi, P., Capalbi, M., Tamburelli, F., Angelini, L., Cusumano, G., Bräuninger, H. W., Burkert, W., & Hartner, G. D. 2005, Space Sci. Rev., 120, 165 [ADS]

Calabretta, M. R. & Greisen, E. W. 2002, A&A, 395, 1077

Caroli, E., Stephen, J. B., Di Cocco, G., Natalucci, L., & Spizzichino, A. 1987, Space Sci. Rev., 45, 349 [ADS]

Chakrabarti, S. K., Nandi, A., Debnath, D., Kotoch, T. C., Rao, A. R., Malkar, J. P., Hingar, M. K., Agrawal, V. K., R. Chidambaram, T., Vinod, P., Sreekumar, S., Kotov, Y. D., Buslov, A. S., Yurov, V. N., Tyshkevich, V. G., Arkhangelskij, A. I., & Zyatkov, R. A. 2009, GCN Circ., 10010 [LINK]

Chandra, P. & Frail, D. A. 2008, GCN Circ., 8625 [LINK]

Clemens, C., Loew, S., Greiner, J., Yoldas, A., Kruehler, T., Yoldas, A. K., Szokoly, G., & Garching), M. 2008, GCN Circ., 7943 [LINK]

Copete, A., Grindlay, J., Allen, B., Hong, J., Markwardt, C., & Gehrels, N. 2008a, GCN Circ., 7242 [ADS]

Copete, A., Grindlay, J., Barthelmy, S., Markwardt, C., & Gehrels, N. 2008b, GCN Circ., 8409 [ADS]

—. 2009a, GCN Circ., 8944 [ADS]

—. 2009b, GCN Circ., 9159 [ADS]

—. 2009c, GCN Circ., 9839 [ADS]

Copete, A., Grindlay, J., Cummings, J., Barthelmy, S., Markwardt, C., & Gehrels, N. 2011, GCN Circ., 12332 [ADS]

Copete, A., Grindlay, J., Hong, J., Barthelmy, S., & Gehrels, N. 2007, GCN Circ., 6653 [ADS]

Copete, A., Grindlay, J., Markwardt, C., & Gehrels, N. 2008c, GCN Circ., 8600 [ADS]

—. 2008d, GCN Circ., 8661 [ADS]

—. 2009d, GCN Circ., 8825 [ADS]

Copete, A., Grindlay, J., Markwardt, C., Gehrels, N., Cummings, J., & Palmer, D. 2008e, GCN Circ., 8602 [ADS]

Copete, A. et al. 2013a, in preparation

—. 2013b, in preparation

—. 2013c, in preparation

—. 2013d, in preparation

Cummings, J., Copete, A., Grindlay, J., Allen, B., Hong, J., Gehrels, N., & Stamatikos, M. 2008a, GCN Circ., 7248 [ADS]

Cummings, J. R. 2009, GCN Circ., 9838 [LINK]

—. 2011, GCN Circ., 11545 [LINK]

Cummings, J. R. & Barthelmy, S. D. 2011, GCN Circ., 11546 [LINK]

Cummings, J. R., Barthelmy, S. D., Baumgartner, W. H., Fenimore, E. E., Gehrels, N., Krimm, H. A., Markwardt, C. B., Page, K., Palmer, D. M., Parsons, A. M., Sakamoto,

T., Sato, G., Stamatikos, M., Tueller, J., & Ukwatta, T. N. 2009a, GCN Circ., 9980 [LINK]

Cummings, J. R., Copete, A., Grindlay, J., Barthelmy, S. D., Gehrels, N., & Guidorzi, C. 2008b, GCN Circ., 8415 [ADS]

Cummings, J. R., Copete, A., Grindlay, J., & Palmer, D. 2008c, GCN Circ., 7924 [ADS]

Cummings, J. R. & Krimm, H. 2009, GCN Circ., 9966 [LINK]

Cummings, J. R., Marisaldi, M., Fuschino, F., Labanti, C., Galli, M., Cocco, G. D., Yamaoka, K., Ohno, M., Fukazawa, Y., Takahashi, T., Tashiro, M., Terada, Y., Murakami, T., Makishima, K., & Hanabata, Y. 2009b, GCN Circ., 9835 [LINK]

Cummings, J. R., Palmer, D. M., Sbarufatti, B., & Gronwall, C. 2011, GCN Circ., 11813 [LINK]

D'Avanzo, P., Covino, S., Antonelli, L. A., Fugazza, D., Calzoletti, L., Campana, S., Chincarini, G., Conciatore, M. L., Cutini, S., D'Elia, V., Dalessio, F., Fiore, F., Goldoni, P., Guetta, D., Guidorzi, C., Israel, G. L., Masetti, N., Melandri, A., Meurs, E., Nicastro, L., Palazzi, E., Pian, E., Piranomonte, S., Stella, L., Stratta, G., Tagliaferri, G., Tosti, G., Testa, V., Vergani, S. D., & Vitali, F. 2008, GCN Circ., 7244 [LINK]

De Pasquale, M., Cummings, J., Markwardt, C., & Evans, P. 2008, GCN Report, 155 [LINK]

Elvis, M., Plummer, D., Schachter, J., & Fabbiano, G. 1992, ApJS, 80, 257 [ADS]

Evans, P. A. 2009a, GCN Circ., 8987 [LINK]

—. 2009b, GCN Circ., 8947 [LINK]

Evans, P. A., Copete, A., & Hoversten, E. A. 2009, GCN Report, 201 [LINK]

Evans, P. A. & Pasquale, M. d. 2008, GCN Circ., 7971 [LINK]

Evans, P. A., Schady, P., & Pasquale, M. d. 2008, GCN Circ., 7931 [LINK]

Fatkhullin, T. A., Sonbas, E., Turkey), U. o. C., & Castro-Tirado, A. J. 2008, GCN Circ., 8651 [LINK]

Fenimore, E. E. & Cannon, T. M. 1978, Appl. Opt., 17, 337 [ADS]

Frontera, F., Guidorzi, C., Montanari, E., Rossi, F., Costa, E., Feroci, M., Calura, F., Rapisarda, M., Amati, L., Carturan, D., Cinti, M. R., Fiume, D. D., Nicastro, L., & Orlandini, M. 2009, ApJS, 180, 192 [ADS]

Gehrels, N., Chincarini, G., Giommi, P., Mason, K. O., Nousek, J. A., Wells, A. A., White, N. E., Barthelmy, S. D., Burrows, D. N., Cominsky, L. R., Hurley, K. C., Marshall, F. E., Mészáros, P., Roming, P. W. A., Angelini, L., Barbier, L. M., Belloni, T., Campana, S., Caraveo, P. A., Chester, M. M., Citterio, O., Cline, T. L., Cropper, M. S., Cummings, J. R., Dean, A. J., Feigelson, E. D., Fenimore, E. E., Frail, D. A., Fruchter, A. S., Garmire, G. P., Gendreau, K., Ghisellini, G., Greiner, J., Hill, J. E., Hunsberger, S. D., Krimm, H. A., Kulkarni, S. R., Kumar, P., Lebrun, F., Lloyd-Ronning, N. M., Markwardt, C. B., Mattson, B. J., Mushotzky, R. F., Norris, J. P., Osborne, J., Paczynski, B., Palmer, D. M., Park, H.-S., Parsons, A. M., Paul, J., Rees, M. J., Reynolds, C. S., Rhoads, J. E., Sasseen, T. P., Schaefer, B. E., Short, A. T., Smale, A. P., Smith, I. A., Stella, L., Tagliaferri, G., Takahashi, T., Tashiro, M., Townsley, L. K., Tueller, J., Turner, M. J. L., Vietri, M., Voges, W., Ward, M. J., Willingale, R., Zerbi, F. M., & Zhang, W. W. 2004, ApJ, 611, 1005 [ADS]

Gehrels, N. & Mészáros, P. 2012, Science, Volume 337, Issue 6097, pp. 932- (2012). [LINK]

Gehrels, N., Ramirez-Ruiz, E., & Fox, D. B. 2009, ARA&A, 47, 567

Giacconi, R., Branduardi, G., Briel, U., Epstein, A., Fabricant, D., Feigelson, E., Forman, W., Gorenstein, P., Grindlay, J., Gursky, H., Harnden, F. R., Henry, J. P., Jones, C., Kellogg, E., Koch, D., Murray, S., Schreier, E., Seward, F., Tananbaum, H., Topka, K., Van Speybroeck, L., Holt, S. S., Becker, R. H., Boldt, E. A., Serlemitsos, P. J., Clark, G., Canizares, C., Markert, T., Novick, R., Helfand, D., & Long, K. 1979, ApJ, 230, 540 [ADS]

Golenetskii, S., Aptekar, R., Frederiks, D., Mazets, E., Pal'shin, V., Oleynik, P., Ulanov, M., Svinkin, D., & Cline, T. 2009a, GCN Circ., 9836 [LINK]

Golenetskii, S., Aptekar, R., Mazets, E., Pal'shin, V., Frederiks, D., Cline, T., Cummings, J., Barthelmy, S., Gehrels, N., & Krimm, H. 2008a, GCN Circ., 8676 [LINK]

Golenetskii, S., Aptekar, R., Mazets, E., Pal'shin, V., Frederiks, D., Oleynik, P., Svinkin, D., Ulanov, M., & Cline, T. 2008b, GCN Circ., 8412 [LINK]

Golenetskii, S., Aptekar, R., Mazets, E., Pal'shin, V., Frederiks, D., Oleynik, P., Ulanov, M., & Svinkin, D. 2009b, GCN Circ., 9968 [LINK]

Golenetskii, S., Aptekar, R., Mazets, E., Pal'shin, V., Frederiks, D., Oleynik, P., Ulanov, M., Svinkin, D., & Cline, T. 2008c, GCN Circ., 8610 [LINK]

—. 2009c, GCN Circ., 9171 [LINK]

—. 2009d, GCN Circ., 9976 [LINK]

Grindlay, J. & Copete, A. 2006–2011, *Swift* Guest Investigator program, cycles 3–7 proposals.

Grindlay, J. E. 2012, Memorie della Societa Astronomica Italiana Supplementi, 21, 147 [ADS]

Grindlay, J. E. & Hong, J. 2004, in Society of Photo-Optical Instrumentation Engineers (SPIE) Conference Series, ed. O. Citterio, Vol. 5168, 402–410 [ADS]

Grupe, D. 2009, GCN Circ., 9902 [LINK]

Grupe, D., Cummings, J. R., Hoversten, E., Barthelmy, S. D., Burrows, D. N., Roming, P., & Gehrels, N. 2009, GCN Report, 241 [LINK]

Grupe, D., Hoversten, E., & Cummings, J. 2009, GCN Circ., 9840 [LINK]

Guidorzi, C., Smith, R. J., Steele, I. A., Mundell, C. G., Bersier, D., Gomboc, A., O'Brien, P., & Tanvir, N. 2009, GCN Circ., 9176 [LINK]

Hakkila, J., Meegan, C. A., Pendleton, G. N., Fishman, G. J., Wilson, R. B., Paciesas, W. S., Brock, M. N., & Horack, J. M. 1994, ApJ, 422, 659 [ADS]

Harmon, B. A., Wilson, C. A., Fishman, G. J., Connaughton, V., Henze, W., Paciesas, W. S., Finger, M. H., McCollough, M. L., Sahi, M., Peterson, B., Shrader, C. R., Grindlay, J. E., & Barret, D. 2004, ApJS, 154, 585 [ADS]

Hiroi, K., Ueda, Y., Isobe, N., Hayashida, M., Eguchi, S., Sugizaki, M., Kawai, N., Tsunemi, H., Matsuoka, M., Mihara, T., Yamaoka, K., Ishikawa, M., Kimura, M., Kitayama, H., Kohama, M., Matsumura, T., Morii, M., Nakagawa, Y. E., Nakahira, S., Nakajima, M., Negoro, H., Serino, M., Shidatsu, M., Sootome, T., Sugimori, K., Suwa, F., Toizumi, T., Tomida, H., Tsuboi, Y., Ueno, S., Usui, R., Yamamoto, T., Yamazaki, K., & Yoshida, A. 2011, PASJ, 63, 677 [ADS]

Holland, S. T. 2008, GCN Circ., 8669 [LINK]

Holland, S. T., Copete, A., Page, K. L., & Pal'shin, V. 2008, GCN Report, 189 [LINK]

Hong, J., Allen, B., Grindlay, J., Barthelemy, S., Baker, R., Garson, A., Krawczynski, H., Apple, J., & Cleveland, W. H. 2011, Nuclear Instruments and Methods in Physics Research A, 654, 361 [ADS]

Immler, S. & Stratta, G. 2011, GCN Circ., 11551 [LINK]

Kaneko, Y., Preece, R. D., Briggs, M. S., Paciesas, W. S., Meegan, C. A., & Band, D. L. 2006, ApJS, 166, 298 [ADS]

Kann, D. A., Schulze, S., Hoegner, C., Klose, S., & Greiner, J. 2008, GCN Circ., 8420 [LINK]

Khamitov, I., Aleksandrovich, N., Burenin, R., Pavlinsky, M., Sunyaev, R., Bikmaev, I., Sakhibullin, N., Eker, Z., Kiziloglu, U., & Gogus, E. 2008, GCN Circ., 8418 [LINK]

Kienlin, A. v. & Bissaldi, E. 2008, GCN Circ., 8483 [LINK]

Kira, C., Hanabata, Y., Uehara, T., Takahashi, T., Fukazawa, Y., Enoto, T., Nakazawa, K., Makishima, K., Sugita, S., Yamaoka, K., Ohno, M., Kokubun, M., Suzuki, M., Takahashi, T., Nakagawa, Y. E., Tamagawa, T., Tashiro, M., Terada, Y., Urata, Y., Endo, A., Onda, K., Kodaka, N., Morigami, K., Sugasahara, T., Iwakiri, W., Sonoda, E., Yamauchi, M., Tanaka, H., Hara, R., Ohmori, N., Kono, K., Hayashi, H., & Hong, S. 2008, GCN Circ., 8445 [LINK]

Kono, K., Sonoda, E., Yamauchi, M., Ohmori, N., Hayashi, H., Noda, K., Daikyuji, A., Nishioka, Y., Ohno, M., Suzuki, M., Kokubun, M., Takahashi, T., Iwakiri, W., Tashiro, M., Terada, Y., Endo, A., Onda, K., Sugasahara, T., Urata, Y., Enoto, T., Nakazawa, K., Makishima, K., Yamaoka, K., Sugita, S., Nakagawa, Y. E., Tamagawa, T., Uehara,

T., Takahashi, T., Fukazawa, Y., Hanabata, Y., Hong, S., & Vasquez, N. 2009, GCN Circ., 9186 [LINK]

Kouveliotou, C., Meegan, C. A., Fishman, G. J., Bhat, N. P., Briggs, M. S., Koshut, T. M., Paciesas, W. S., & Pendleton, G. N. 1993, ApJ, 413, L101 [ADS]

Krimm, H. 2006, Swift/BAT Hard X-ray Transient Monitor [LINK]

Krimm, H., Barbier, L., Barthelmy, S. D., Cummings, J., Fenimore, E., Gehrels, N., Markwardt, C., Palmer, D., Parsons, A., Sakamoto, T., Sato, G., Sanwal, D., Stamatikos, M., & Tueller, J. 2006, The Astronomer's Telegram, 904, 1

Krivonos, R., Tsygankov, S., Lutovinov, A., Revnivtsev, M., Churazov, E., & Sunyaev, R. 2012, A&A, 545, A27 [ADS]

Levine, A. M., Lang, F. L., Lewin, W. H. G., Primini, F. A., Dobson, C. A., Doty, J. P., Hoffman, J. A., Howe, S. K., Scheepmaker, A., Wheaton, W. A., Matteson, J. L., Baity, W. A., Gruber, D. E., Knight, F. K., Nolan, P. L., Pelling, R. M., Rothschild, R. E., & Peterson, L. E. 1984, ApJS, 54, 581 [ADS]

Mao, J. 2008, GCN Circ., 8514 [LINK]

Mao, J., Guidorzi, C., & Margutti, R. 2008, GCN Circ., 8411 [LINK]

Mao, J., Guidorzi, C., Margutti, R., Cummings, J., Schady, P., Burrows, D., Roming, P., & Gehrels, N. 2008, GCN Report, 175 [LINK]

Markwardt, C., Barthelmy, S. D., Baumgartner, W., Copete, A., Cummings, J., Fenimore, E., Gehrels, N., Grindlay, J., Krimm, H., McLean, K., Palmer, D., Sakamoto, T., Sato, G., Stamatikos, M., Tueller, J., & Ukwatta, T. 2008, GCN Circ., 7937 [ADS]

Markwardt, C. B., Barthelmy, S. D., Cummings, J. C., Hullinger, D., Krimm, H. A., & Parsons, A. 2007, The Swift-BAT Software Guide, v6.3 edn., NASA/GSFC—BAT Instrument Team [LINK]

Markwardt, C. B., Tueller, J., Skinner, G. K., Gehrels, N., Barthelmy, S. D., & Mushotzky, R. F. 2005, ApJ, 633, L77 [ADS]

Marshall, F. E. & Sbarufatti, B. 2011, GCN Circ., 11817 [LINK]

Minowa, Y., Pyo, T. ., Terada, H., Aoki, K., & Kawai, N. 2009, GCN Circ., 8832 [LINK]

Myers, J. 2012, *Swift* website [LINK]

Nissinen, M. & Hentunen, V. 2009, GCN Circ., 9181 [LINK]

Norris, J. P., Gehrels, N., & Scargle, J. D. 2010, ApJ, 717, 411 [ADS]

Norris, J. P., Marani, G. F., & Bonnell, J. T. 2000, ApJ, 534, 248 [ADS]

Ohmori, N., Sonoda, E., Kono, K., Hayashi, H., Daikyuji, A., Nishioka, Y., Noda, K., Yamauchi, M., Ohno, M., Suzuki, M., Kokubun, M., Takahashi, T., Yamaoka, K., Sugita, S., Nakagawa, Y. E., Tamagawa, T., Hong, S., Vasquez, N., Hanabata, Y., Uehara, T., Takahashi, T., Fukazawa, Y., Iwakiri, W., Tashiro, M., Terada, Y., Endo, A., Onda, K., Sugasahara, T., Urata, Y., Enoto, T., Nakazawa, K., & Makishima, K. 2009, GCN Circ., 9992 [LINK]

Olivares, F., Rossi, A., Yoldas, A. K., Greiner, J., & Yoldas, A. 2009, GCN Circ., 8826 [ADS]

Page, K. L. 2009, GCN Circ., 9977 [LINK]

Page, K. L., Evans, P. A., & Holland, S. T. 2008a, GCN Circ., 8666 [LINK]

Page, K. L., Osborne, J. P., & Holland, S. T. 2008b, GCN Circ., 8683 [LINK]

Palmer, D. M., Barthelmy, S. D., Baumgartner, W. H., Cummings, J. R., Gehrels, N., Krimm, H. A., Markwardt, C. B., Melandri, A., Sakamoto, T., Stamatikos, M., Tueller, J., & Ukwatta, T. N. 2011, GCN Circ., 11818 [LINK]

Pélangeon, A., Atteia, J.-L., Nakagawa, Y. E., Hurley, K., Yoshida, A., Vanderspek, R., Suzuki, M., Kawai, N., Pizzichini, G., Boër, M., Braga, J., Crew, G., Donaghy, T. Q., Dezalay, J. P., Doty, J., Fenimore, E. E., Galassi, M., Graziani, C., Jernigan, J. G., Lamb, D. Q., Levine, A., Manchanda, J., Martel, F., Matsuoka, M., Olive, J.-F., Prigozhin, G., Ricker, G. R., Sakamoto, T., Shirasaki, Y., Sugita, S., Takagishi, K., Tamagawa, T., Villasenor, J., Woosley, S. E., & Yamauchi, M. 2008, A&A, 491, 157 [ADS]

Perley, D. A. 2008, GCN Circ., 8637 [LINK]

Perley, D. A. & Bloom, J. S. 2008, GCN Circ., 8631 [LINK]

Rau, A. 2009, GCN Circ., 9962 [LINK]

Read, A. M., Saxton, R. D., Esquej, M. P., Freyberg, M. J., & Altieri, B. 5 years of Science with XMM-Newton, ed. , U. G. BrielS. Sembay & A. Read, 137–139 [ADS]

Roming, P. W. A., Kennedy, T. E., Mason, K. O., Nousek, J. A., Ahr, L., Bingham, R. E., Broos, P. S., Carter, M. J., Hancock, B. K., Huckle, H. E., Hunsberger, S. D., Kawakami, H., Killough, R., Koch, T. S., McLelland, M. K., Smith, K., Smith, P. J., Soto, J. C., Boyd, P. T., Breeveld, A. A., Holland, S. T., Ivanushkina, M., Pryzby, M. S., Still, M. D., & Stock, J. 2005, Space Sci. Rev., 120, 95 [ADS]

Rossi, A., Kruehler, T., Greiner, J., & Olivares, F. 2009, GCN Circ., 8850 [LINK]

Rowlinson, B. A. & Page, K. L. 2009a, GCN Circ., 8828 [LINK]

—. 2009b, GCN Circ., 8840 [LINK]

Sakamoto, T., Barthelmy, S. D., Barbier, L., Cummings, J. R., Fenimore, E. E., Gehrels, N., Hullinger, D., Krimm, H. A., Markwardt, C. B., Palmer, D. M., Parsons, A. M., Sato, G., Stamatikos, M., Tueller, J., Ukwatta, T. N., & Zhang, B. 2008, ApJS, 175, 179

Sakamoto, T., Barthelmy, S. D., Baumgartner, W. H., Cummings, J. R., Fenimore, E. E., Gehrels, N., Krimm, H. A., Markwardt, C. B., Palmer, D. M., Parsons, A. M., Sato, G., Stamatikos, M., Tueller, J., Ukwatta, T. N., & Zhang, B. 2011, ApJS, 195, 2

Sakamoto, T., Donato, D., Gehrels, N., Okajima, T., Ukwatta, T. N., Urata, Y., & Wallace, C. 2009a, GCN Circ., 8830 [LINK]

Sakamoto, T., Sato, G., Barbier, L., Barthelmy, S. D., Cummings, J. R., Fenimore, E. E., Gehrels, N., Hullinger, D., Krimm, H. A., Lamb, D. Q., Markwardt, C. B., Palmer, D. M., Parsons, A. M., Stamatikos, M., Tueller, J., & Ukwatta, T. N. 2009b, ApJ, 693, 922 [ADS]

Saxton, R. D., Read, A. M., Esquej, P., Freyberg, M. J., Altieri, B., & Bermejo, D. 2008, A&A, 480, 611 [ADS]

Sbarufatti, B. 2011a, GCN Circ., 11814 [LINK]

—. 2011b, GCN Circ., 11820 [LINK]

Sbarufatti, B., Parola, V. L., & Mangano, V. 2008a, GCN Circ., 8605 [LINK]

—. 2008b, GCN Circ., 8612 [LINK]

Scargle, J. D. 1998, ApJ, 504, 405

Schady, P. 2009, GCN Circ., 8827 [LINK]

Schady, P. & Mao, J. 2008, GCN Circ., 8414 [LINK]

Schady, P., Marshall, F. E., & Sbarufatti, B. 2008, GCN Circ., 8606 [LINK]

Schady, P. & Stamatikos, M. 2008, GCN Circ., 7245 [LINK]

Siegel, M. H. & Page, K. L. 2009, GCN Circ., 9981 [LINK]

Skinner, G. K. 1995, Experimental Astronomy, 6, 1

Skinner, G. K., Ponman, T. J., Hammersley, A. P., & Eyles, C. J. 1987, Ap&SS, 136, 337

Starling, R. L. C., Evans, P. A., O'Brien, P. T., Guidorzi, C., & Stamatikos, M. 2008, GCN Circ., 7247 [LINK]

Starling, R. L. C. & Stamatikos, M. 2008, GCN Circ., 7243 [LINK]

Stratta, G. 2011, GCN Circ., 11565 [LINK]

Stratta, G., D'Elia, V., Evans, P. A., & Goad, M. R. 2011, GCN Circ., 11547 [LINK]

Stratta, G., D'Elia, V., Immler, S., Cummings, J. R., Barthelmy, S. D., Burrows, D. N., Siegel, M., & Gehrels, N. 2011, GCN Report, 317 [LINK]

Swift Science Center. 2008, The *Swift* Technical Handbook, v4.1 edn. [LINK]

Terada, Y., Tashiro, M., Urata, Y., Endo, A., Onda, K., Kodaka, N., Morigami, K., Sugasahara, T., Iwakiri, W., Sugita, S., Yamaoka, K., Ohno, M., Kokubun, M., Suzuki, M., Takahashi, T., Nakagawa, Y. E., Tamagawa, T., Enoto, T., Nakazawa, K., Makishima, K., Uehara, T., Takahashi, T., Fukazawa, Y., Kira, C., Hanabata, Y., Sonoda, E., Yamauchi, M., Tanaka, H., Hara, R., Ohmori, N., Kono, K., Hayashi, H., & Hong, S. 2008, GCN Circ., 8638 [LINK]

Tueller, J., Baumgartner, W. H., Markwardt, C. B., Skinner, G. K., Mushotzky, R. F., Ajello, M., Barthelmy, S., Beardmore, A., Brandt, W. N., Burrows, D., Chincarini, G., Campana, S., Cummings, J., Cusumano, G., Evans, P., Fenimore, E., Gehrels, N., Godet, O., Grupe, D., Holland, S., Kennea, J., Krimm, H. A., Koss, M., Moretti, A., Mukai, K., Osborne, J. P., Okajima, T., Pagani, C., Page, K., Palmer, D., Parsons, A., Schneider, D. P., Sakamoto, T., Sambruna, R., Sato, G., Stamatikos, M., Stroh, M., Ukwata, T., & Winter, L. 2010, ApJS, 186, 378 [ADS]

Tueller, J., Mushotzky, R. F., Barthelmy, S., Cannizzo, J. K., Gehrels, N., Markwardt, C. B., Skinner, G. K., & Winter, L. M. 2008, ApJ, 681, 113 [ADS]

Updike, A., Greiner, J., Kruehler, T., Schrey, F., Nicuesa Guelbenzu, A., & Klose, S. 2011, GCN Circ., 11815 [LINK]

Updike, A. C., Clemens, C., Greiner, J., & Afonso, P. 2009, GCN Circ., 8958 [LINK]

Updike, A. C. & Hartmann, D. H. 2009a, GCN Circ., 8831 [LINK]

—. 2009b, GCN Circ., 8829 [LINK]

Willmore, A. P., Bertram, D., Watt, M. P., Skinner, G. K., Ponman, T. J., Church, M. J., Herring, J. R. H., & Eyles, C. J. 1992, MNRAS, 258, 621